Coffin, M.F., Frey, F.A., Wallace, P.J., et al., 2000
Proceedings of the Ocean Drilling Program, Initial Reports Volume 183

5. SITE 1137[1]

Shipboard Scientific Party[2]

BACKGROUND AND OBJECTIVES

Site 1137 lies on Elan Bank (Houtz et al., 1977), the Kerguelen Plateau's large western salient, which is flanked on three sides by presumed Cretaceous oceanic crust of the Enderby Basin (Fig. **F1**). Before we drilled Site 1137, no basement samples had been retrieved from Elan Bank; hence, the age and geochemistry of the igneous crust, and its relationship to the contiguous central and southern Kerguelen Plateau, were unknown. We located Site 1137 on Australian Geological Survey Organisation *Rig Seismic* multichannel seismic (MCS) line RS179/601 (Fig. **F2**). The site lies at a depth of 1005 m on Elan Bank's eastern crest. We chose this location as representative of the entire Elan Bank on the basis of its relatively simple structural setting and thin sedimentary section (Fig. **F3**). Interpreted igneous basement contains some internal reflections. The top of the basaltic basement has an apparent dip of 1.5° to the east (assuming a sediment velocity of 1.9 km/s), and a strong intrabasement reflection beneath has an apparent dip of 4.8° to the east (assuming a basement velocity of 3.8 km/s). Overlying basement, we observed two seismic sequences, an extremely thin (~25 m, or 0.02 s two-way traveltime [TWT]) lower sequence characterized by a velocity of 2.3 km/s, and an thicker (~200 m, or 0.21 s TWT) upper sequence with a velocity of 1.9 km/s (Fig. **F3**).

Summary of Objectives

The main objectives at this site were to

1. Characterize the petrography and compositions of the lavas;
2. Determine the age of the lavas, testing the hypothesis that the uppermost igneous basement of Elan Bank is ~85 Ma, the age

F1. Satellite-derived free-air gravity map of the Kerguelen Plateau, **p. 62.**

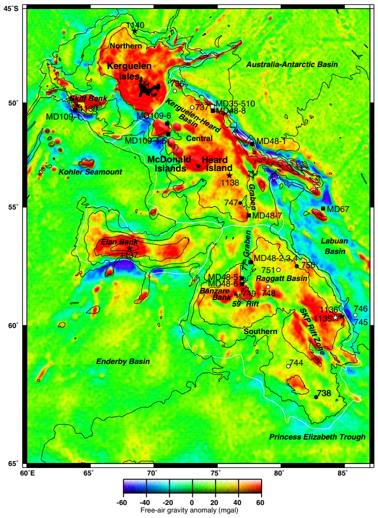

F2. Location of Site 1137 and site-survey data, **p. 64.**

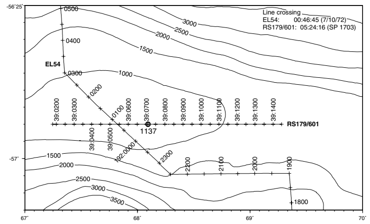

F3. *Rig Seismic* RS179/601 multichannel seismic profile across Site 1137, **p. 65.**

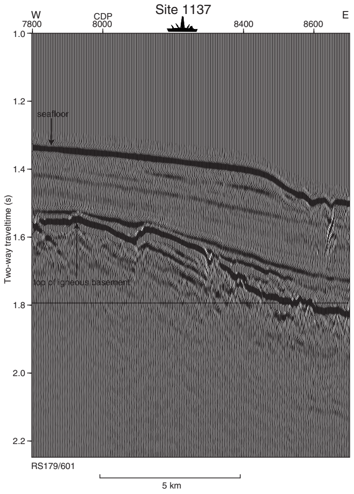

---

[1] Examples of how to reference the whole or part of this volume.
[2] Shipboard Scientific Party addresses.

yielded by basalts from Site 747 on the central Kerguelen Plateau (Pringle et al., 1994; Storey et al., 1996);
3. Determine the physical characteristics of the lava flows;
4. Identify the environment of eruption (subaerial or submarine);
5. Obtain minimum estimates for the age of basement from overlying sediment;
6. Estimate the duration of possible subaerial and shallow marine environments from the sedimentary and igneous record;
7. Determine the facies of the seismic stratigraphic sequences;
8. Define the ages of seismic sequence boundaries; and
9. Determine the paleoceanographic history of this high latitude site.

OPERATIONS

Site 1137

The 1027-km transit from Site 1136 to Site 1137 was made in 57 hr at an average speed of 9.7 kt. The ship arrived at Site 1137 on New Year's Eve, 31 December 1998. Weather conditions upon arrival were quite mild compared to those at departure from the last site. At 2100 hr on 31 December 1998, we deployed a beacon on the precise Global Positioning System (GPS) coordinates for Site 1137.

Hole 1137A

We spudded Hole 1137A at 0215 hr on 1 January 1999 using the rotary core barrel (RCB) coring assembly and an RBI C-4 core bit. Accurate identification of the seafloor is quite difficult with the RCB system. The driller reported some weight loss around the 3.5-kHz precision depth recorder depth of 1020.4 mbrf. The bit was advanced a full 9.5 m from the last connection at 1016.0 m, and, when recovered, the core barrel had 9.62 m of recovery. Because an accurate seafloor depth was not considered essential to the science objectives, we did not take the time to attempt recovering mudline. Coring continued with a seafloor depth adjusted to the rig floor of 1016.0 m below rig floor, equivalent to 1004.5 m below sea level.

Continuous wireline coring proceeded in homogenous white foraminifer-bearing nannofossil ooze through Core 183-1137A-21R to a depth of 1215.5 m (199.5 meters below seafloor [mbsf]). No chert was encountered. Recovery for this interval averaged 53.8% but was highly variable, ranging from 0% to 108%. A summary of core numbers, depths, and recovery is given in Tables T1 and T2. The average rate of penetration (ROP) was 40.1 m/hr. The formation then became glauconite-bearing sandy packstone with abundant shell fragments until contacting basement at ~1240 m (~224 mbsf). The average recovery in this 24.5-m interval was an extremely poor 10.7%, and the average ROP dropped to 30.5 m/hr. Basement consisted of a series of basalt flows interspersed with volcaniclastic sandstone, conglomerate, and crystal-vitric tuff.

T1. Coring summary, p. 168.

T2. Expanded coring summary, p. 169.

After recovering Core 183-1137A-37R from 327.5 mbsf, a short trip was made to recover five knobby drilling joints. This was to enable the drilling depth objective of 374.0 mbsf to be reached using knobby joints. These joints were required because of the slow ROP and frequent severe sea states experienced while on site. Upon returning to bottom, ~1.3 m of hard fill was found. While attempting to ream through this material, the weather and sea state continued to deteriorate to the point where the heave compensator was exceeding its stroke length. In addition, the yellow (2%) dynamic positioning warnings were becoming more frequent. The pipe was pulled to the top of the hole and hung off using knobby joints at a depth of 1336.0 m (320.0 mbsf). After waiting on weather for 6.75 hr, the weather conditions moderated and the pipe was run back to bottom. Only 30 min was required to clean out the hole, and coring resumed. Coring was terminated with Core 183-1137A-46R at a total depth of 371.2 mbsf. This was ~150 m into basement and satisfied the scientific depth objective for this site. Average recovery in basement was 69.2%, but recovery was quite variable, ranging from 19% to 102%. A total of 14 half cores were cut to maximize recovery. The overall ROP averaged 4.5 m/hr; however, it varied considerably from 5.5 to 1.7 m/hr.

A wiper trip was initiated to prepare the hole for wireline logging; however, this was halted because of deteriorating weather conditions when the pipe reached a depth of 120.3 mbsf. After waiting on weather for 10.75 hr, the wiper trip was completed. The hole was swept with a 25-bbl sepiolite mud pill, the bit released, and 112 bbl of sepiolite mud was displaced into the hole for logging. The pipe was pulled to a depth of 100.3 mbsf, and preparations for logging began. The first logging run was with the triple combo suite of tools, which includes the dual laterolog (DLL) for resistivity, the accelerator porosity sonde (APS) for porosity, and the high-temperature lithodensity tool. Also included in this tool string was the hostile-environment natural gamma-ray sonde (HNGS) and the Lamont-Doherty Earth Observatory (LDEO) high-temperature/acceleration/pressure tool (TAP). This run was very successful, reaching a depth of 367.0 mbsf (~4 m above bottom). The next run was with the Formation MicroScanner (FMS) and dipole shear sonic imager (DSI) tool suite. A natural gamma-ray tool was included for calibrating between logging runs. This deployment was also very successful, reaching the same depth as the first run. During the second pass with the FMS-DSI, the tool would not pass a tight spot at ~174 mbsf. Unfortunately, the tool was stuck at that point, requiring ~3,500 lb of force to pull it free. In looking at the FMS caliper log, it appeared that a fairly large portion of the hole (~75 m) had closed in significantly, in places to a diameter of ~4 in. Because it was not likely that the well seismic tool would pass this spot, the remainder of the wireline logging program was canceled for this hole. Opening up the hole with open-ended pipe was unlikely to be successful and would have put the drill string and bottom-hole assembly at risk.

While the drill string was being recovered, several attempts were made to release the positioning beacon. While it acknowledged the commands, on each occasion the beacon failed to release and was ultimately left on the seafloor. The pipe trip was completed when the mechanical bit release reached the rig floor at 1645 hr. The ship was immediately secured for transit, and, at 1645 hr on 6 January 1999, we were under way for Site 1138.

LITHOSTRATIGRAPHY

Introduction

Site 1137 is located in 1005 m of water on Elan Bank, a submarine promontory of the western margin of the Kerguelen Plateau. Hole

1137A was rotary cored continuously to a depth of 371 mbsf. Sediments were recovered from 0 to 224 mbsf, and basalts with interbedded sedimentary and volcaniclastic rock layers were recovered from the lower 147.2 m of the hole (Fig. F4). The sedimentary section above basaltic basement consists of ~200 m of pelagic ooze that overlies about 20 m of glauconitic sandy packstone (Fig. F5; Table T3). This packstone rests unconformably on basaltic basement. We recognize three sedimentary lithologic units (I–III) in the upper part (0–224 mbsf) of Hole 1137A (Figs. F4, F5). The basement basalts and their interbedded sediments are designated lithologic Unit IV and are subdivided into basement Units 1–10 (Fig. F4). Various aspects of these basement units are described in **"Igneous Petrology,"** p. 28, **"Physical Volcanology,"** p. 13, and **"Alteration and Weathering,"** p. 38. In this section, we describe the sedimentary and volcaniclastic rocks of Unit IV (basement Units 5, 6, and 9) (Fig. F6; Table T3). Core recovery varied from good to poor throughout the sedimentary sections of Hole 1137A (Fig. F4).

F4. Composite stratigraphic section, p. 66.

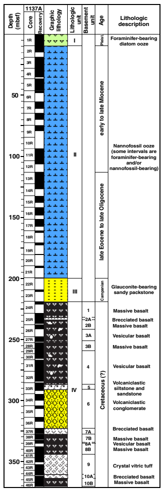

Unit I

Interval: 183-1137A-1R-1, 0 cm, to 1R-CC, 10 cm
Depth: 0–9.50 mbsf
Age: middle Pleistocene

Unit I is foraminifer-bearing diatom ooze (Fig. F5; Table T3). Radiolarians and silicoflagellates are present as minor components. Foraminifers decrease in abundance downcore. Most of the unit is very light gray; however, the top of the unit (interval 183-1137A-1R-1, 0–123 cm) is very pale brown. The ooze has a carbonate content of 51% (Sample 183-1137-1R-1, 90 cm). X-ray diffraction (XRD) data show opal-A with minor traces of opal-CT and very minor quartz. Sand- to granule-sized grains of basalt are dispersed throughout Core 183-1137A-1R. An angular pebble-sized fragment of basalt is found in interval 183-1137A-1R-4, 70–71 cm, an angular pebble-sized fragment of pumice is found in interval 183-1137A-1R-2, 70–71 cm, and an angular granule of quartz is found in interval 183-1137A-1R-5, 18–19 cm. All sections of Core 183-1137A-1R are highly disturbed (soupy); thus, these coarse materials were probably dispersed in the ooze by drilling disturbances. Interval 183-1137A-1R-2, 68–120 cm, contains angular 2- to 7-cm-sized pieces of white ooze dispersed in an ooze matrix. In Sections 183-1137A-1R-3 through 1R-5, similar white clasts are deformed into clumps and streaks. Again, these dispersed, deformed fragments probably result from drilling disturbance, rather than primary mass-wasting (e.g., debris flow) processes.

F5. Composite stratigraphic section for Hole 1137A from 0 to ~225 mbsf, p. 67.

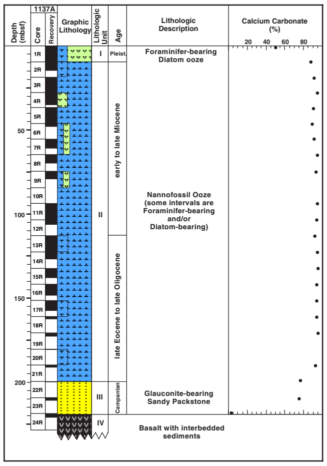

T3. Summary of lithologic units, p. 174.

Unit II

Interval: 183-1137A-2R-1, 0 cm, to 21R-CC, 10 cm
Depth: 9.50–199.50 mbsf
Age: late Miocene to Eocene

Unit II is white nannofossil ooze (Fig. F5; Table T3). Most of the ooze is homogeneous, and bioturbation is not apparent. In the upper part of the hole, diatoms are common to abundant in the sediments of Cores 183-1137A-2R through 9R. Some intervals of Cores 183-1137A-2R, 6R, 7R, 9R, 13R, 17R, and 20R are foraminifer-bearing nannofossil ooze. Radiolarians are present in Cores 183-1137A-2R-1 through 12R-1. Benthic foraminifers were observed in the lower part of Unit II (Cores 183-

F6. Composite stratigraphic section for Hole 1137A from ~275 to 370.16 mbsf, p. 68.

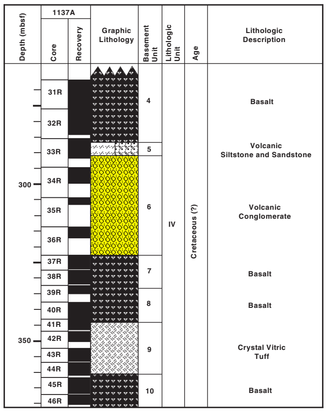

1137A-14R, 15R, 17R, and 19R) (i.e., mainly in the Oligocene sediments). The carbonate content of sediments in Unit II ranges from 88 to 96 wt% $CaCO_3$ (Fig. **F5;** Table **T4**) with the lower values in Cores 183-1137A-2R through 7R. These lower values probably reflect the presence of diatoms (amorphous silica), as the XRD analyses show no significant amount of minerals other than calcite throughout Unit II.

T4. XRD results and carbonate contents, **p. 175.**

Silt-sized black pyrite nodules are disseminated through intervals 183-1137A-13R-6, 99–101 cm; 13R-6, 137–138 cm; 16R-1, 135–142 cm; 17R-1, 90–115 cm; and 19R-1, 8–9 cm. Pebbles and sand-sized grains of basalt are scattered through Core 183-1137A-2R. Interval 183-1137A-6R-1, 85–94 cm, contains disseminated silt-sized shards of yellow palagonitized glass and a pebble of black basalt; however, the pebble, which is found along the edge of the core, may not be in place. Intervals 183-1137A-15R-3, 25–44 cm, and 16R-1, 12–25 cm, contain slightly darker clay-rich layers with sparse fragments of volcanic glass. A short interval (interval 183-1137A-19R-2, 0–27 cm) of light greenish gray (5G8/1), indurated nannofossil chalk is highly burrowed. Dark silt-sized grains are sparsely disseminated through intervals 183-1137A-21R-1, 70–126 cm, and 21R-CC, 1–8 cm. A major unconformity apparently separates Units II and III (see **"Biostratigraphy,"** p. 8); however, the lower contact of Unit II was not recovered.

Unit III

Interval: 183-1137A-22R-1, 0 cm, to 24R-1, 71 cm
Depth: 199.50 to 219.51 mbsf
Age: Campanian

Unit III is predominantly glauconite-bearing sandy packstone (Fig. **F5;** Table **T3**). The upper 25 cm of this unit (interval 183-1137A-22R-1, 0–25 cm) consists of light gray, well-cemented packstone with abundant bioclasts and minor dispersed grains of glauconite. A concentration of large (as much as 1 cm) shell fossils, including an inoceramid, is found in interval 183-1137A-22R-1, 10 to 12 cm (Fig. **F7**). This uppermost interval grades into very light gray to green ("salt and pepper") glauconite-bearing sandy packstone, which grades downward from fine to medium sand-sized grains. A thin section from near the top of the unit (Sample 183-1137A-22R-1, 26–33 cm) (Table **T5**) reveals the composition to be 30% clay-sized carbonate matrix, 25% quartz sand, 25% brachiopods, bivalves and ostracodes, 15% glauconite, 5% benthic foraminifers with rare planktonic foraminifers, and rare sponge spicules. Many intraparticle pores are filled with chalcedony cement. However, many dissolution pores of bivalve shells (aragonite) are still open and undeformed, which suggests that dissolution has occurred after lithification, probably in deep water below the aragonite compensation depth. Carbonate content is high (75–77 wt%) throughout most of Unit III but abruptly drops to only 3 wt% $CaCO_3$ (Sample 183-1137A-24R-1, 40–41 cm) near the base (Fig. **F5;** Table **T4**). Petrographic study of a thin section from near the base of the unit (Sample 183-1137A-24R-1, 35–38 cm) (Table **T5**) has 40% glauconite, 40% brown silicified matrix, 15% pore-filling opal, and 5% bioclasts and mineral grains, including shell fragments, benthic and planktonic foraminifers, a possible ooid, and brown hornblende. XRD analysis of this sample shows the presence of quartz, opal-A or glass, opal-CT, glauconite, calcite, pyrite, hematite(?), and marcasite(?). Hence, the packstone grades into a glauconite-bearing sandstone just above the base of the unit. Unit III rests unconformably on massive ba-

F7. Glauconite-bearing sandy packstone near and at the top of Unit III, **p. 69.**

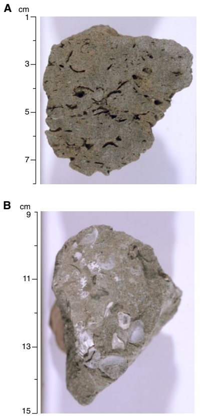

T5. Summary of thin sections, **p. 176.**

salt (basement Unit 1 of Unit IV). The absence of a brecciated top on this lava flow suggests a period of erosion before deposition of Unit III began (see "Physical Volcanology," p. 13).

Unit IV

Interval: 183-1137A-24R-1, 71 cm, to 46R-3, 36 cm
Depth: 219.51–370.17 mbsf
Age: Campanian or older

Lithologic Unit IV consists of basalt flows and interbedded volcaniclastic and sedimentary rocks (Figs. F4, F6; Table T3). Unit IV is subdivided into 10 basement units, which include seven basalt flows and three intervals of volcaniclastic sedimentary rocks. The volcanic basement units are described in "Physical Volcanology," p. 13, "Igneous Petrology," p. 28, and "Alteration and Weathering," p. 38. In this section, we describe the sedimentary features of the volcaniclastic and sedimentary rocks of basement Units 5, 6, and 9. Additional description of other features of basement Units 5, 6, and 9 (e.g., composition of clasts) may be found in "Physical Volcanology," p. 13, "Igneous Petrology," p. 28, and "Alteration and Weathering," p. 38.

Basement Unit 5 (interval 183-1137A-33R-1, 122 cm, to 33R-4, 121 cm; 286.72–291.01 mbsf) is a 4.3-m-thick succession of interbedded dark greenish gray crystal-lithic volcanic siltstones and light gray crystal-lithic volcanic sandstones (Fig. F6; Table T3). A thin section (Sample 183-1137A-33R-3, 50–53 cm) (Table T5) shows angular, well-sorted medium sand composed of mainly volcanic lithic grains, minor feldspars and quartz, and traces of garnet, hornblende, and biotite (see "Igneous Petrology," p. 28, for additional description of grain compositions). Beds are thin to medium in thickness. Several beds are normally graded (e.g., from silt- to medium-sand-sized in interval 183-1137A-33R-3, 42–53 cm) (Fig. F8A). Many sandstone beds show sharp, irregular bases. Some sandstone beds have gradational tops, but others have sharp, irregular tops. A few sandstone beds show subtle, low-angle cross-stratification (e.g., interval 183-1137A-33R-3, 82–90 cm) (Fig. F8B). Some siltstone and sandstone beds show parallel laminations. Burrows are rare. Thin black flakes (1 mm × 2 cm) that appear to be fragments of coal are observed within at least one sandstone bed (interval 183-1137A-33R-4, 102–106 cm). The beds are locally broken along small normal faults with ~1-cm offsets and a few small areas of ductilely deformed sediment suggest minor soft-sediment deformation (see "Structural Geology," p. 43). The uppermost sediment of this basement unit (interval 183-1137A-33R-1, 123–129 cm) is black and dense and may have been metamorphosed by the overlying lava flow.

F8. Normally graded bed grading and cross-stratification in basement Unit 5, p. 70.

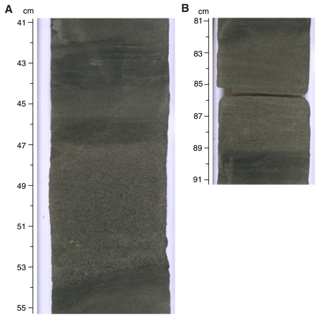

Basement Unit 6 (interval 183-1137A-33R-4, 121 cm, to 37R-1, 0 cm; 291.01–322.80 mbsf) is a thick (31.8 m) unit of mainly gray lithic volcanic conglomerate (Figs. F6, F9; Table T3). In cores, stratification is not apparent except for one sand layer. The downhole logs clearly show other fine-grained layers that separate thick conglomerate beds (see "Downhole Measurements," p. 54). Grain sizes within the conglomerate range from granules to small boulders. Grains are well rounded and most are equant. Colors are light gray to rusty brown. Most intervals are clast supported, but matrix-supported intervals also are present. The matrix is mostly coarse, well-sorted sand with calcareous cement. Pebbles and cobbles in interval 183-1137A-34R-3, 20–100 cm, appear to display imbricate structure with the long axes of pebbles oriented at an-

F9. Examples of conglomerates in basement Unit 6, p. 71.

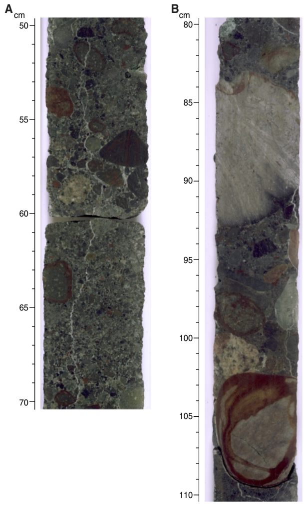

gles of 35°–50° from horizontal (Fig. **F9C**). The conglomerate is slightly polymictic. The clasts are mainly volcanic rocks but also include rare granitoid and garnet-biofite gneiss (see **"Igneous Petrology,"** p. 28). Many of the pebbles and cobbles display concentric weathering rinds (see Fig. **F9**).

Basement Unit 9 (interval 183-1137A-41R-1, 103 cm, to 44R-4, 49 cm; 344.03–360.67 mbsf) is a 16.6-m-thick succession of crystal-vitric tuff (Fig. **F6;** Table **T3**). The tuff is composed of ~40% coarse (1–2 mm) angular crystals of white sanidine and <5% lithic clasts enclosed within a light to dark green dense matrix. The distribution of white crystals in a green matrix produces a "salt and pepper" appearance. The dense matrix is composed of green clay and felsic glass shards (see **"Igneous Petrology,"** p. 28, and **"Physical Volcanology,"** p. 13). Dark green blebs (~1 mm in length) are common in this matrix; in some intervals, they are elongate and define a subtle horizontal fabric. Otherwise, the entire unit is massive and without visible sedimentary structures. The lithic clasts, dispersed through most intervals, include well-rounded to angular granules and pebbles as much as 5 cm in diameter. These clasts are composed predominantly of basalt and felsic materials (Fig. **F10**). At least one ragged, flattened pumice fragment is present within this unit. A rounded pebble (2 cm × 1 cm) of garnet-biotite gneiss is present near the base of the tuff (Sample 183-1137A-44R-4, 44–46 cm). A 1-cm-thick layer of gray siltstone is at the base of the tuff (interval 183-1137A-44R-4, 48–49 cm), and the top centimeter of the tuff (interval 183-1137A-41R-1, 103–104 cm) is brown (oxidized) and contains only sparse K-feldspar crystals (interval 183-1137A-41R-1, 112–113 cm). Interval 183-1137A-41R-1, 104–112 cm, contains several pieces of black dense rock with disseminated small feldspar crystals.

F10. Crystal-vitric tuff from basement Unit 9, **p. 73.**

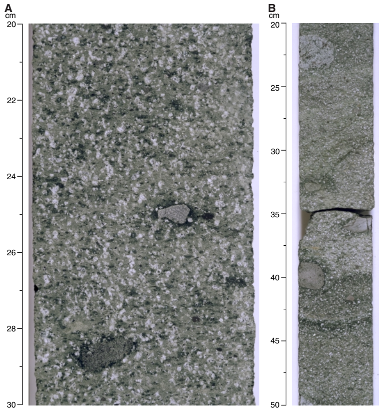

Discussion

The basaltic lava flows and interbedded volcaniclastic sediments, recovered from the uppermost basement rocks (Unit IV) of Elan Bank (Site 1137) formed before late Campanian time (~75 Ma; see **"Biostratigraphy,"** p. 8). Silt and sand accumulated in association with the conglomerates but also intermingled with the lava flows. For example, silts and sands are observed to infiltrate into lava-flow Units 3, 7, and 10 (see **"Physical Volcanology,"** p. 13). Siltstone and sandstone constitute a discrete fine-grained unit (basement Unit 5) on top of the conglomerates (basement Unit 6).

Our observations cannot constrain the depositional environment of the crystal-vitric tuff (basement Unit 9). Larger pebbles dispersed (i.e., "floating") throughout the matrix indicate that if deposition was by gravity-controlled processes, then this sediment was deposited by a plastic (laminar) mass flow, such as a sandy debris flow.

The conglomerates of basement Unit 6 clearly indicate that Site 1137 was proximal to a region of high relief. The absence of marine microfossils, the probable occurrence of coal in basement Unit 5 (Core 183-1137A-33R-4, 102–105 cm), and oxidized tops on basaltic lava flows strongly suggest that the environment was nonmarine. Within an interstice of a lava flow near the basement Unit 3/Unit 4 contact (interval 183-1137A-29R-2, 57–64 cm), mud drapings, graded beds, and "mud chip" sand (resedimented desiccated mud drapings) indicate deposition by flowing ground water in a vadose environment. Also, baked siltstones beneath lava flows of basement Units 4 and 8 indicate a nonmarine environment (see **"Physical Volcanology,"** p. 13).

Sedimentary features of basement Units 5 and 6 are consistent with a high-energy fluvial (braided stream) environment. The moderate size sorting and an interval of apparently imbricated pebbles in the conglomerates of Unit 6 (Fig. F9C) suggest fluvial deposition. The imbricated pebbles have apparent dips of 35°–50°, which is consistent with a braided river system (Reineck and Singh, 1980). In the overlying silts and sands of basement Unit 5, normally graded beds, subtle cross-stratification, and paucity of burrows are also consistent with fluvial deposition.

Following cessation of basaltic volcanism, at least minor subaerial erosion occurred (Unit IV–Unit III unconformity) before the area subsided into a quiet shallow marine setting during late Campanian time (~75 Ma). Littoral facies were not observed at Site 1137. The glauconite-bearing sandy packstones of Unit III suggest that carbonate and quartz sand were transported to a quiet marine environment where interstices were filled with micrite and glauconite was formed.

A major hiatus exists from Late Cretaceous to late Eocene time at this drill site. Subsequently, the pelagic oozes of Unit II accumulated in a deep marine environment from latest Eocene through late Miocene time (as Broken Ridge and the Kerguelen Plateau separated along the Southeast Indian Ridge).

Diatom ooze records the movement of a high productivity zone (Polar Frontal Zone) into the region sometime before Pleistocene time (Mackensen et al., 1992), and the paucity of calcareous nannofossils suggests decreased sea-surface temperature (Wei and Wise, 1992). The basalt sand in Unit I could be ice-rafted debris from Antarctica; however, the predominantly volcanic material points to a local source.

BIOSTRATIGRAPHY

Site 1137 was drilled primarily to establish the age and rock types forming Elan Bank, a shallow western salient of the central and southern Kerguelen Plateau. The hole penetrated 219.4 m of sediment with 59% recovery. In the first core, a disconformity separates a middle Pleistocene diatom ooze (lithologic Unit I) from an expanded 190-m-thick upper Miocene to uppermost Eocene nannofossil ooze section, which is remarkably devoid of chert (lithologic Unit II). This is underlain by a 20-m-thick glauconitic volcanic sand (lithologic Unit III) in which best recovery was in the last sediment core above basaltic basement. This sand contains exceptionally well-preserved foraminifers, calcareous nannofossils, and a few dinoflagellates and spores dated as late Campanian in age, between ~72 and 76 Ma by a conservative estimate, but between ~74 and 75 Ma using more narrowly defined biostratigraphic criteria based on Leg 183 preliminary drilling results (see discussion below on **"Basal Sediment Age,"** p. 12). This provides a minimum age for the basaltic basement beneath the sediments. The basement may be somewhat older here, as seismic stratigraphic studies suggest that we have sampled the top of a basal sedimentary unit that thickens east of the site (see **"Background and Objectives,"** p. 1, and **"Seismic Stratigraphy,"** p. 52).

Sedimentation rates in Unit II pelagic sediments are exceptionally high (20 m/m.y.) (Fig. F11). Because the Tertiary sequence of Elan Bank has not been diluted by fine clastic material as at Sites 1138–1140 to the north and northeast, these high rates indicate high siliceous and calcar-

F11. Site 1137 age-depth plot, **p. 74.**

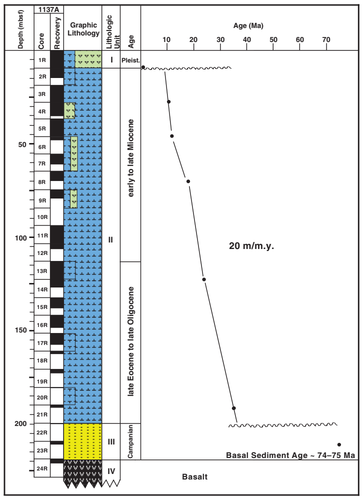

eous planktonic productivity in this locality, which is ~6°S of the present-day Polar Front (Antarctic Convergence).

Calcareous Nannofossils and Diatoms

We examined smear slides prepared for calcareous nannofossil studies of core-catcher samples as well as for diatoms in the Neogene. Diatom preservation was good in the Neogene, and biostratigraphic control by coccoliths was poor because of high-latitude assemblages of low diversity. We made no attempt to process samples for diatom study, and our preliminary results could be greatly improved by shore-based study by diatom specialists. Sample 183-1137A-1R-CC from foraminifer-bearing diatom ooze of lithologic Unit I contains no calcareous nannofossils but does contain abundant diatoms from the *Actinocyclus ingens* Zone. Although the nominate taxon is abundant, we noted no *Fragilariopsis barronii,* indicating a mid-Pleistocene age for this sample.

Nannofossils are abundant in Sample 183-1137A-2R-CC, which we assigned to the combined Zone CN11–CN5b, but diatoms are few; thus, we could not determine a more precise age. Nannofloras in Samples 183-1137A-3R-CC to 4R-CC are dominated by reticulofenestrids, particularly *R. perplexa,* and also belong to Zone CN11–CN5b. They also contain common *Denticulopsis dimorpha,* indicating a diatom age between 10.6 and 11.7 Ma (assuming no *Nitzschia denticuloides* are present).

Sample 183-1137A-5R-CC contains the diatom *Denticulopsis dimorpha,* but the nannoflora is strongly dominated (95% of the assemblage) by *Cyclicargolithus floridanus/abisectus,* indicating the top of the combined Zone CN5a–CN3. This zone continues downhole through the next two core-catcher samples. Sample 183-1137A-6R-CC contains rare *Pontosphaera multipora* and is dominated by approximately equal numbers of reticulofenestrids and *Coccolithus pelagicus,* whereas the subjacent core catcher (7R-CC) contains the first downhole occurrences of *Sphenolithus moriformis* (rare) and *Discoaster* sp. cf. *D. deflandrei* (heavily overgrown) in the hole.

Calcidiscus leptopora/macintyrei is absent in Sample 183-1137A-8R-CC, which we therefore assigned to the combined lower Miocene Zone CN2–CN1. Approximately 65% of the assemblages is composed of *Cyclicargolithus* and 30% of *Coccolithus pelagicus; Coccolithus miopelagicus, Discoaster* sp. cf. *D. deflandrei, Sphenolithus moriformis,* and *Helicosphaera granulata* are few. We also assigned Samples 183-1137A-9R-CC to 12R-CC to Zone CN2–CN1, with the exception of 10R-CC, for which there was no core. Minor amounts of Oligocene taxa are reworked in these samples. *Coccolithus miopelagicus* is very abundant, and *C. pelagicus* and small reticulofenestrids strongly dominate Sample 183-1137A-11R-CC. On the other hand, *Cyclicargolithus floridanus/abisectus* constitute about 10% of the assemblage in Sample 183-1137A-12R-CC.

Large (up to 18 µm) *Reticulofenestra bisecta* are abundant in Sample 183-1137A-13R-CC, where they mark the top of the Oligocene and the zone of the same name. The nominate taxon for the next zone downhole, *Chiasmolithus altus,* is abundant (~5% of the assemblage) in Sample 183-1137A-14R-CC, which is still dominated by *Cyclicargolithus* (about 95%). *Reticulofenestra bisecta* is small (up to 12 µm) and only few to common. We also assigned Samples 183-1137A-14R-CC to 18R-CC to the *Chiasmolithus altus* Zone. *Zygrhablithus bijugatus* are rare and quite possibly reworked in Sample 183-1137A-15R-CC, but common in Sample 16R-CC. The succession of these three last occurrence datums are apparently quite consistent at all Leg 183 sites at which they have been encountered (Sites 1137 to 1140). Thus, the dissolution-susceptible *Z. bijugatus* can serve as a useful guide fossil on the central and northern Kerguelen Plateau, where the drill sites are all well above the Oligocene calcite compensation depth.

Isthmolithus recurvus, Reticulofenestra umbilica/hillae (up to 20 µm), *Chiasmolithus altus,* and *Clausicoccus fenestratus* are abundant to very abundant in Sample 183-1137A-19R-CC; *Chiasmolithus oamaruensis* is common to few. The co-occurrence of the first two taxa may indicate a hiatus within the core. Although the range of *I. recurvus* crosses the Oligocene/Eocene boundary, abundant *C. fenestratus* plus the strong dominance of *C. altus* over *C. oamaruensis* places this sample in the Oligocene (*Blackites spinosus* Zone or ~CP16; compare with the Eocene/Oligocene sequence at Deep Sea Drilling Project Hole 511 [Leg 71] on the Falkland Plateau and Ocean Drilling Program (ODP) Hole 737B [Leg 119] on the southern Kerguelen Plateau [Wise, 1983, table 1A; Wei and Thierstein, 1991, table 3]).

We did not observe *Isthmolithus recurvus* in Sample 183-1137A-20R-CC, but it is abundant in 21R-CC. A few *Reticulofenestra oamaruensis* and *Discoaster tani* are present in both samples. We did not see, however, *Clausicoccus fenestratus;* in addition, *Chiasmolithus oamaruensis* was abundant and considerably more prevalent than *C. altus*. Although both *I. recurvus* and *R. oamaruensis* span the Oligocene/Eocene boundary, the criteria cited in the above paragraph regarding the distribution of *C. fenestratus* and the chiasmoliths place these two samples on the Eocene side of the boundary, within Subzone CP15b. One notable difference in these samples and the Oligocene Sample 183-1137A-19R-CC is the larger size of *Coccolithus,* which reaches 19 µm (= *C. eopelagicus*) in Sample 183-1137A-21R-CC. Other differences may be more apparent than real, in that Sample 183-1137A-21R-CC contains some taxa reworked from the middle to lower Eocene, including *Chiasmolithus solitus, C. expansus, Reticulofenestra onusta, Lapideacasis cornuta,* and perhaps a single but well-preserved specimen of *Discoaster saipanensis* and several of *Markalius inversus* (which is common in Sample 183-1137A-21R-CC and rare in 20R-CC).

Nannofossils were very rare in well-cemented, moldic packstone at the top of Sample 183-1137A-22R-1, 10–14 cm, consisting mostly of a few of the Mesozoic *Watznaueria barnesae*. Sample 183-1137A-23R-CC, however, contains abundant, well-preserved coccoliths, presumably of the same assemblage as in the superjacent core. These include *Biscutum coronum, B. magnum, B. dissimilis, B. constans, Arkhangelskiella cymbiformis, Eiffellithus touriseiffelii, Ahmuellerella octoradiata, Teichorhabdus ethmos, Chiastozygus garrisonii, Misceomarginatus pleniporus, Cribrosphaerella ehrenbergii, Repagulum parvidentatum,* and several species of *Cretarhabdus,* but no *Eiffellithus eximius, Aspidolithus parcus,* or *Nephrolithus*. This assemblage is characteristic of the upper Campanian *Biscutum coronum* Zone, probably of the *Repagulum parvidentatum* Subzone (although the upper boundary of that subzone, the first occurrence of *Nephrolithus corystus,* was inconsistent in the Leg 183 sites, possibly because of preservation problems).

Planktonic Foraminifers

All core-catcher samples from the 200-m-thick diatom and nannofossil ooze succession yielded abundant and well-preserved planktonic foraminifers. The single core catcher from the Upper Cretaceous glauconite-bearing sandy packstone (Unit III) that lies unconformably below the Eocene ooze contains surprisingly well-preserved microfossils. Planktonic foraminifers are extremely scarce in this sample, however, because of dilution by common inoceramid prisms, volcanic glass, and mineral grains.

The Pleistocene is represented by ~10 m of diatom ooze in the first core (lithologic Unit I). Sample 183-1137A-1R-CC, contains a low-diversity planktonic fauna dominated by sinistrally coiled *Neogloboquadrina pachyderma* with occasional *Globigerina bulloides* and *Turborotalia quinquelobula*. This low-diversity assemblage belongs to the long-ranging biozone NK7, contains no age-diagnostic species, and is typical of the subantarctic upper Neogene (Pliocene, Pleistocene, and uppermost Miocene). Diatoms provide greater biostratigraphic control in this interval.

The biostratigraphic utility of planktonic foraminifers increases in the Neogene. Globorotalids are common in Sample 183-1137A-2R-CC. Owing to the presence of abundant *Neogloboquadrina continusoa, Neogloboquadrina nympha,* and *Globorotalia scitula,* we assign this sample to the uppermost Miocene zonal range NK5–NK6. The fauna in Sample 183-1137A-3R-CC is characterized by notably large forms of both *Globorotalia scitula* and globigerinids, including *Globigerina bulloides, Globigerina falconensis* and *Globigerina woodi,* and rather small *Neogloboquadrina* spp. This sample does not contain *Globorotalia miozea,* the marker for the zone below; therefore, we also assigned it to the NK5–NK6 zonal range. The size of faunal elements fluctuates and species dominance (globorotalids over globigerinids) varies throughout the Miocene. This may be an ecological effect, reflecting local or global variations in surface-water temperature. Alternatively, physical processes at the seafloor or during deposition may have winnowed assemblages. Because assemblages dominated by large forms also contain a range of small species, and vice versa, the former explanation is more probable. Sample 183-1137A-4R-CC, which we also place in Zones NK5–NK6, is dominated by rather small globigerinids, with less common, large (~250–300 µm) *Globorotalia scitula*.

Abundant, large middle Miocene globigerinids occur with *Globorotalia miozea* in Sample 183-1137A-4R-CC. Because of the presence of a small *Neogloboquadrina*-type form, we placed this sample in Zone NK5. We did not find this form in the subjacent two samples and, therefore, placed them in the zone below, Zone NK4. The downhole first occurrence datum of *Globorotalia miozea* occurs in Sample 183-1137A-7R-CC. The planktonic fauna in this sample is composed of large globigerinids and *Globorotalia praescitula* but no catapsydracids, indicting a late Zone NK3 age.

Globorotalia pseudoscitula does not occur in the subjacent two samples. Because of the presence of *Globorotalia zealandica* and *Paragloborotalia incognita* in assemblages dominated by rather small globigerinids, paragloborotalids, *Globorotaloides suteri,* and catapsydracids, we assigned these samples to the lower Miocene Zone NK2. No core-catcher sample was obtained for Core 183-1137-10R.

Paragloborotalia incognita is absent from Samples 183-1137A-11R-CC to 13R-CC. On this basis we assigned these samples to lowermost Miocene Zone NK1, above the top of the *Subbotina euapertura* range. We note the presence of extremely large *Globigerina brazieri* and *G.* cf. *G. labiacrassata* in Sample 183-1137A-12R-CC.

Globigerina euapertura, the nominate taxon of the upper Oligocene Zone AP16, first appears in Sample 183-1137A-14R-CC, accompanied by catapsydracids, tenuitellids, *Globigerina brazieri, Globorotaloides suteri,* and a variety of indeterminate globigerinids of upper Oligocene affinities. We assigned this and the subjacent sample to the AP15–AP16 zonal range. We could not delineate the boundary between AP15 and AP16 (defined by the last appearance datum [LAD] of *Globigerina labiacrassata* s.s). This was a result of the overlapping range of similar-looking *Globigerina* cf. *Globigerina labiacrassata* with the zonal marker.

Chiloguembelina cubenis is present in Sample 183-1137A-16R-CC, indicating that the top of Zone AP14 had been reached. In addition to *C. cubensis,* Samples 183-1137A-16R-CC and 17R-CC contain *Globigerina praebulloides, Globigerina brazieri,* and common tenutitellids. In the absence of *Subbotina angiporoides,* (the LAD of which marks the top of the zone below), we assigned these samples to Zone AP14. *S. angiporoides* is present in the next interval of samples, Samples 183-1137A-18R-CC to 20R-CC. On this basis, and in the absence of *Globigerinatheka index,* we assign these samples to Zone AP13. In addition to the distinctive lower Oligocene marker species *Subbotina angiporoides,* these samples contain catapsydracids, tenutitellids, *Chiloguembelina cubensis,* and *Subbotina utilusindex* that are difficult to distinguish from *Subbotina linaperta.*

The uppermost Eocene is indicated by *Globigerinatheka index* in Sample 183-1137A-21R-1, 75–79 cm. This sample, which we assigned to the AP11–AP12 zonal range, represents the stratigraphically lowest Cenozoic horizon above the disconformity. We cannot delineate the base of AP12 (the lower boundary of which is denoted by the LAD of *Subbotina linaperta* [Stott and Kennett, 1990]) because of difficulties in distinguishing *S. utilusindex* from the zonal marker *S. linaperta.* Huber (1991) noted that the range of *S. linaperta* extended into the lower Oligocene on the southern Kerguelen Plateau.

Core 183-1137A-22R contained no material in the core catcher, but glauconite-bearing sandy packstone in Sample 183-1137A-23R-CC yielded rare and moderately well-preserved planktonic foraminifers. This sample represents the stratigraphically lowest sediments above igneous basement. The planktonic assemblage included *Globigerinelloides multispinatus, Archeoglobigerina australis, Globotruncana* spp. and a single specimen of *Globigerinelloides impensus,* the nominate taxon for the upper Campanian biozone. Inoceramid prisms are also common in this sample.

Basal Sediment Age

Constraints on the age of the oldest sediment above basement in Cores 183-1137A-22R and 23R were derived by shipboard analyses of calcareous nannofossils, planktonic foraminifers, and paleomagnetic stratigraphy. Further shore-based study of the palynomorph assemblages may yield further age-diagnostic taxa.

The richest assemblages were in Core 183-1137A-23R, where we assigned the calcareous nannofossil assemblage to the middle to upper *Biscutum coronum* Zone and the planktonic foraminifers to the *Globigerinelloides impensus* Zone. Apart from the stratigraphic charts compiled by Cita et al. (1997), previous Southern Hemisphere high-latitude correlations do not show an overlap between these two zones (Huber, 1992). At this site as well as at Site 1135, however, there was a clear overlap between these two zones, with the extinction (LAD) of *G. impensus* recorded stratigraphically above rather than well below that of *Aspidolithus parcus.* We consider it unlikely that *G. impensus* is reworked at this locality because the site is located reasonably high on Elan Bank, above and presumably upcurrent from most likely sources of contaminants during Campanian times.

For the reasons outlined above, we have adjusted the LAD of *G. impensus* upward on the biostratigraphic correlation chart (see Fig. **F6D,** p. 65, in the "Explanatory Notes" chapter), to at least 74 Ma. This level is still within Chron C33n, as determined by Huber (1992) for this LAD. This correlation also adheres to our shipboard magnetic polarity data for this site (see **"Paleomagnetism,"** p. 45). We noted a similar set of relationships in Core 183-1135A-39R on the southern Kerguelen Plateau. Assuming, therefore, that this correlation is correct, the basal sediment age is ~74 to 75 Ma. A more conservative estimate would be ~72 to 76 Ma.

PHYSICAL VOLCANOLOGY

Introduction

The volcanic units encountered in Hole 1137A include crystal-lithic volcanic siltstone and sandstone (basement Unit 5), lithic volcanic conglomerate (basement Unit 6), crystal-vitric tuff (basement Unit 9) (Table T6), and seven lava flows (Units 1–4, 7, 8, and 10) (Table T7; Fig. F4) (see **"Lithostratigraphy,"** p. 3). In addition, lithologic Unit I contains disseminated volcanic detritus of mixed origin in foraminifer bearing diatom ooze (Unit 1).

T6. Summary of volcaniclastic components, **p. 177.**

T7. Curated positions and depths of basement units, **p. 178.**

Unit Descriptions

Unit I: Foraminifer-Bearing Diatom Ooze (interval 183-1137A-1R-1, 0 cm, through 1R-CC)

The pelagic sediment in Unit I (Core 183-1137A-1R) contains 2% disseminated silt- to sand-sized crystal-lithic volcanic fragments, glass shards, and pumice lapilli. The shards include palagonitized basaltic glass and unaltered felsic glass. The abundance of volcanic detritus decreases downward through the unit, but sediments in Core 183-1137A-1R were highly disturbed by drilling, so the glass shards may have originated from one or more discrete ash layers. Shards show an array of morphologies; commonly the felsic shards show cuspate fragmental bubble-wall shapes or are formed from disrupted tube pumice, whereas basaltic shards are more blocky and equant. The felsic glass is translucent and isotropic; mafic glass ranges from pale golden brown or dark brown to dark red. Some basaltic shards have a green rim, a few microns wide, of a more crystalline phase, probably iron-rich smectite (nontronite) after palagonite. No microcrystallites or vesicles were observed; however, shards are small (<0.3 mm). Incorporated fine to coarse sand-sized lithic, mostly basaltic, clasts are angular to subrounded.

Basement Units

Depth in core for each of the basement units is summarized in Table T7. However, because ODP curation procedures assume that the top of recovered core comes from the top of the cored interval, the curated depths and thicknesses are often poor recorders of the actual downhole positions (see **"Introduction,"** p. 1, in the "Explanatory Notes" chapter). The measurements of the depths of important boundaries and flow thicknesses from the logging data (Table **T8**) are discussed in the interpretive part of this section (see **"Recovery of Basement Units,"** p. 20). The unit thicknesses and recovery are detailed in Table **T9**.

We divided the basaltic basement into units that generally consist of a single lava flow. The unit and subunit boundaries were chosen based on changes in color, structure, grain size, and mineral occurrence and abundance. Because of the interpretation inherent in choosing these boundaries, the description of the specific criteria used to separate each unit and subunit are discussed in the interpretive part of this section (see **"Basement Units,"** p. 13).

Unit 1 (interval 183-1137A- 24R-1, 71 cm, through 25R-3, 100 cm)

The first basement unit consists of massive plagioclase-phyric basaltic lava. However, the first 5-cm-long piece of lava is a well-cemented breccia containing 0.5–2 cm of angular fragments of vesicular lava. The recovered lava below this piece is massive with predominantly 2%–5% vesicularity. A few, thin, undulating subhorizontal vesicular regions are located at Section 183-1137A-24R-1, 80 cm, through 25R-1, 40 cm. A wider and less distinct vesicular zone is at interval 183-1137A-24R-2, 6–10 cm. Vesicularity increases systematically in Section 183-1137A-25R-2, reaching 15% at 97.5–99.5 cm.

Subunits 2A and 2B (interval 183-1137A-25R-3, 100 cm, through 27R-1, 0 cm)

Unit 2 consists of an aphyric basalt with a brecciated upper part and a massive interior. The four loose pieces of well-cemented angular breccia at the top of Unit 2 differ in character from the bulk of the brecciated top of Unit 2. Immediately below these pieces is a vesicular lobe that extends down to Section 183-1137A-25R-4, 35 cm. The vesicles are elongate in the margin and more spherical toward the center and make up ~30% of the lobe (Fig. **F12**). This lobe is wider than the core (6 cm) at the top and only ~4 cm wide near the base. Under this lobe, the breccia is made up of 3- to 20-cm-diameter clasts that contain 10%–40% rounded to subrounded vesicles (Fig. **F13**). The clasts are variously oxidized, ranging from dusky yellowish brown (10YR2/2) to reddish brown (2.5YR4/3). The larger clasts are subrounded in shape, but their margins are commonly broken into 3- to 10-mm angular fragments that can be fit back to the larger clast. A few clasts envelop other clasts. Clasts >1 cm make up 80–90 vol% of the breccia, and fines <1 mm in size are confined to the lowermost 10 cm of the breccia and make up only about 2%–3% of the volume. However, large (>>1 cm) voids between clasts make up 8% of the breccia. These voids are notably free of sediments and are filled by a variety of secondary minerals (see **"Alteration and Weathering,"** p. 38). The breccia gradationally becomes more welded with depth and reaches a coherent lava at approximately interval 183-1137A-25R-5, 27 cm.

The upper part of the coherent lava remains quite vesicular (5%–30%) but the vesicles appear in 5- to 30-cm-scale domains with variable vesicularity, vesicle size, and vesicle shape. The core is broken into similar sized pieces, and most pieces contain a single style of vesicularity. This obscures the transitions between these vesicle domains. The lava becomes relatively vesicle poor (0.01%–3%) beginning at Section 183-1137A-25R-6, 79 cm. A 5-cm, flat megavesicle marks this point (Fig. **F14**). Only one undulating subhorizontal vesicular region is present at interval 183-1137A-25R-7, 90.5–91.5 cm. Wispy blebs of vesicular, glassy mesostasis are common through most of the more vesicle poor part of Unit 2. These blebs are generally 0.1–0.3 mm wide and 1–3 mm

T8. Curated downhole depths of key horizons in the lava flows, **p. 179.**

T9. Flow thicknesses and recovery, **p. 180.**

F12. Close-up photograph of interval 183-1137A-25R-3, 112–144 cm, **p. 75.**

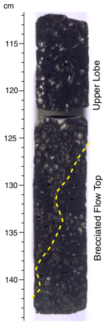

F13. Close-up photograph of interval 183-1137A-25R-4, 44–91 cm, **p. 76.**

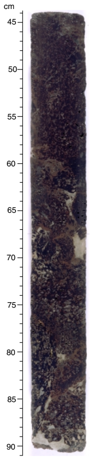

long, though in some sections they are equant spots and in other areas are 10–20 mm long. There is no significant increase in vesicularity at the base of the recovered portion of Unit 2.

Subunits 3A and 3B (interval 183-1137A-27R-1, 0 cm, through 29R-2, 64 cm)

Unit 3 is a coherent plagioclase-phyric basalt with a more vesicular part overlying a more massive section, and the vesicularity as a function of depth is shown in Fig. F15. The upper part of Unit 3 was recovered as discontinuous pieces that contain large (2–3 mm average diameter) elongated and irregular subangular vesicles. By Section 183-1137A-27R-1, 78 cm, the vesicles are consistently very large (some >5 cm in length) and elongate in a subhorizontal direction. Several pieces show brecciation in the form of vertical compression of these large vesicles (Fig. F16). Wispy blebs of mesostasis and near-spherical megavesicles replace the elongated vesicles at Section 183-1137A-27R-3, 77 cm, where vesicularity drops from >20% to 10%–15%. The mesostasis blebs and microvesicle trains persist with variable prominence until Section 183-1137A-28R-3, 50 cm. In some areas these wisps define a foliation/fabric inclined at a high angle across the core. Recovery improved in Section 183-1137A-27R-4 where vesicularity dropped to 10%. Subhorizontal vesicular regions are quite common between Sections 183-1137A-27R-4, 50 cm, and 28R-2, 4.3 cm. Vesicularity begins to increase again near the base of Unit 3 and reaches 25% in interval 183-1137A-29R-2, 48–53 cm. Although vesicle size initially increases toward the base, it becomes smaller again in the lowermost centimeters.

An enigmatic piece of lava is found in Section 183-1137A-29R-2 (Pieces 3 and 4) (Fig. F17). Because the clast has the same unoxidized color and aphyric petrology as lava of Unit 3, whereas the upper portion of Unit 4 is highly oxidized and is moderately plagioclase phyric, we include this piece of lava with Unit 3. This piece of lava is separated from the rest of Unit 3 by a 2- to 5-cm void filled with a variety of sediments and reworked lava fragments. The interior lava surface of the cavity has an intricately convoluted margin including 0.2-mm-wide, 2-mm-long protuberances. The base of the piece has a fluidal shape with a 1- to 2-cm wavelength, small stretched elongate vesicles parallel to the lower margin, and a fine grained matrix.

Unit 4 (interval 183-1137A-29R-2, 64 cm, through 33R-1, 122 cm)

Unit 4 is dominated by moderately plagioclase-phyric coherent basalt of variable vesicularity. Figure F18 plots vesicularity as a function of depth within Unit 4. However, the uppermost 8 cm of Unit 4 consists of very fine-grained, oxidized, laminated, volcanic silt that has been subsequently brecciated into 1- to 20-mm subangular clasts. The clasts in the uppermost 2 cm are flattened vertically. The top of the lava flow is a smooth pahoehoe surface at Section 183-1137A-29R-2, 72 cm, with a 2-mm-wide margin of black fine-grained rock with 10 vol% very small (<<1 mm) vesicles (Fig. F19). The remainder of the upper part of the flow is pervasively oxidized to a dusky red (10R3/4). Farther down, the lava is gray to dark gray (N4–N5), but in vesicular areas it is oxidized to a dark reddish gray or reddish black (10R3/1-10R2.5/1).

Unit 4 has 5 distinct vesicular zones (Fig. F18). The uppermost of these extends from the vesicular top down to Section 183-1137A-31R-4, 52 cm. Subhorizontal, subplanar vesicular domains appear in the denser lava at Section 183-1137A-31R-4, 105 cm. The second and third vesicular zones are close together, starting at Section 183-1137A-31R-4, 124 cm, and returning to dense lava with subhorizontal, vesicular do-

F14. Close-up photograph of interval 183-1137A- 25R-6, 70–83 cm, p. 77.

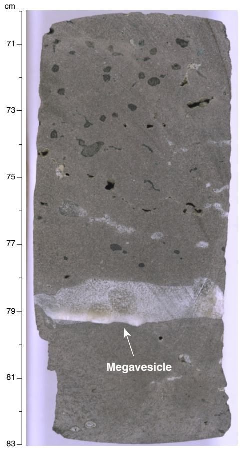

F15. Vesicularity and vesicle number density as a function of depth in basement Unit 3, p. 78

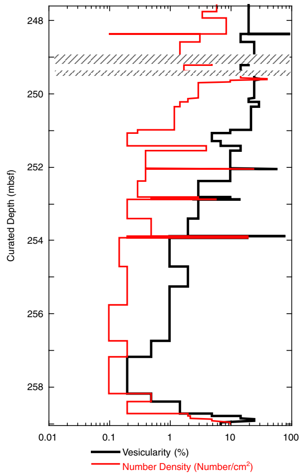

F16. Close-up photograph of interval 183-1137A-27R-1, 114–125 cm, p. 79.

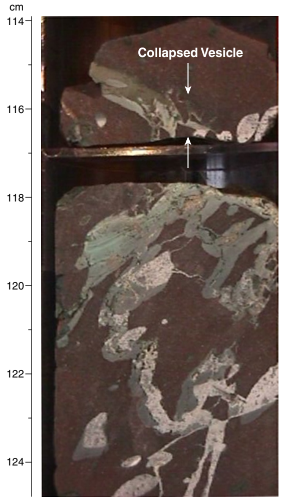

mains at Section 183-1137A-32R-2, 0–17 cm. The fourth vesicular zone is between Sections 183-1137A-32R-4, 27 cm, and 32R-7, 17 cm. Below this the lava is again dense, and a subvertical cylindrical vesicular domain with finer-grained groundmass extends from interval 183-1137A-33R-1, 20–25 cm. A final gradual increase in vesicularity begins at Section 183-1137A-33R-1, 82 cm, reaching 20% at interval 183-1137A-33R-1, 113–120 cm. Vesicle shapes are rounded throughout Unit 4, except in Section 183-1137A-32R-2. In general, vesicle size increases in the zones of increased vesicularity. However, in the bottom 2.5 cm of Unit 4, the vesicles are very small (<<1 mm) despite making up 10 vol% of the lava.

An exquisite basal contact of the lava over sediments is preserved (Fig. **F20**). The base of the flow shows 1- to 5-mm amplitude, 0.5- to 2-cm wavelength undulations.

Unit 5 (interval 183-1137A-33R-1, 122 cm, through 33R-4, 121 cm)

Unit 5 is composed of interbedded dark greenish gray crystal-lithic volcanic siltstone and light gray crystal-lithic volcanic sandstone. The top of the unit (interval 183-1137A-33R-1, 122–124 cm) is black and has been baked during emplacement of the overlying lava flow. Total carbon (TC) analysis of this interval was low (0.9% TC) (see **"Organic and Inorganic Geochemistry,"** p. 51), indicating that soil had not developed on the silty sand prior to baking. Adjacent to the sediments, the basalt has a glassy chilled margin that is pervasively altered to iron-oxide (hematite) and oxyhydroxide (goethite)-stained clay minerals, probably iron-rich smectite nontronite and saponite (Fig. **F21**). The black color of the sediment is attributed to baking and dehydration of the clay mineral component (>10% of total matrix) in the siltstone (Fig. **F21**).

Siltstone and sandstone beds range from a few millimeters to tens of centimeters in thickness. Many beds are normally graded. Sandstone intervals commonly have sharp irregular bases (e.g., interval 183-1137A-33R-3, 50–53 cm) (Fig. **F22**) and gradational tops, but some have sharp irregular tops. Some siltstone and sandstone beds have planar lamination and low-angle cross-stratification (Figs. **F8A, F8B**) (see **"Lithostratigraphy,"** p. 3). Rare burrows penetrate the sediments. Thin, bladed flakes (<5%), probably organic material, are scattered through the siltstone and sandstone, and in places form more concentrated intervals. No marine fossils were observed. Small-scale faulting offsets bedding in some sections.

The siltstone and sandstone contain angular to subangular crystal-lithic volcanic grains, mostly basaltic and felsic volcanic fragments (Fig. **F22**). Some (<2%) reworked laminated lithic clasts (siltstone) are incorporated. Abundant crystals in the sandstone are dominated by simply twinned feldspar (sanidine) with subordinate plagioclase (10%–15% total feldspar). There is minor quartz (~5%), and there are isolated crystals of garnet and opaque minerals (<5%). Glass shards were not observed in these sediments; however, there is a significant component (5%–10%) of secondary grayish green smectite nontronite or saponite.

Unit 6 (interval 183-1137A-33R-4 through 37R-1, 0 cm)

The conglomerate is dominated by well-rounded volcanic clasts in the granule, pebble, and cobble size range within a poorly to moderately well-sorted matrix of crystal-lithic volcanic clasts of fine- to coarse-sand size (see **"Lithostratigraphy,"** p. 3). Matrix minerals include altered clinopyroxene and, possibly, olivine and titanomagnetite. The matrix is variably altered and cemented with green clay minerals

F17. Close-up photograph of Sample 183-1137A-29R-2 (Piece 4, 54–62 cm), **p. 80.**

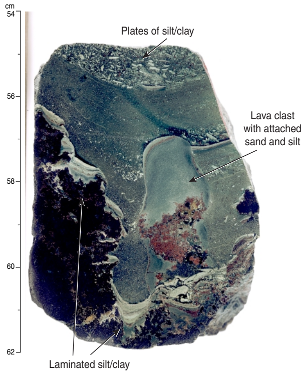

F18. Vesicularity and vesicle-number density as a function of depth in basement Unit 4, **p. 81.**

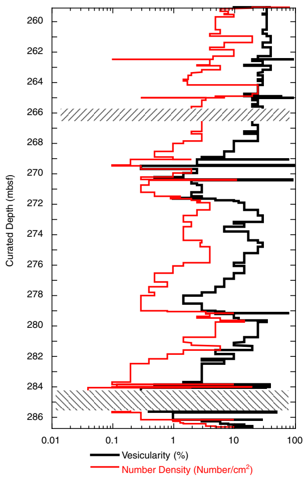

F19. Close-up photograph of interval 183-1137A-29R-2, 65–81 cm, **p. 82.**

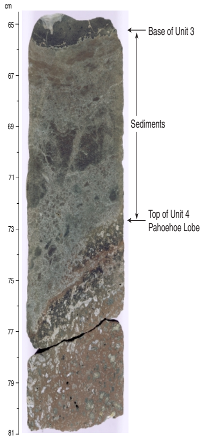

(nontronite?), calcite, and silica. Some veins of calcite are present. Clasts have a range of volcanic lithologies dominated by highly plagioclase-phyric basalt (>80%), with lesser alkali-feldspar-plagioclase-clinopyroxene-phyric massive trachyte and alkali-feldspar-plagioclase-phyric flow-banded trachyte (10%–15%). There are scattered pebbles (<5%) of other lithologies, including granitoid and gneiss (see **"Igneous Petrology,"** p. 28). Clasts are commonly oxidized along their margins with oxidation rims as wide as 1 cm (Fig. **F9A**) (see **"Lithostratigraphy,"** p. 3).

A point count of clasts in the lithic volcanic conglomerate allows quantification of the characteristics of Unit 6 (Fig. **F23**). The proportion of matrix in each section is generally <25%, but discrete intervals are granular and preserve fewer large clasts (Fig. **23A**). In Section 183-1137A-35R-1, a discrete well-sorted medium sand interval is partially preserved in Pieces 17 and 18 (98–118 cm), which is considered a separate sedimentary event and not included in the granulometry (Fig. **F23**). A poorly sorted, coarse sand to granular interval is preserved in Section 183-1137A-35R-1 from 131 to 136 cm, and a moderately well-sorted medium sand between 58 and 65 cm in Section 183-1137A-35R-2. These sand intervals can be broadly related to planar fine-grained intervals observed in FMS log data (see **"Downhole Measurements,"** p. 54).

The average clast size in the lithic volcanic conglomerate ranges from 1.5 cm × 2.0 cm to 3.0 cm × 5.0 cm and is relatively constant in the pebble size range throughout the conglomerate. There are slightly larger average clast sizes in the upper half of Unit 6 (Fig. **F23B**). The maximum clast size ranges from 3.0 cm × 5.5 cm to 9.0 cm × 16.0 cm. The distribution of maximum clast size reflects the presence of two broad intervals in the conglomerate with reverse graded cobbles at the base and more normal graded cobble to pebble distribution above (Fig. **F23C**). One of these intervals lies below the >20-cm-thick medium sand interval in Section 183-1137A-35R-1 (98–118 cm) and the other lies above it. Sorting is relatively poor with a range in clast size from granule to cobble throughout most of the conglomerate. The calculated standard deviation for the clast size data provides a good indication of the degree of sorting (Fig. **F23D**). The standard deviations range from 1.4 to 3.2 cm, which is significant compared to the average clast size for the conglomerate (2.0 cm × 3.2 cm).

The conglomerate is an almost uniformly closed framework, or clast supported (Fig. **F9B**) (see **"Lithostratigraphy,"** p. 3) with very few open-framework, or matrix-supported, intervals. Open-framework intervals are present in the more matrix-rich parts of Sections 183-1137A-34R-1, 34R-2, 35R-1, and 36R-1 (Fig. **F23A**). Imbrication of cobbles is apparent in some parts of the FMS log (Fig. **F94**) (see **"Downhole Measurements,"** p. 54) and is present in Section 183-1137A-34R-3, from 57 to 85 cm (Fig. **F9C**) (see **"Lithostratigraphy,"** p. 3). The clasts are moderately elongate, commonly subspheroidal to oblate, and subrounded to rounded (Fig. **F9C**) (see **"Lithostratigraphy,"** p. 3).

Subunits 7A and 7B (interval 183-1137A-31R-1, 0 cm, through 39R-2, 64 cm)

Unit 7 is a plagioclase-phyric basalt with a brecciated section on top and a coherent portion below. The breccia extends down to Section 183-1137A-38R-1, 23 cm. No contact is preserved between the Unit 6 conglomerate and Unit 7 lava flow, but the uppermost 10 cm of the recovered breccia has smaller and more rounded clasts than the remainder of the breccia. The breccia is made up of three different types of

F20. Close-up photograph of interval 183-1137A-33R-1, 110–140 cm, **p. 83.**

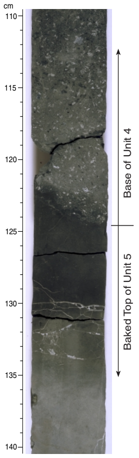

F21. Photomicrograph of the base of basement Unit 4, **p. 84.**

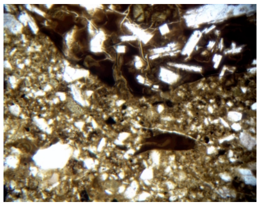

F22. Photomicrograph showing typical internal texture of sandstone and siltstone in basement Unit 5, **p. 85.**

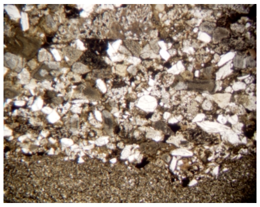

F23. Summary of some grain-size characteristics for the volcanic conglomerate, **p. 86.**

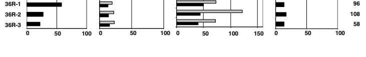

clasts and has a sediment matrix (Figs. F24, F25). Overall, 50–60 vol% of the breccia is in the form of clasts >1 cm, 40%–30% is 1- to 10-mm fragments, and ~10% is <1-mm fine-grained material. This fine-grained portion includes large sediment filled voids that make up 2% of the breccia. The three types of clasts are (1) larger clasts with 1- to 3-cm vesicles, (2) larger dense clasts with small, irregular elongate vesicles, and (3) smaller fragments of both of these larger clasts. The larger clasts are up to 30 cm in size and subrounded in shape. The largest (i.e., most intact) vesicular clasts have rounded vesicles elongated parallel to the clast margins. Interestingly, the dense clasts are common only in the lowermost part of the breccia. The dense clasts also contain a few small fragments of oxidized lava within their interiors. The smaller fragments are angular and are concentrated in subplanar zones surrounding the dense clasts. Other small angular fragments show a jigsaw-fit pattern with the margins of larger vesicular clasts.

Starting in Section 183-1137A-38R-1, 23 cm, the lava is welded into a coherent rock. Patches of small irregular angular vesicles are in interval 183-1137A-38R-1, 69–103 cm. The remainder of the coherent lava is quite massive with only 0.5%–3% vesicles. Wispy mesostasis blebs are evident in Section 183-1137A-38R-3 through 39R-2, 43 cm (Fig. F26). Vesicularity is higher (5%–15%) in interval 183-1137A-39R-2, 55–62 cm, immediately above a glassy chill margin.

Subunits 8A and 8B (Core 183-1137A-39R-2, 64 cm, through 41R-1, 103 cm)

Unit 8 is predominantly a coherent plagioclase-phyric basalt with a vesicular portion overlying a massive interior. Included at the top of Unit 8 are four pieces of breccia whose origin is not immediately obvious (Fig. F27). However, the breccia pieces have nearly identical clast and vesicle size, number density, and morphology as the breccia at the top of Unit 7.

The lava immediately below this breccia is recovered as 2- to 5-cm-long pieces, with each piece consisting of coherent lava with no evidence for clast margins (Fig. F27). The vesicles in this coherent lava are large, rounded, elongated vesicles of a type not seen anywhere in Unit 7, but very similar to the vesicles in the upper part of Unit 3. Some of the largest vesicles show evidence for vertical compression identical to that seen in Unit 3. Vesicle sizes gradually increase with depth in Unit 8, with the average size increasing from 2.5 to 16 mm. Unit 8 continued to be recovered only as isolated 2- to 5-cm pieces until Section 183-1137A-40R-2, where vesicularity decreased below 15%. The underlying denser lava has a vesicularity of 0.1%–5%. Subhorizontal vesicle-rich regions with a distinct groundmass first appear at Section 183-1137A-40R-1, 31 cm, and are not found below Section 183-1137A-40R-3, 65 cm. A vertically elongate, 2- to 4-cm-diameter vesicle-rich zone with similar groundmass is present in interval 183-1137A-40R-3, 97–106 cm. Wispy mesostasis blebs are most common from Section 183-1137A-40R-4, 79 cm, through 40R-5, 111 cm, and near the base of the flow. Vesicularity at the base of the flow begins to increase from Section 183-1137A-41R-1, 22 cm, reaching a peak of 12% in the lowermost piece recovered. The lowermost 10 cm of recovered Unit 8 contains large, horizontally elongated vesicles of the same character as those at the top of the coherent lava. No glassy basal chill zone was recovered. However, several chips of black rock were recovered between the bottom of Unit 8 and the first recognizable piece of the crystal-vitric tuff of Unit 9.

F24. Close-up photograph of interval 183-1137A-37R-1, 27–47 cm, p. 87.

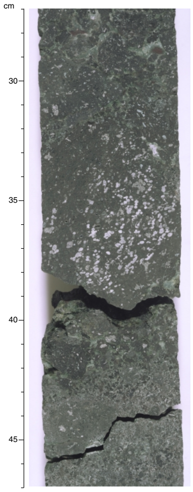

F25. Close-up photograph of interval 183-1137A-37R-5, 20–40 cm, p. 88.

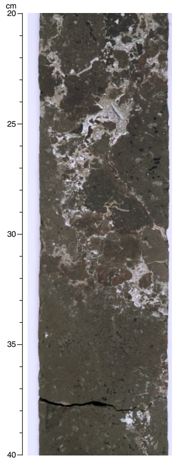

F26. Close-up photograph of interval 183-1137A-39R-1, 105–118 cm, p. 89.

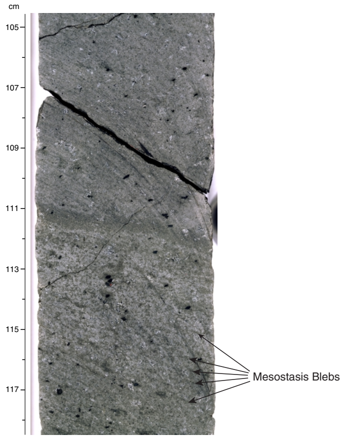

Unit 9 (interval 183-1137A-41R-1, 103 cm, through 44R-4, 49 cm)

Unit 9 is a green, internally massive 14.8-m-thick interval of crystal-vitric tuff. The upper part of the tuff (interval 183-1137A-41R-1, 103–112 cm) is very fine grained and black with scattered broken feldspar crystals (<5%) and was probably baked during emplacement of the overlying lava flow (Fig. **F10**) (see **"Lithostratigraphy,"** p. 3). Total carbon analysis on this interval was very low (0.15% TC), indicating that soil had not developed on the tuff before baking. The basalt has a glassy chilled base adjacent to the sediments. The black color of the uppermost tuff is probably caused by dehydration of the clay mineral component during baking.

The tuff consists of 30%–40% angular, euhedral, broken, or disrupted simply twinned sanidine crystals, up to 5 mm in diameter. The balance of the mineral component includes <5% amphibole, <5% plagioclase feldspar, 1%–3% quartz, and <3% opaques (see **"Igneous Petrology,"** p. 28). The tuff contains 1%–2% subangular to rounded, granule- to pebble-sized lithic clasts. Clast lithologies include plagioclase-phyric basalt, aphyric basalt, trachyte, garnet gneiss, and granitoid (see **"Igneous Petrology,"** p. 28).

Cuspate and tricuspate, bubble-wall glass shards (40%–50%), now partially altered to green clay minerals (kaolinite, nontronite) and possibly micas (celadonite), form the matrix between crystals (Fig. **F28**). The tuff is more altered and oxidized toward the top, and correspondingly the glass shards are harder to resolve in thin section. Lower in Unit 9, many glass shards retain original morphologies and flattening is not apparent, but in more altered zones, the relict shards are slightly flattened and aligned. There is no evidence of welding in the tuff.

Subunit 10A and 10B (interval 183-1137A-44R-4, 49 cm, through 49R-3, 37 cm)

No clear contact between Units 9 and 10 was recovered. However, from Section 183-1137A-44R-4, 49 cm, through 45R-2, 100 cm, there is a breccia consisting of basaltic clasts in a matrix of pale green, feldspar-rich, silty sand. The silty sand differs from the overlying Unit 9 crystal vitric tuff in its grain size and mineralogy, particularly the greater abundance of biotite in the silty sand. Downhole FMS log data indicate that there is an ~1-m-thick (logged interval 360–361 mbsf) (see **"Downhole Measurements,"** p. 54) bedded interval at the base of the crystal vitric tuff (Unit 9).

Within the breccia, basalt clasts are 0.5 to 35 cm in diameter. Smaller clasts are angular to subangular, and larger clasts are subrounded to rounded with 10% to 40% vesicles. One clast has a denser margin and more vesicular interior. Vesicle shapes are variable, and one clast has a margin with vesicles elongated parallel to the margin and more spherical vesicles toward the center. More intact clasts have irregular fluidal margins, but fragmented and jigsaw-fit margins are common (Figs. **F29**, **F30**). Welded margins are rare in the upper part of the breccia but common lower down. Green silty sand fills most of the space between the clasts and fragmented clast margins. Domains of sediment make up ~4% of the breccia. Disaggregated, 3- to 20-mm, angular, fragments with some curviplanar faces appear suspended in the sediments in interval 183-1137A-45R-2, 10–25 cm (Fig. **F31**), but there may be some clast-clast contact between these lava fragments in three dimensions. A zone of red (10R 3/2–10R 3/4) oxidized, jigsaw-fit, dense lava fragments, 0.5–2 cm in size, is present in interval 183-1137A-45R-2, 20–67 cm (Fig. **F32**).

F27. Photograph of Core 183-1137A-39R-2, **p. 90.**

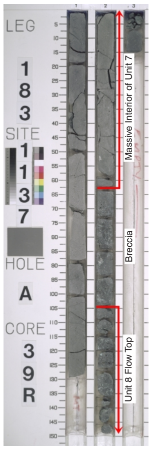

F28. Photomicrograph from near the base of the crystal-vitric tuff, **p. 91.**

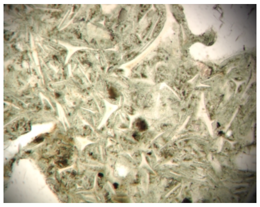

F29. Photomicrograph from the breccia at the top of basement Unit 10, **p. 92.**

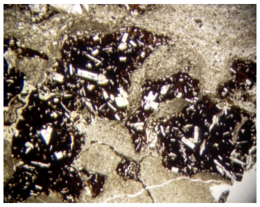

F30. Photomicrograph from the breccia at the top of basement Unit 10, **p. 93.**

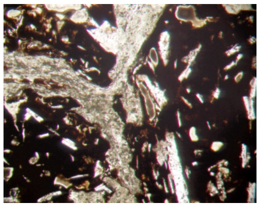

Several thin sections show the contact relationships between the basalt clasts and the sediment (Sample 183-1137A-45R-1, 80–84 cm; Sample 183-1137A-45R-2, 7–10 cm; Sample 183-1137A-45R-2, 19–21 cm) (see **"Igneous Petrology,"** p. 28). In Sample 183-1137A-45R-1, 80–84 cm, sediment grain size ranges from silt to fine sand, and sorting is generally poor. Some discrete domains of coarser or finer grained material appear to have flowed around clasts (Fig. F33). There is no evidence of grading. The sandy silt is either internally massive or it has fine silt distributed around and between clasts with coarser sand concentrated in stringers or domains of aligned particles farther from clasts (Fig. F33). Basalt clasts are glassy and aphanitic. They have angular polygonal shapes with some curviplanar surfaces, and there is possible evidence of breakage across a few crystals (Fig. F34) and through vesicles. However, breakage seems to preferentially take place through glassy parts of the basalt.

The breccia becomes more welded in Section 183-1137A-45R-2, 70 cm, and the lava becomes coherent from about Section 183-1137A-45R-2, 100 cm. However, a dense margin is present in Section 183-1137A-45R-3, 47 cm, around a >3-cm-elongate irregular shaped void, which extends out of the core. Irregular vesicular clumps are in the coherent lava down to Section 183-1137A-45R-3, 120 cm. Thin, wispy subhorizontal vesicle and glassy mesostasis-rich regions first appear at Section 183-1137A-45R-4, 36.5 cm. These grade upward in size and are associated with megavesicles through Section 183-1137A-46R-1, 61 cm. The last of these subhorizontal vesicle-rich regions is closely followed by a vertically elongate pod of similar material extending down to Section 183-1137A-46R-1, 83 cm, where it exits the core. Other than these vesicle-rich domains, the lava is <2% vesicles through Core 183-1137A-46R, and the hole ends with massive lava in Section 183-1137A-46R-3, 36 cm.

Interpretation

Lithologic Units

Unit I: Foraminifer-Bearing Diatom Ooze

Disseminated volcanic components in this unit are a mixture of mafic and felsic volcanic ash, which were partially homogenized during drilling. The low concentration of volcanic components is consistent with these materials being deposited by settling through the water column, possibly reworked on the seafloor, and disturbed during coring.

Basement Units

Recovery of Basement Units

Downhole logging data allowed in situ determination of the depths of lithologic boundaries and thicknesses of flow units. The curated depths and depths determined from the logging data are compared in Table T8. In the following sections, all depths and thicknesses are derived from the logging data, unless otherwise stated.

Based on the depths derived from logging data (Table T8), and the amount of rock recovered from each subunit, it is possible to calculate the actual recovery of each unit and subunit (Table T9). There is consistently excellent recovery of the massive portions of lava flows (92%–

F31. Close-up photograph of interval 183-1137A-45R-2, 10–25 cm, **p. 94.**

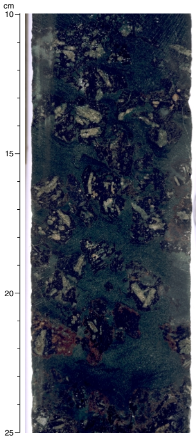

F32. Close-up photograph of interval 183-1137A-45R-2, 20–67 cm, **p. 95.**

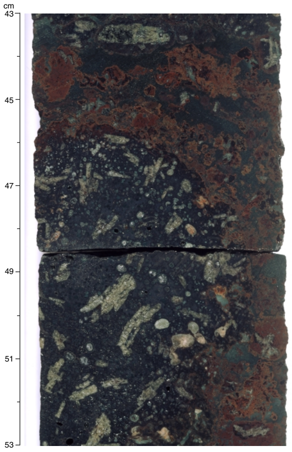

F33. Photomicrograph of a constriction through which sediment has flowed, **p. 96.**

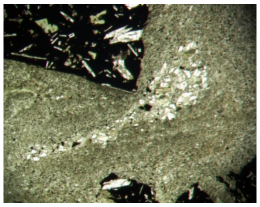

F34. Photomicrograph from the breccia at the top of basement Unit 10, **p. 97.**

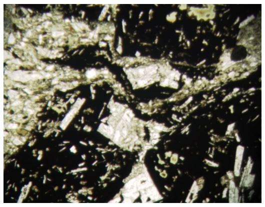

100%) and significantly poorer recovery of breccias (62%–87%). The material that proved most difficult to retrieve was the rock with long, elongated vesicles in the upper portions of Units 3 and 8 (27%–49% recovery). These patterns of preferential recovery of massive lava are only apparent in light of the true unit thicknesses derived from logging data.

Unit 1

The recovered rocks from Unit 1 are from the massive interior and basal part of a single thick lava flow. The subhorizontal vesicular regions with more glassy mesostasis are interpreted to be thin, horizontal vesicle sheets (HVSs) but the 5- to 6-cm diameter of the core is inadequate to confirm a sheet-like morphology. However, these features have at least a 20:1 horizontal to vertical aspect ratio. The increase in vesicularity at the base of Section 183-1137A-25R-2 is interpreted to be a ~30-cm-thick lower vesicular crust. However, the actual chill margin at the base of the flow is missing. What happened to the top of the flow is equivocal. The logging data indicate that no coherent basalt exists above 227 mbsf. However, the zone with high gamma-ray intensity at 223–226 mbsf might be consistent with an extremely altered flowtop if the basalt is highly altered to clay minerals. With both the flow top and bottom missing, it is difficult to interpret the morphology of the flow. However, it is at least 7 m thick, and, if the high gamma region is the flow top, it might have had a total thickness of about 10 m. The internal features are consistent with, but not diagnostic of, an inflated pahoehoe flow.

Unit 1/Unit 2 Boundary

Although the basal glassy chill from Unit 1 was not recovered, the four loose, slightly brecciated pieces at the top of Unit 2 appear to be from the upper margin of the lobe at the top of Unit 2. The downward necking of this lobe suggests that it is intruding the breccia from above. Thus, it is possible that this lobe is part of Unit 1 or represents a completely different lava flow. However, the most likely scenario is that this lobe is part of the Unit 2 flow-top breccia. The oxidation of the upper part of Unit 2 is consistent with exposure in a subaerial environment, and probably there was a significant, but geologically very short, time interval between the emplacement of these two units.

Subunit 2A. The breccia at the top of Unit 2 does not fit any established category of basaltic lava flow. It distinctly differs from aa or slab pahoehoe. Instead, the breccia appears to consist of variously fragmented 15- to 30-cm-diameter pahoehoe lobes. The brecciation must have taken place during the emplacement of the flow for clasts to be able to entrain fragments of earlier clasts. The elongated, ellipsoidal vesicles in the margins of many clasts indicate that the flow was not in the extremely non-Newtonian flow regime of aa breccia formation, and the fact that the clasts are surrounded by such margins indicates that they were not broken from within by surges, as in the case of slab pahoehoe. It is likely that the earlier lobes were fragmented by a combination of the intrusion of more lobes from below and shearing of the mangled flow top. The range of oxidation of the different parts of the breccia supports the idea that the breccia formed over a significant time interval with the last clasts to form being the least oxidized.

Subunit 2A/Subunit 2B Boundary. The boundary between the breccia and the massive interior of Unit 2 is marked by a gradational increase in welding over a distance of tens of centimeters. As such, the precise location of this boundary is arbitrary. The vesicular patches within the interior of the flow (interpreted to be remelted vesicular breccia clasts) show that the breccia was being entrained into the interior of the flow.

Subunit 2B. The massive interior of Unit 2 is less vesicular than that of Unit 1, suggesting that it is more thoroughly degassed. The dearth of HVSs and the presence of finer mesostasis wisps may indicate that the segregated material had difficulty separating from the rest of the lava. This can occur if the flow did not stop moving (and mixing) until it was too crystalline and viscous for the differentiated material to move far before complete crystallization. The lack of a basal vesicular zone or breccia probably reflects the poor (or nonexistent) recovery of the contact zone between Units 2 and 3.

Unit 2/Unit 3 Boundary

Although the boundary between Units 2 and 3 was not recovered, the lowermost pieces of Unit 2 include a piece with vesicles and oxidation similar to Unit 3. This is probably a result of drilling disturbance.

Subunit 3A. The poor recovery of the upper part of Unit 3 is probably directly related to the fact that the individual vesicles in the top of Unit 3 are similar in size to the core diameter. Furthermore, the lava is brecciated by collapse of many of the largest vesicles. This collapse must have happened after solidification of the lava and might plausibly have been caused by the weight of Unit 2 riding over the top of Unit 3. Although overall vesicularity and vesicle shapes in Unit 3 are similar to those in many inflated pahoehoe flows, their size is quite unusual. The formation of such large vesicles suggests an unusually high degree of bubble coalescence and, thus, an unusually long time in transit from the vent. The elongate but round shapes indicate moderately high shear of a relatively fluid lava.

Subunit 3A/Subunit 3B Boundary. The boundary between the vesicular and massive portions of Unit 3 was drawn where overall vesicularity dropped below 5%. This break is clear in the core and is easily discerned in the logging data. However, the boundary between the vesicular upper crust and the interior of the flow that cooled stagnantly is 1.5–2 m higher up, within what is designated Subunit 3A. This critical internal boundary within Unit 3 is located just above the first HVS. Overall vesicularity drops from ~25% to ~10% at this point and the vesicles switch from elongated shapes to near spherical megavesicles. These megavesicles have been interpreted to be related to coalescence of bubbles grown during crystallization (i.e., the same population that produces HVSs). Using the Thordarson (1995) technique (see **"Interpretation,"** p. 19, in the "Explanatory Notes" chapter), the estimated emplacement duration for Unit 3 is about a year. Using the Subunit 3A/Subunit 3B boundary as the upper crust, massive interior boundary would overestimate the emplacement duration.

Subunit 3B. The HVSs and megavesicles are generally confined to the upper part of Subunit 3B (and the lowermost part of Subunit 3A), as would be expected in the massive interior of an inflated pahoehoe lava flow. The wispy mesostasis blebs defining a high angle foliation are not understood, though they have been observed in some large inflated pahoehoe flows. The distribution of vesicles at the base of Unit 3 is a classic example of a vesicular basal crust of an inflated pahoehoe flow, except for the presence of the sediment-filled cavity.

Unit 3/Unit 4 Boundary

The sediments inside the cavity in the bottom of Unit 3 clearly indicate the periodic influx of water-borne fine-grained sediments followed by settling in a quiescent environment. Some of the pulses of water were energetic enough to rip up and transport small clay flakes and the oxidized lava fragment with attached sediments. A lake or ephemeral stream provides such a depositional environment, and we speculate that a very similar environment could exist where water moves through an extremely permeable lava flow.

The presence of the volcanic silt horizon between the base of Unit 3 and the first lava in Unit 4 indicates a time interval between emplacement of the flows. The brecciation of this thin laminated volcanic silt horizon is probably a secondary alteration texture that formed after induration of the silt.

Unit 4

The morphology of the top of the Unit 4 lava indicates that it is a pahoehoe flow. The thickness and vesicularity of the chill margin are diagnostic of subaerial emplacement. The five vesicular zones are interpreted to be the upper vesicular crust, three horizontal vesicular zones (HVZs), and a lower vesicular crust. The uppermost vesicular zone is continuous to the top of the flow and is a typical example of the vesicular upper crust of an inflated pahoehoe flow. The base of the vesicular crust transitions to a dense interior including HVSs. The gradual increase and decrease in vesicularity below this is an excellent example of an HVZ, as described in **"Interpretation,"** p. 19, in the "Explanatory Notes" chapter. The near spherical bubbles, the fining of vesicle size both upward and downward from the peak in vesicularity, and the generally large size and moderate number density all identify this zone of vesicularity as an HVZ and distinguish it from HVSs and vesicular flow bases. The preferred interpretation for HVZs is that they represent renewed injection of bubble-laden lava into the molten interior of a recently stagnated inflated flow. The third vesicular zone also has a gradational change within the flow and is interpreted as a second HVZ. However, this HVZ exhibits somewhat less smooth changes, and poor recovery precludes definitive identification as an HVZ as opposed to a flow base and flow top. The return to massive lava with HVSs suggests that after this second injection of bubble laden lava, the flow again stagnated and the separation of differentiated material restarted. The fourth vesicular zone is somewhat more difficult to interpret. The size of the vesicles is smaller and the distribution is not that different from that of a contact between a vesicular base and a vesicular flow top. Furthermore, it is extremely rare to find an HVZ this deep within a flow. Most commonly, HVZs are confined to the upper half of the flow. However, the excellent recovery of Unit 4 suggests that the chill contact between two flows should be in the cores, if it existed. There is no glassy chill zone seen in either the core or the logging data but there is a minor decrease in groundmass crystal size (see the barrel sheet for Section 183-1137A-32R-4 in **"Site 1137 Core Descriptions,"** p. 69). We suggest that this is an unusual HVZ relatively deep within a flow that received a third pulse of lava late in its cooling history. The last increase in vesicularity is a vesicular lower crust, including the basal chill zone. The smaller vesicles in the lower (once) glassy margin are the most common type found in the basal chill margins of large inflated pahoehoe flows. The observation that the sizes and shapes of vesicles in the lower chill are identical to those 27 m above in the upper chill zone support the idea that this is a single inflated pahoehoe flow that initially was a relatively slow moving (<<1 m/s), small (<<1 m thick) lobe. If this flow was indeed active during the freezing of 23–24 m of upper crust, the Thordarson (1995) technique would imply a flow that remained intermittently active for about a decade.

Unit 4/Unit 5 Boundary

Immediately below the basal chill margin of Unit 4, the top of the siltstone and sandstone of Unit 5 are black (N1) for 5 cm and grade to a grayish brown color over the following 5 cm. The dark color of the sediment near the contact probably results from the baking caused by the emplacement of Unit 4.

Unit 5

The fine grain size of the crystal-lithic volcanic siltstone and sandstone and the preserved sedimentary structures including lamination, normal grading, and low-angle cross-stratification are consistent with their deposition in a relatively quiet water environment with a limited amount of current activity. Together with the underlying conglomerate, the siltstone and sandstone form a sedimentary succession that was probably deposited in a braided river environment (see **"Lithostratigraphy,"** p. 3).

The siltstone and sandstone are dominantly composed of volcanic detritus generated by physical erosion and chemical weathering of volcanic rocks. The crystal content in the sandstone is high (40%–50%), and the abundance of feldspar, especially K-feldspar, supports the observation that more evolved lavas (trachytes and rhyolites) form a significant volume of the eruptives in this area (see **"Igneous Petrology,"** p. 28). Lithic clasts within the sediment include basalt, trachyte, and possibly rhyolitic volcanic fragments. Although this sediment is well sorted, it is relatively immature (angular to subangular), reflecting its proximity to the source area. However, many clasts have subangular to subrounded shapes reflecting reworking in a fluvial environment.

We interpret these sediments to have accumulated in a quieter section of a braided river. The larger clasts of a channel succession are represented by the underlying volcanic conglomerate. Once this channel system has migrated laterally or flow no longer continues along the channel, a quiet water environment is established. Low-angle cross-stratification indicates that some directed flow continued to take place; however, the system had considerably lower energy than was required to emplace the conglomerate.

Unit 5/Unit 6 Boundary

The boundary between the siltstone and sandstone (Unit 5) and the conglomerate (Unit 6) is not well preserved, but it appears that the finer sediments are an onlapping facies in the same succession as the conglomerate.

Unit 6

The clasts in the lithic volcanic conglomerate are reworked from a volcanic hinterland, dominated by basaltic and trachytic lithologies. In addition to the presence of felsic volcanic rock, isolated pebbles of continental lithologies, including gneiss and granitoid pebbles, require that continental rocks must have been exposed near this site (see **"Igneous Petrology,"** p. 28).

Clasts are dominantly subspheroidal to oblate in shape. The high number of clast-clast contacts in the conglomerate, high degree of rounding of large clasts, and presence of imbrication in the sediments as well as lack of marine fossils, supports a fluvial environment, probably a braided stream, as the environment of deposition for this conglomerate (see **"Lithostratigraphy,"** p. 3).

At least two large-scale reverse- to normal-graded sequences were identified in the granulometric data for the conglomerate (Fig. **F23C**). These may reflect the lateral migration of a channel. Initially, pebble and cobble size coarsens as the axis of the channel migrates toward the drill site and coarse clast size decreases as it migrates past or away again. At Site 1137, this channel may have migrated at least twice. The two periods of channel migration are separated by an 80-cm-thick sandy interval deposited in a quieter period (interval 183-1137A-35R-1, 98–118 cm) (see Fig. **F94**) (see **"Downhole Measurements,"** p. 54). Other intercalated sands may reflect periods of quieter or off-axis deposition during emplacement of the conglomerate.

Clasts are variably oxidized, reflecting differing intensities of chemical weathering before incorporation of eroded material into the conglomerate.

Unit 6/Unit 7 Boundary

Although deposition of the volcanic conglomerate (Unit 6) took place in a high energy environment, the underlying flow-top breccia (Subunit 7A) has not been severely eroded. However, the increased rounding and sorting of the top 10 cm of Subunit 7A is consistent with some reworking of the uppermost part of the breccia.

Subunit 7A. Given that a conglomerate lies over Unit 7, it would be reasonable to expect the breccia at the top of the unit to be largely composed of reworked material. However, the breccia on the top of Unit 7 is broadly similar to the breccia on Unit 2, and the evidence for welding near the base of the breccia suggests that Unit 7 formed a brecciated top during emplacement. The welding also argues against interaction with significant volumes of water or wet sediments during emplacement. Like Unit 2, this breccia is unlike any recognized category of basaltic lava flow and probably involved the break-up of intruding pahoehoe lobes. The lower number of large open voids relative to the breccia on Unit 2 and the rounding of the uppermost recovered clasts may be evidence for some reworking of these breccia by sedimentary processes. The dense clasts in the lower part of the breccia also are unlike the clasts in the Unit 2 breccia. These clasts/lobes are composed of lava similar to the interior of Unit 7, providing additional evidence that the breccia was being intruded by material from inside the massive part of the flow.

Subunit 7A/Subunit 7B Boundary. The increase in welding and the coherence of the lava is gradational over at least 1 m, and the precise location of this boundary is arbitrary.

Subunit 7B. The two vesicular patches within Subunit 7B are interpreted to be entrained breccia clasts. The lack of any HVSs and the relatively high abundance of wispy mesostasis blebs suggest that late-stage liquids were not able to segregate into large sheets or cylinders. This indicates that the lava continued to move even as it became largely crystalline. This idea is supported by the dense intrusions in the breccia in Subunit 7A. The increase in vesicularity at the base indicates that the massive part of the lava was cooled from the base while it still contained ~15% vesicles.

Unit 7/Unit 8 Boundary: Unit 7 Basal Breccia

The origin of the breccia at the base of Unit 8 is not immediately clear, but following examination of clast and vesicle morphology, we have interpreted it as a basal breccia for the lava flow in Unit 7. This interpretation suggests that Unit 8 had a coherent top.

Subunit 8A. The vesicular top of Unit 8 is almost identical to the vesicular top of Unit 3, including its poor recovery. The only puzzle is exactly how the extremely large elongated vesicles formed. It must have involved the coalescence of smaller bubbles and significant shear of a lava that could not return to a spherical shape before freezing. However, despite the evidence of shear of a relatively viscous lava, the very rounded, elliptical shapes of the vesicles clearly indicates that the lava was not close to the regime in which aa forms. The lowermost part of Subunit 8A is not interpreted to be part of the vesicular upper crust, as explained in the next section.

Subunit 8A/Subunit 8B Boundary. The change from vesicular to dense lava in Unit 8 is gradational and rather poorly recovered. However, the first appearance of HVSs, which coincides with the drop below 15% vesicularity, is interpreted as the boundary between the vesicular upper crust and the part of the flow that crystallized in a more stagnant fashion. Because of the poor recovery, it is not possible to locate this contact with precision, but it must be at least 30 cm above the Subunit 8A/8B boundary (where overall vesicularity drops below 10%). The logging data do not clearly locate this contact because it is not possible to distinguish the vesicles in HVSs from primary flow-top vesicles. It is noteworthy that this leaves a relatively thin (~2.5 m) upper vesicular crust on Unit 8. This suggests that Unit 8 could have been emplaced in ~6 weeks (see **"Physical Volcanology,"** p. 16, in the "Explanatory Notes" chapter), which is quite fast for a 10-m-thick inflated pahoehoe flow.

Subunit 8B. The upper part of the interior of Unit 8 is quite vesicular because of the concentration of HVSs and has been placed in Subunit 8A. The remaining, more massive part of Unit 8 contains a few more HVSs in the upper portions and what is interpreted to be a vesicle cylinder that passes through the core obliquely. The basal vesicular zone is very similar to other lower crusts, except that the vesicles are larger and more elongated than is typical of most pahoehoe flows. These vesicles have exactly the same form as the vesicles interpreted to be the top of the lava flow, which makes up the bulk of Unit 8.

Unit 8/Unit 9 Boundary

A dark colored, sanidine-bearing indurated material beneath Unit 8 is interpreted to be a baked horizon at the top of the crystal-vitric tuff (Unit 9).

Unit 9

The presence of broken bubble-wall (cuspate and tricuspate) shards and abundant embayed, broken, and disrupted crystals is consistent with genesis of the tuff in an explosive volcanic eruption. The high sanidine crystal content (40%–50%) and well-preserved delicate glass shards indicate that the sediments have not been transported long distances from their source. Incorporated lithic clasts are not genetically related to the tuff and are interpreted to be accidental clasts that were incorporated during transport.

The coarse grain size of both the enclosed pebbles and the primary sanidine crystals precludes deposition of this material by settling from an ash cloud. Transport in a pyroclastic flow is more likely. However, no internal stratification is preserved, and the absence of a basal breccia or fine flow top, the total lack of normal grading of lithics and crystals or reverse hydraulic grading of glassy material strongly suggests that this pyroclastic material has been reworked.

The even distribution of crystals and of pebbles throughout the tuff and the massive internal texture of the deposit provides evidence for plastic mass flow redeposition of these sediments to their present location. It is not apparent whether this redeposition took place in a subaerial or submarine environment, although it is likely that water helped mobilize the tuff. However, the upper part of the crystal-vitric tuff is discolored by red/orange oxidation. This staining of secondary minerals with iron oxides (hematite) and oxyhydroxides (goethite) suggests some subaerial weathering.

Several mechanisms may have concentrated crystals in this interval, including explosive eruption of crystal-rich magma, elutriation of fine particles during eruptive transport, and elutriation of fine particles during mass-flow redeposition of the crystal-rich pyroclastic sediment.

The crystal vitric tuff has a green clay-rich matrix, and, although internally massive, it has a subtle, subhorizontal alteration fabric. This fabric is related to the flattening of partially altered glass shards caused by load compaction during diagenesis.

Unit 9/Unit 10 Boundary

A contact between the crystal-vitric tuff (Unit 9) and the underlying basaltic breccia (Subunit 10A) was not recovered. However, the top of basalt (Unit 10) is mingled with a green, fine-grained altered silty sand. FMS logs show that this interval of bedded silty sand at the base of the crystal vitric tuff is ~1 m thick (see **"Results,"** p. 56).

Subunit 10A. The breccia at the top of Unit 10 may have formed in part by the interaction of hot magma with fluidized, silty sand and, in part, by disruption of the breccia by intrusion of basalt lobes. The sediment commonly has massive internal textures or preserves textures consistent with dynamic interaction with the brecciated clasts, and the brecciated clasts show irregular to angular morphologies. The textures are consistent with the quench fragmentation of basaltic magma in water saturated sediment resulting in peperite formation.

Penetrative brecciation of the glassy basalt observed in thin section is consistent with magma-sediment interaction at the time of quenching (Fig. **F34**). Jigsaw-fit textures indicate in situ brecciation of the basalt by quenching and infiltration of fractures by fluidized sediment (Figs. **F29, F30, F34**). The lower part of the breccia shows less interaction with sediment and more interaction between breccia clasts and crosscutting lobes. Chilled margins, lobes incorporating earlier clasts, and welding of lobe-lobe contacts indicate that the lobes were hot.

An alternative to Subunit 10A being a peperite is that it is a flow-top breccia like Subunits 2A and 7A that has been reworked by sedimentary processes. The in situ brecciation could be the result of cooling in air and secondary alteration. The sediments in the breccia could have been deposited after the flow was emplaced.

Lava Emplacement Styles

Two principal types of lava flow are represented at Site 1137: inflated pahoehoe flows and flows with a flow-top breccia composed of pahoehoe lobes. Flows within each basic type show a great deal of individuality. The thickest pahoehoe flow (27 m of Unit 4) suggests a single lobe being active for a decade, longer than has been previously suggested for any single pahoehoe lobe (Self et al., 1998). The thinnest pahoehoe flow (10.6 m of Unit 8) is estimated to have been emplaced in a matter of weeks. The lack of a breccia on top of Unit 8 means that even such relatively rapidly emplaced ponded flows moved as smooth surfaced pahoehoe and did not involve wholesale disruption of their flow tops.

The brecciated flow type seen at Site 1137 is similar to some flows in the Columbia River Basalt, but this flow type has never been described in detail (see **"Physical Volcanology,"** p. 16, in the "Explanatory Notes" chapter). The interior of these flows is noticeably less vesicular than that of the inflated pahoehoe flows, suggesting more efficient degassing during the brecciation process. There are few or no horizontal vesicle sheets or other signs of large-scale concentration of late stage differentiates. Factors that should hinder this type of late-stage segregation include relatively rapid cooling of the flow interior by entrained clasts and continued motion of the flow stirring the interior.

The presence of a basal breccia on Unit 7 means that brecciation we observe at Site 1137 was taking place at the flow front and is not a remobilized pahoehoe flow (see **"Interpretation,"** p. 19, in the "Explanatory Notes" chapter). It is worth noting that the only characteristic separating Unit 7 from classic aa flows is the insufficient angularity of the clasts and vesicles.

Eruption Environment

The basement at Site 1137 formed in environments ranging from subaerial to fluvial. The environment in which Unit 1 was erupted is equivocal, but the internal characteristics of the lava are consistent with known subaerial pahoehoe flows emplaced on gentle slopes (≤1°). Unit 2 is subaerial, based on both the morphology of the breccia and its oxidation. Unit 3 has poor recovery of key portions but is again consistent with subaerial eruption. The sediments within the base of Unit 3 suggest periodic influx of silt-laden water, most easily explained by the lateral migration of ground water and deposition near the water table (see **"Lithostratigraphy,"** p. 3). Unit 4 appears to be subaerial, based on its highly vesicular nature, the thin chill margin, and deep oxidation. However, the overlying laminated siltstone was probably deposited in quiet, shallow water. Units 5 and 6 indicate a fluvial setting. The lithic volcanic conglomerate (Unit 6) probably formed in a braided river environment, near a region of significant relief. The welding and morphology of the breccia on Unit 7 suggests eruption in a subaerial environment with subsequent infilling by water-lain sediments. The features of Unit 8 are consistent with subaerial emplacement on a gentle slope. Mass flow redeposition of the crystal vitric tuff (Unit 9) probably involved water, but mass flow redeposition in a subaerial environment is possible. The breccia at the top of Unit 10 has characteristics that suggest that lava may have intruded into wet sediments.

IGNEOUS PETROLOGY

Introduction

We recovered 10 basement units totaling 144.2 m at Site 1137, with an average recovery of 73%. Seven units are subaerial basaltic lavas with a total thickness of 94.1 m; three are volcaniclastic sedimentary interbeds within the basalt sequence. For lavas not separated by sedimentary layers, we have identified units representing single lava flows by using marked differences in flow structure, vesicularity, and phenocryst content and type occurring over a short interval of recovered section. We have subdivided some of the lava-flow units into subunits corresponding to brecciated or highly vesicular and more massive parts (see **"Physical Volcanology,"** p. 13).

In this section we describe the lithology, petrography, primary mineralogy, and geochemistry of the seven igneous basement units at Site 1137. Volcanic structures are described in **"Physical Volcanology,"** p. 13, and secondary mineralogy is described in **"Alteration and Weathering,"** p. 38. We also describe the igneous constituents of the three volcaniclastic sedimentary units in the basement sequence. The sedimentological features of these units are described in **"Lithostratigraphy,"** p. 3, and **"Physical Volcanology,"** p. 13.

Curated depths of the units (Table **T7;** Fig. **F35**) assume that the top of a core comes from the top of the cored interval (see **"Introduction,"** p. 1, in the "Explanatory Notes" chapter), so the curated depths of flow boundaries (in mbsf) normally differ from their actual depths in the hole. Relatively good core recovery and the high quality of the logging results enabled us to determine true thicknesses of the basement units through core-log integration (see **"Physical Volcanology,"** p. 13, and **"Downhole Measurements,"** p. 54). In this section we refer to sample locations and unit boundaries according to curated depths in mbsf as described above, but unit thicknesses were derived from core-log integration (Tables **T9, T10;** Fig. **F35**).

F35. Interpretative summary lithology and some key chemical and physical properties, **p. 98.**

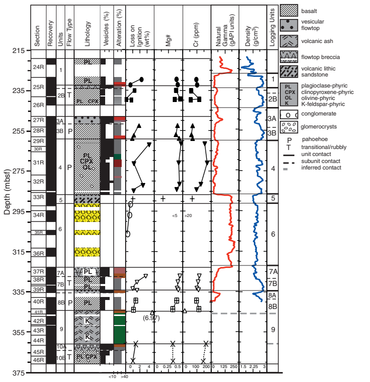

T10. Petrographic and unit summary of igneous basement sampled, **p. 181.**

Lithology

The upper four basement units form a 59.4-m-thick sequence of lava flows. Unit 1 is slightly altered, massive, nonvesicular to slightly vesicular, sparsely plagioclase-phyric basalt. The top of this unit is marked by an erosional unconformity; thus, the recovered 6.1 m is a minimum estimate for the original flow thickness. Unit 2 (10.1 m thick) is divided into a 2.9-m upper brecciated subunit (2A) and a 7.2-m lower massive subunit (2B). Subunit 2A is moderately to highly altered, very sparsely to highly vesicular, sparsely plagioclase-phyric basaltic breccia that is interpreted as a flow top. Subunit 2B is slightly to moderately altered, massive, aphyric to sparsely plagioclase-phyric basalt.

Unit 3 is 16.6 m thick, and its top is marked by an abrupt increase in vesicularity, vesicle size, and alteration. Subunit 3A is 9.6 m thick and consists mostly of highly vesicular aphyric basalt. It is highly oxidized and altered at the top, but the level of alteration decreases downward to slight at the base of the subunit. Subunit 3B is a 7.0-m-thick, massive, slightly to moderately altered, aphyric to sparsely plagioclase-phyric basalt. Beneath its base is an ~8-cm-thick laminated, brecciated volcanic siltstone (interval 183-1137A-29R-2, 64–73 cm) that blankets the top of the thick (26.6 m) underlying Unit 4 basalt flow (Fig. **F19**). Below a classic pahoehoe top, the moderately plagioclase + clinopyroxene + olivine-phyric basalt of Unit 4 varies from massive to highly vesicular. Bulk-rock alteration varies with vesicularity from slight to high. Vesicle fillings constitute most of the alteration, whereas the phenocrysts and groundmass tend to be only slightly altered. The basal chill zone of this flow and the baked contact with the underlying sediment of Unit 5 are well preserved near Section 183-1137A-33R-1, 122 cm (Fig. **F20**).

Units 5 and 6 are sediments and represent a significant hiatus of unknown duration between the eruption of Units 1–4 and 7–10. Unit 5 is a 4.4-m-thick sequence of interbedded crystal-lithic volcanic sandstone and siltstone (see **"Lithostratigraphy,"** p. 3). Unit 6 is a 31-m-thick lithic volcanic conglomerate containing well-rounded, granule to small boulder-sized clasts embedded in a poorly to moderately sorted matrix of coarse to fine sand-sized crystal-lithic volcanic fragments, including altered glass (see **"Lithostratigraphy,"** p. 3, and **"Physical Volcanology,"** p. 13). The clasts are predominantly volcanic lithologies and are moderately to highly altered; many have distinct, concentric oxidation rims (Fig. **F9**). In the upper part of the unit, the predominant clast lithologies are massive trachyte (sanidine-plagioclase-clinopyroxene-phyric), flow-banded rhyolite (sanidine-plagioclase-phyric), and highly plagioclase-phyric basalt. Minor lithologies include granitoid and garnet-biotite gneiss. In the lower part of the unit, aphyric and plagioclase-phyric basaltic pebbles are more abundant. Primary textures and mineralogy of the clasts within the conglomerate are described below.

Units 7, 8, and 10 form a basaltic sequence that is 34.7 m thick, interrupted only by the Unit 9 tuff. Unit 7 is a 13.0-m-thick, sparsely to moderately plagioclase-phyric basalt that has a 5.8-m-thick, highly to completely altered flow-top breccia (Subunit 7A) and a 7.2-m-thick, slightly to moderately altered massive flow interior (Subunit 7B). Subunit 8A is the upper 3.4-m-thick, brecciated and vesicular part of Unit 8 and consists of moderately to highly altered, sparsely to moderately plagioclase-phyric basaltic breccia that grades into massive basalt. Subunit 8B (7.6 m thick) is slightly to moderately altered, moderately plagioclase-clinopyroxene-phyric, massive basalt. Unit 10 is moderately to highly plagioclase-clinopyroxene-phyric basalt at least 10.7 m thick (drilling ceased before reaching the bottom of the flow), with a 3.5-m-thick moderately to highly altered, brecciated top (Subunit 10A) and a >7.2-m-thick slightly altered, massive underlying interior (Subunit 10B). Both subunits contain abundant plagioclase-dominated glomerocrysts, as large as 20 mm in size.

The lower basalt sequence is interrupted by Unit 9, a 14.9-m-thick, highly altered crystal-vitric tuff that contains ~40% feldspar crystals and <5% oxidized mafic phenocrysts (see **"Physical Volcanology,"** p. 13, for a detailed description of the tuff). Scattered (<5%), round to elongate, lithic fragments as large as several centimeters (Fig. **F10**) consist of basalt, trachyte, granitoid, and garnet-biotite gneiss, generally similar to those found in the conglomerate (Unit 6). Primary minerals in the tuff as well as several of the clasts within the tuff are described below.

Petrography and Primary Mineralogy

Basalts (Units 1–4, 7–8, 10)

At least one massive flow interior and one finer-grained sample closer to a chilled zone were sampled from each flow for shipboard X-ray fluorescence (XRF) and thin-section analysis. Other interesting macroscopic features were also sampled for thin-section and, in some cases, XRF analysis. Table **T10** summarizes the principal petrographic characteristics of each unit; phenocryst abundance for each of the basaltic units is shown in Figure **F36**. For the complete thin-section descriptions, see the **"Core Descriptions"** contents list.

Alteration is only slight to moderate in the interiors and bases of the units (Subunits "B"), but moderate to high in the vesicular and/or brecciated flow tops (Subunits "A") (Fig. **F35**). The major minerals are relatively unaltered within flow interiors, but glass and olivine are always

F36. Phenocryst and glomerocryst abundance variations in the basaltic units, **p. 99.**

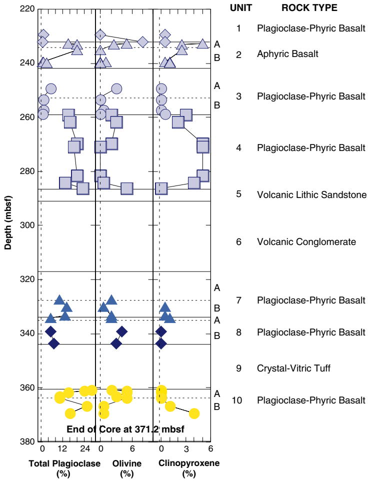

replaced by clays. Skeletal habits of titanomagnetite and, to a lesser extent, plagioclase reflect rapid cooling during extrusion of the basalts, especially in the brecciated clasts and flow-boundary chill zones. Vesicles are generally, but not exclusively, concentrated at flow margins and are either partially or totally filled with clay and/or zeolite, with subordinate amorphous silica (see **"Alteration and Weathering,"** p. 38, and **"Physical Volcanology,"** p. 13).

The basalts are sparsely to highly porphyritic. As in basalt flows at Site 1136, phenocryst phases are present in different forms as (1) discrete, single crystals of plagioclase (0.5%–20%), clinopyroxene (0%–5%), and olivine (0%–8%) or (2) as compact glomeroporphyritic intergrowths (0%–23%), which are usually monomineralic (plagioclase) or occasionally bimineralic (plagioclase with subordinate clinopyroxene). Although there is a hiatus in volcanism between Units 4 and 7, we observed no significant differences in mineralogy or texture between the upper (Units 1–4) and lower (Units 7–8) basalts. However, the lowermost unit (Unit 10) is petrographically distinct from the other basalt units in that it contains much larger (and generally more abundant) plagioclase phenocrysts and glomerocrysts.

Normal and oscillatory zoning and resorption features are common in the glomeroporphyritic plagioclase throughout the basement sequence and also in the larger discrete plagioclase phenocrysts of Unit 10. Some of these larger plagioclase crystals have overgrowths and display sieve textures (Fig. **F37**). A spectacular example of oscillatory zoning is in Unit 10 (Sample 183-1137A-45R-4, 118–120 cm), where a 20-mm glomerocryst contains dramatically zoned plagioclase (Fig. **F38**). Subunit 2B contains a coarser-grained microgabbro xenolith (~1 cm diameter) with somewhat embayed, subhedral to anhedral clinopyroxene and plagioclase (~An_{70}) reacting with the basalt host (Fig. **F39**).

We estimated plagioclase phenocryst compositions to be between An_{55} and An_{65}, except in Unit 8 and perhaps Unit 7, where the plagioclase is more calcic (An_{70-75}). In several units, plagioclase glomerocryst compositions, An_{65} to An_{75}, appear to be slightly more calcic than smaller, discrete phenocryst plagioclase. In flow tops and basal contacts, plagioclase phenocrysts are commonly altered to a mixture of zeolite ± sericite ± clay and are locally replaced by carbonate. This alteration preserves Carlsbad twinning in places but destroys finer-scale albite twins, giving plagioclase the appearance of an alkali feldspar or feldspathoid (Fig. **F40**).

Clinopyroxene phenocrysts are found predominantly in the interior of flow units. Altered microphenocrysts of olivine and possibly clinopyroxene (replaced by clay or zeolite pseudomorphs) (Fig. **F41**) are present in fine-grained flow tops and bases. In some of the units, the abundances of clinopyroxene and olivine phenocrysts exhibit a broad inverse relationship through the sequence, with olivine being more abundant at flow margins and clinopyroxene in the flow interiors (Fig. **F36**).

The groundmass of all the basaltic rocks is fine-grained to aphanitic and consists of plagioclase (≤45%), pyroxene (≤35%), titanomagnetite (≤10%), and altered mesostasis. The most significant difference in primary mineralogy and texture of the groundmass is between massive flow interiors and the finer-grained flow-top breccias and vesicular flow bottoms. We observed intergranular to intersertal and rare subtrachytic textures in the interiors of the flows. Toward the flow margins, the grain size decreases dramatically and the textures become more hyalo-

F37. Photomicrograph of plagioclase phenocryst from Unit 4, **p. 100.**

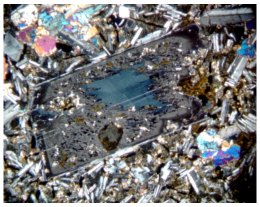

F38. Photomicrograph of a plagioclase glomerocryst from Subunit 10B, **p. 101.**

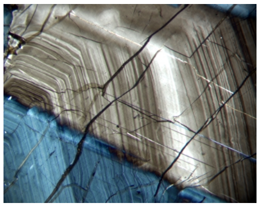

F39. Photomicrograph of microgabbro xenolith from Unit 2B, **p. 102.**

F40. Photomicrograph of a highly altered plagioclase phenocryst from Unit 10A, **p. 103.**

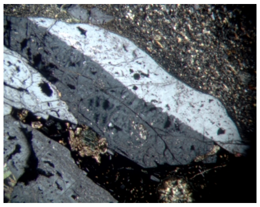

pilitic, almost vitrophyric, as the proportion of glass increases. This is particularly evident in the flow breccias where the groundmass is dominated by altered glass. In places, this glass contains a myriad of minute (<0.01 mm) titanomagnetite crystals (e.g., Subunit 10A).

The dominant opaque phase, titanomagnetite, is present in two forms: (1) skeletal, acicular crystals with serrated edges, and (2) tabular subhedral octahedra. Unlike Site 1136, we observed no maghemite exsolution, although in Subunit 2B (Sample 183-1137A-25R-5, 113–115 cm) ilmenite has exsolved from titanomagnetite in a few crystals (Fig. **F42**). Sulfides are rare in these basalts, but trace amounts of pentlandite were found in Units 2 and 4 and pyrrhotite in Unit 10. The most abundant sulfide was found in Subunit 2B (Sample 183-1137A-26R-2, 38–40 cm), where pentlandite is a late-stage vein segregation and pervades into the groundmass (Fig. **F43**).

Unit 5: Crystal-Lithic Volcanic Siltstone and Sandstone

We examined a sample from one of the coarsest layers (medium sand size) in the sandstone of Unit 5 in thin section and by XRF analysis (Sample 183-1137A-33R-3, 50–53 cm) (see Fig. **F8**). Volcaniclastic detritus dominates the section, with ~75% angular to subangular trachytic and basaltic lithic fragments (≤0.5 mm) and only minor alkali feldspar (~10%) and quartz (~5%). The alkali feldspar component contains both clear sanidine and inclusion-rich, perthitic grains. Subhedral garnet grains up to 0.4 mm in diameter (~1%) (Fig. **F44**) and rare biotite are also present. Thus, the mineralogy of the sandstone is similar to that in clasts in the immediately underlying conglomerate (Unit 6). In addition, unaltered, angular to subangular, brown hornblende up to 0.2 mm is present. This mineral is not present in the lavas and is distinct from the brown amphibole in the crystal-vitric tuff.

Unit 6: Conglomerate—Igneous Clasts

The conglomerate contains diverse igneous clasts. Some clasts appear similar to lavas in the basalt flow units and were not studied in further detail. Clasts of sanidine-phyric trachyte and rhyolite are relatively abundant, and we also found cobbles of granitoid. We studied these distinctive clasts in thin section, and two were analyzed by XRF.

Sanidine-Plagioclase-Clinopyroxene-Phyric Trachyte

This clast lithology is common in the upper two-thirds of recovered core from Unit 6 and decreases in abundance toward the base; the examined clast (Sample 183-1137A-33R-5, 10–12 cm) is from the top of the unit. The trachyte contains ~20% subhedral (rounded) to euhedral sanidine phenocrysts and ~4% subhedral plagioclase phenocrysts, some of which have a continuous overgrowth of either sanidine or relatively Na-rich plagioclase (Fig. **F45**). Clinopyroxene phenocrysts (2%) are moderately altered, although fresh cores persist. Minor euhedral titanomagnetite phenocrysts (0.5%) are present. The groundmass is dominated by feldspar with minor titanomagnetite and glass and trace amounts of zircon.

Sanidine-Phyric Flow-Banded Rhyolite

As with the trachytic clasts, this lithology is common throughout the upper two-thirds of the recovered unit and decreases in abundance in the bottom third. The examined clast (Sample 183-1137A-34R-2, 113–117 cm) contains subhedral to rounded sanidine phenocrysts (8%–

F41. Photomicrographs of altered olivine, **p. 104.**

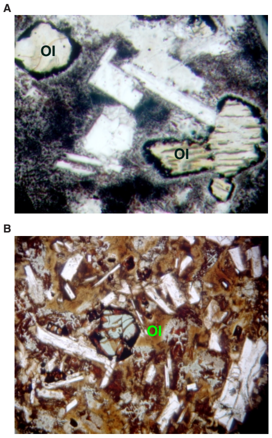

F42. Photomicrograph of ilmenite exsolution in titanomagnetite in Unit 2B, **p. 105.**

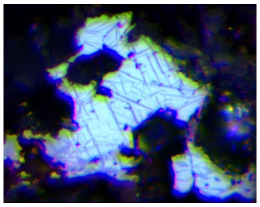

F43. Photomicrograph of pentlandite in vein segregation in Unit 2B, **p. 106.**

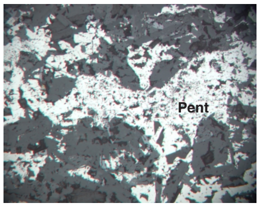

F44. Photomicrograph of garnet and brown hornblende grains in the volcanic sandstone of Unit 5, **p. 107.**

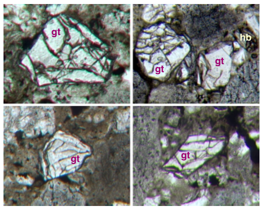

15%) and subordinate plagioclase (1%–3%). No quartz phenocrysts were identified, but the high SiO_2 content of the rock (74 wt%) indicates a rhyolitic composition (see **"Geochemistry: Major and Trace Element Compositions,"** p. 34). The entire groundmass is marked by conspicuous flow banding, a series of millimeter-scale alternating light and dark layers that bend around the phenocrysts (Fig. **F46**). The lighter, translucent bands are recrystallized quartz and feldspar, whereas the darker, opaque bands are devitrified glass containing microspherulites. A minor amount (1%–2%) of groundmass titanomagnetite is present, as well as trace amounts of zircon and apatite.

Granitoid

A granitoid clast from the bottom of Unit 6 consists of alkali feldspar (50%) and plagioclase (38%), with subordinate quartz (12%) and no significant mafic or hydrous phases. Symplectite intergrowths between the two feldspars are ubiquitous (Fig. **F47**), and the feldspars are generally untwinned. Titanomagnetite and zircon are present in trace amounts.

Units 6 and 9: Metamorphic Clasts

Metamorphic clasts are found in both the conglomerate of Unit 6 and the crystal vitric tuff of Unit 9. We studied four in thin section, two from each unit, and selected one for XRF analysis.

Garnet-Biotite Gneiss

Two clasts from Unit 9 and one from Unit 6 are garnet-biotite gneiss. Garnets are distinctively poikiloblastic in the clasts from the conglomerate (Sample 183-1137A-35R-2, 46–47 cm) (Fig. **F48**) and from the bottom of Unit 9 (Sample 183-1137A-44R-4, 44–46 cm) but are porphyroblastic in the other clast from Unit 9 (Sample 183-1137A-43R-4, 57–60 cm). This latter sample, unlike the other two, contains no obvious quartz and also exhibits symplectic intergrowths between plagioclase and K-feldspar. All three clasts have a xenoblastic groundmass with a weak gneissic fabric delineated by biotite (4%–20%) and plagioclase (5%–20%). The groundmass is dominated by alkali feldspar (45%–60%), with quartz (10%–20%), and subordinate amounts of plagioclase (5%–20%). Accessory zircon is distinctive in the two quartz-bearing gneisses and absent from the other clast.

Actinolite Gneiss

Another clast sampled from Unit 6 is actinolite-bearing gneiss (Fig. **F49**). It is dominated by xenoblastic alkali feldspar (70%), with subordinate quartz (20%) and minor actinolite (~3%), plagioclase, magnetite, and microcline. A weak gneissic fabric is evident.

Unit 9: Crystal-Vitric Tuff

We examined seven thin sections from different levels within the 14.9-m-thick crystal-vitric tuff sequence. In the upper half of the sequence, the original glassy matrix has been almost completely altered to relatively isotropic, pale green to brown clay, making it difficult to discern any original structure in the matrix (Samples 183-1137A-41R-1, 127–128 cm; 41R-2, 98–99 cm; 41R-3, 42–46 cm; and 43R-3, 42–44). However, in the lower part of the tuff (Samples 183-1137A-43R-4, 57–60; 44R-4, 6–9 cm; and 44R-4, 44–46 cm), outlines of 0.1- to 0.2-mm-wide cuspate and tricuspate glass shards are still apparent (Figs. **F28,**

F45. Photomicrographs of plagioclase phenocrysts with continuous feldspar overgrowths in a massive trachyte from Unit 6, **p. 108.**

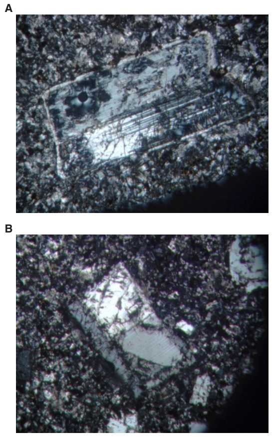

F46. Photomicrograph of flow-banded texture around sanidine phenocryst in the flow-banded rhyolite in Unit 6, **p. 109.**

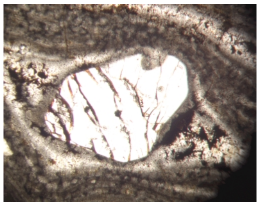

F47. Photomicrograph of symplectite intergrowths between plagioclase and alkali feldspar in a granite clast from the base of Unit 6, **p. 110.**

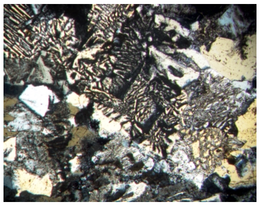

F48. Photomicrographs of garnet-biotite gneiss, **p. 111.**

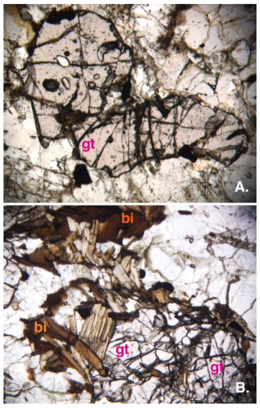

F50, F51, F52), including some patches of relatively unaltered, pale yellow isotropic glass (Fig. F52).

The modal abundance of the major phenocryst phases is relatively uniform throughout the tuff, with 35%–40% sanidine, minor but significant amounts of plagioclase and quartz (1%–3% each), and trace amounts of opaques, zircon, and kaersutite. Sanidine and quartz vary from euhedral to deeply embayed (Fig. F50); some are broken or disrupted (Fig. F51). Most of the symplectite growths on sanidine phenocrysts appear to be an alteration reaction with the groundmass. However, rare isolated garnet crystals and some of the symplectic and inclusion-rich alkali feldspar are probably xenocrystic. Mafic pseudomorphs after biotite(?) are now nearly completely altered to pleochroic brown-green clay and usually have inclusions of opaques, zircon, and kaersutite (Fig. F53). Relatively large (up to 0.15 mm) melt inclusions are present in some sanidine phenocrysts (Fig. F52).

Geochemistry: Major and Trace Element Compositions

Basalt Compositions

We analyzed 20 basalt samples by XRF (Table T11). Seven samples are from relatively unaltered flow interiors, three were specifically chosen to investigate the effects of alteration, and two were chosen to investigate macroscopic features (a microgabbro xenolith and a glass-rich segregation vein from Unit 7). To characterize intraflow variation, chilled margins, and vesicle filling, we also analyzed multiple samples from Units 3, 4, and 7 (Table T11).

Most Site 1137 basalts are slightly quartz-normative tholeiitic basalts; SiO_2 contents vary from 50.4 to 54.0 wt%, MgO from 4.4 to 7.4 wt%, and TiO_2 from 1.84 to 2.68 wt% (Table T11, Figs. F54, F55). The low MgO, Cr, and Ni contents of most samples indicate that these are not primary melts from peridotite (Fig. F55; Table T11). The three samples chosen specifically to investigate alteration have compositions in the alkalic field (see the square symbols in Fig. F54), presumably because postmagmatic alteration increased their alkali content, especially K_2O. The two other basalts with compositions in the alkalic field, as well as the three samples in the tholeiitic field closest to the Macdonald-Katsura line (see the diamond symbols in Fig. F54), are chilled flow-margin samples with up to 50% clay and zeolite after glass and very fine-grained groundmass phases. These samples are also likely to have elevated total alkali contents as a result of alteration.

The relatively unaltered nature of the flow interiors is reflected in their low loss on ignition (LOI). Of the seven flow interior samples, only one has LOI >1.6 wt%. In contrast, the more altered samples from Units 3, 4, 7, and 10 have generally higher LOI values (as much as 3.3 wt%), together with higher K_2O and Rb contents. The large concentration range of K and Rb shows that their abundances were affected by postmagmatic alteration (Fig. F56A, F56B). In the least-altered basalts (Fig. F56C, F56D), primitive mantle–normalized Ba abundance is, with one exception, greater than normalized values of the more compatible elements, and abundance ratios of Ba to these elements are relatively constant. On this basis, we tentatively conclude that high Ba content is an original magmatic feature of Site 1137 basalts. Abundances of Nb, Ce, Zr, and Y are very similar in the altered and least-altered basalts, indicating that secondary processes did not affect these elements (Fig. F56A, F56B).

F49. Photomicrograph of actinolite and microcline in the actinolite-bearing gneiss in Unit 6, p. 112.

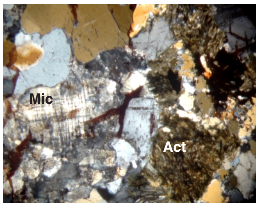

F50. Photomicrograph of a deeply embayed quartz crystal in Unit 9 tuff, p. 113.

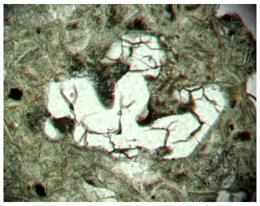

F51. Photomicrograph of fractured sanidine phenocryst from Unit 9 tuff, p. 114.

F52. Photomicrograph of melt inclusions in sanidine crystals from Unit 9, p. 115.

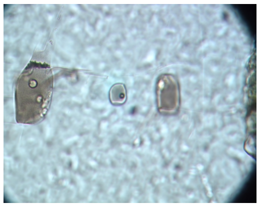

Comparison of the basaltic flow units at Site 1137 shows few systematic downhole trends (Fig. **F57**). Mg numbers (Mg# = molar MgO/[MgO + FeO], where FeO is estimated as being 80% of the total iron [reported as Fe_2O_3] present) vary from 0.33 to 0.48 and show no systematic trend from Units 1 to 8. The lower sample from Unit 7 and the two samples from Unit 10 share a lower Mg# of 0.33 (Fig. **F57A**), surprisingly accompanied in Unit 10 samples by relatively higher Ni contents (59–61 ppm). Trace element ratios such as Zr/Y and Nb/Ce decrease down section (Fig. **F57B**). Relative to its host lava, a microgabbro xenolith from Unit 2 (Sample 183-1137A-26R-1 [Piece 12, 143–146 cm]) has significantly higher Mg#, CaO, and Cr and lower Ti, Zr, P_2O_5, and V contents (Table **T11;** Fig. **F57A**). The chilled margin of Unit 10 has much higher Y and Ce abundances than the other samples (Table **T11;** Fig. **F57A**), perhaps the result of interaction or contamination with sediment (see **"Physical Volcanology,"** p. 13).

The relatively evolved quartz-normative tholeiite of Unit 4, a 26.6-m-thick compound lava flow ("see **"Physical Volcanology,"** p. 13), has the largest internal variation in SiO_2 (50.6 to 54.0 wt%), Mg# (0.48 to 0.40), and TiO_2 (2.05 to 2.52 wt%). Units 8 and 10 show higher Mg#, Cr, and olivine abundances near flow margins but no significant variation in Ni (Figs. **F35, F36;** Table **T11**); the absence of olivine in the interiors of these flows (Fig. **F36**) may reflect olivine reacting out as the melt evolved during cooling.

Comparison with Other Sites

Site 1137 basalts differ from Cretaceous basalts recovered from other sites on the Kerguelen Plateau (Figs. **F54, F55, F58, F59**) in several significant ways. In general, Site 1137 basalts have unusually high concentrations of highly to moderately incompatible trace elements and slight depletion of Nb relative to Ba and Ce. Compared to Site 1136, concentrations of Ba, Nb, Ce, and Zr in most 1137 basalts exceed those of 1136 by a factor of two (Fig. **F58, F59**). Site 1137 basalts are in the low MgO, high SiO_2 and TiO_2 portion of the overall concentration range for Kerguelen Plateau basalts, but do not extend to the very low MgO contents of Site 738 basalts (Fig. **F55**). In comparison to all other Kerguelen Plateau basement sites, Site 1137 basalts have distinctly higher Zr, Nb, and Ce contents but comparable Y contents; only basalts from Sites 738, 747, and 1137 have distinctly high Ba (Fig. **F58**). The degree of trace element enrichment in Site 1137 basalts does not, however, reach the levels observed in the younger, more alkaline rocks on Heard Island, Kerguelen Archipelago, and Site 748 (see **"Previous Sampling of Igneous Basement: Ages and Geochemical Characteristics,"** p. 5, in the "Leg 183 Summary" chapter). However, compared to other Cretaceous basalts from the Kerguelen Plateau, basalts from Sites 738 and 1137 have the highest Zr/Ti and Zr/Y (Fig. **F60**).

In primitive mantle–normalized incompatible element diagrams (Figs. **F56, F59**), the Site 1137 basalts show moderate negative Nb anomalies. A second perspective on relative Nb depletion (Fig. **F60**) shows that Site 1137 basalts have Nb/Ce similar to Site 747 and the high Zr/Ti ratios that characterize basalts from Sites 738 and 747. As described in **"Previous Sampling of Igneous Basement: Ages and Geochemical Characteristics,"** p. 5, in the "Leg 183 Summary" chapter, similar ratios have been used together with isotope data as evidence for a continental crustal component in these basalts.

F53. Photomicrographs highlighting the breakdown of mafic crystals in the Unit 9 tuff, **p. 116.**

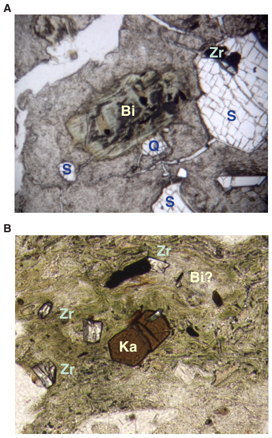

T11. Major and trace element data for basalt samples, **p. 183.**

F54. Total alkali vs. SiO_2 abundance, **p. 117.**

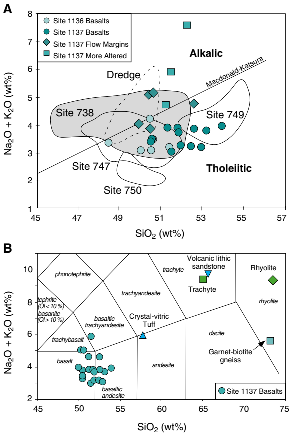

F55. Covariation diagrams comparing basalts from Site 1137 with those from other parts of the Kerguelen Plateau, **p. 118.**

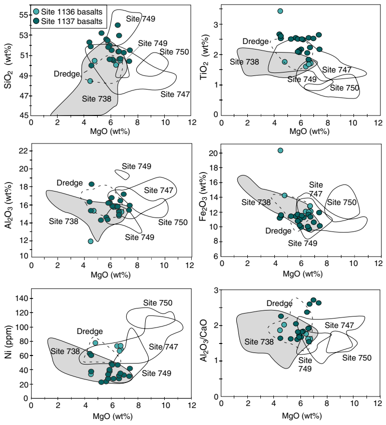

Fitton et al. (1997, 1998) used Nb/Y vs. Zr/Y to distinguish Icelandic plume-related basalts from depleted mid-ocean ridge basalt (MORB). In such a plot (Fig. **F61**), Kerguelen Plateau basement basalts range from the plume field (Sites 749 and 750) to near the plume-MORB boundary (Sites 1136 and 747) to well within the MORB field (Sites 738 and 1137). The Site 1137 lavas trend to the highest Nb/Y and Zr/Y; despite plotting within the MORB field, these lavas do not have the incompatible element depletion that characterizes MORB (cf. Fig. **F56**). Two possible interpretations are (1) contamination of plume-derived lavas with continental crust as proposed for Sites 738 and 747 and discussed above or (2) the mantle source of Site 1137 lavas had lower Nb/Y at a given Zr/Y compared to the source of basalts from Iceland.

Felsic Volcanic Rocks

Three of the analyzed volcanic rocks have nonbasaltic compositions (Table **T12**). Two are sanidine-phyric clasts from the Unit 6 volcanic conglomerate, and the other is a sample from the crystal-vitric tuff of Unit 9. We also analyzed a coarse layer in the lithic volcanic sandstone (Unit 5), which is composed almost entirely of lithic volcanic fragments and phenocrysts (Table **T10, T12**).

Moderate to high SiO$_2$ contents (64.9 to 73.5 wt%), total alkalis (~9.5 wt%), and high normative quartz and alkali feldspar abundances all reflect the evolved nature of these clasts. In petrologic classification diagrams such as total alkalis vs. SiO$_2$ (Fig. **F54B**) and normative quartz-orthoclase-albite (not shown), the sanidine-plagioclase-clinopyroxene-phyric clast (Sample 183-1137A-33R-5 [Piece 1, 7–9 cm]) is a trachyte and the sanidine-phyric flow-banded clast (Sample 183-1137A-34R-2 [Piece 1D, 111–113 cm]) is a rhyolite. The crystal-lithic volcanic sandstone has a very similar major element composition to the trachyte, suggesting that the lithic volcanic fragments are dominantly intermediate in composition. The crystal-vitric tuff exhibits an intermediate composition plotting on the line dividing andesite and trachyandesite. However, the tuff sample is highly altered (LOI = ~7%), and the high crystal content suggests that crystal enrichment may have resulted from pyroclastic and/or sedimentary processes (see **"Physical Volcanology,"** p. 13). The phenocryst assemblage (sanidine >> plagioclase, minor quartz) is consistent with a highly evolved bulk composition, although the likely sedimentary redeposition of the tuff allows for incorporation of xenocrysts and other complications.

These samples have very high concentrations of incompatible trace elements (e.g., Zr from 582 to 1274 ppm, Ce from 164 to 373 ppm) (Table **T12**). For these evolved rocks, the mantle-normalized trace element patterns are distinctive, with levels of Rb, K, Nb, Ce, and Zr that are three to five times higher than in the basalts, and highly variable Ba abundance (Fig. **F56E**). The rhyolite and trachyte are relatively depleted in Sr and Ti, probably because of fractional crystallization of plagioclase and Fe-Ti oxides, respectively. The trace element compositions are very similar to those of Miocene to Holocene trachytes from Heard Island and the Kerguelen Archipelago (Fig. **F62**).

The evolved volcanic rocks at Site 1137 share some of the distinctive chemical characteristics of the basalts, such as high Zr/Y ratios (Fig. **F61**), but do not exhibit a Nb anomaly on a primitive mantle–normalized plot (Fig. **F56E**). The tholeiitic basalts at Site 1137 are not suitable parental magmas for the trachytes because low-pressure fractional crystallization does not produce alkalic magmas such as trachytes from sil-

F56. Trace element contents of basalts, **p. 119.**

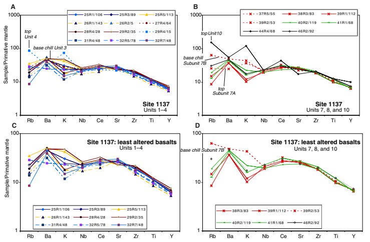

F57. Variations of major and trace element abundances with depth in Hole 1137A, **p. 121.**

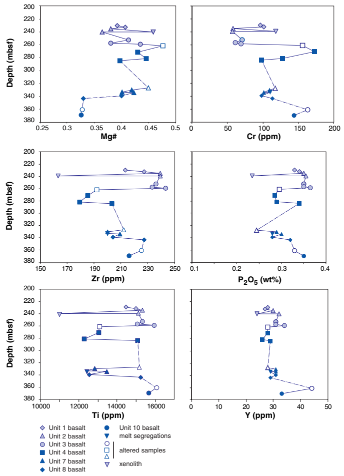

F58. Incompatible trace element compositions of basalts, **p. 123.**

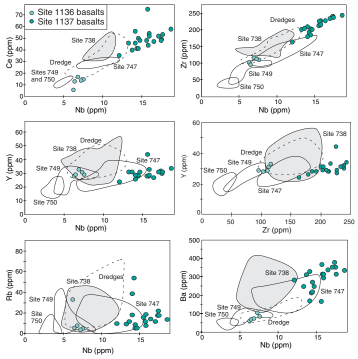

ica-oversaturated parents, and magmas with relatively high Nb/Ce are not normally formed from parental magmas with low Nb/Ce.

Garnet-Biotite Gneiss

Sample 183-1137A-35R-2 (Piece 5, 44–46 cm) (Table **T12**) is a garnet-biotite gneiss clast from the Unit 6 conglomerate. With 73.3 wt% SiO_2 and 5.6 wt% $Na_2O + K_2O$, the sample is a granite (i.e., in a total alkalis-silica classification diagram, it is in the rhyolite field) (Fig. **F54**). The rock is metaluminous but contains corundum in the norm and has a relatively low Na_2O content. The primitive mantle–normalized trace element pattern for the garnet-biotite gneiss shares the low Sr and Ti contents of the trachytic and rhyolitic samples but is distinguished by the large negative Nb anomaly characteristic of continental crust (Fig. **F56E**). As seen on a Nb/Y vs. Zr/Y diagram (Fig. **F61**), the composition of the gneiss is distinct from average continental crust estimates, such as those of Rudnick and Fountain (1995).

Source Implications

Three distinctive aspects of the chemical compositions of basalts from Site 1137 hint at their origin: (1) the relative depletion of Nb (Fig. **F56A, F56B, F56C, F56D**), (2) the high concentrations of incompatible trace elements (Fig. **F58**), and (3) the fractionation of highly incompatible elements from moderately incompatible elements (e.g., Zr from Y) (Fig. **F60**).

The relatively low Nb contents indicate that Site 1137 basalts contain a component from the continental lithosphere. In the absence of other constraints, evidence for such a component in the source of a basalt erupted in an oceanic environment could indicate that the component was an integral part of the mantle source of the basalt. However, given the firm evidence of continental crust in the vicinity (clasts of garnet-biotite gneiss in the conglomerate and tuff, and detrital garnet in the sandstone), it is more likely that this component was introduced as a contaminant as the basalts passed through continental crust.

The presence of a continental component in the Site 1137 basalts may have influenced the relative abundances of elements other than Nb. However, the addition of continental crust to magmas with relatively high concentrations of incompatible elements, such as the basalts from Site 1137, would have only a minor effect on abundance ratios of elements such as Zr and Y because the Zr/Y ratios of continental crust and enriched magmas, such as those of Site 1137, are similar (Fig. **F61**). We conclude that the Zr/Y ratio in Site 1137 basalts is little affected by the crustal component and that the primary magma for Site 1137 basalt probably had a high Zr/Y ratio (i.e., ~3) (Fig. **F61**). This feature was either inherited from a mantle source that was relatively enriched in incompatible elements or was derived by degrees of melting that were lower than those that produced the other tholeiitic basalts of the Kerguelen Plateau. Investigating these hypotheses—the extent of continental contamination, variation in source compositions, and the degree of partial melting—will be the focus of shore-based geochemical studies on the origin of basalt at Site 1137.

F59. Primitive mantle–normalized incompatible element contents of basalts, **p. 124.**

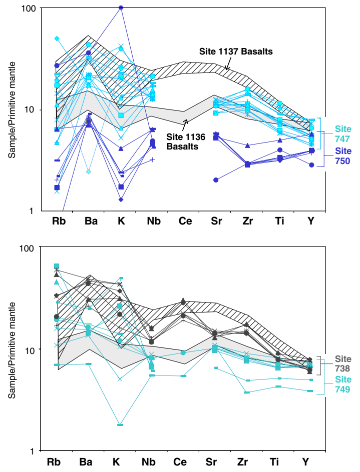

F60. Primitive mantle–normalized Nb/Ce, Zr/Ti, and Nb/Zr vs. Zr/Y ratio or Zr content, **p. 125.**

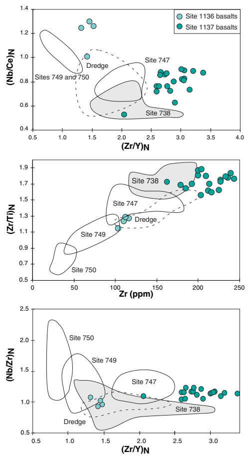

F61. Nb/Y vs. Zr/Y diagram for Kerguelen Plateau basement basalt, **p. 126.**

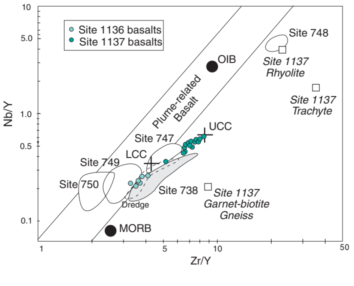

T12. Major and trace element data for felsic samples, **p. 186.**

ALTERATION AND WEATHERING

Ten basement units have been defined at Hole 1137A, including seven igneous units interpreted as separate subaerial lava flows (see **"Igneous Petrology,"** p. 28, and **"Physical Volcanology,"** p. 13) and three volcaniclastic sedimentary units (see **"Lithostratigraphy,"** p. 3, and **"Physical Volcanology,"** p. 13). The three sedimentary units include siltstone interbedded with sandstone, conglomerate, and a crystal vitric tuff that has been reworked by fluvial and/or mass wasting processes. Fluid-rock interaction has variably altered all basement units after emplacement, as indicated by secondary minerals that partly replace primary minerals, partly to completely replace mesostasis, and partly to completely fill veins and vesicles. Although the alteration in Hole 1137A is predominantly manifested by limited secondary minerals (clays, zeolites, calcite, amorphous silica, and quartz), the abundance of these phases in veins, vesicles, and breccias varies distinctly downhole. In this section, we describe these patterns and other notable features related to alteration for each basement unit.

Downhole variations in alteration, including the distribution of secondary minerals, are recorded in the alteration and vein/structural logs (see the **"Supplementary Materials"** contents list; Fig. **F63**). In general, the most highly altered rocks are associated with horizons characterized by higher permeability, including brecciated or vesicular flow tops and flow bases and zones with high vein and fracture densities.

F62. Mantle–normalized incompatible element composition of felsic volcanic rocks, **p. 127.**

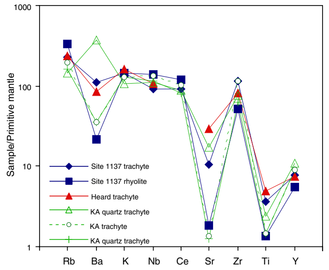

F63. Distribution and abundance of secondary minerals vs. depth, **p. 128.**

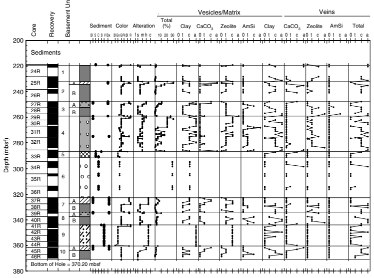

Unit 1

Basement Unit 1 is overlain by a highly oxidized and well-indurated sedimentary breccia consisting of highly vesicular clasts cemented by amorphous silica, calcite, and zeolite (interval 183-1137A-24R-1, 0–70 cm). The flow top of Unit 1 is not present; consequently, the first basement rocks encountered in Hole 1137A represent the massive interior of a basalt flow. The dark gray interior of Unit 1 is slightly altered with the mesostasis replaced by saponite. Sparse vesicles (<2%) are filled with saponite and zeolite. Saponite lines vesicles where both phases coexist, indicating clay formation before zeolite.

Numerous 0.1- to 8.0-mm-wide veins in Unit 1 are filled with clay and calcite in the upper part of the flow (219.51–228.40 mbsf) and clay and zeolite in the bottom part of the flow (228.45–232.22 mbsf). Similar to the paragenesis indicated for vesicles, clay minerals tend to line veins, suggesting clay formation before zeolite and calcite. Well-defined vein halos are absent.

F64. Close-up photograph of interval 183-1137A-25R-4 (Piece 1, 10–30 cm), **p. 130.**

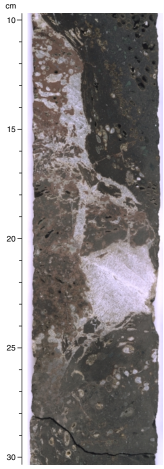

Unit 2

Unit 2 has been subdivided into two subunits: a brecciated flow top (Subunit 2A) and a massive flow bottom (Subunit 2B). The brecciated flow top is highly to completely altered and consists of oxidized vesicular basalt clasts (some with chilled margins) cemented by calcite and zeolite (Fig. **F64**). Vesicles are numerous in the clasts (as much as 30%) and are filled with calcite, zeolite, and blue-green celadonite. The massive interior of this flow (Subunit 2B) is slightly to moderately altered with well-defined mesostasis bands altered to saponite. Vesicle abundance decreases from ~15% near the base of Subunit 2A to <1% in the flow interior, with clay, zeolite, and (to a lesser extent) calcite as vesicle fillings. Mineral zonations within vesicles suggest early formation of a celadonite lining followed by saponite and zeolite.

Numerous 0.1- to 3.0-mm-wide veins are present in Subunit 2B, and vein minerals exhibit irregular downhole distributions through the flow. Calcite and clays are the most abundant vein fillings from the top of Subunit 2B to 237.50 mbsf. From 237.50 to 240.75 mbsf, calcite is absent, and vein filling is dominated by green clays and zeolite. In addition, one vein within this interval (Sample 183-1137A-26R-2 [Piece 11, 87–95 cm]) contains as much as 10% pyrite. Finally, from 240.75 mbsf to the base of Subunit 2B, zeolite is absent, and vein filling is again dominated by clays and calcite.

Unit 3

A highly vesicular upper half (Subunit 3A) and massive lower half (Subunit 3B) characterize the third basalt flow. Well-indurated and laminated blue-green siltstones also occur in the upper portion of Subunit 3A (Fig. **F65**), and in some sections they comprise as much as 50% of the rock (e.g., Section 183-1137-27R-2). XRD analysis of this material shows celadonite in addition to quartz and orthoclase (Table **T13**), which are probably clastic components instead of alteration minerals. High induration of these altered siltstones contrasts with the soft, waxy green clay that fills nearby vesicles. The laminated sediments display an intricate contact with the basalt, and a possible chilled margin (~5 mm wide) suggests that the sediments could have been indurated and altered by baking. Alternatively, high induration of these sediments could have been a product of silicification long after cooling. It is noteworthy that the first occurrence of amorphous silica in the basement of Hole 1137A is <2 m below the first appearance of these indurated sediments.

The degree of alteration in Subunit 3A progressively decreases from high to slight with depth through the unit. A general decrease in oxidation is suggested by a progressive change in color from red near the top of Subunit 3A to pink-gray and, finally, to gray near the bottom. This decrease in alteration with depth also coincides with a progressive decrease in vesicularity (Fig. **F63**). Vesicles are filled with green clays, calcite, and zeolite from 247.60 to 250.60 mbsf. Vesicle mineralogy changes markedly at 250.43 mbsf with the first appearance of amorphous silica as well as clays and zeolite, a mineral assemblage that is present to the base of Subunit 3A. Moreover, geopetal structures are common in this interval and are characterized by a subhorizontal boundary with agate filling below and zeolite or green clay filling above (Fig. **F66**). Calcite is absent in vesicles within this lower portion of Subunit 3A.

Vein mineralogy mimics changes in vesicle mineralogy with depth through Subunit 3A. Calcite- and clay-filled veins as much as 3 mm wide are common from the top of Subunit 3A (247.60 mbsf) to 248.75 mbsf. In contrast, from 251.15 mbsf to the bottom of Subunit 3A (253.00 mbsf), veins are ≤1 mm wide and contain green clay, amorphous silica, and zeolite (with calcite absent).

Subunit 3B exhibits only slight to moderate alteration, with well-defined bands of mesostasis that have been altered to saponite (Fig. **F67**). Vesicles are sparse and are lined with light green saponite and filled with zeolite. Veins are as much as 5 mm wide and also contain clay, zeolite, and (more rarely) amorphous silica. Distinct green alteration halos

F65. Close-up photograph of interval 183-1137A-27R-1 (Piece 12, 77–84 cm), **p. 131.**

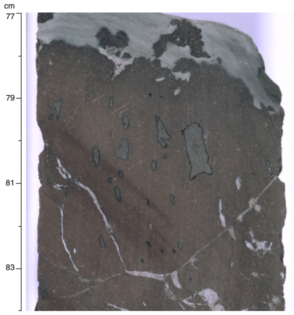

T13. Alteration minerals within basement units, **p. 187.**

F66. Close-up photograph of interval 183-1137A-27R-4 (Piece 4, 15–22 cm), **p. 132.**

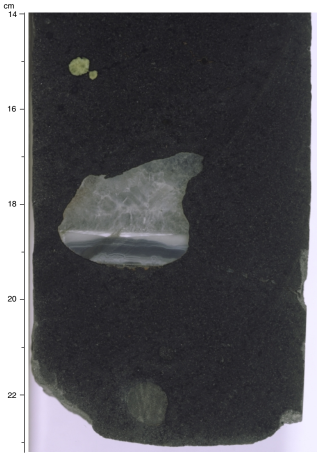

F67. Close-up photograph of interval 183-1137A-28R-2 (Piece 4, 83–102 cm), **p. 133.**

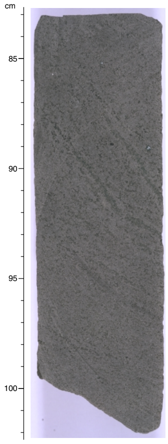

are common around veins from 258.00 to 258.45 mbsf (e.g., Sample 183-1137-29R-1 [Piece 1]).

The contact between Units 3 and 4 is complicated by a narrow interval of highly altered volcaniclastic debris (Fig. **F68**). Within this interval, the basalt clasts are variably oxidized and highly vesicular. Well-indurated blue-green sediments are present along with green clays (saponite and nontronite), zeolite (clinoptilolite), and calcite (e.g., Sample 183-1137-29R-2 [Pieces 3–4]), similar to the sediments observed in Subunit 3A.

F68. Close-up photograph of interval 183-1137A-29R-2 (Pieces 2–4, 50–80 cm), **p. 134.**

Unit 4

Basement Unit 4 (259.10–286.72 mbsf), a basalt flow, has a thick, highly vesicular upper section and three highly vesicular horizons within the flow that are more highly altered than the massive portions. Vesicles comprise ~20%–30% of Unit 4 from 259.10 to 267.75 mbsf. The color within this upper interval varies from red near the top to pink gray and, finally, to gray near the bottom, suggesting an overall decrease in oxidation with depth. The most abundant alteration phases in this portion of Unit 4 include blue-green clay (celadonite), light green clay (saponite), and zeolites. These minerals replace groundmass and also fill vesicles and veins.

Vesicle mineralogy displays irregular paragenetic sequences within the highly vesicular upper portion of Unit 4. Some vesicles are progressively filled from rim to core with blue-green clay (celadonite), light green clay (saponite), and zeolite (clinoptilolite and heulandite), suggesting that clay formation preceded zeolite formation (e.g., Sample 183-1137A-29R-4 [Pieces 1–7]). In other cases, zeolite lines vesicles with clay interiors, indicating an opposite paragenetic sequence (e.g., Sample 183-1137A-30R-4 [Pieces 1–9]). In rare cases, multiple generations of zeolite minerals are present in a single vesicle. Geopetal structures are also common in some vesicles, with light green saponite below and zeolite or amorphous silica above a subhorizontal boundary (Sample 183-1137A-30R-2 [Piece 1]).

Three other highly vesicular intervals are within Unit 4, all with vesicle abundances generally exceeding 10% of the rock. The color of these intervals tends to be slightly more red to pink compared to more massive adjacent intervals, which suggests higher degrees of oxidation. Vesicle mineralogy is virtually identical to that described above for the upper portion of Unit 4, although we observed calcite in small amounts (<5%) within vesicles in one section (Sample 183-1137A-31R-7 [Pieces 14–23]). In addition, one large vesicle (Fig. **F69**) is lined with clinoptilolite and filled with barite (confirmed by XRD).

F69. Close-up photograph of interval 183-1137A-31R-5 (Piece 9, 101–113 cm), **p. 135.**

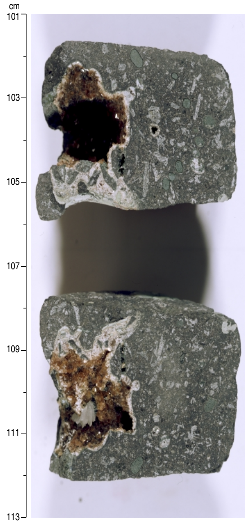

Less vesicular portions of Unit 4 are gray to dark gray in color and generally show similar vesicle fillings, except for an anomalous 4-cm-wide vesicle completely filled with quartz and surrounded by a 2-m-wide alteration halo (interval 183-1137A-31R-2 [Piece 11, 142–145 cm]). As a consequence of such a large vesicle, quartz represents ~3% of this section of core. In addition, small amounts of calcite (<8%) fill vesicles in one less-vesicular portion of the flow (Sample 183-1137A-32R-5 [Pieces 1–6]).

Numerous veins from 0.1 to 3.0 mm wide in Unit 4 are filled with iron-rich saponite/nontronite, celadonite, zeolites, calcite, and quartz (Table **T13**). Calcite is notably absent from veins within most of Unit 4, but calcite increases abruptly within veins near the base of the unit from 285.50 to 286.72 mbsf (Sample 183-1137A-33R-1 [Piece 1]).

Within this interval, numerous veins as much as 1 mm wide are filled with calcite and green saponites, but zeolites are absent.

Unit 5

The interbedded siltstones and sandstones of Unit 5 are very dark brown to black immediately below the contact with Unit 4, suggesting a baked zone (Sample 183-1137A-33R-1 [Piece 3]). Below this possible baked zone, Unit 5 is light green and is cut by a number of veins as wide as 2 mm, filled with green clays (saponite?) and calcite and identical to the calcite-bearing veins at the base of Unit 4.

Unit 6

The conglomerate (Unit 6) is composed of variably altered volcanic clasts set within a green clay (saponite?) and blue-green clay (celadonite?) matrix along with minor calcite. The clasts are well rounded and display continuous oxidation rims as much as 1 cm wide. Saponite replaces primary minerals in the clasts, and in rare circumstances calcite replaces plagioclase laths (e.g., Sample 183-1137A-36R-2 [Piece 1]). Vesicles within clasts are filled with saponite, and we observed some geopetal structures. Veins are sparse (as much as 10 mm wide) and generally crosscut the matrix but not the clasts. Calcite was the only vein mineral observed.

Unit 7

Basement Unit 7 represents another subaerial basalt flow with a brecciated flow top (Subunit 7A) and a more massive flow bottom (Subunit 7B). The flow-top breccia (Fig. F70) is highly to completely altered and is composed of angular clasts that exhibit different degrees of oxidation, as suggested by the highly variable color of this unit (brick red, brown red, pink gray, and gray). Secondary minerals within the matrix, vesicles, and veins of this breccia include calcite, blue-green clays, red-brown clays, and zeolites. In addition, calcite replaces plagioclase laths locally (e.g., Sample 183-1137A-37R-1 [Piece 1]). Variably oxidized, well-laminated, and highly indurated sediments within the breccia resemble those sediments described from other basalt flows at higher stratigraphic levels within Hole 1137A.

F70. Close-up photograph of interval 183-1137A-37R-3 (Piece 1, 35–55 cm), p. 136.

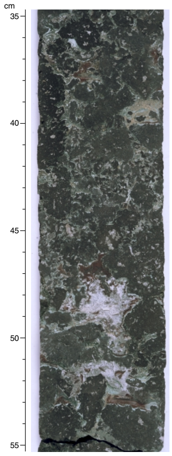

The more massive flow bottom (Subunit 7B) is slightly to moderately altered, with well-defined subhorizontal bands of mesostasis altered to saponite. Overall, the color of Subunit 7B varies from pink gray near the top to dark gray in the middle of the unit to pink gray near the base, close to the highly vesicular flow top of Unit 8 below. This emphasizes that flow contacts represent more permeable horizons with higher degrees of alteration. Vesicles are not abundant (<2%) and are filled with calcite, zeolite, amorphous silica, and saponite. Numerous veins and thin fractures between 0.1 and 1.0 mm wide in Subunit 7B contain the same minerals filling vesicles, with saponite most abundant. Similar to the alteration patterns observed in other units within Hole 1137A, calcite veins and vesicles are not randomly distributed and are only found near the top of Subunit 7B from 327.73 to 328.15 mbsf (Sample 183-1137A-38R-1 [Piece 3]).

A narrow interval contains highly vesicular and variably brecciated basalt from 334.11 to 334.85 mbsf near the base of Subunit 7B. Although the rocks in this interval contrast sharply with the relatively massive Subunit 7B above, the morphology of the vesicles in the lower unit suggests that a portion of this interval (down to 334.14 mbsf) may represent the brecciated bottom of Unit 7. The remainder represents the highly vesicular flow top of Unit 8 (see **"Physical Volcanology,"** p. 13). The rocks in this interval are highly altered, with matrix and vesicle filling characterized by abundant calcite, celadonite, saponite, and smaller quantities of zeolite (clinoptilolite and chabazite). Fairly well indurated blue-green sediments are similar to those described in other units within Hole 1137A.

Unit 8

Subunit 8B, a more massive flow interior, exhibits slight to moderate alteration with a generally uniform dark gray color. The mesostasis is clearly visible and altered to saponite. Vesicles are not abundant (<3%) and are filled with saponite, zeolite, and amorphous silica. Minor calcite (<1%) is present in some vesicles in the lower portion of the flow from 342.29 to 344.03 mbsf. The character of veins in Subunit 8B, including frequency and mineralogy, is very similar to that of veins in Subunit 7B. Numerous 0.1- to 1.0-mm-wide veins are filled with green saponite, zeolite, and rare amorphous silica. Calcite is present only in veins near the base of Subunit 8B (Sample 183-1137A-41R-1 [Piece 1]).

Unit 9

Basement Unit 9 in Hole 1137A is a thick and relatively homogeneous crystal vitric tuff. The tuff consists of 40% sanidine phenocrysts that show little, if any, alteration in a matrix that has been uniformly altered to green clay (saponite/nontronite) and minor lithic fragments (Fig. **F71**). The color of the tuff changes progressively with depth from red brown near the top to green in the middle to a deep blue green near the base, suggesting an overall decrease in oxidation with depth. Dark green alteration halos that surround lithic fragments contain rare specks of native copper. Pyrite is present within narrow (<1 cm wide) oxidation bands (e.g., Sample 183-1137A-41R-2 [Piece 1]). Pyrite was also locally abundant within two fault planes characterized by distinct slickensides and by alteration to celadonite and saponite/nontronite (e.g., Sample 183-1137A- 41R-2 [Piece 1]). Numerous lighter olive-green bands throughout the unit possibly represent recrystallized (shear?) zones.

F71. Close-up photograph of interval 183-1137A-42R-4 (Piece 1, 20–30 cm), **p. 137.**

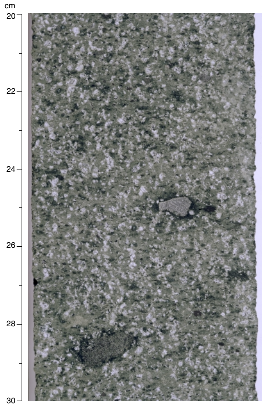

Unit 10

The lowermost basement unit in Hole 1137A is a basaltic flow with a brecciated flow top (Subunit 10A) and a massive interior (Subunit 10B). The flow top is highly altered and contains intercalated sediments (see **"Physical Volcanology,"** p. 13) and other delicate clast structures that suggest either intrusion of lava into wet sediment or reworking of an autobrecciated flow top. Partially indurated blue-green silts are abundant, and the extent of oxidation appears to be variable, as indicated by both red and green basalt clasts. In addition to the indurated sediments, the breccia matrix contains calcite, which locally replaces plagioclase phenocrysts, zeolite, and green saponite. Clasts are highly vesicular with calcite, zeolite, and saponite fillings.

The more massive flow interior (Subunit 10B) is the least-altered unit encountered in Hole 1137A. It is uniformly dark gray with relatively fresh plagioclase phenocrysts aligned subhorizontally. Vesicle abundance decreases with depth from ~2% near the top of the unit to <0.5%. Vesicles are filled with blue-green celadonite, zeolite, and amorphous silica; calcite-filled vesicles are present only near the top of the subunit (Sample 183-1137A-45R-3 [Piece 1]). Calcite veins as wide as 2 mm are present near the top of Subunit 10B but are absent below 364.26 mbsf, where sparse, narrow (<1 mm) clay-filled veins are present. We observed a trace of native copper in some veins and locally in the groundmass. The bottom of Hole 1137A is at a depth of 371.20 mbsf within Subunit 10B.

The patterns of alteration observed in Hole 1137A likely result from both weathering and low-temperature alteration. Both processes are most developed in the more permeable brecciated and/or vesicular contacts between flows. Unlike alteration in typical oceanic crust, the alteration history of this portion of the Kerguelen Plateau is potentially complex. There is the possibility of submarine weathering and alteration superimposed on subaerial weathering as well as the low-temperature interaction of basement units with groundwater.

STRUCTURAL GEOLOGY

Ten basement units have been defined in Hole 1137A, including seven igneous units interpreted to be individual lava flows and three volcaniclastic sedimentary units (Units 5, 6, and 9) (Fig. F72) (see "Lithostratigraphy," p. 3, "Physical Volcanology," p. 13, and "Igneous Petrology," p. 28). Rocks from Site 1137 exhibit relatively few structures, and we recorded no significant tectonic features from the sediments and sedimentary rocks overlying basement. We measured the orientation, location, and mineral filling of features from all basement units (see vein-structure log on the "Core Descriptions" contents list). The massive interiors and bases of the lava flows yield the vast majority of the measurements, and most structural orientations relate to mineral-filled passive fractures and joints, although a few, very minor, normal faults are present in the core. Highly vesicular or brecciated flow tops are common features above the massive interiors of most lava flows, but the chaotic, clastic internal arrangement of these intervals does not lead to planar structural features. Hence, the relatively few orientation measurements from these intervals do not mean that these breccias are either structureless or unaltered.

F72. Diagrams and histograms showing vein orientations, p. 138.

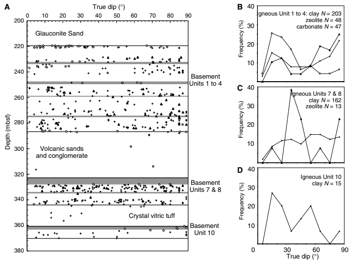

Mineral-filled veins are the most common structural phenomena, and we recorded the orientation of more than 550 features from the basement units (Fig. F72). To interpret the structural data at this site, we have divided the lava flows into three packets (Units 1, 2, 3, and 4; Units 7 and 8; and Unit 10) separated by the volcanic-derived sediments. Veins are most abundant in the uppermost basement rocks (basement Unit 1; Core 183-1137A-24R) that underlie glauconitic sandy packstone of lithologic Unit III. Thick (10 mm), predominantly subhorizontal calcium carbonate veins abound in these rocks (Fig. F72). This part of the basement is the most heavily veined and is the only portion of the basement where gently dipping features dominate. The abundance of veins in this most heavily fractured portion of Hole 1137A is similar to the average vein abundance in Hole 1136A (see "Structural Geology," p. 22, in the "Site 1136" chapter). In the remainder of the basement rocks, vein minerals are less prevalent even though the fracture density may be similar (cf. Units 7 and 8) (Fig. F73).

F73. Diagrams showing mineral abundance and fracture distribution, p. 139.

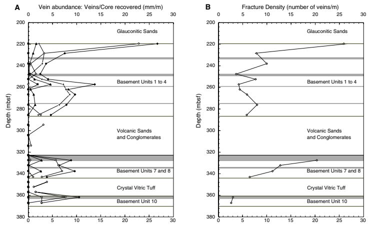

Large vesicles and other open voids in brecciated or highly vesicular portions of Units 3 and 4 are commonly filled or partly filled with well indurated, laminated siliceous mudstone (see **"Alteration and Weathering,"** p. 38). On average, these laminations are gently inclined (true dip ~16°, $N = 6$), requiring a subtle rotation of the lava pile if an original subhorizontal sedimentary layering is assumed.

The boundary between basement Unit 4 and the underlying volcanic sediments comprises a gently-dipping irregular contact between a cryptocrystalline to glassy chilled basalt and dark black baked silty sediments. This contact is well-preserved in the archive half of Section 183-1137A-33R-1 and dips ~20°. The boundary is also clearly recognizable in the FMS logs from this hole with a true orientation of 24°/076 (dip/dip direction) (see **"Downhole Measurements,"** p. 54), and this should allow the determination of (true) orientation of structural and paleomagnetic features in both the overlying basalts and underlying sediments.

The sediments below (~10 cm) the black, baked zone are intensely fractured and brecciated by a network of predominantly subhorizontal carbonate veins. A single subvertical fracture cuts across bedding in the upper 50 cm of Unit 5 and is carbonate filled directly below the upper contact yet filled with dark green clay slightly deeper in the section. The crystal-lithic volcanic siltstones and sandstones of Unit 5 have both sedimentary bedding and cross-bedding with subhorizontal to gently dipping orientations (cf. geopetal structures described later in this section). These beds are offset by at least two high angle (65° to 70°) normal faults with minor offsets (≤2 cm; Section 183-1137A-33R-2). Disruption of bedding at the margins of the core suggests that these minor offsets may be peripheral to a more significant fault.

Sedimentary structures in the volcanic conglomerate and sands (Unit 6) are comprehensively described elsewhere (see **"Lithostratigraphy,"** p. 3, and **"Physical Volcanology,"** p. 13), and we observed few features of direct tectonic origin. The most prominent structures are moderately to steeply dipping, irregular carbonate veins (~2 to 10 mm) that generally do not form planar features but meander around the margins of the volcanic clasts and only rarely crosscut smaller cobbles.

Basement Units 7 and 8 are sandwiched between the volcanic conglomerate and the crystal vitric tuff (Units 6 and 9, respectively), and the massive portions of these lava flows are heavily veined with numerous moderately to steeply dipping fractures filled with dark green clay that dissect the core. Many fractures appear to have formed in conjugate sets and many very thin (0.1 to 0.5 mm) veins filled with dark green clay. Although veins abound in these units, the abundance of vein minerals (in millimeter veins per meter of core) (see Fig. **F73**) is low compared to the uppermost part of the basement, because the veins are generally thin (<0.5 mm). We observed rare zeolite-filled, high-angle (>75°) veins in Unit 7. These veins display a staircase pattern with dilated steep ramps (1 to 2 mm) filled with pink and transparent zeolites and thin clay-lined (~0.2 mm) flats, indicating normal displacement.

The crystal vitric tuff (basement Unit 9) displays a weak, subhorizontal fabric delineated by the clayey matrix and the feldspar crystals. This fabric may be related to the compaction and alteration of the glassy tuff matrix. Flattened lithic clasts with intense green clay halos are aligned subparallel to the fabric of the tuff, and this may delineate sedimentary bedding. The most prominent features within the tuff are diffusely bounded sections of contrasting color, reflecting the presence of different clay minerals (saponite and celadonite) and their oxidation products. High-angle (>60°) normal fault surfaces intersecting the core are strongly grooved, and the clay-lined surfaces are polished to a resinous luster. Trace pyrite is present on these surfaces. Also present are ragged, subhorizontal shear-zones comprising dense networks of anastomosing wispy olive-green clay veinlets.

The uppermost part of Unit 10 is brecciated, and irregular clasts of quenched lava are supported in a matrix of blue-green, indurated silty sandstone (see **"Physical Volcanology,"** p. 13). These textures are consistent with the interaction of magma with water-saturated sediments or reworking of a flow-top breccia by sedimentary processes. Calcium carbonate and zeolites are only minor constituents of these complex breccias, partially filling open voids and vesicles. The underlying massive portion of Unit 10 is highly plagioclase phyric. The phenocrysts exhibit subtle subhorizontal alignment and are commonly replaced by calcium carbonate. Veins are uncommon in Unit 10, though in contrast to the uppermost parts of the basement, the rare carbonate veins present are inclined at steep angles (Figs. **F72, F73**).

Wispy segregations of mesostasis, now completely altered to clay minerals, are common in massive parts of all the lava flows (see Fig. **F74**). These glassy streaks are commonly oriented subparallel to vesicle trails. Rare subvertical vesicle-rich zones appear to be vesicle cylinders (see **"Physical Volcanology,"** p. 13) that cut the volcanic fabric. Both sets of features generally dip gently (~25°), requiring either a nonhorizontal original orientation or a slight tilting of the basement. The orientations of both mesostasis segregations and vesicle trails are consistent throughout the lava pile. Although some evidence, from the gentle dip of the vesicle trails, the mesostasis segregations, and the included, indurated laminated sediments, suggests slight rotation of the lava flows, the subhorizontal bedding in the intercalated volcaniclastic sediments indicates negligible tectonic tilting.

F74. Unoriented true dips of mesostasis segregations and vesicle trails with depth, **p. 140.**

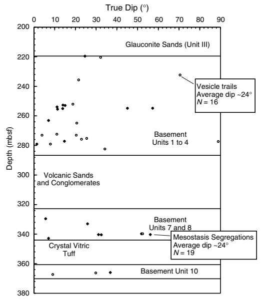

Abundant geopetal structures are preserved in the igneous rocks of the basement. These features are present in vesicles and other voids that are partially or completely filled by alteration minerals, most commonly clays or banded agate (amorphous silica). There is no consistent paragenetic sequence of mineral filling, and voids with clay overlying agate, as well as vice versa, are present. These geopetal structures consistently dip horizontally or subhorizontally (<10°), indicating negligible rotation of the basement after precipitation of the minerals.

PALEOMAGNETISM

We measured the natural remanent magnetization (NRM) of all archive halves from Hole 1137A with the pass-through cryogenic magnetometer using measurement intervals of 5 and 2.5 cm for sediment and basement sections, respectively. Subsequently, all sediment and basement sections were demagnetized up to 20 and 60 mT, respectively. Discrete sediment samples were stepwise demagnetized with an alternating field (AF) of up to 30 mT. Discrete basalt samples were stepwise AF demagnetized in a peak field of 60 mT or thermally demagnetized in temperatures of up to 620°C. We determined the anisotropy of magnetic susceptibility (AMS) of discrete basement samples to obtain information about the magnetic fabric.

We obtained stable remanent directions from the sediments of Hole 1137A. Reliable paleomagnetic results in undisturbed sediment cores with high recovery were used to correlate normal and reversed segments with biostratigraphic zones (see **"Biostratigraphy,"** p. 8). We measured magnetic susceptibility and remanent magnetization to determine the magnetic properties of basement units. We found an 8° difference between the paleolatitude and the present latitude of Elan Bank.

Sediments

After measuring the NRM, all sediment cores were demagnetized with a peak AF of 20 mT. One archive section from each core was stepwise demagnetized up to 30 mT. We took two discrete samples per section, and 28 samples were stepwise AF demagnetized up to 30 mT to confirm the reliability of whole-core measurements. We obtained reliable paleomagnetic results in undisturbed cores with high recovery, and correlated normal and reversed segments with biostratigraphic zones (see **"Biostratigraphy,"** p. 8). The sediments of Hole 1137A generally have a stable magnetization, which was obtained after AF demagnetization at 20 mT, especially for sediments with a high median destructive field (MDF) (Fig. **F75**). For magnetostratigraphic studies of Hole 1137A (Fig. **F76**), we used the data selection criteria described in **"Paleomagnetism,"** p. 27, in the "Explanatory Notes" chapter). The selection criteria were that (1) the intensity of remanent magnetization after AF demagnetization at 20 mT was >5 × 10^{-4} A/m and hence above the noise level of the magnetometer in rough-sea conditions, (2) the inclination was > ±40°, (3) at least two consecutive values (which corresponds to a 10-cm length of split core) had the same polarity, and (4) there was no significant core disturbance. We calculated characteristic remanent magnetic directions of discrete samples using component analysis. Characteristic inclinations from discrete samples generally agree well with selected inclinations from whole-core measurements (Fig. **F76**). We observed geomagnetic reversals within seven sections.

Correlation of biostratigraphic data and polarity reversals (Fig. **F76**) suggests that the reversed and normal chrons in Hole 1137A are Pleistocene to late Eocene in age (see **"Biostratigraphy,"** p. 8). We propose the following correlations with paleontological data from the core catcher of each core (see **"Biostratigraphy,"** p. 8). We correlate reversed polarity intervals at ~6 and ~11 mbsf to Chrons C1r and C2r, respectively. Normal and reversed segments between 100 and 107 mbsf and between 113 and 123 mbsf are Chrons C5–C6 and C7–C8, respectively. The underlying normal and reversed segments between 125 and 173 mbsf correspond to the chrons between C8 and C13. We correlate the reversed polarity interval at ~190 mbsf to Chron C13r or C15r.

We obtained a reliable paleomagnetic record from lithologic Units I and II (see **"Lithostratigraphy,"** p. 3). In the upper part of Unit II, especially between 30 and 80 mbsf (nannofossil ooze), we observed negative susceptibilities and weak NRM intensities (Fig. **F76**). Remanent magnetization is less stable, and magnetizations of discrete samples from this interval are too weak for reliable measurements with the shipboard magnetometer. We observed weaker positive susceptibilities and stronger NRM intensities in the lower part of Unit II than in the upper part. Progressive AF demagnetization and measurement of discrete samples were successful and provided a reliable paleomagnetic record (Fig. **F75**). We observed high susceptibilities (Table **T14**) in Unit III (sandy pack-

F75. AF demagnetization of a discrete sediment sample, **p. 141.**

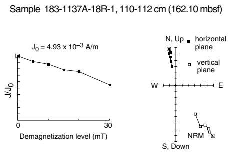

F76. Inclination, intensity, and susceptibility of sediments, **p. 142.**

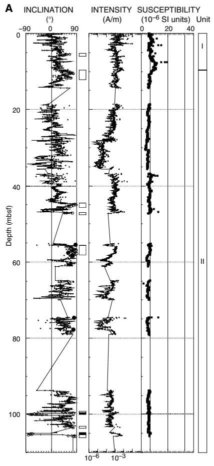

T14. Summary of NRM intensity and susceptibility, **p. 188.**

stone). We could not obtain a reliable magnetic record from Unit III as a result of either weak magnetization or core disturbance.

Basement Rocks

We determined the magnetic properties of each basement unit (see **"Igneous Petrology,"** p. 28, and **"Physical Volcanology,"** p. 13) and the variation of magnetic properties within each unit (**Fig. F77**). Three independent types of susceptibility measurements (MST, AMST, and discrete samples) show consistent results. We observed no significant differences in the average susceptibility and NRM intensity from the seven lava flows (basement Units 1, 2, 3, 4, 7, 8, and 10; Table **T14**). However, susceptibilities and NRM intensities did vary significantly within Units 2, 7, and 10. The brecciated flow tops have higher susceptibilities and stronger NRM intensities than the massive interiors. Differences in susceptibility and NRM intensity are caused by variations in magnetic mineral content, the size of magnetic mineral grains, and/or different magnetic minerals. We observed no significant variation within Units 1, 3, 4, and 8. The crystal-lithic volcanic siltstones and sandstones (Unit 5) and volcanic conglomerates (Unit 6) show lower susceptibilities and weaker NRM intensities than the lava flows. However, the volcanic clasts and grains produced higher average susceptibilities and stronger NRM intensities than in typical nonvolcanic sediments. Among the basement units, the tuff layer (Unit 9) has the lowest susceptibilities and the weakest NRM intensities as well as significant variations in susceptibilities and NRM intensities. Susceptibilities and NRM intensities increase downward in Unit 9 except for the uppermost ~1 m. We observed the highest susceptibilities and strongest NRM intensities at the top of the tuff layer. This variation is probably related to variable abundances of magnetic minerals or the type and size of magnetic minerals. All basement units except Unit 6 have steep negative inclinations corresponding to normal polarity. Scattered remanent directions from the conglomerate layer of Unit 6 suggest that the basement rocks at Site 1137 have not been reheated since their formation.

F77. Inclination, intensity, and susceptibility of basement rocks, **p. 144.**

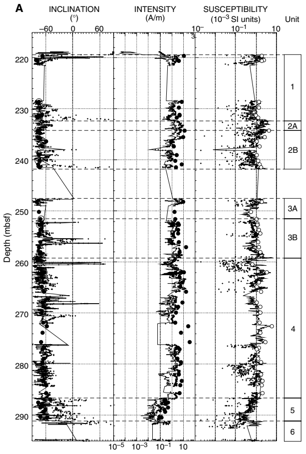

We measured the susceptibility of eight discrete samples in basement Unit 1 in 15 different directions to determine AMS and magnetic fabric. The average ratio between maximum and minimum axes (degree of anisotropy) is only 1.027. As the shape parameter of different samples has negative as well as positive values, both oblate (disk) and prolate (rod) shapes of fabric are present. We found no grouping of the axis directions (Fig. **F78**) and can make no conclusions about the flow direction for this unit.

F78. Directional anisotropy data from Unit 1, **p. 146.**

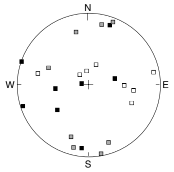

We chose two discrete samples from each lava flow (basement Units 1, 2, 3, 4, 7, 8, and 10) for stepwise thermal demagnetization up to 620°C and AF demagnetization up to 60 mT. We measured susceptibility of the samples after each heating step to detect changes of their magnetic minerals. Most samples have high MDFs and stable single-component remanent magnetization (Fig. **F79A**), except for one sample from Unit 7 with a low MDF (8 mT; Fig. **F79B**). Therefore, we expect a stable and primary remanent magnetization in the lava flows. Even the sample with a low MDF shows a difference of ~10° between its characteristic inclination (–61.5°), calculated by component analysis, and the recent (Brunhes normal epoch) inclination (–71.9°) at Site 1137, assuming a geocentric dipole field. Therefore, the remanent magnetization of this sample does not represent a recent overprint. Low MDFs are observed in most parts of Subunit 7B from whole-core measurements (Fig.

F79. AF demagnetization of discrete basement samples, **p. 147.**

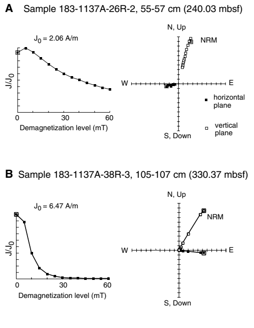

F77B). We found two magnetic phases during stepwise thermal demagnetization and susceptibility measurements. The high-temperature phase is characterized by an unblocking temperature of ~580°C (Fig. F80A) and the low-temperature phase by an unblocking temperature of ~300°C (Fig. F80B). The high-temperature phase probably corresponds to magnetite or titanium-poor titanomagnetite and the low-temperature phase to (titano)maghemite (see **"Paleomagnetism,"** p. 23, in the "Site 1136" chapter). Samples 183-1137A-40R-4, 50–52 cm (Subunit 8B), and 46R-1, 77–79 cm (Subunit 10B), show only high-temperature components. Sample 183-1137A-38R-4, 107–109 cm (Subunit 7B), exhibits only a low-temperature component. The other four samples from Units 1, 2, 3, and 4 have both high- and low-temperature components.

F80. Thermal demagnetization of discrete basement samples, **p. 148.**

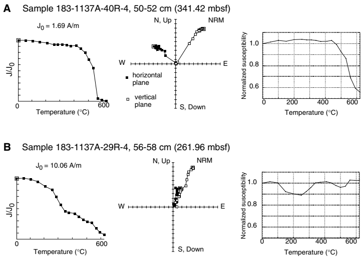

T15. Characteristic inclinations and NRM intensities of discrete basalt, **p. 189.**

We calculate characteristic inclinations of discrete samples using component analysis (Table T15). Mean inclinations of each flow unit range from –59° to –74°, and differences between the inclinations of samples treated with AF or thermal demagnetization within each flow unit range from 1° to 8°. The maximum difference between mean flow inclinations is 15°, and the differences of inclinations between units are larger than differences within each unit. Variations of inclination between units are probably caused by geomagnetic secular variation. Because of basement penetration through seven flow units, interbedded sediment, and tuff, we believe that our paleomagnetic data are adequate for averaging secular variation. This is necessary for the accurate determination of a paleomagnetic direction. We calculated a mean inclination of –66°, which corresponds to a paleolatitude of 48°S assuming a geocentric dipole field. The difference between Elan Bank's present latitude of 57°S (Site 1137) and its paleolatitude during the Cretaceous (see **"Biostratigraphy,"** p. 8) is 8°, suggesting that either Elan Bank has moved south or the basement has been tilted since Cretaceous time. The top of basaltic basement has an apparent dip of 1.5° to the east and an intrabasement reflection has an apparent dip of 4.8° to the east (see **"Background and Objectives,"** p. 1). Our preliminary interpretation is that Elan Bank has moved ~10° south since its formation. The southward movement of Elan Bank seems consistent with the southward movement of the southern Kerguelen Plateau (Inokuchi and Heider, 1992); however, limited measurements preclude definitive paleolatitude estimates at this time.

PHYSICAL PROPERTIES

Introduction

Physical properties measurements of whole-core sections from Hole 1137A using the multisensor track (MST) included magnetic susceptibility, gamma-ray attenuation porosity evaluator (GRAPE), bulk density, and natural gamma radiation (NGR) measurements. We determined compressional wave velocities (V_p) from the split cores in transverse x directions for soft sediments in liners and for hard-rock pieces without the liner. Measurements in the longitudinal (z) and transverse (x and y) directions on cut samples of consolidated sediment and hard rocks were done when possible. Index properties determinations included bulk density, water content, porosity, and grain density. We also routinely determined thermal conductivity for sediment and basalt. Finally, we compared velocities, bulk densities, and porosities with logging data and results.

Index Properties

We determined index properties using gravimetric methods (Table **T16;** Figs. **F81A, F81B, F81C, F82B, F82C, F82D**). The sedimentary sections of lithologic Units I and II yielded fairly smooth downhole trends in grain density, bulk density, and porosity. Grain densities in Units I and II are generally between 2.6 and 2.7 g/cm^3; these are significantly more scattered than those of coeval units in other Leg 183 sites (see **"Physical Properties,"** p. 15, in the "Site 1135" chapter). In Cores 183-1137A-2R through 12R, radiolarians may cause the low grain densities, but because carbonate contents within Units I and II are consistently >90% (see **"Lithostratigraphy,"** p. 3), we cannot conclude that variable grain densities are caused alone by differences in siliciclastic or siliceous biogenic components and patches of disseminated pyrite. Further investigation remains to be done. Bulk densities in these two units maintained nearly constant values of ~1.7 g/cm^3, and porosities clustered between 50% and 63%.

At ~200 mbsf, there is a major change in lithology from pelagic ooze to glauconite-bearing sandy packstone (see **"Lithostratigraphy,"** p. 3). Major abrupt changes in bulk density and porosity are present at this depth (Fig. **F81A**). Bulk densities increase to 2.10 g/cm^3. Grain densities range from 2.68 to 2.92 g/cm^3, and porosities decrease sharply from ~50% to ~12%.

Lithologies in the basement at Site 1137 (219.5–370.2 mbsf) include basalt flows and interbedded fluvial and volcanic sediments (lithologic Unit IV). Bulk density for the basement units approaches 2.52 g/cm^3, close to the mean grain density of 2.78 g/cm^3, and the mean porosity is 16.8%.

The general trend exhibited by the index properties data at Site 1137 reflect downhole variations in lithology. In particular, carbonate contents of sediment vary from 50 wt% CaCO$_3$ in Unit I (foraminifer-bearing diatom ooze) to ~90 wt% CaCO$_3$ in Unit II (nannofossil ooze) and most of Unit III (sandy packstone), to as low as 3 wt% CaCO$_3$ (near a depth of 219 mbsf) at the base of Unit III (see **"Lithostratigraphy,"** p. 3).

T16. Index properties data, **p. 190.**

F81. Downhole index properties and V_p, **p. 149.**

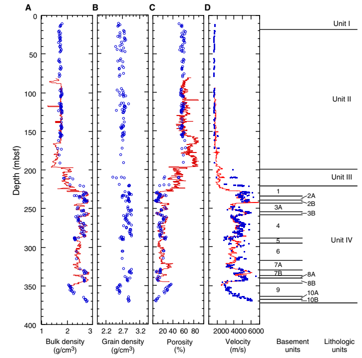

F82. Downhole physical properties profiles of basement units, **p. 150.**

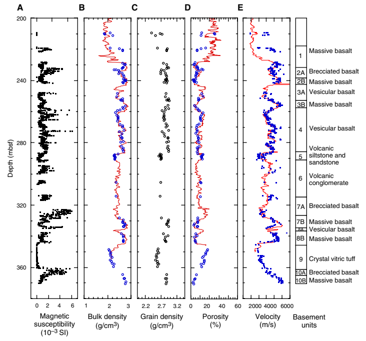

MST Measurements

GRAPE Density

Bulk density was measured by the GRAPE every 4 cm on whole sections of cores. GRAPE data are most reliable in full-sized RCB cores and offer the potential for direct correlation with downhole bulk density of discrete samples (Fig. **F83A**). In pelagic ooze (Units I and II), GRAPE densities correspond well with wet bulk densities determined from discrete samples and logging data. Below ~220 mbsf, basalt and interbedded sediments exhibit much higher bulk densities than overlying sediments. The downhole bulk density profile, bulk density data obtained from discrete samples, and logging values generally correlate, except that logging and discrete sample data for the basement units consistently show higher values than the GRAPE density data. The GRAPE sensor is calibrated with a filled core liner. The larger scatter in the GRAPE bulk density data for the basement units results from the empty space between pieces of core and the fractured nature and narrow diameters of the cores, which, consequently, do not fill the core liner. As expected, the smaller diameter of the RCB cores results in lower

F83. Downhole profiles of MST measurements and discrete sample densities, **p. 151.**

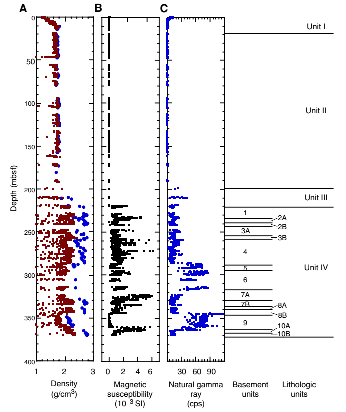

bulk density values than if the core liner is filled. Best-fitting results of the logging and GRAPE density data yield a rather good fit between the two data sets, after removing spurious data points from the GRAPE density profile (for details, see "Downhole Measurements," p. 54).

Natural Gamma Radiation

We measured NGR every 12 cm on unsplit sections of cores from Site 1137. Gamma-ray values are fairly constant in Units I and II (Fig. F83C). NGR count increases distinctly at a depth of ~200 mbsf, corresponding to the boundary between Units II and III. In lava flows of the basement units, the count increases to an average value of 15 cps. Between ~285 and 320 mbsf, within basement, gamma-ray values reached an average high value of more than 55 cps, corresponding to the volcanic siltstone, sandstone, and conglomerate in basement Units 5 and 6 (see "Lithostratigraphy," p. 3). The highest count (more than 70 cps) is present in the crystal-vitric tuff (basement Unit 9) between a depth of 344.0–360.7 mbsf. The downhole spectral gamma-ray logging data (see "Downhole Measurements," p. 54) reveals fluctuations similar to those of downhole NGR profile, corroborating the shipboard measurements.

Magnetic Susceptibility

We determined magnetic susceptibility on all cores from Site 1137. In general, magnetic susceptibility values within the basement units are much higher than those in the sedimentary sections. Specifically, susceptibility values were higher in the flow tops of basement Units 7, 8, and 10. More detailed results are discussed in "Paleomagnetism," p. 45.

Compressional Wave Velocity

We determined compressional wave velocity (V_p) of discrete samples using the contact probe system (PWS3). The compressional wave velocity data for Units I and II, which consist of foraminifer-bearing diatom and nannofossil ooze, respectively, show very little scatter, with a mean value of 1656 m/s (Table T17; Fig. F81). $CaCO_3$ contents are consistently high in Units I and II (see "Lithostratigraphy," p. 3). The velocities for Units I and II should be lower than in situ velocities because soft sediments are disturbed when drilled by RCB. A notable velocity contrast at a depth of ~200 mbsf marks the boundary between Units II and III. Compressional wave velocity in Unit III increase abruptly from 1939 to 4342 m/s. These changes correspond to a decrease in porosity from 57% to 12%. Within the basement units, velocities typically exceed 3000 m/s (Figs. F81D, F82E); the highest velocity is 6565 m/s. Velocities within basement Units 7, 8, and 10 correlate with the degree of alteration estimated from visual inspection (see "Alteration and Weathering," p. 38). The least-altered samples have velocities greater than the most, and flow tops that are highly altered and brecciated.

T17. Compressional wave velocity of discrete samples, p. 193.

Logging in Hole 1137A yielded good quality velocity data that can be used to compare with velocity results from physical properties measurements. Because the PWS3 technique does not allow velocity determination at in situ temperature-pressure conditions, velocity values from the sonic log should be higher than shipboard laboratory values. However, we obtained similar velocity values from the two techniques for sediments within Units I and II (Fig. F81). We think this agreement is coincidental because low ultrasonic velocities result from core disturbance, and lower sonic velocity values are caused by an enlarged borehole in Units I and II during logging (see discussion in **"Results,"** p. 56). Within the basement units, discrete velocity results agree well with the sonic log data. However, within the basement Unit 6 (~300 mbsf) the discrete velocity values are much more scattered (Figs. F81D, F82E). This discrepancy is caused by the large size of clasts in the conglomerate (>3 cm), which prevents representative discrete sampling of this unit for shipboard physical properties measurements. The good agreement between logging and shipboard results at Hole 1137A provides a valuable tool for cross-checking core depths in those sections where core recovery was not 100%. For example, a log-derived compressional wave velocity increase is ~9 m lower than the curated core depth for Core 183-1137A-24R (219.4 mbsf) (Fig. F82E), suggesting that the correct depth for this core should be shifted ~9 m downward (see more discussion in **"Downhole Measurements,"** p. 54). The highest velocities (~6000 m/s) in the lowermost massive basalt (basement Unit 10B) seem high and could be influenced by the calibration method, but relatively the trend is correct (see **"Physical Properties,"** p. 31, in the "Explanatory Notes" chapter).

Thermal Conductivity

We determined thermal conductivities for sediment cores and basement rocks, although we could not determine thermal conductivity in the sandy packstone (Unit III) (Fig. F84; Table T18). Thermal conductivity, physical properties, and lithology are strongly related. Thermal conductivity values for sediments from Units I and II are commonly between 1.0 and 1.2 W/(m·K), with a mean value of 1.1 W/(m·K). For the basement units, thermal conductivity values are generally >1.2 W/(m·K), but <2.0 W/(m·K), with a mean value of 1.5 W/(m·K).

F84. Downhole profile of whole-core measurements of thermal conductivity, **p. 152.**

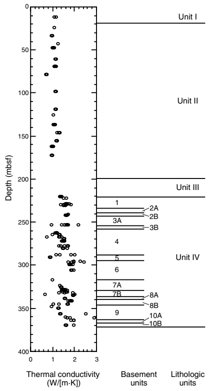

Concluding Discussion

At Site 1137, we observed more scatter of grain densities in the nannofossil ooze units than in Site 1135 and Site 1136 oozes. Radiolarians in the Site 1137 can partially account for the scatter, but further studies are needed to investigate other possibilities. Trends in index properties and MST measurements, coupled with changes in compressional wave velocity and thermal conductivity, compare well with the lithologic units and logging data for Hole 1137A. Velocities within basement Units 7, 8, and 10 also strongly correlate with the degree of alteration estimated from visual inspection. The least-altered samples have velocities greater than the highly altered flow tops.

T18. Thermal conductivity values, **p. 199.**

ORGANIC AND INORGANIC GEOCHEMISTRY

We determined concentrations of carbonate in sediments from Hole 1137A on ~1 sample per core (Table T19). In addition, we analyzed nine of the sediment samples for organic carbon, total nitrogen, sulfur, and hydrogen. The results of the analyses are discussed in **"Lithostratigraphy,"** p. 3.

T19. Carbon, nitrogen, sulfur, and hydrogen analyses of sediment, **p. 200.**

For volcanic rocks that were analyzed by XRF, we determined total carbon, total nitrogen, sulfur, and hydrogen using the NCS analyzer

(Table T20). These data are useful for assessing the degree of alteration (e.g., total carbon and hydrogen can be converted to CO_2 and H_2O, respectively, and compared with loss on ignition values). Further discussion of these data can be found in **"Igneous Petrology,"** p. 28, and **"Alteration and Weathering,"** p. 38.

SEISMIC STRATIGRAPHY

Introduction

Seismic stratigraphy depends on linking seismic reflections to lithostratigraphy and to physical properties of sediments and hard rocks by means of synthetic seismograms. In the absence of downhole logs, physical properties measurements on cores or core samples can be used for this purpose if recovery is sufficiently high. The high quality of the downhole logs at this site enables us to assess the quality of both densities and velocities determined from discrete samples through synthesizing seismograms. This is relevant for other sites that were not logged where we use index properties or MST data to tie the lithostratigraphy to MCS reflection data.

Data

The sampling interval of the downhole velocity log at Site 1137 is 15 cm. In comparison, sampling intervals of index properties measurements may vary from 20 cm to >10 m where recovery is low or zero. Low core recovery results in phase shifts between velocity anomalies from logs and samples, which may amount to several meters (Fig. F85). Amplitude differences in velocities from downhole logs and discrete samples are primarily caused by different temperatures and pressures for the in situ and laboratory measurements, which affect material properties, as well as differences in measurement techniques. High-frequency positive velocity peaks from downhole logs are typically lower than corresponding velocities from samples. Alternatively, sample velocities also show large scatter when collected at small intervals, which partly results from measurement uncertainties. These uncertainties vary depending on what kind of sample is used (i.e., cube, minicore, half core with or without liner), how well contact between the sample and transducers can be established, and how much the core was disturbed by RCB drilling.

To quantitatively assess the correlation of velocities from samples and logs at this site, we computed the coherence between the two profiles for Site 1137. Coherence, a dimensionless parameter that is a function of wavelength (or frequency), is zero when two data series are completely out of phase (i.e., a phase difference of 90°) and is 1 when they are in phase. When coherence is larger than 0.5, the two time series are considered to be coherent.

We applied Welch's method of periodiogram averaging, as implemented in Matlab, using nonoverlapping windows 128 samples long, corresponding to 19.2 m at a sampling interval of 15 cm. In terms of spatial wavelength, this implies an assessment of the coherence at wavelengths between 30 cm and 48.4 m. The resulting estimate of the coherence function (Fig. F86) illustrates that a unit has to be at least ~5 m thick to be detected at the same location downhole both by logs and index properties measurements. The lack of coherence for thinner units

T20. Carbon, nitrogen, sulfur, and hydrogen analyses of basalts, **p. 201.**

F85. Comparison of densities determined from core samples, GRAPE, and MST, and V_p from downhole logs and core samples, **p. 153.**

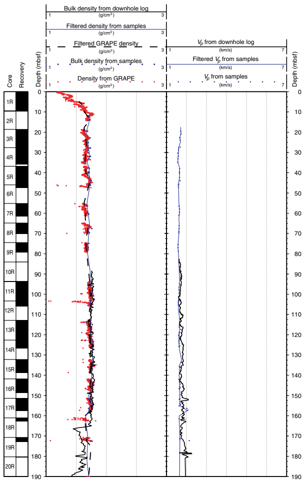

F86. Coherence function estimate of velocities from downhole logs and discrete samples, **p. 155.**

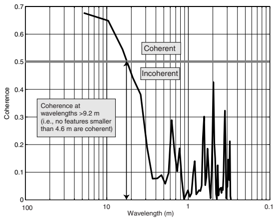

mainly results from two factors: (1) "misplaced" sample-velocity measurements in terms of depth caused by discrepancies between curated and real depths from incomplete core recovery and (2) the inherent difference between in situ and laboratory measurements, including core disturbance. A third effect that may also play a role is velocity measurement uncertainties.

We experimented with different filters to remove noise from index properties data from various sites before computing coherence and found independently that a robust mode filter with a width of 3.5–5 m appears to give the most acceptable result for cleaning both velocity and density measurements from samples (see **"Downhole Measurements,"** p. 54). Based on these results, we adapted the approach to apply a 5-m-long robust mode filter to all those index properties data used to synthesize seismograms for other sites. The filter was applied at 1-m increments. Both the velocity and the density log show a distinct inversion in Unit IV. It is caused by an altered crystal vitric tuff that separates the two lowermost basalt flows.

Synthetic Seismograms

We used velocity and density data from logs (90–350 mbsf), filtered data from physical properties measurements (12–90 and >350 mbsf), and GRAPE measurements (0–12 mbsf) to synthesize seismograms for linking the cores and logs with MCS data. Velocity data were extrapolated from 0 to 18 mbsf, assuming constant velocity. We summed transit times to create a log of TWT vs. depth. We resampled this log linearly using a sampling interval of 0.1 ms, resulting in oversampling to avoid aliasing. We then resampled velocities and densities using the TWT array and obtained impedance from the product of velocity and density and computed reflection coefficients from impedance contrasts (Fig. **F87**).

We constructed synthetic seismograms with and without multiples and transmission losses as described in the **"Seismic Stratigraphy,"** p. 47, in the "Explanatory Notes" chapter. Comparison of the two synthetic seismograms (Fig. **F87**) shows that the phase of all large-amplitude peaks is nearly identical. However, lower-amplitude reflections within the sediments show more severe differences in phase, and the amplitude of the lowermost reflections within basement is diminished in the synthetic seismogram that includes transmission losses (Fig. **F87**). The attenuated reflections, including transmission losses, match the MCS data better than the synthetic trace without multiples and transmission losses (Figs. **F87, F88**). This is caused by the large impedance contrasts between massive basalts and overlying brecciated basalts, volcanics or sediments resulting in rapid loss of energy with increasing depth.

Superimposing the synthetic seismogram with (or without) multiples shows that it covers a range in TWT that is larger than in the MCS data. In other words, the seafloor and basement reflections cannot be matched at the same time, as the summed transit times have resulted in a total TWT that is larger than that measured from the MCS data at Site 1137. This implies that we have underestimated velocities overall. Core recovery should be biased toward more indurated sediments with higher velocities; therefore, the discrepancy is not likely caused by velocities based on discrete samples. Without check shots, it is not possible to investigate where velocities are incorrect. To tie our synthetic

F87. Composite of core recovery, depth, lithostratigraphy, age, density, and velocity, **p. 156.**

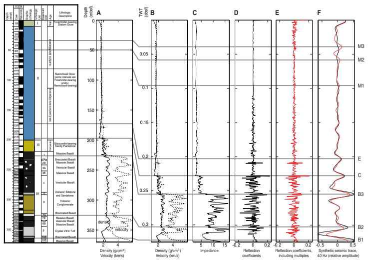

F88. Seismic reflection data and a synthetic seismic trace, **p. 158.**

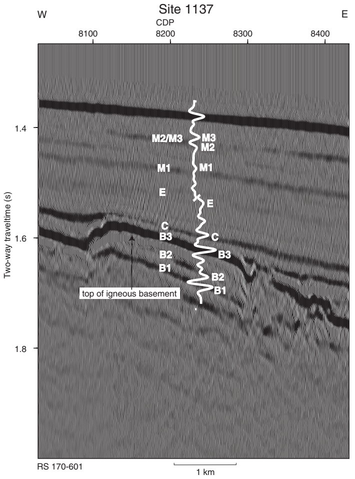

seismogram to the MCS data, we simply split the former into two segments, matched to the seafloor and to the basement, respectively.

Reflections M1 and M2 (early to middle Miocene) in the synthetic seismogram largely result from interbed multiples. However, they cannot be tied unequivocally to the MCS data, where one broad peak, rather than two distinct reflections, is present at the same TWT. We tentatively tie reflection M1 to a broad reflection in the MCS data. We cannot match reflection E (late Eocene to late Oligocene) to the MCS data, but it may correspond to a broad reflection at that depth. It is caused by a logged drop in density between 165 and 195 mbsf, and it also corresponds to an increase in shear wave velocity (V_s) and decrease in Poisson Ratio at this depth interval (see **"Downhole Measurements,"** p. 54).

Four large reflections mark the Cretaceous part of the section, which match the MCS data well: (C) the top of the glauconite bearing sandy packstone (Unit III, Campanian), (B3) the massive basalt at the top of acoustic basement (basement Unit 1), (B2) the top of the massive basalt at basement Subunit 7B, and (B1) the top of the massive basalt at basement Subunit 10B (i.e., the deepest unit drilled). However, the reflection caused by the massive basalts of basement Subunit 7B is slightly shallower than in the MCS data. This may be attributed to cumulative errors in the TWT computed from interval transit times, as no check shots are available for testing.

These results show that below acoustic basement, the only features resolved by the MCS data are massive basalts overlain by a low-velocity unit at least 15–20 m thick. For instance, we cannot resolve the boundary between basement Units 2 and 3, even though they are separated by a low-velocity brecciated basalt flow top ~10 m thick. At average velocities of ~5 km/s within basaltic basement, and a peak wavelet frequency of 40 Hz, the tuning thickness (one-quarter of the wavelet length) is ~30 m. This implies that a low-velocity unit separating two basalt units would have to be at least 30 m thick for both its top and its base to be imaged. The theoretical limit for detecting a high- or low-velocity layer within basement given a velocity of 5 km/s and a frequency of 40 Hz would be one-thirtieth of the wavelet length (Badley, 1985), or ~4 m. However, the integration of the MCS data with downhole logs and the lithostratigraphy demonstrates that in fact we cannot resolve any layers thinner than ~15 m at Site 1137.

All basement units imaged in the seismic reflection data at Site 1137 have an apparent dip to the east, and the glauconite-bearing sandy packstone overlying basement thickens to the east (Fig. **F88**). This indicates that the age of the oldest sediments probably increases toward the east. Basement Unit 7 is not laterally continuous for more than 1.5 km, and we can trace basement Unit 10 for a total of ~3 km in an east–west direction.

DOWNHOLE MEASUREMENTS

Logging Operations

We completed two logging runs at Site 1137 (Table **T21**) (see **"Operations,"** p. 2). First, we logged the hole from 364.7 mbsf to seafloor with the triple combo logging string (resistivity, neutron porosity, and density tools), the HNGS, and the LDEO TAP tool. Interactions between the opening of the caliper and the DLL measurements degraded log quality

T21. Summary of logging operations, **p. 202.**

at the bottom of the hole because both measurements used the same electrical connections in the wireline. While we opened the caliper at the bottom, the DLL current was disabled. We repeated the logs from 364.7 to 310 mbsf. In the sedimentary section (195 to 81 mbsf), borehole diameter exceeded 19 in, preventing good contact of the tools with the borehole wall. Normally, the mudline is located with the gamma-ray data to obtain the depth of the seafloor. However, in Hole 1137A, we could not detect the seafloor by natural gamma-ray gradients because of the extremely low radioactivity of the nannofossil ooze. Consequently, we used the drillers' water depth (1016 m) to shift the logging data to that seafloor reference.

For the second run, we used the spectral gamma-ray, FMS tool and the DSI combination from 367.9 to 81 mbsf. Despite difficulties in passing a series of bridges at 170–185 mbsf, well above the sediment/basement transition, we logged the hole successfully. A bridge at 165–180 mbsf, where caliper measurements for the two runs clearly show progressive closure of the borehole wall, prevented a second pass. Because the bit had already been released, drilling through the tight section was not feasible. Therefore, we abandoned logging operations, and the tool was rigged down.

Log Quality

Logging data of Hole 1137A range from poor to high quality (Fig. F89). The HNGS provides the highest quality data because high measurement precision and corrections for borehole diameter are possible. In the sedimentary section from 81 to 195 mbsf, the logging data are of poor quality. The density and neutron tools did not maintain contact with the borehole wall, and the DSI could not be run centralized. The maximum aperture of the caliper was 19 and 15 in for the first and second runs, respectively. In both runs, the tools lost contact with the borehole wall above 153 mbsf. In the lowermost part of the sediments, from 195 to 227 mbsf, the logging data are of good quality.

The DSI provided high quality compressional wave and shear wave data in the igneous basement. The P&S mode (providing compressional and shear waves) produced good compressional wave data, and we obtained a continuous shear wave profile in the lower dipole mode, even when the formation velocity approached mud velocity. We processed the velocity data in realtime with the Schlumberger MAXIS unit by slowness time coherence (STC) analysis. However, the analysis resulted in erroneous velocities from 177 to 192 and 242 to 244 mbsf. We deleted incorrect velocities from our data files and plots (Fig. F89). In the sedimentary section, shear wave velocities are very low; consequently small changes in compressional wave velocity have a relatively high impact on the V_p/V_s ratios and should not be used for lithologic interpretations. In the basement section the V_p/V_s ratio averages ~2 (Fig. F89B).

Logged compressional wave velocities and densities show good agreement with data obtained from discrete core samples (Fig. F90) in the basement section (below ~225 mbsf). In basement, GRAPE density data are consistently lower than both the logging densities and the discrete core data, as the core liner was not entirely filled. Despite this offset, GRAPE data may be useful for postcruise core-log integration because the high sampling rate produces measurements that generally follow the shape of the log density curve, but are offset (Fig. F90).

We observed a large mismatch between compressional wave velocities from core samples and logs between 200 and 225 mbsf (Fig. F90),

F89. Logging data, p. 159.

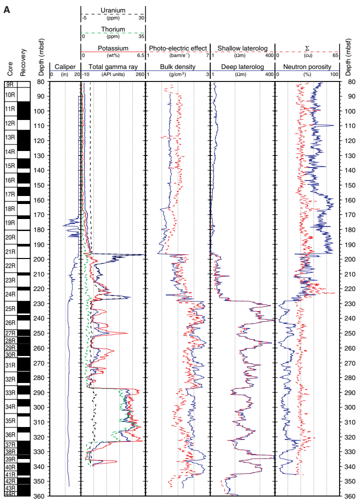

F90. Comparison of densities and *P*-wave velocities and data trends after filtering, p. 161.

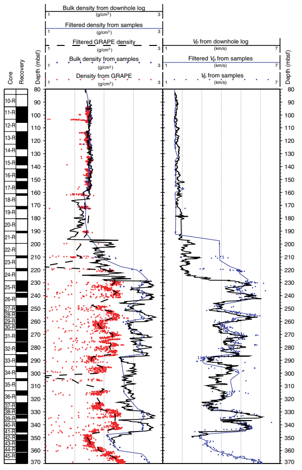

corresponding to the glauconite-bearing sandy packstone above basement. Given our revised log stratigraphy (Fig. F91), we attribute the mismatch in Core 183-1137A-24R to low recovery, implying that Unit III is substantially thicker than shown in the core stratigraphy. The remaining mismatch, between 205 and 210 mbsf, is similar to other discrepancies between the two data sets, indicating that velocity peaks in core samples are commonly not sampled by the compressional wave velocity log. Densities from discrete samples and the downhole log agree. Amplitudes in the two datasets are generally comparable, including narrow density peaks.

F91. Comparison of logging data and core-derived lithology, p. 162.

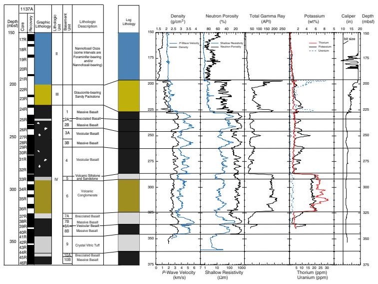

Above 200 mbsf, the density and velocity data from discrete core measurements and logs appear to agree well. However, this agreement is misleading, as the borehole size exceeded the maximum caliper extension for large parts of the sedimentary section. This results in low-quality velocity and density logs, which show values lower than those expected for the formation. In addition, strong core disturbance of soft sediments caused low discrete core density and velocity values (see "Physical Properties," p. 48). Natural gamma-ray logs and MST natural gamma-ray data agree well in the basement section (below ~225 mbsf) (see Fig F82; "Physical Properties," p. 48). Neutron porosity and porosity measured on the core samples also agree well. In contrast, previous logging studies in basalts have a general offset of 6% and 10% between core and log measurements observed (Broglia and Moos, 1988; Lysne, 1989). The good agreement of our results is attributable to the use of the new neutron tool, the APS, which measures porosity more accurately in this geologic environment (Schlumberger, 1994).

Shipboard processing provides preliminary FMS images. Because of excellent hole conditions in basement, the FMS images show most features seen in the cores. In basalts, we can distinguish vesicles, fractures, brecciation, and massive zones. In the sedimentary beds within Unit IV, grain-size differences are apparent in the coarser clastic sediments. However, these data sets require further postcruise processing to remove effects of tool sticking.

Results

High core recovery allows calibration of the logging results with core observations. In sections with low core recovery, the combination of standard logs and FMS images allows us to calculate true bed and flow thicknesses (Fig. F91; Table T7). Furthermore, within single flow units, we can estimate the thickness of brecciated, vesicular, or fractured parts.

From standard logging data and the FMS images, we distinguish the boundaries of lithologic Units II, III, and IV (Fig. F91). Unit II shows generally low density, resistivity, and velocity. This is mainly related to the large borehole, and, to a lesser degree, the unconsolidated character of these sediments. Nannofossil ooze shows low spectral gamma-ray values (SGR) (<50 gAPI) because of the absence of clay minerals. At 196.5 mbsf a sharp increase in the SGR marks the boundary to the underlying glauconite-bearing sandy packstone in lithologic Unit III. This unit extends to 227 mbsf, and its log-derived thickness is 30.5 m vs. the ~20 m estimated from the cores. Logging results indicate considerable lithologic heterogeneity within Unit III. It can be subdivided into an upper, middle, and lower part by the SGR. The highest SGR (150–250 gAPI) and uranium values (up to 30 ppm) are in the bottom and top of this unit. The high formation capture cross-section values (Σ) in Figure

F89A correspond to high potassium contents in the lower part. That is related to glauconite.

Based on interpretation of FMS images and the standard logs, the transition to basaltic basement is at 227 mbsf (Fig. F92). At this depth, SGR and porosity decrease and density and resistivity increase. The different basaltic lava flows in basement show similar characteristics and trends in the logging data. Brecciated and vesicular, and mostly altered, flow tops and vesicular flow bottoms show the lowest densities, resistivities, and photoelectric factors within a single flow. Density ranges from 2.4 to 2.5 g/cm^3, resistivity from 8 to 20 Ωm, velocity from 5.5 to 6 km/s, and porosity from 25% to 30%. Depending on the degree of alteration, flow tops and bottoms show slightly increased natural gamma-ray values caused by potassium enrichment. Massive parts of the lava flows show the highest densities (>2.7 g/cm^3), resistivities (>50 Ωm), and velocities (3–4.5 km/s) combined with the lowest porosities (<15%). The transition from the massive to the vesicular part of basement Unit 2 is clearly visible in FMS images (Fig. F93). Differences are also apparent among lava flows. For example, basement Unit 4 does not include a homogeneous massive part but is altered and enriched in potassium corroborating the alteration observed in the cores (see **"Alteration and Weathering,"** p. 38). Between 272 and 276.4 mbsf, we observe fractures that are mainly filled with dark green clay minerals (see **"Alteration and Weathering,"** p. 38). The high amount of clay minerals affects physical properties because density, resistivity, and photoelectric factor are reduced, whereas the porosity and gamma-ray values are increased. In the V_p/V_s ratio (Fig. F89B), we observe only a few deviations from the average ratio of 2, notably at depths of 239–247, 287–288, 322–327, 336–338, and 345–349 mbsf, where the ratios range between 2 and 3.2. These depths correspond to zones within interbedded sedimentary rocks, brecciated basalt, vesicular basalt, and a crystal-vitric tuff, respectively (see Fig. F91). However, the basement units in which the high V_p/V_s values are found do not show elevated V_p/V_s ratios for their entire depths. Some but not all positive V_p/V_s anomalies correspond to peaks in natural gamma-ray values, suggesting a relationship with the local degree of weathering and alteration, and, thus, clay-mineral content.

The volcanic siltstone and sandstone (Unit 5) and the volcanic conglomerate (Unit 6) are clearly distinguishable in the total gamma-ray log. The clasts in Units 5 and 6 are mainly eroded volcanics (see **"Lithostratigraphy,"** p. 3). We found the highest potassium (4.5–6 wt%) and thorium contents (>20 ppm) in these two units. The high thorium content is significant and indicates the more evolved character of most components (see **"Igneous Petrology,"** p. 28). We distinguish the 4.4-m-thick volcanic siltstone and sandstone from the volcanic conglomerate by lower density, photoelectric factors, and resistivity and higher porosity values. The volcanic conglomerate varies widely in grain size and bed thicknesses with depth in the FMS images. Low resistivity and density correlate with finer grained beds from 302 to 303 mbsf and from 308.4 to 309.2 mbsf (Fig. F94).

Scatter plots of density vs. compressional and shear wave velocity and resistivity vs. porosity (Fig. F95) reveal various relationships among these parameters. Igneous rocks and consolidated sediments show a linear, positive correlation between velocity and density (Fig. F95A, F95B) and a linear, negative correlation of porosity with both density and resistivity (Fig. F95C, F95D). Furthermore, igneous rocks can be distin-

F92. FMS image displaying the sediment–igneous basement transition, **p. 163.**

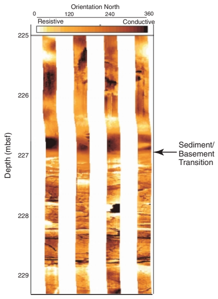

F93. FMS image displaying basement Unit 2, **p. 164.**

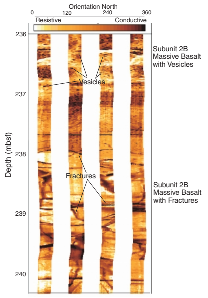

F94. FMS image displaying basement Unit 6, **p. 165.**

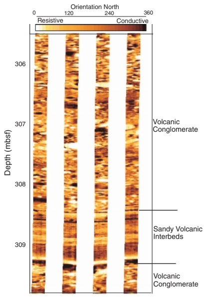

F95. Scatter plots of bulk density vs. *P*-wave velocity, *S*-wave velocity, and porosity, and resistivity vs. porosity, **p. 166.**

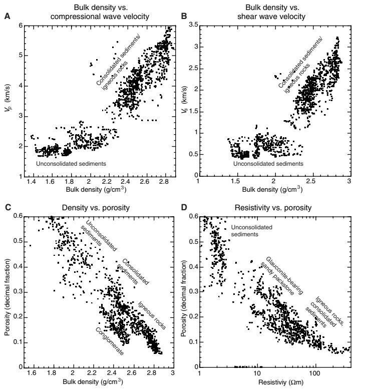

guished from the conglomerate in the density-porosity scatter plot (Fig. **F95C**), as both rock types have similar low porosity, but the conglomerate has a lower bulk density caused by lower grain density. In unconsolidated sediments, only porosity and density show any correlation. At densities lower than ~2.4 g/cm³, velocities appear fairly constant (Fig. **F95A, F95B**). This may largely be a consequence of insufficient velocity log quality where hole diameter is large. Resistivities are fairly constant at porosities >40% (Fig. **F95D**). However, the linear correlation of porosity and density even for porosities as high as 40%–60% and densities as low as 1.8–2.2 g/cm³ suggests that both log measurements reflect formation properties in this range, rather than reflecting drilling mud properties, as the latter is expected to result in constant porosity and density readings (Fig. **F95C**).

The caliper logs from the FMS-DSI logging run show remarkable hole symmetry (Fig. **F96**). No evidence suggests substantial hole deformation or breakouts below 230 mbsf. However, above this depth, the hole is severely enlarged in unconsolidated sediments (Fig. **F89**).

F96. Caliper log showing changes in hole diameter measured along caliper 1 and 2 and the azimuth of caliper 1, **p. 167.**

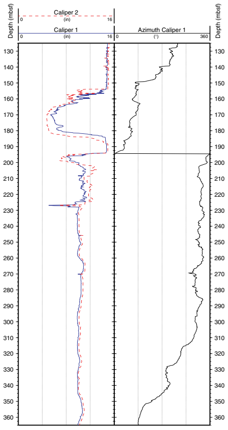

REFERENCES

Alibert, C., 1991. Mineralogy and geochemistry of a basalt from Site 738: implications for the tectonic history of the southernmost part of the Kerguelen Plateau. *In* Barron, J., Larsen, B., et al., *Proc. ODP, Sci. Results,* 119: College Station, TX (Ocean Drilling Program), 293–298.

Badley, M.E. (Ed.), 1985. *Practical Seismic Interpretation* (Vol. 6): Boston (Int. Human Resour. Dev. Corp.).

Barling, J., Goldstein, S.L., and Nicholls, I.A., 1994. Geochemistry of Heard Island (Southern Indian Ocean): characterization of an enriched mantle component and implications for enrichment of the sub-Indian Ocean Mantle. *J. Petrol.,* 35:1017–1053.

Broglia, C., and Moos, D., 1988. In-situ structure and properties of 110-Ma crust from geophysical logs in DSDP Hole 418A. *In* Salisbury, M.H., Scott, J.H., et al., *Proc. ODP, Sci. Results,* 102: College Station, TX (Ocean Drilling Program), 29–47.

Cita, M.B., Coccioni, R., Edwards, A.R., Monechi, S., Morgans, H.E.G., Strong, C.P., Watkins, D.K., and Webb, P.-N., 1997. Nannofossils and foraminifera. *In* Hannah, M.J., and Raine, J.I. (Eds.), *Southern Ocean Late Cretaceous/Early Cenozoic Biostratigraphic Datums.* Inst. Geol. Nucl. Sci., Sci. Rep., 97/4:5–10.

Davies, H.L., Sun, S.-S., Frey, F.A., Gautier, I., McCulloch, M.T., Price, R.C., Bassias, Y., Klootwijk, C.T., and Leclaire, L., 1989. Basalt basement from the Kerguelen Plateau and the trail of the DUPAL plume. *Contrib. Mineral. Petrol.,* 103:457–469.

Fisher, R.L., 1997. Bathymetry of the Southern Indian Ocean. *General Bathymetric Chart of the Oceans.* GEBCO, Sheet 97.1.

Fitton, J.G., Saunders, A.D., Larsen, L.M., Hardarson, B.S., and Norry, M.J., 1998. Volcanic rocks from the southeast Greenland Margin at 63°N: composition, petrogenesis, and mantle sources. *In* Saunders, A.D., Larsen, H.C., and Wise, S.W., Jr. (Eds.), *Proc. ODP, Sci. Results,* 152: College Station, TX (Ocean Drilling Program), 331–350.

Fitton, J.G., Saunders, A.D. Norry, M.J., Hardarson, B.S., and Taylor, R., 1997. Thermal and chemical structure of the Iceland plume. *Earth Planet. Sci. Lett.,* 153:97–208.

Houtz, R.E., Hayes, D.E., and Markl, R.G., 1977. Kerguelen Plateau bathymetry, sediment distribution and crustal structure. *Mar. Geol.,* 25:95–130.

Huber, B.T., 1991. Paleogene and early Neogene planktonic foraminifer biostratigraphy of Sites 738 and 744, Kerguelen Plateau (southern Indian Ocean). *In* Barron, J., Larsen, B., et al., *Proc. ODP, Sci. Results,* 119: College Station, TX (Ocean Drilling Program), 427–449.

————, 1992. Upper Cretaceous planktic foraminiferal biozonation for the Austral Realm. *Mar. Micropaleontol.,* 20:107–128.

Inokuchi, H., and Heider, F., 1992. Paleolatitude of the southern Kerguelen Plateau inferred from the paleomagnetic study of Upper Cretaceous basalts. *In* Wise, S.W., Jr., Schlich, R., et al., *Proc. ODP, Sci. Results,* 120: College Station, TX (Ocean Drilling Program), 89–96.

Le Bas, M.J., Le Maitre, R.W., Streckeisen, A., and Zanettin, B., 1986. A chemical classification of volcanic rocks based on the total alkali-silica diagram. *J. Petrol.,* 27:745–750.

Lysne, P., 1989. Investigation of neutron-porosity log uncertainties: Ocean Drilling Program Hole 642E. *In* Eldholm, O., Thiede, J., Taylor, E., et al., *Proc. ODP, Sci. Results,* 104: College Station, TX (Ocean Drilling Program), 973–977.

Macdonald, G.A., and Katsura, T., 1964. Chemical composition of Hawaiian lavas. *J. Petrol.,* 5:82–133.

Mackensen, A., Barrera, E., and Hubberten, H.-W., 1992. Neogene circulation in the southern Indian Ocean: evidence from benthic foraminifers, carbonate data, and stable isotope analyses (Site 751). *In* Wise, S.W., Jr., Schlich, R., et al., *Proc. ODP, Sci. Results,* 120: College Station, TX (Ocean Drilling Program), 867–878.

Mahoney, J., Jones, W., Frey, F.A., Salters, V., Pyle, D., and Davies, H., 1995. Geochemical characteristics of lavas from Broken Ridge, the Naturaliste Plateau and southernmost Kerguelen Plateau: early volcanism of the Kerguelen hotspot. *Chem. Geol.,* 120:315–345.

Mahoney, J.J., Jones, W.B., Frey, F.A., Salters, V.J.M., Pyle, D.G., and Davies, H.L., 1995. Geochemical characteristics of lavas from Broken Ridge, the Naturaliste Plateau and southernmost Kerguelen Plateau: Cretaceous plateau volcanism in the Southeast Indian Ocean. *Chem. Geol.,* 120:315–345.

Mehl, K.W., Bitschene, P. R., Schminke, H.-U., and Hertogen, J., 1991. Composition, alteration, and origin of the basement lavas and volcaniclastic rocks at Site 738, southern Kerguelen Plateau. *In* Barron, J., Larsen, B., et al., *Proc. ODP, Sci. Results,* 119: College Station, TX (Ocean Drilling Program), 299–322.

Pringle, M.S., Storey, M., and Wijbrans, J., 1994. ^{40}Ar/^{39}Ar geochronology of mid-Cretaceous Indian ocean basalts: constraints on the origin of large flood basalt. *Eos,* 75:728.

Reineck, H.E., and Singh, I.B., 1980. *Depositional Sedimentary Environments* (2nd ed.): Berlin (Springer-Verlag).

Rudnick, R.L., and Fountain, D.M., 1995. Nature and composition of the continental crust: a lower crustal perspective. *Rev. Geophys.*, 33:267–309.

Salters, V.J.M., Storey, M., Sevigny, J.H., and Whitechurch, H., 1992. Trace element and isotopic characteristics of Kerguelen-Heard Plateau basalts. *In* Wise, S.W., Jr., Schlich, R., et al., *Proc. ODP, Sci. Results,* 120: College Station, TX (Ocean Drilling Program), 55–62.

Sandwell, D.T., and Smith, W.H.F., 1997. Marine gravity anomaly from Geosat and ERS-1 satellite altimetry. *J. Geophys. Res.,* 102:10039–10054.

Schlumberger, 1994. *IPL Integrated Porosity Lithology* (Schlumberger Wireline and Testing), SMP-9270.Self, S., Keszthelyi, L., and Thordarson, T., 1998. The importance of pahoehoe. *Annu. Rev. Earth Planet. Sci,* 26:81–110.

Storey, M., Kent, R.W., Saunders, A.D., Salters, V.J., Hergt, J., Whitechurch, H., Sevigny, J.H., Thirlwall, M.F., Leat, P., Ghose, N.C., and Gifford, M., 1992. Lower Cretaceous volcanic rocks on continental margins and their relationship to the Kerguelen Plateau. *In* Wise, S.W., Jr., Schlich, R., et al., *Proc. ODP, Sci. Results,* 120: College Station, TX (Ocean Drilling Program), 33–53.

Storey, M., Pringle, M.S., Coffin, M.F., and Wijbrans, J., 1996. Geochemistry and geochronology of Kerguelen Plateau basalts: results from ODP Legs 117 and 120. *Eos,* 76:123.

Stott, L.D., and Kennett, J.P., 1990. Antarctic Paleogene planktonic foraminifer biostratigraphy: ODP Leg 113, Sites 689 and 690. *In* Barker, P.F., Kennett, J.P., et al., *Proc. ODP, Sci. Results,* 113: College Station, TX (Ocean Drilling Program), 549–569.

Sun, S.-S., and McDonough, W.F., 1989. Chemical and isotopic systematics of oceanic basalts: implications for mantle composition and processes. *In* Saunders, A.D., and Norry, M.J. (Eds.), *Magmatism in the Ocean Basins*. Geol. Soc. Spec. Publ. London, 42:313–345.

Thordarson, T., 1995. Volatile release and atmospheric effects of basaltic fissure eruptions [Ph.D. thesis]. Univ. of Hawaii at Manoa, Honolulu.

Wei, W., and Thierstein, H.R., 1991. Upper Cretaceous and Cenozoic calcareous nannofossils of the Kerguelen Plateau (southern Indian Ocean) and Prydz Bay (East Antarctica). *In* Barron, J., Larsen, B., et al., *Proc. ODP, Sci. Results,* 119: College Station, TX (Ocean Drilling Program), 467–494.

Wei, W., and Wise, S.W., Jr., 1992. Selected Neogene calcareous nannofossil index taxa of the Southern Ocean: biochronology, biometrics, and paleoceanography. *In* Wise, S.W., Jr., Schlich, R., et al., *Proc. ODP, Sci. Results,* 120: College Station, TX (Ocean Drilling Program), 523–537.

Weis, D., Bassias, Y., Gautier, I., and Mennesier, J.-P., 1989. DUPAL anomaly in existence 115 Ma ago: evidence from isotopic study of the Kerguelen Plateau (South Indian Ocean). *Geochim. Cosmochim. Acta,* 53:2125–2131.

Weis, D., Frey, F.A., Giret, A., and Cantagrel, J.M., 1998. Geochemical characteristics of the youngest volcano (Mount Ross) in the Kerguelen Archipelago: inferences for magma flux and composition of the Kerguelen plume. *J. Petrol.,* 39:973–994.

Weis, D., Frey, F.A., Leyrit, H., and Gautier, I., 1993. Kerguelen Archipelago revisited: geochemical and isotopic study of the Southeast Province lavas. *Earth Planet. Sci. Lett.,* 118:101–119.

Wise, S.W., Jr., 1983. Mesozoic and Cenozoic calcareous nannofossils recovered by Deep Sea Drilling Project Leg 71 in the Falkland Plateau region, Southwest Atlantic Ocean. *In* Ludwig, W.J., Krasheninnikov, V.A., et al., *Init. Repts. DSDP,* 71 (Pt. 2): Washington (U.S. Govt. Printing Office), 481–550.

Figure F1. Satellite-derived free-air gravity map of the Kerguelen Plateau (after Sandwell and Smith, 1997). The five plateau province sectors are northern, central, southern, Elan Bank, and Labuan Basin (outlined in white). Current (Leg 183) and previous (Legs 119 and 120) ODP sites are indicated by circles and stars, respectively (black = basement sites; white = sediment sites). Squares indicate dredge and piston core sites where igneous rock (black) and sediment (white) were recovered. **(Figure shown on next page.)**

Figure F1. (Caption on previous page.)

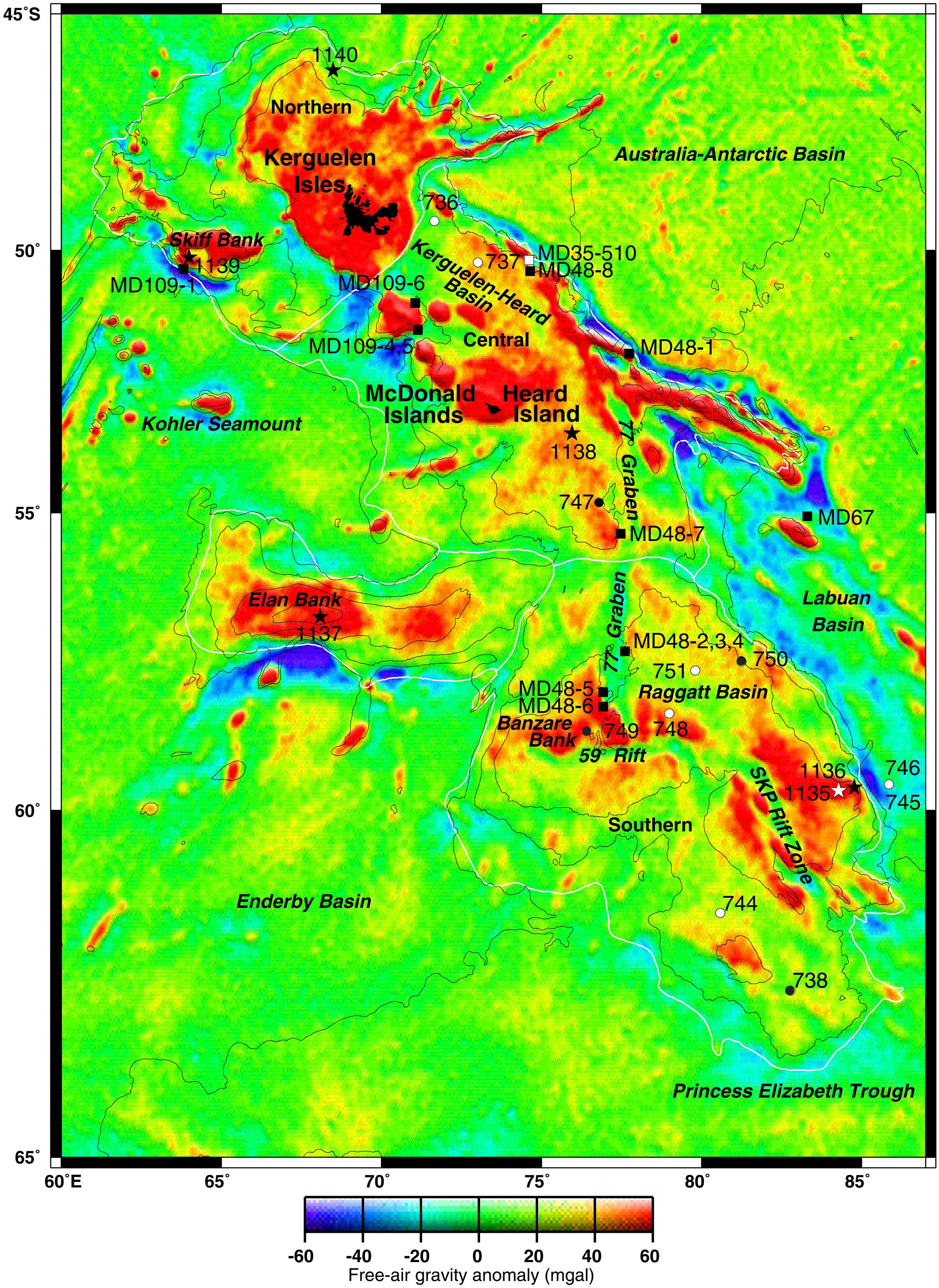

Figure F2. Location of Site 1137 and site-survey data. Navigation for *Rig Seismic* survey 179, line 601 (RS179/601), and *Eltanin* cruise 54 (EL54) data is shown in Julian day:time. Bathymetric contour interval = 500 m (Fisher, 1997).

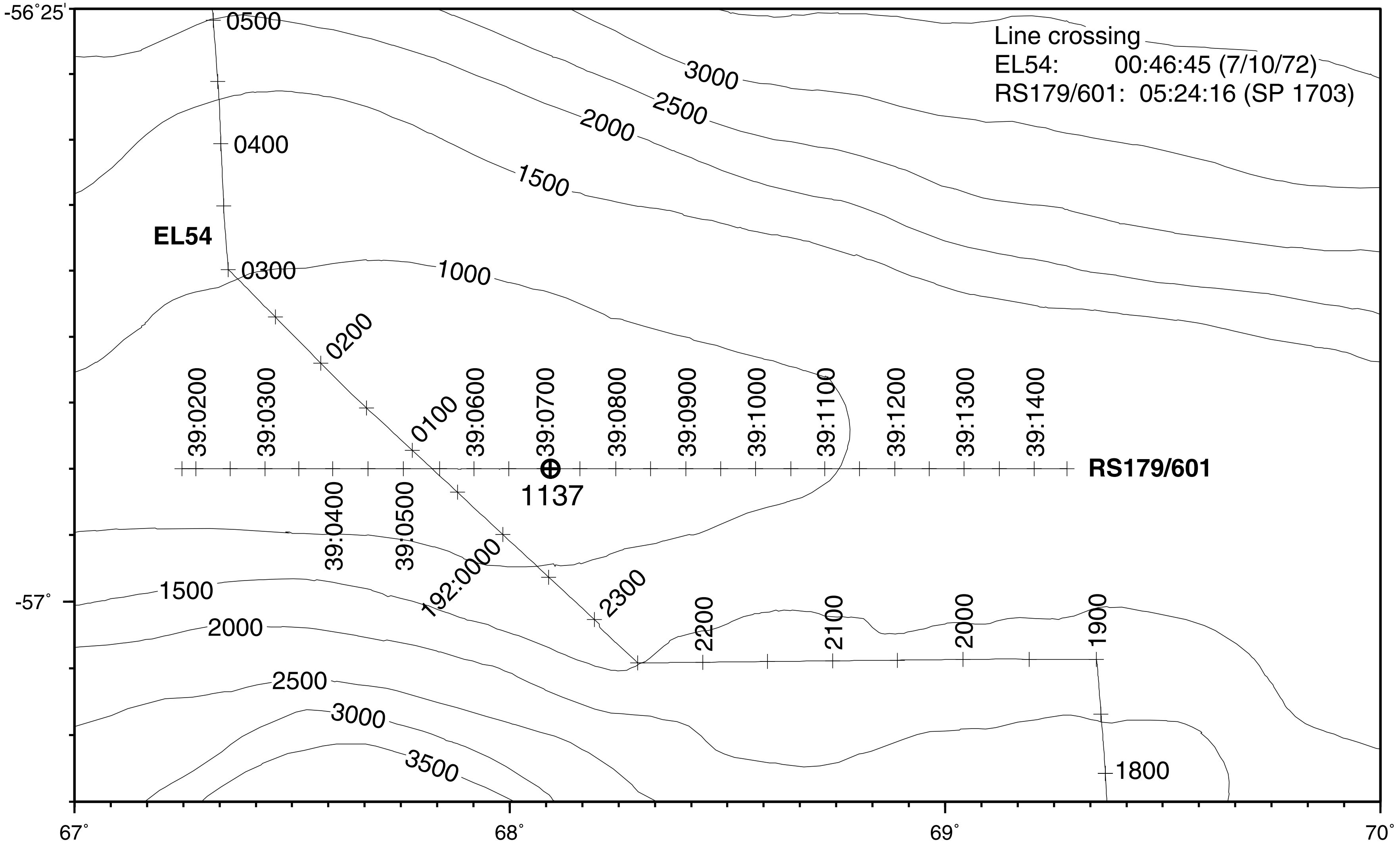

Figure F3. *Rig Seismic* RS179/601 multichannel seismic profile across Site 1137. Vertical exaggeration = ~16 at seafloor.

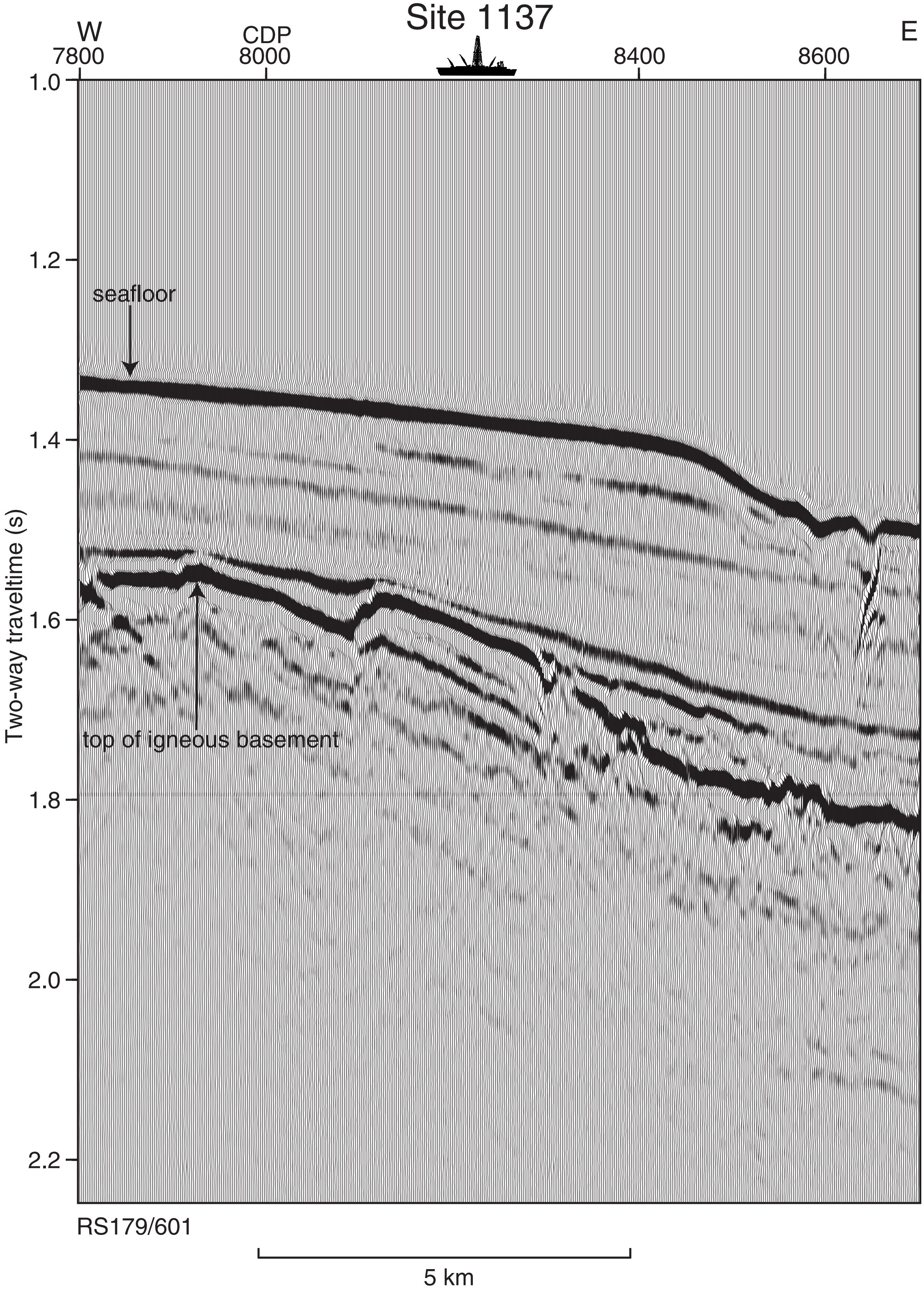

Figure F4. Composite stratigraphic section for Site 1137 showing core recovery, a simplified summary of lithology, lithologic unit boundaries, basement unit boundaries, ages of units, and names of lithologies. The lithologic symbols are explained in Figure F2, p. 56, in the "Explanatory Notes" chapter.

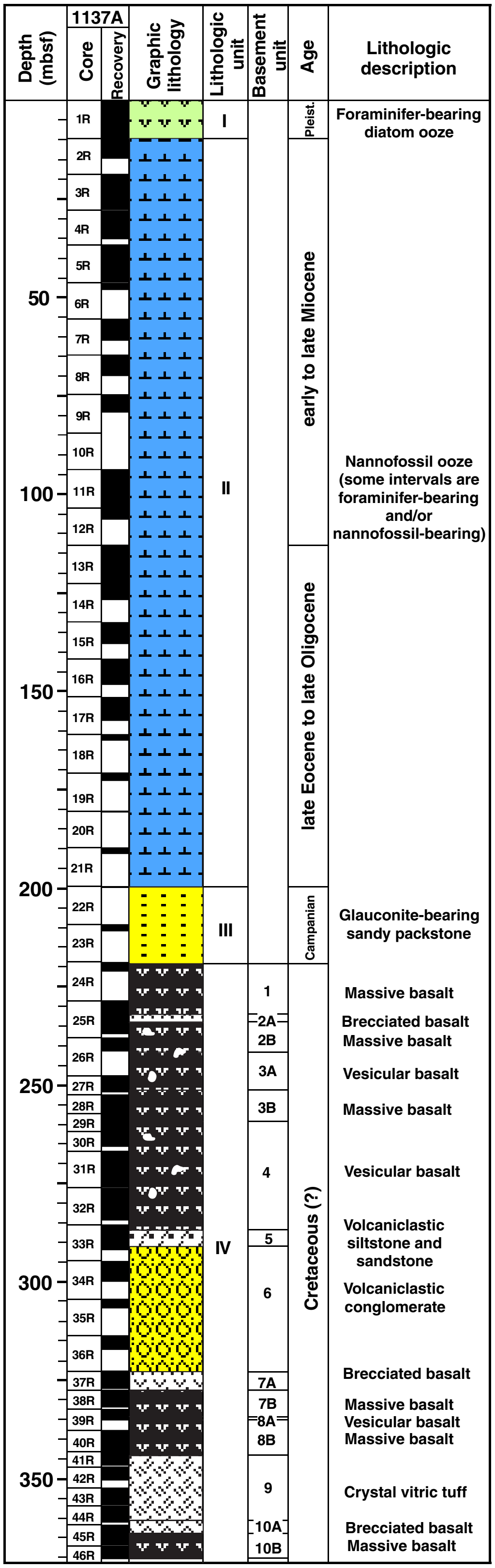

Figure F5. Composite stratigraphic section for Hole 1137A from 0 to ~225 mbsf, showing core recovery, a simplified summary of lithology, lithologic unit boundaries, ages of units, names of lithologies, and calcium carbonate content downhole (see Table T4, p. 175). The lithologic symbols are explained in Figure F2, p. 56, in the "Explanatory Notes" chapter.

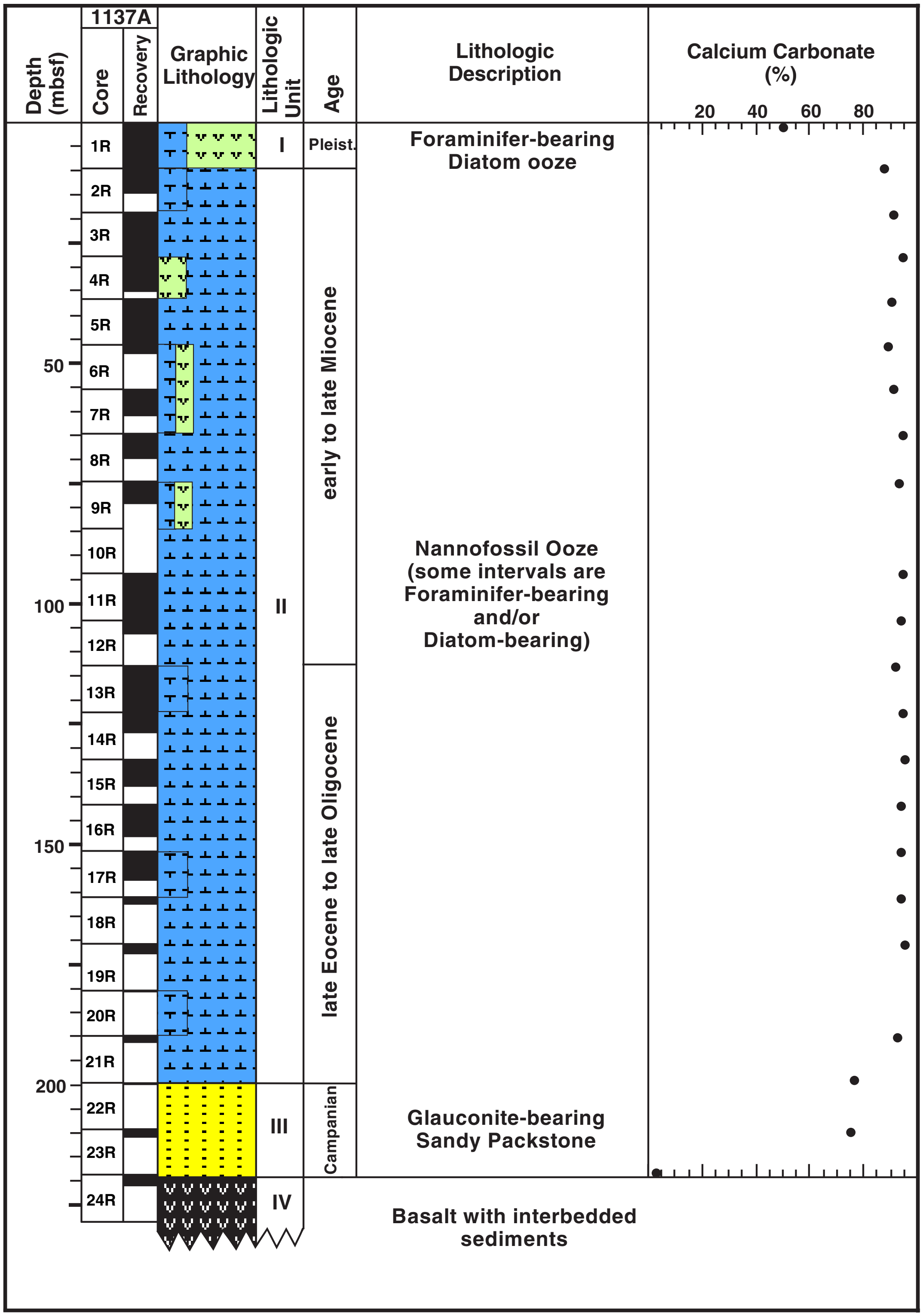

Figure F6. Composite stratigraphic section for Hole 1137A from ~275 to 370.16 mbsf, showing core recovery, a simplified summary of lithology, lithologic unit boundaries, basement unit boundaries, ages of units, and names of lithologies. The lithologic symbols are explained in Figure F2, p. 56, in the "Explanatory Notes" chapter.

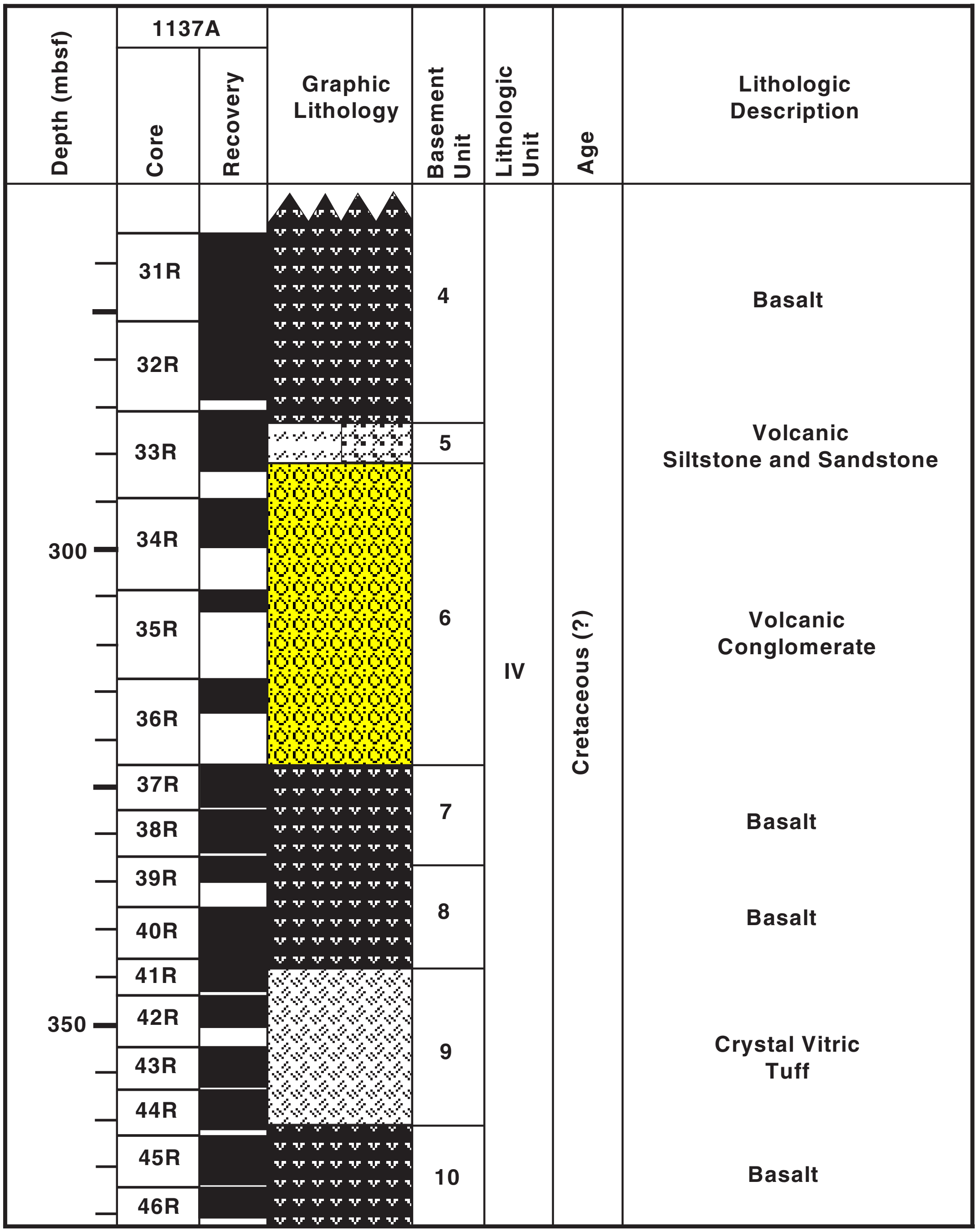

Figure F7. A. Glauconite-bearing sandy packstone at the top of Unit III (interval 183-1137A-22R-1, 1–8 cm). **B.** Glauconite-bearing sandy packstone near the top of Unit III showing concentration of large bivalve shell fragments (interval 183-1137A-22R-1, 9–15 cm).

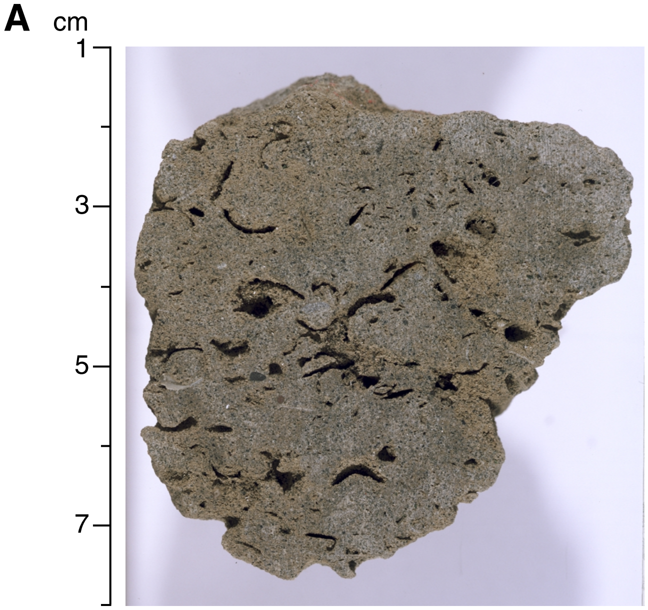

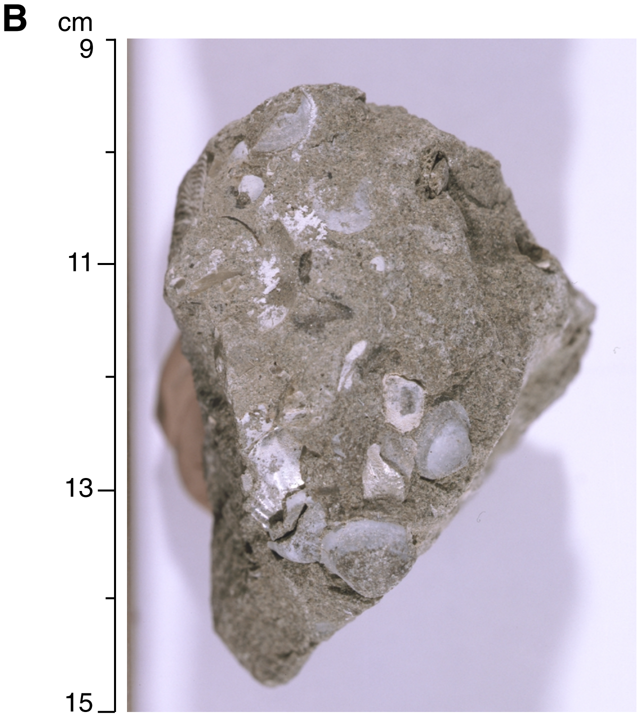

Figure F8. **A.** Normally graded bed grading downward from silt- to medium sand-sized particles in basement Unit 5 (interval 183-1137A-33R-3, 41–55 cm). **B.** Cross-stratification in sandstone bed of basement Unit 5 (interval 183-1137A-33R-3, 81–91 cm).

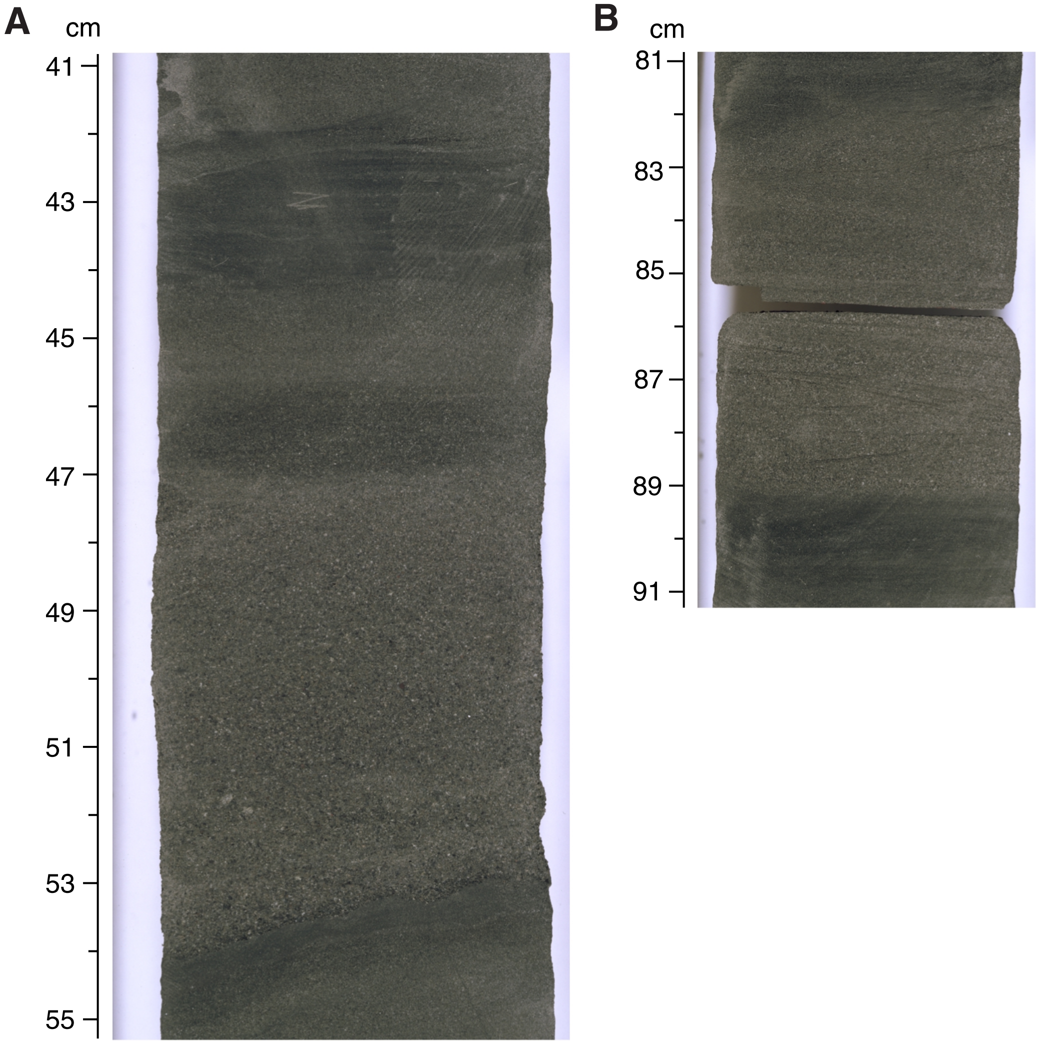

Figure F9. Examples of conglomerates in basement Unit 6. **A.** Interval 183-1137A-34R-2, 50–70 cm. **B.** Interval 183-1137A-34R-2, 80–110 cm. (Continued on next page.)

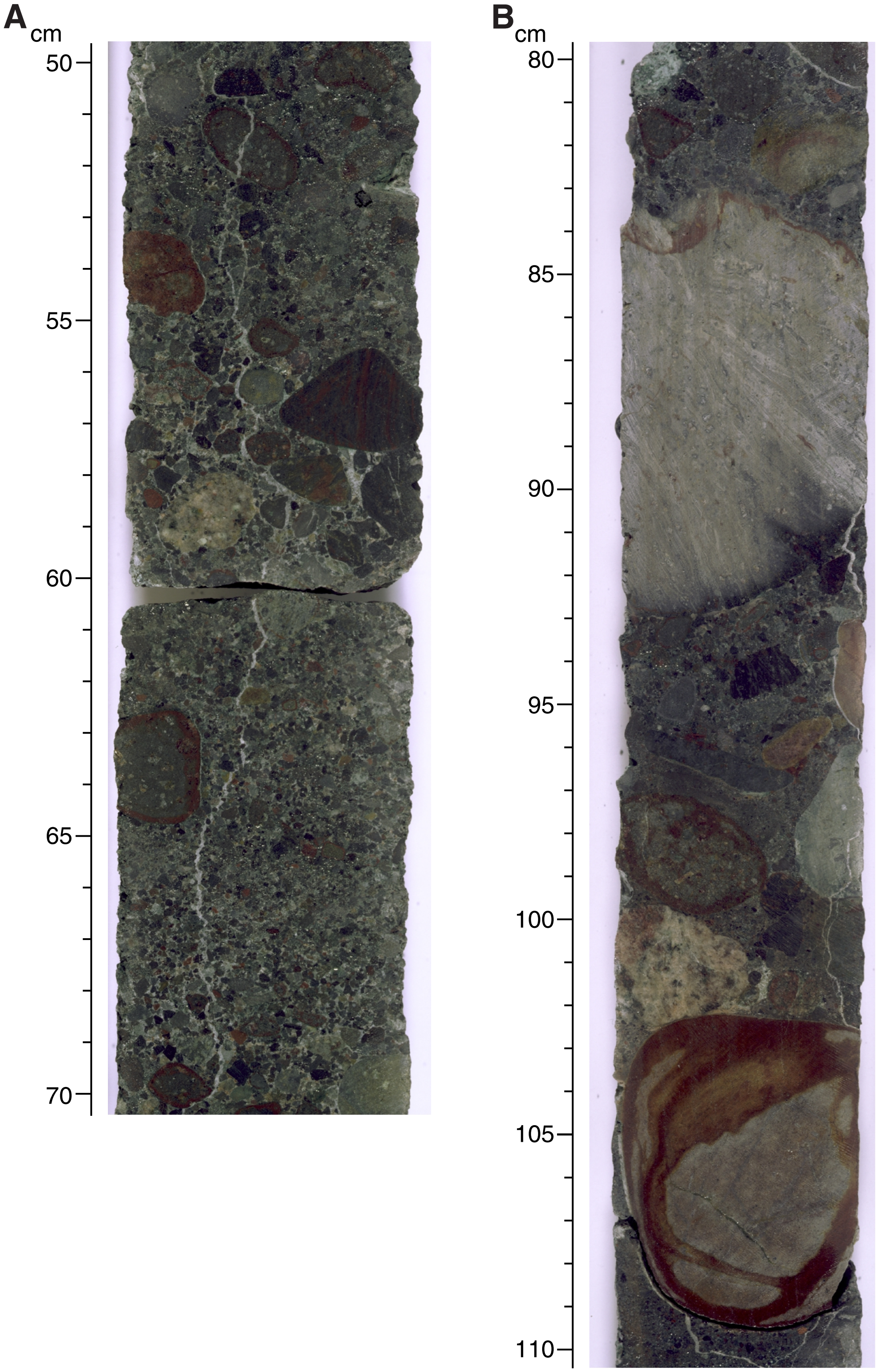

Figure F9 (continued). **C.** Interval 183-1137A-34R-3, 57–80 cm; note the apparent, steeply dipping imbricate structure of the pebbles. **D.** Interval 183-1137A-34R-3, 82–112 cm.

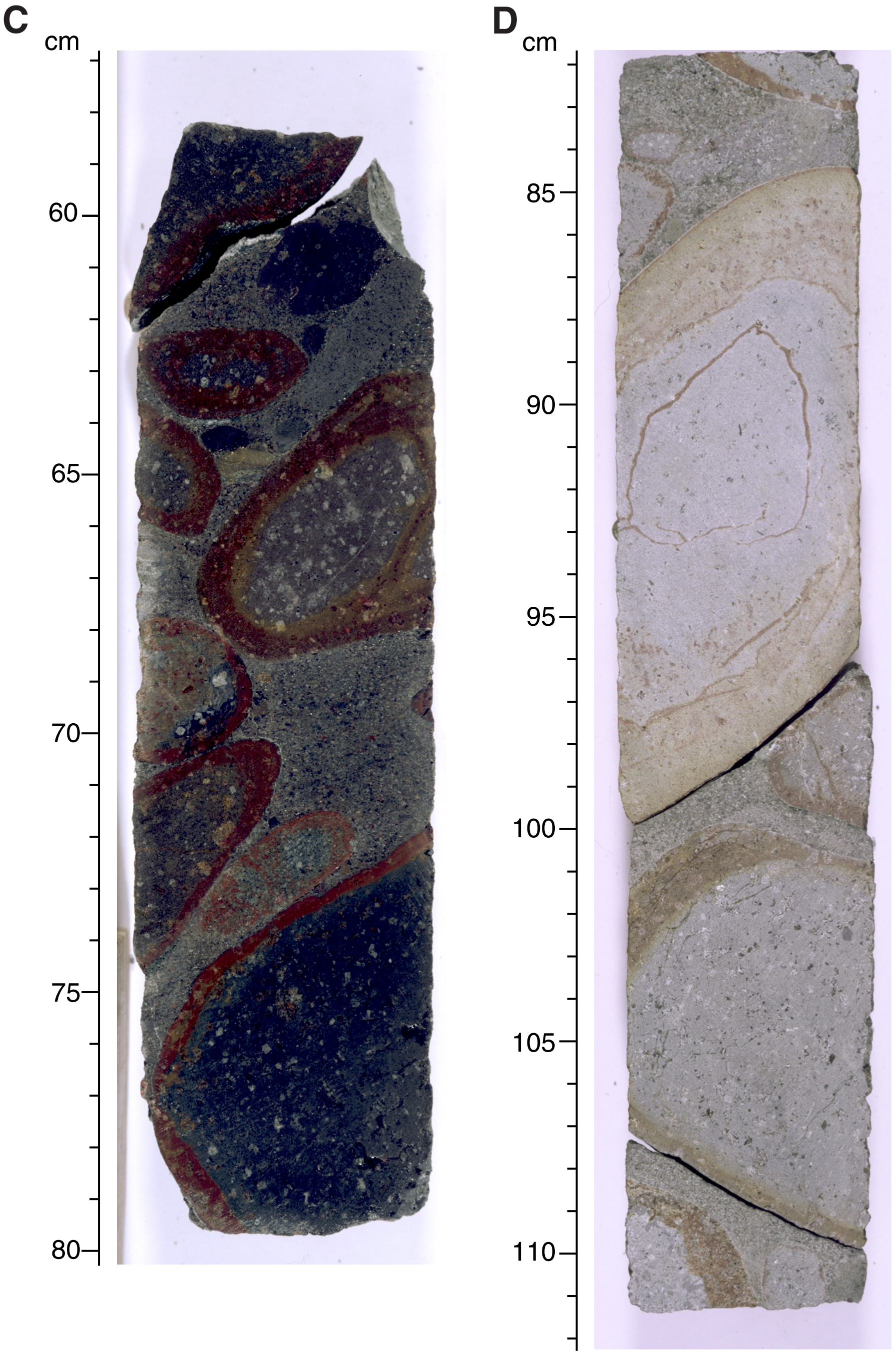

Figure F10. Crystal-vitric tuff from basement Unit 9; note large basalt and rock pebble clasts. **A.** Interval 183-1137A-42R-4, 20–30 cm. **B.** Interval 183-1137A-44R-3, 20–50 cm.

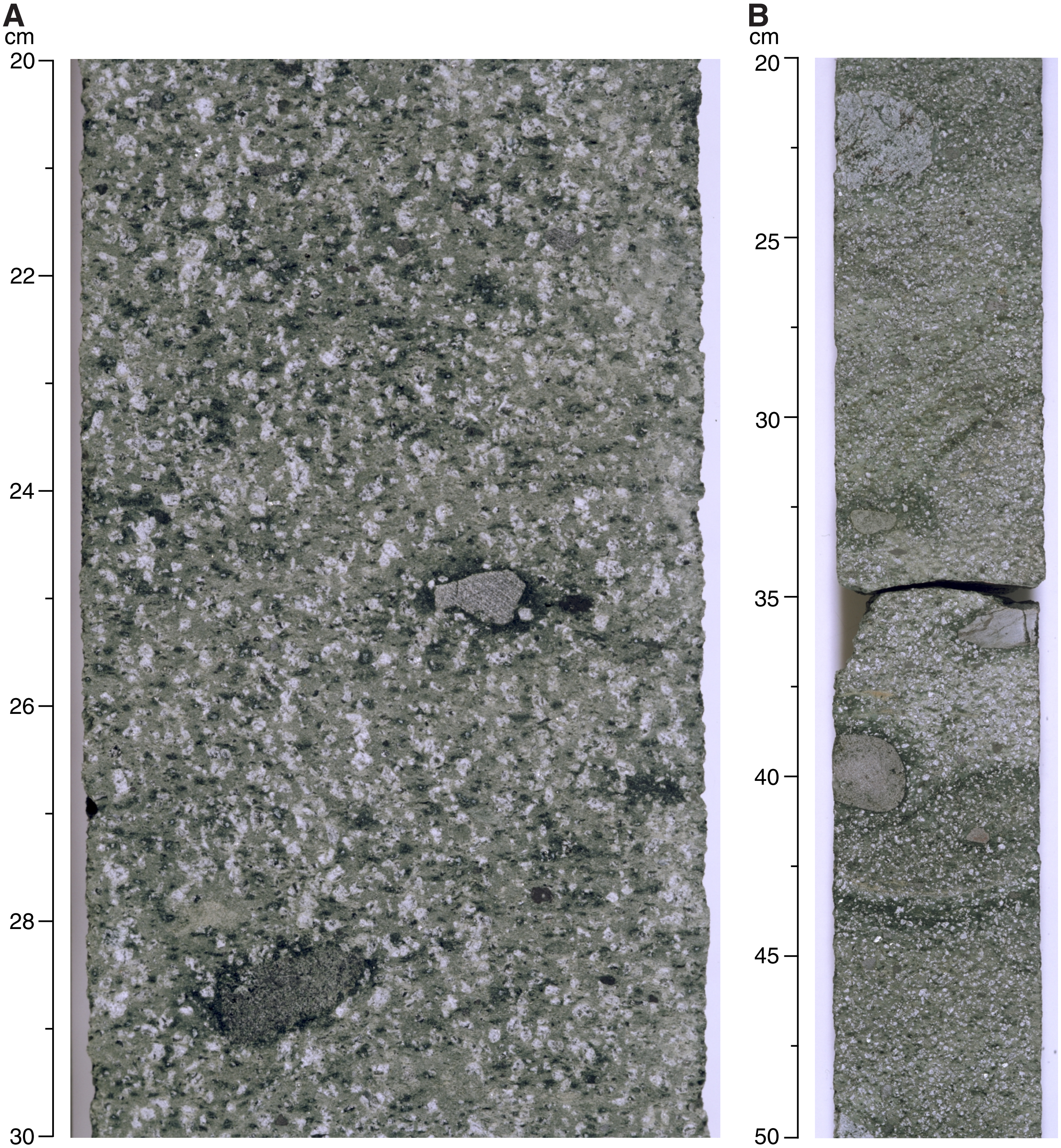

Figure F11. Site 1137 age-depth plot. The lithologic symbols are explained in Figure F2, p. 56, in the "Explanatory Notes" chapter.

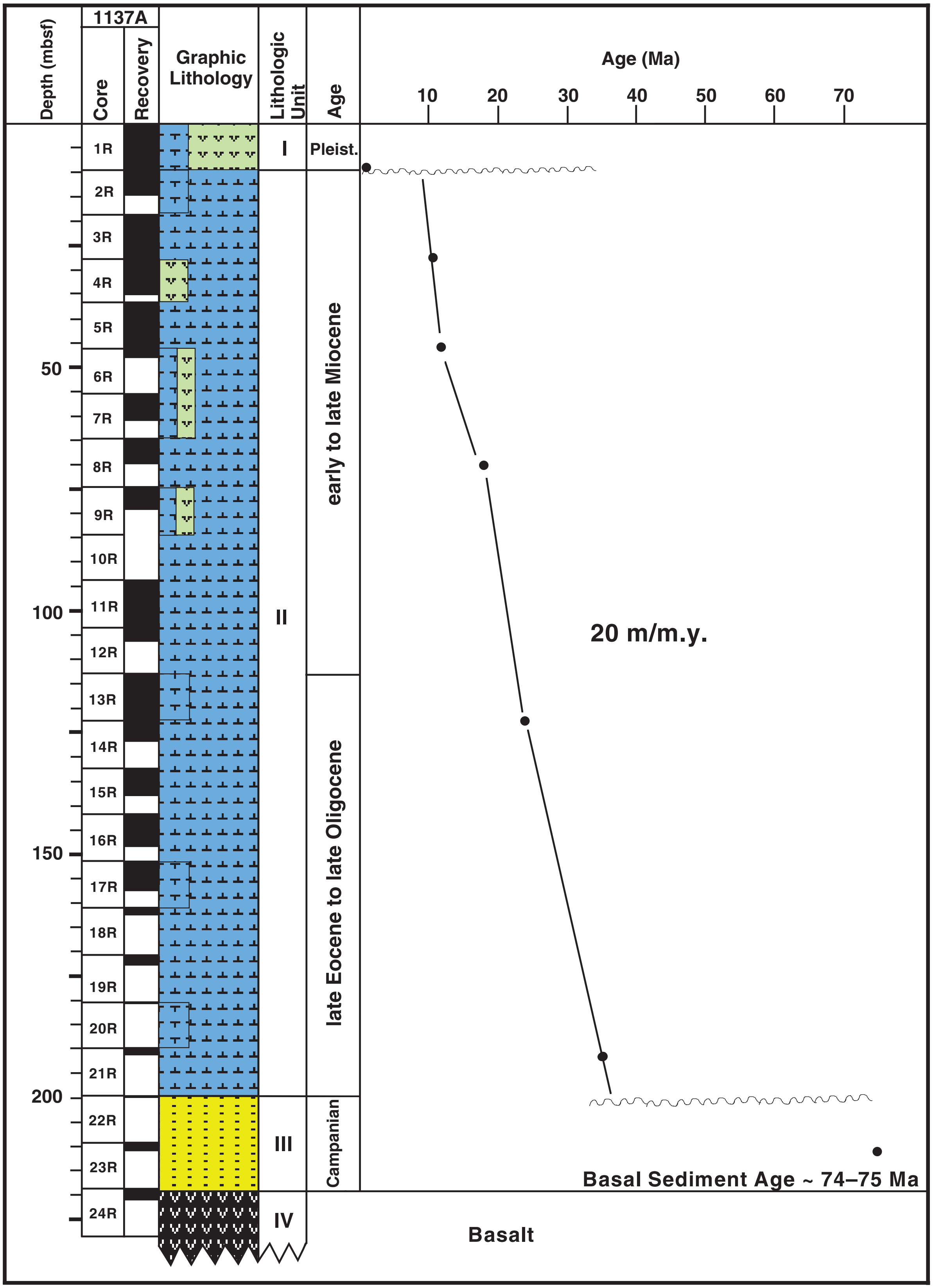

Figure F12. Close-up photograph of interval 183-1137A-25R-3, 112–144 cm, showing pahoehoe lobe at the top of basement Unit 2.

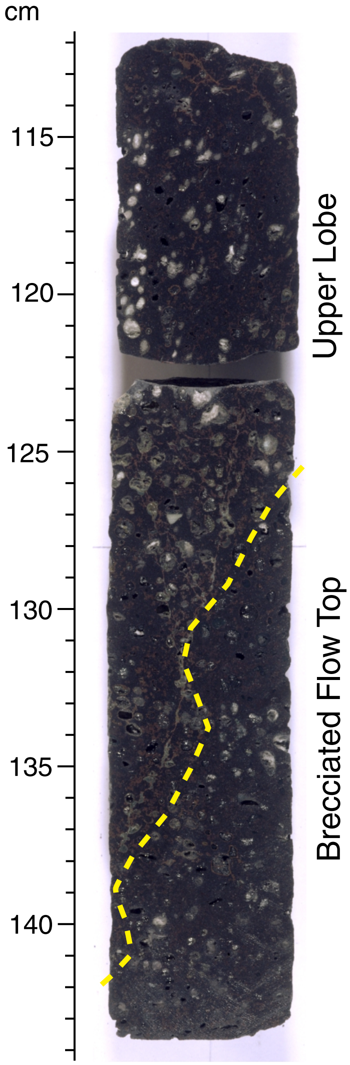

Figure F13. Close-up photograph of interval 183-1137A-25R-4, 44–91 cm, showing various clasts in the flow-top breccia on basement Unit 2.

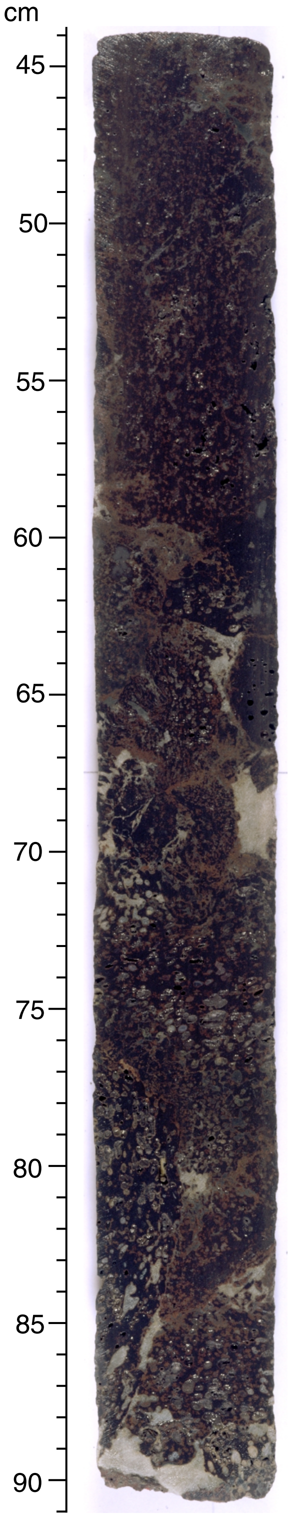

Figure F14. Close-up photograph of interval 183-1137A- 25R-6, 70–83 cm, showing megavesicle marking the transition from the coherent vesicular part of basement Unit 2 to the massive interior.

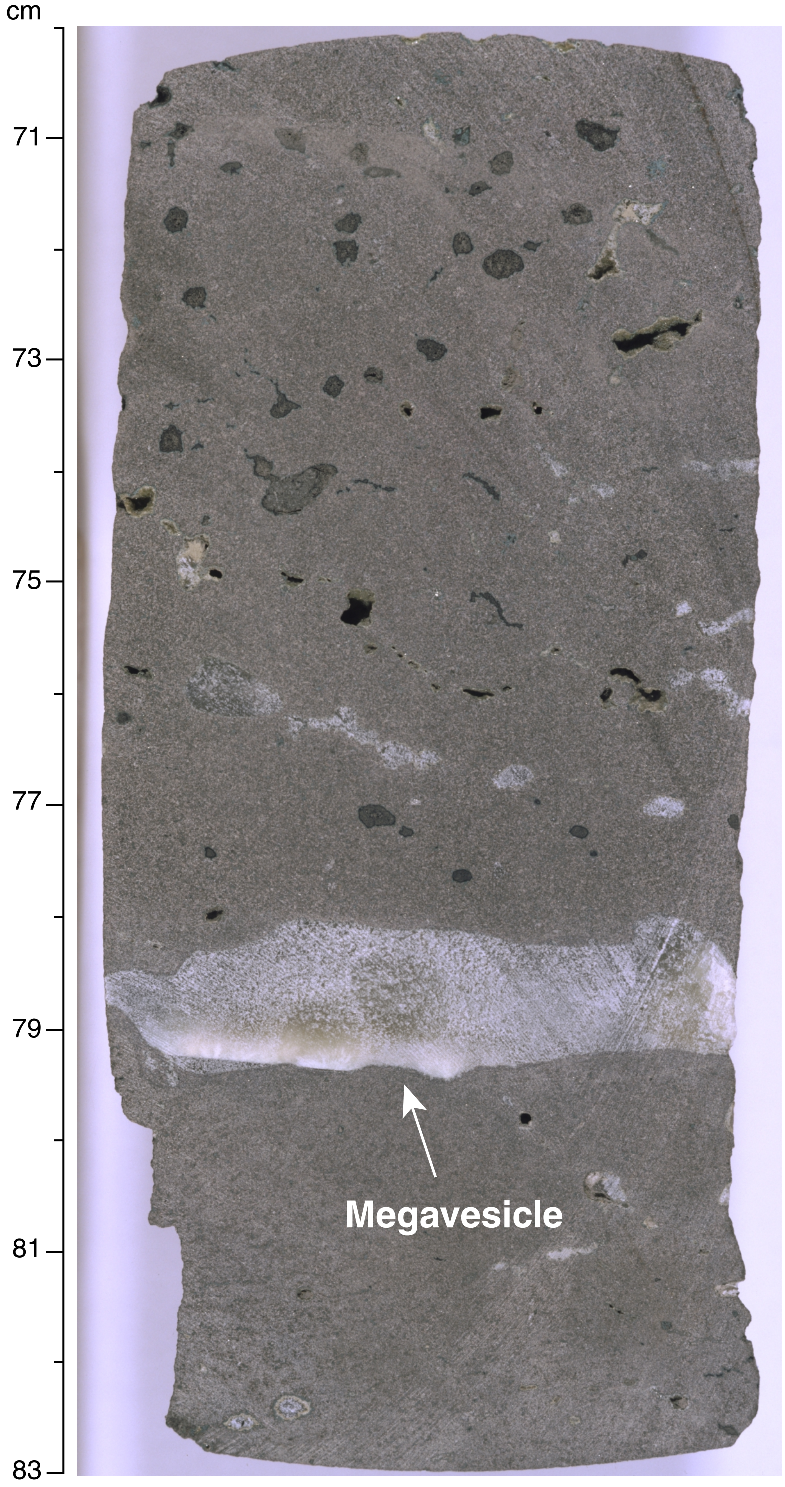

Figure F15. Vesicularity and vesicle number density as a function of depth in basement Unit 3. Note that x-axis is logarithmic. Hatched intervals designate zones of nonrecovery.

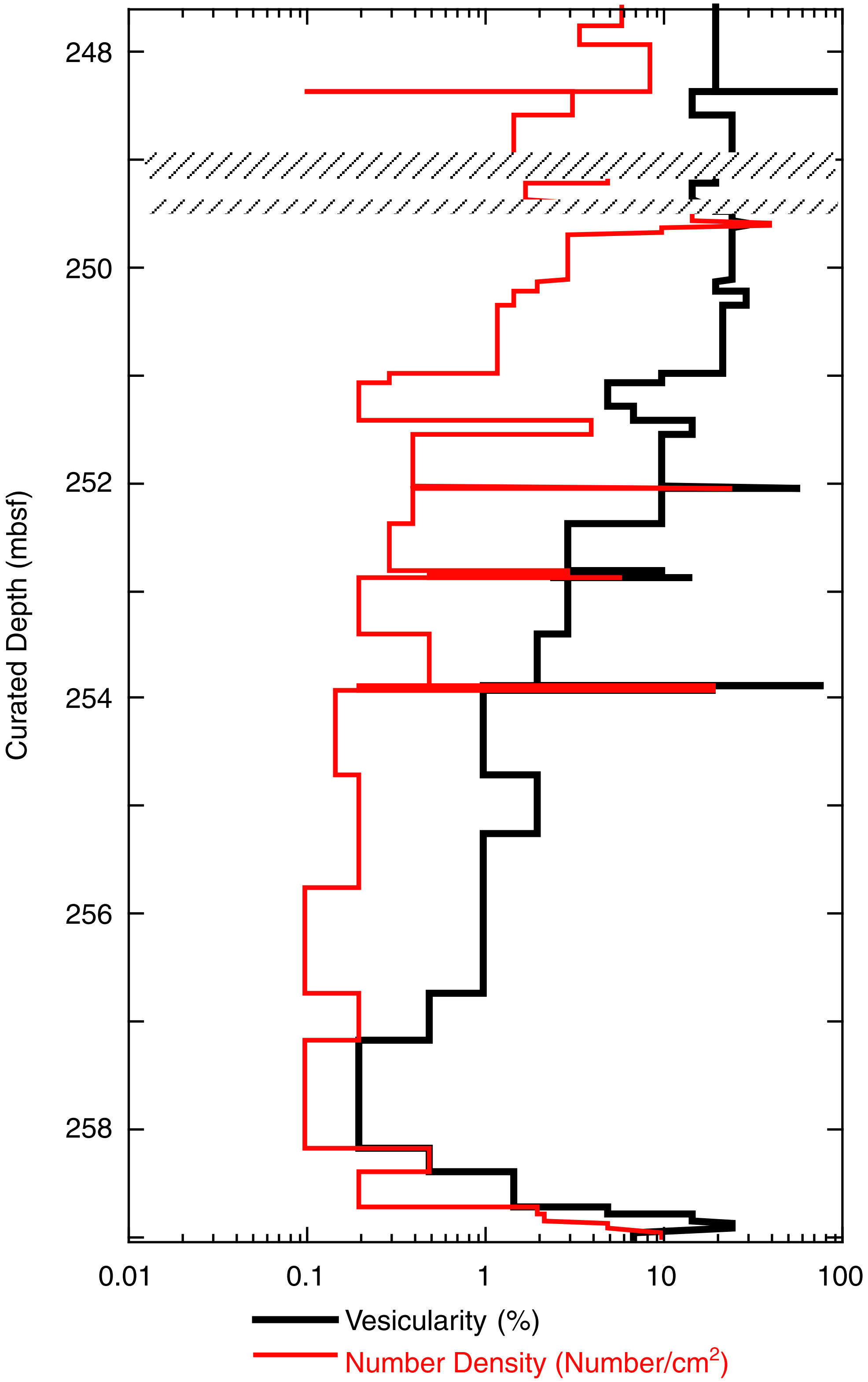

Figure F16. Close-up photograph of interval 183-1137A-27R-1, 114–125 cm, showing large, horizontally elongated vesicles. Note that some vesicles have been vertically compressed, possibly as a result of collapse from the weight of the overlying lava.

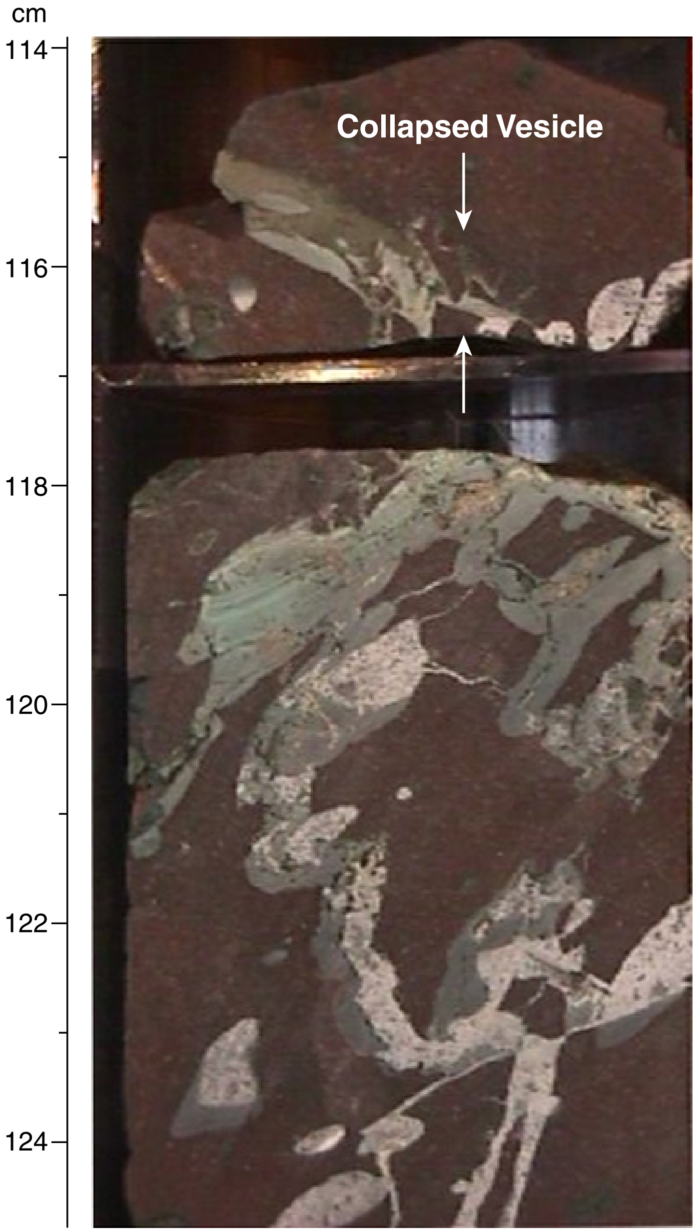

Figure F17. Close-up photograph of Sample 183-1137A-29R-2 (Piece 4, 54–62 cm) showing sediment-filled cavity at the base of basement Unit 3. The sediments are a sequence of finely laminated silts/clays, ~1-cm-thick graded beds of fine sands to silts, and a 1.5-cm angular oxidized lava clast with 1.5 cm of attached fine sands to silts. The graded beds fine upward, and the bases are marked by 0.3- to 5-mm-long, tabular silt-clay laminae. Discrete lamina have concentrations of oxidized material (lava). Note the intricately convoluted margin of the lava facing the cavity. We interpret this as an open cavity in the base of the lava flow that was filled by sediments and reworked pieces of lava transported by water moving along the base of the highly permeable lava flow.

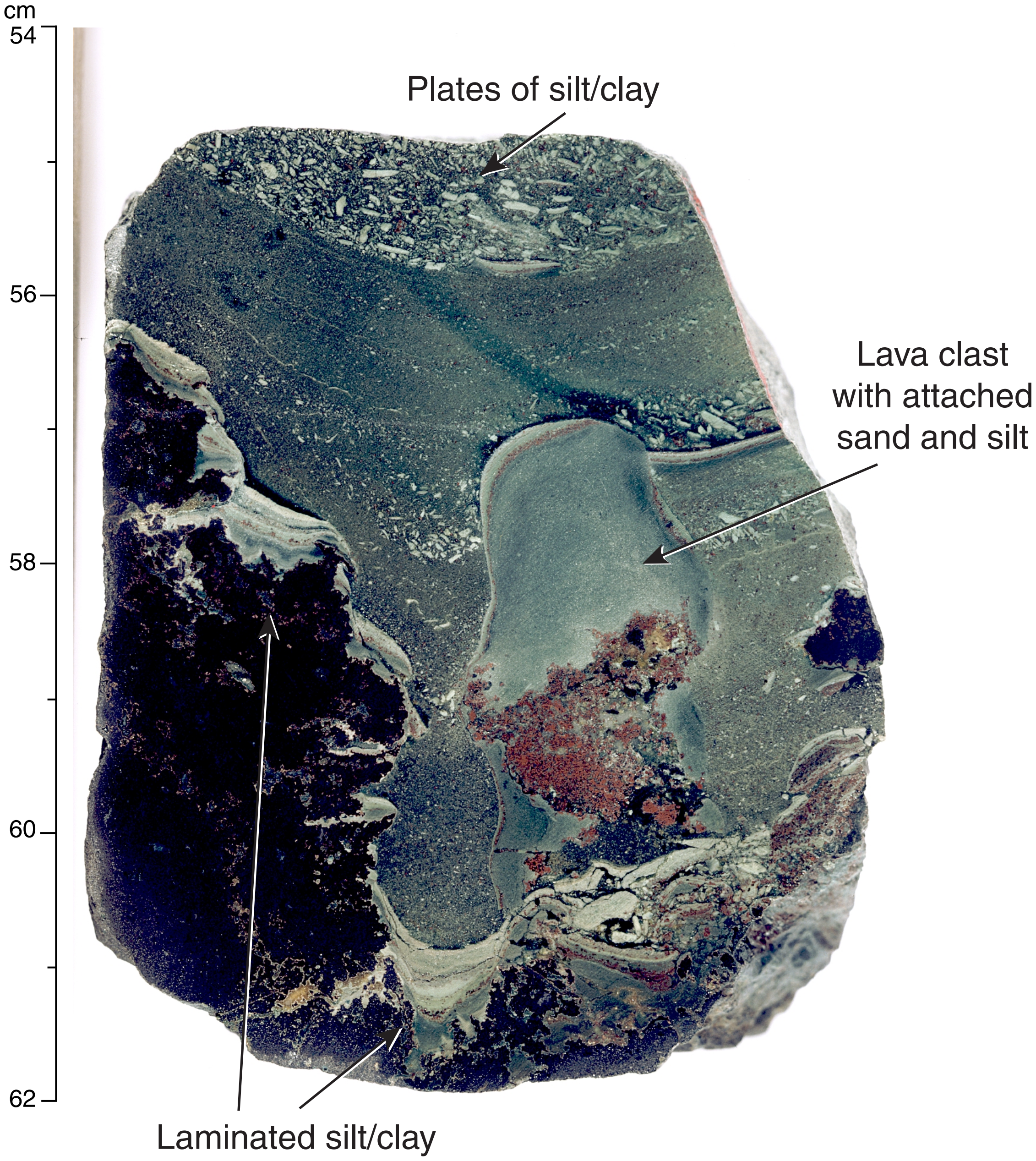

Figure F18. Vesicularity and vesicle-number density as a function of depth in basement Unit 4. Note that x-axis is logarithmic. Hatched intervals designate zones of nonrecovery.

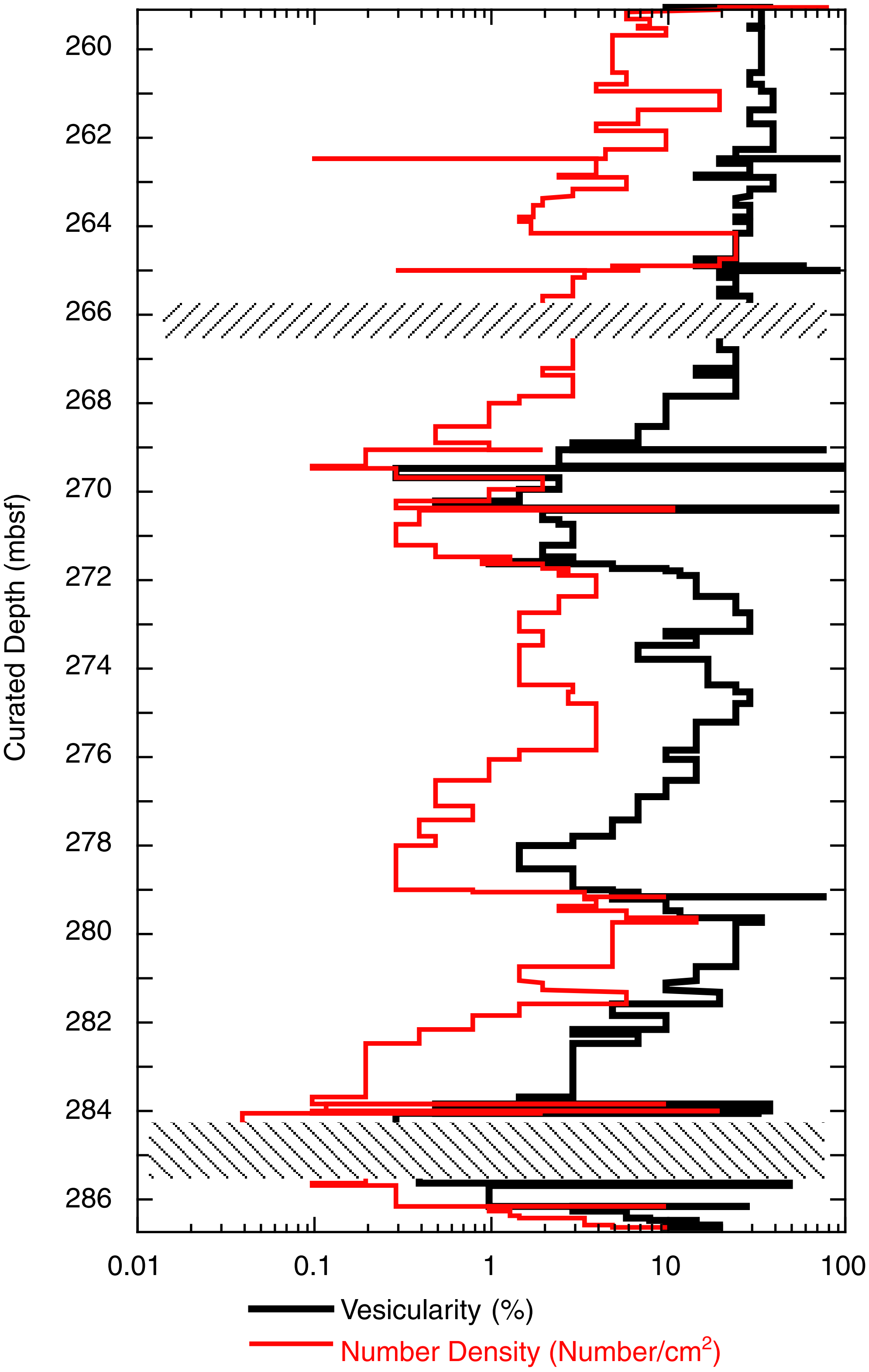

Figure F19. Close-up photograph of interval 183-1137A-29R-2, 65–81 cm, showing the base of Unit 3, the interbedded sediments included with Unit 4, and the pahoehoe top of basement Unit 4. The dark margin is interpreted to be altered glassy material.

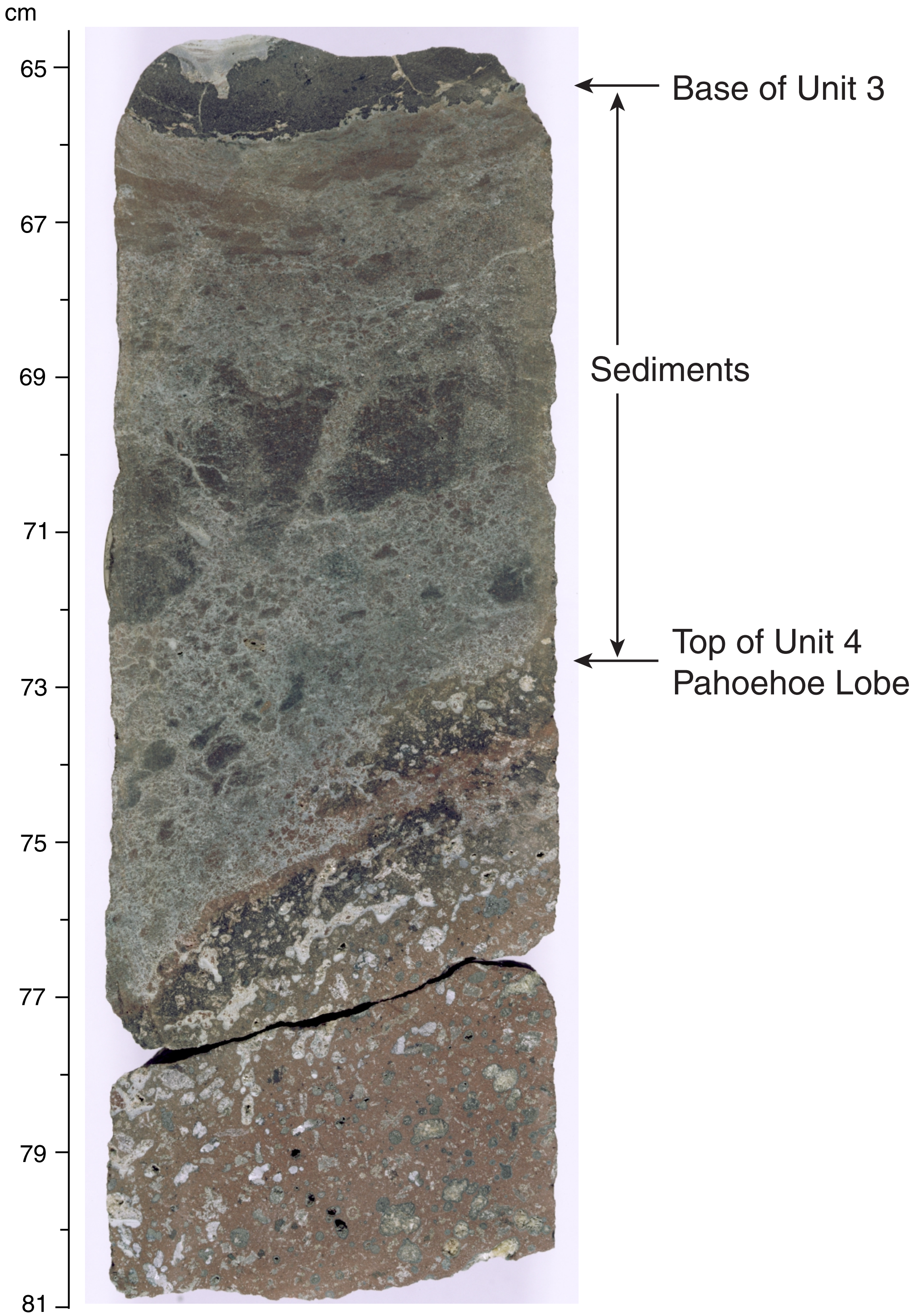

Figure F20. Close-up photograph of interval 183-1137A-33R-1, 110–140 cm, showing contact between basement Units 4 (inflated pahoehoe lava) and 5 (crystal-lithic volcanic siltstone and sandstone).

Figure F21. Photomicrograph of the base of basement Unit 4 (Sample 183-1137A-33R-1 [Piece 1E, 121–124 cm]) showing the contact between highly oxidized, feldspar phyric basalt and the baked top of the crystal-lithic volcanic sandstone/siltstone (basement Unit 5). Note the abundance of angular (broken?) feldspar crystals in the sediment, probably of volcanic origin. Field of view = 2.75 mm (plane-polarized light).

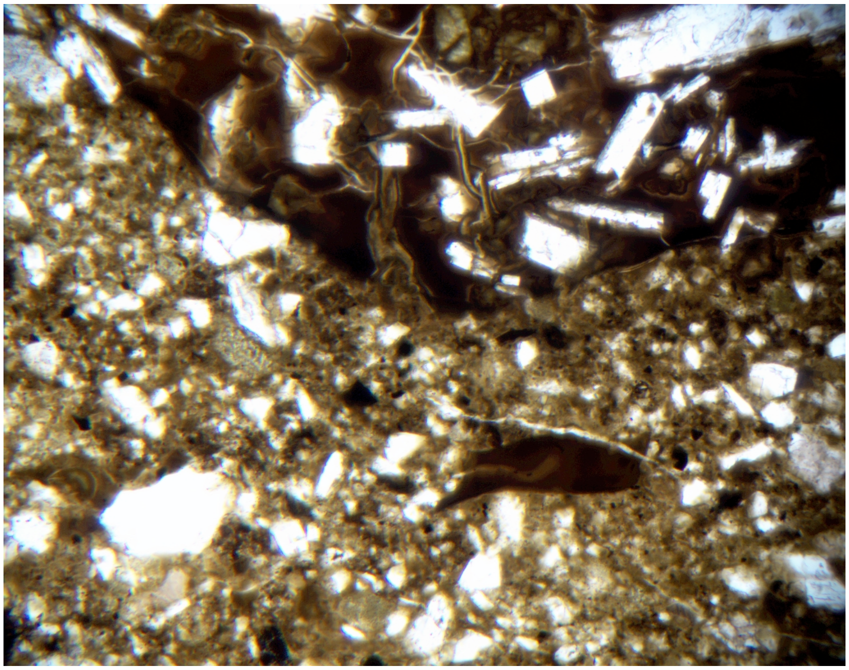

Figure F22. Photomicrograph of Sample 183-1137A-33R-3 (Piece 1B, 50–53 cm) showing typical internal texture of crystal-lithic volcanic sandstone and siltstone in basement Unit 5. Despite the sharp contact between the two intervals, their content is similar: both siltstone and sandstone contain abundant angular feldspar crystals and crystal-lithic volcanic fragments throughout. Field of view = 2.75 mm (plane-polarized light).

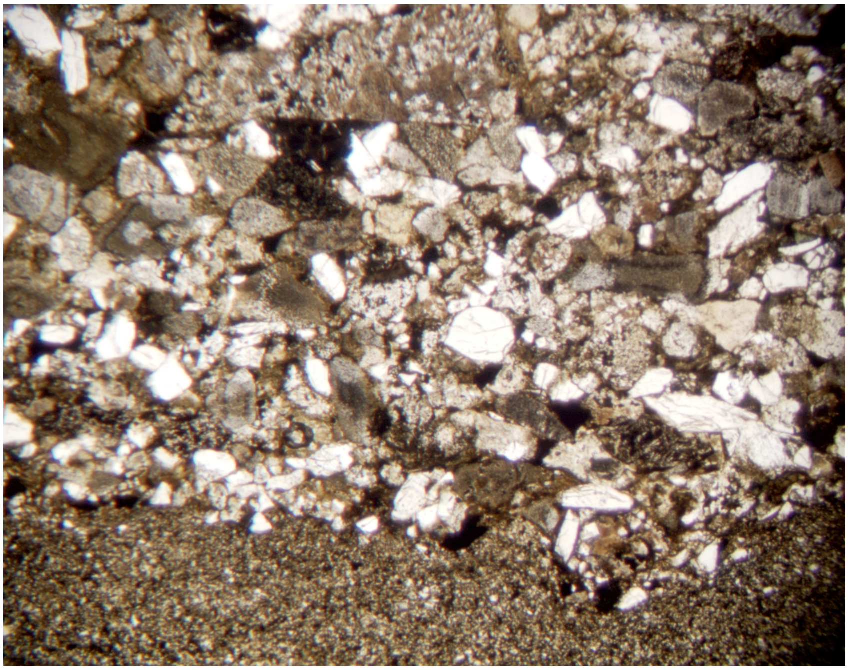

Figure F23. Summary of some grain-size characteristics (granulometry) for the volcanic conglomerate (basement Unit 6). **A.** Percentage matrix in the conglomerate (fine to very coarse sand fraction). Note that the >20-cm-thick sand in interval 183-1137A-35R-1, 98–118 cm, is not included in this analysis. The percentage matrix in each section is generally >25%; however, discrete intervals are granular and contain fewer large clasts. **B.** The average clast size is relatively constant in the pebble size range throughout the volcanic conglomerate. There are slightly larger average clast sizes in the upper half of basement Unit 6. The oblate nature of the clasts is represented by the long-to-short axis ratios. **C.** The maximum clast size shows two broad intervals with reverse graded cobbles at the base and more normal graded cobble to pebble distribution above. A >20-cm-thick sand (interval 183-1137A-35R-1, 98–118 cm) sits between these two broad intervals. The oblate nature of the clasts is represented by the long to short axis ratios. **D.** The sorting is relatively poor with a range in clast size from granule to cobble throughout most of the conglomerate. The standard deviation ranges from 1.4 to 3.2 cm, which is significant compared to the average clast size (2.0 cm × 3.2 cm).

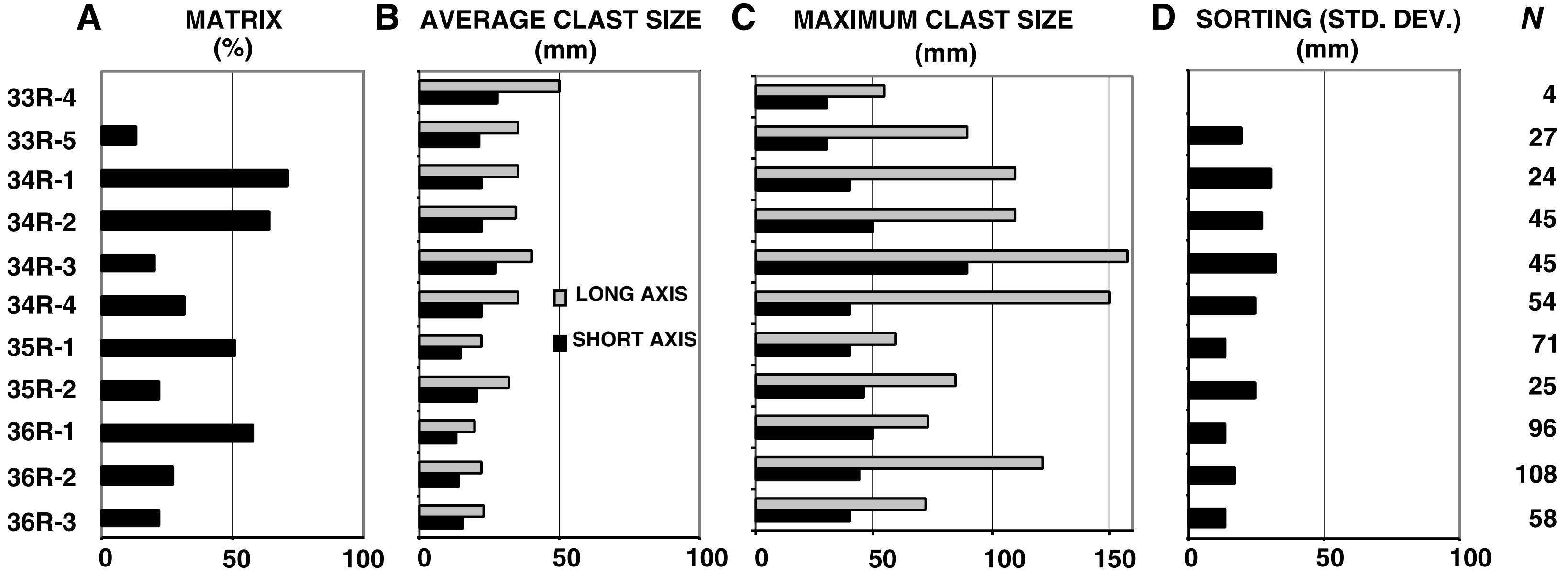

Figure F24. Close-up photograph of interval 183-1137A-37R-1, 27–47 cm, showing the variety of clasts in the upper part of the breccia on basement Unit 7. Compare with Figure F25, p. 88, for differences with lower parts of the breccia.

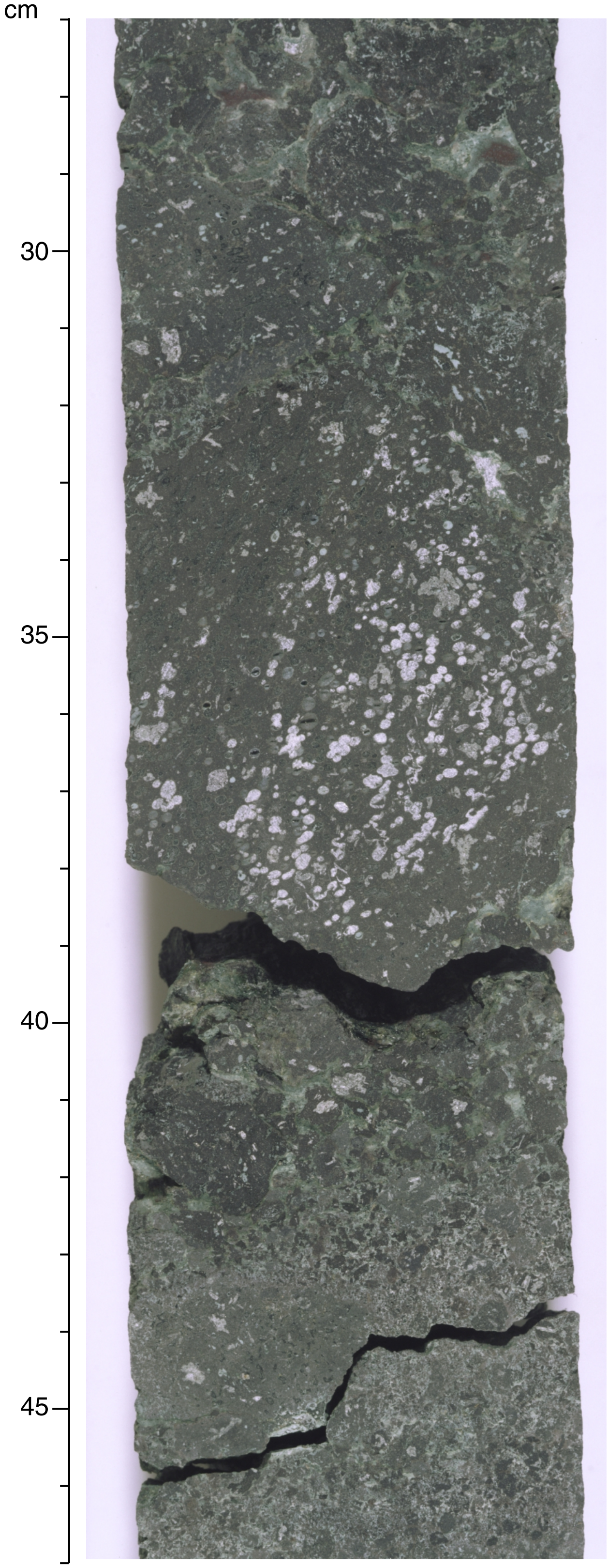

Figure F25. Close-up photograph of interval 183-1137A-37R-5, 20–40 cm, showing the variety of clasts in the lower part of the breccia on basement Unit 7. Compare with Figure **F24,** p. 87, for differences with the upper part of the breccia.

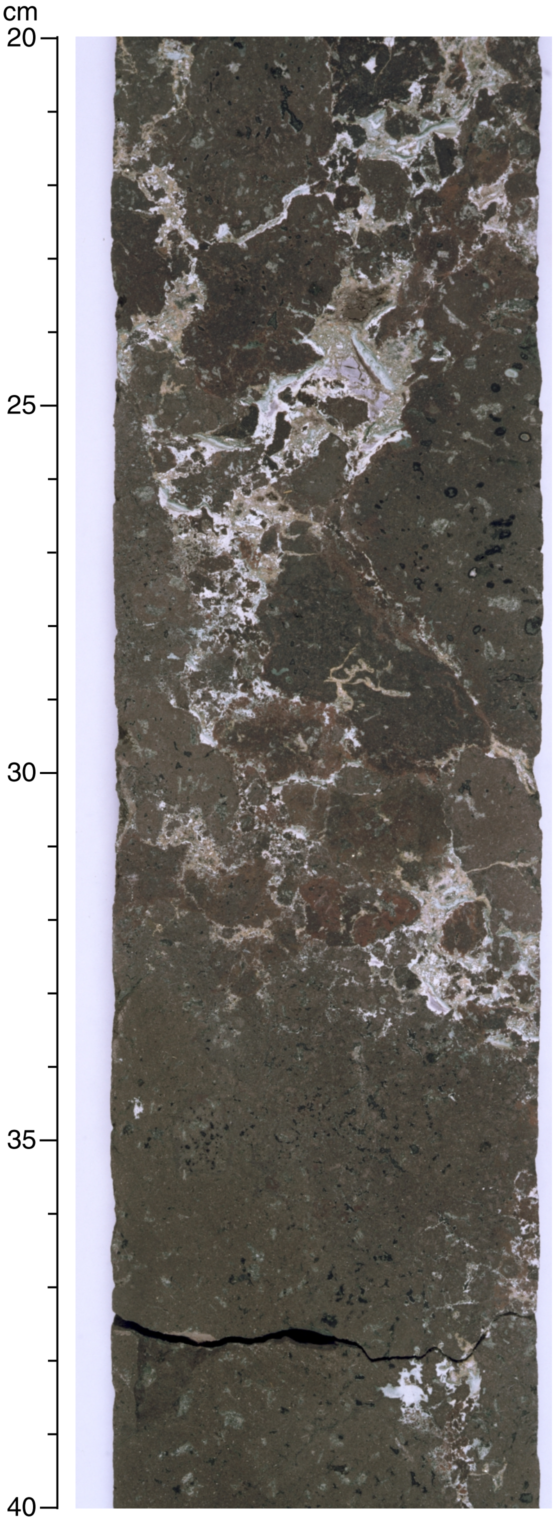

Figure F26. Close-up photograph of interval 183-1137A-39R-1, 105–118 cm, showing mesostasis blebs in the massive interior of basement Unit 7.

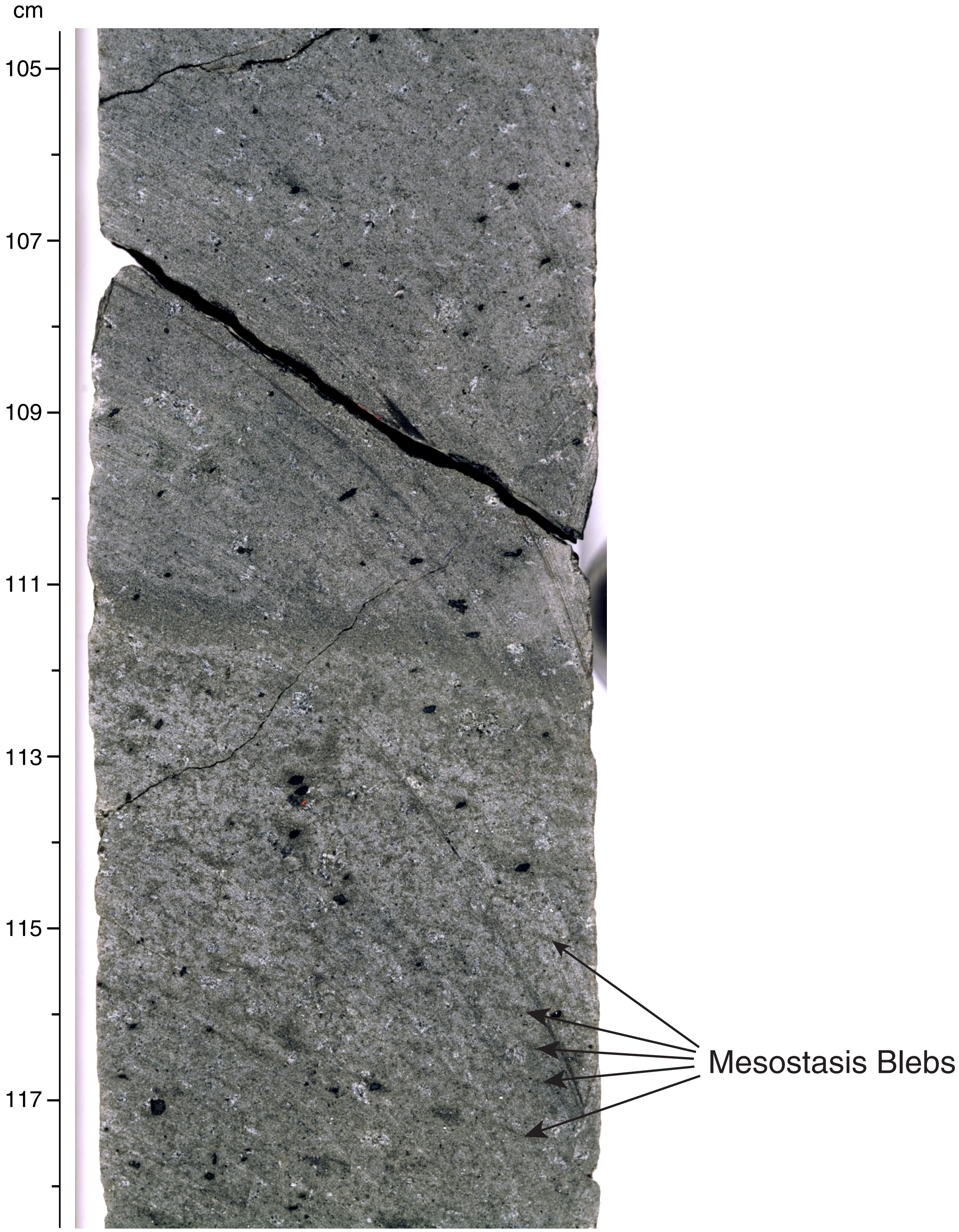

Figure F27. Photograph of Core 183-1137A-39R-2. Note the change from the massive interior of basement Unit 7 to four pieces of breccia and then the poorly recovered coherent top of basement Unit 8. The breccia was placed in Unit 8 on gross similarity, but careful inspection suggests it may actually be a basal breccia for Unit 7.

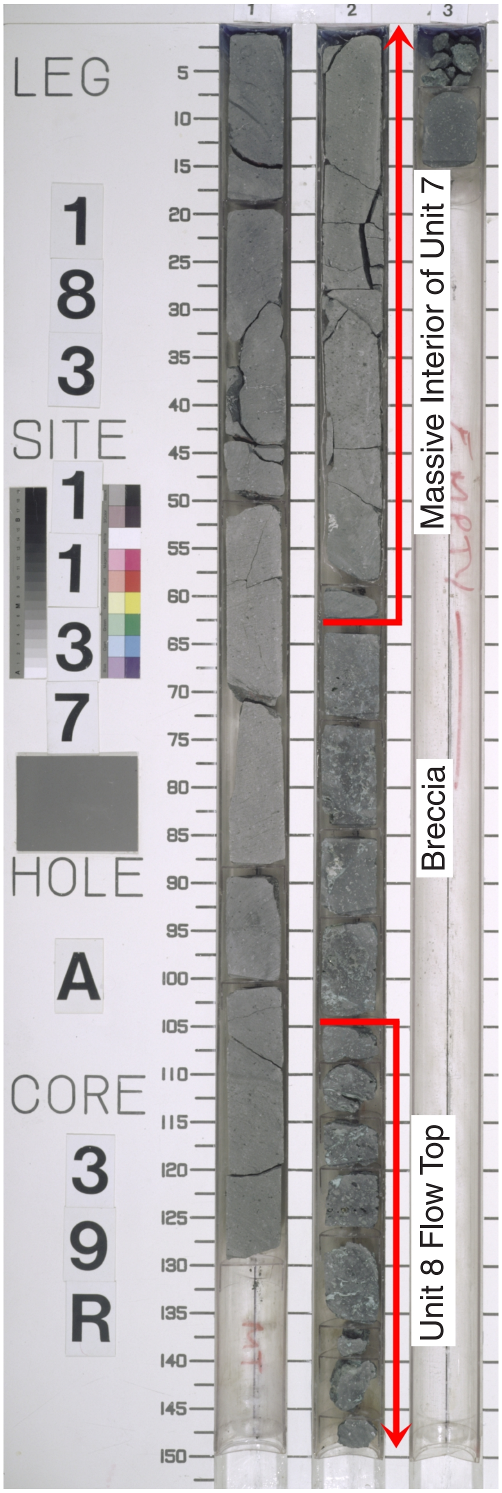

Figure F28. Photomicrograph of Sample 183-1137A-44R-4, 44–46 cm, from near the base of the crystal-vitric tuff in basement Unit 9 showing well-preserved cuspate and tricuspate glass shards. Such shards form during pyroclastic disruption of vesiculating magma. There is no evidence of welding in this interval. Note the embayed margins of sanidine crystals (see **"Igneous Petrology,"** p. 28). Field of view = 1.40 mm (plane-polarized light).

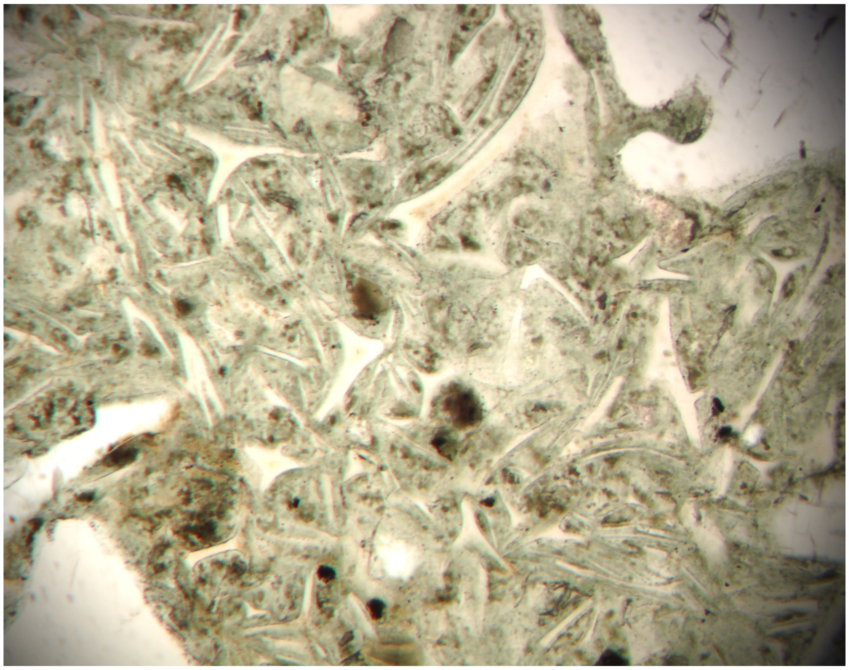

Figure F29. Photomicrograph of Sample 183-1137A-45R-2 (Piece 1A, 7–10 cm) from the breccia at the top of basement Unit 10 showing in situ brecciation of glassy volcanic clasts forming jigsaw-fit textures. Penetrative brecciation could be caused by the dynamic injection of fluidized sediment or a combination of subaerial cooling and mechanical grinding. Field of view = 5.50 mm (plane-polarized light).

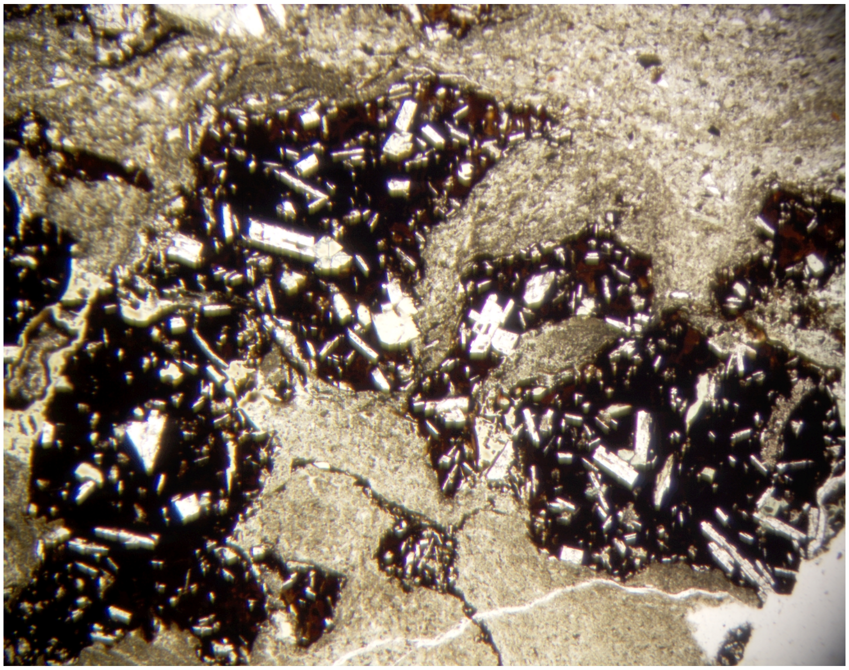

Figure F30. Photomicrograph of Sample 183-1137A-45R-2 (Piece 1A, 7–10 cm) from the breccia at the top of basement Unit 10 showing in situ brecciation of glassy volcanic clasts forming jigsaw-fit textures. Field of view = 1.40 mm (plane-polarized light).

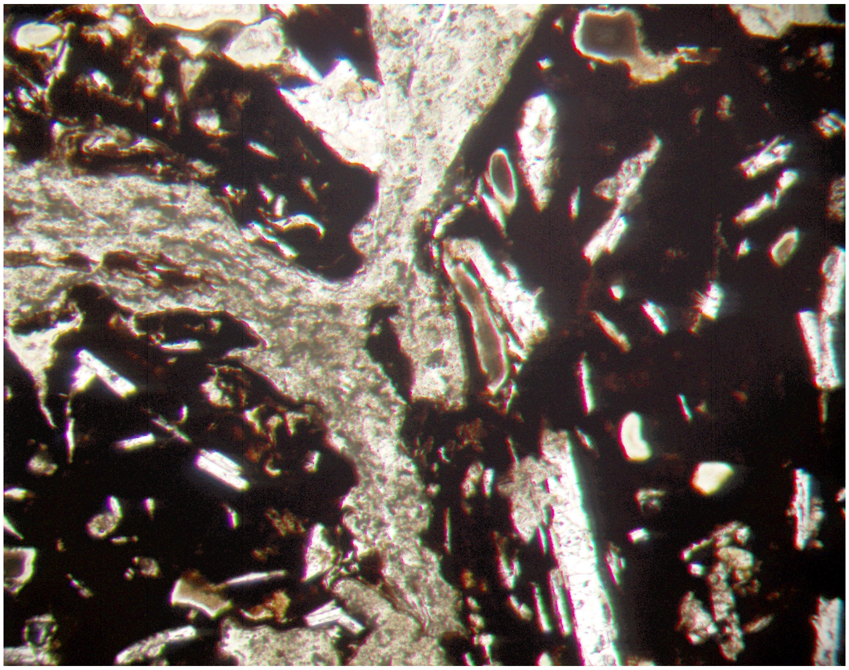

Figure F31. Close-up photograph of interval 183-1137A-45R-2, 10–25 cm, showing the distribution of quench fragmented clasts suspended in the enclosing silty sand (peperitic texture).

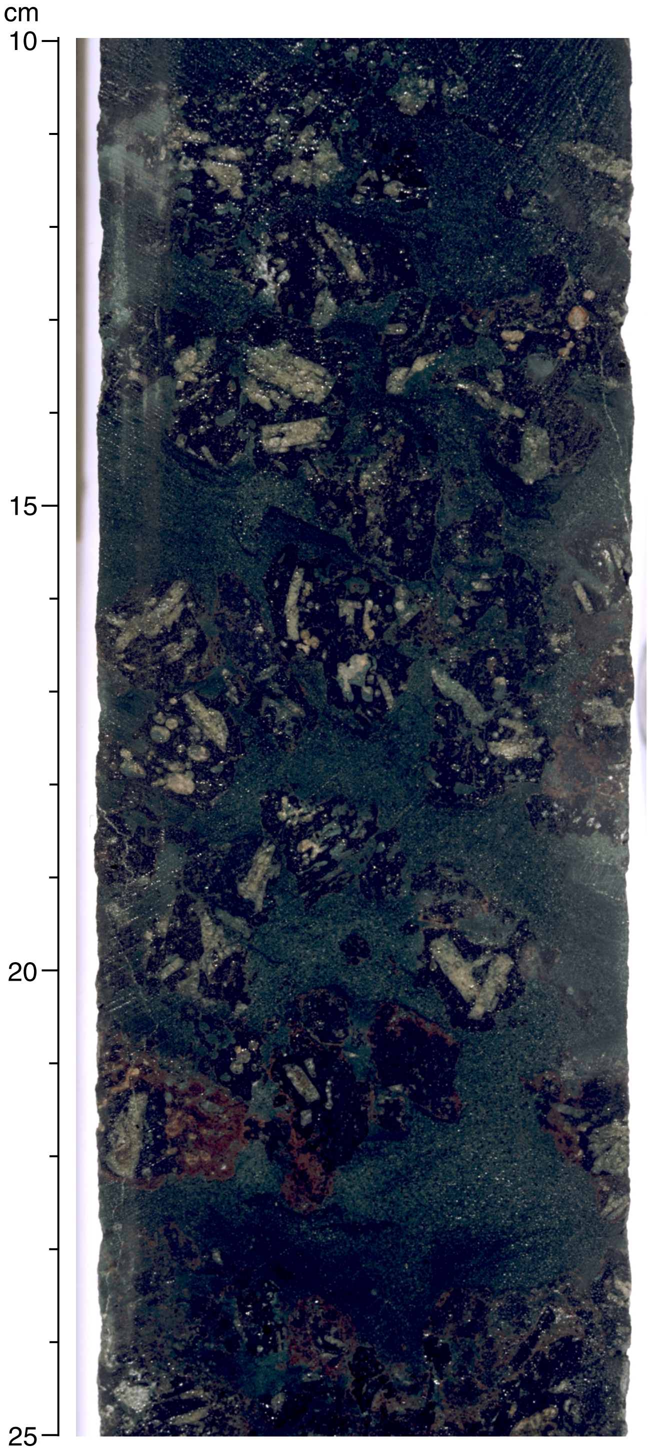

Figure F32. Close-up photograph of interval 183-1137A-45R-2, 43–53 cm, showing oxidized jigsaw-fit dense lava clasts. This is probably an in situ brecciation texture overprinted by oxidation.

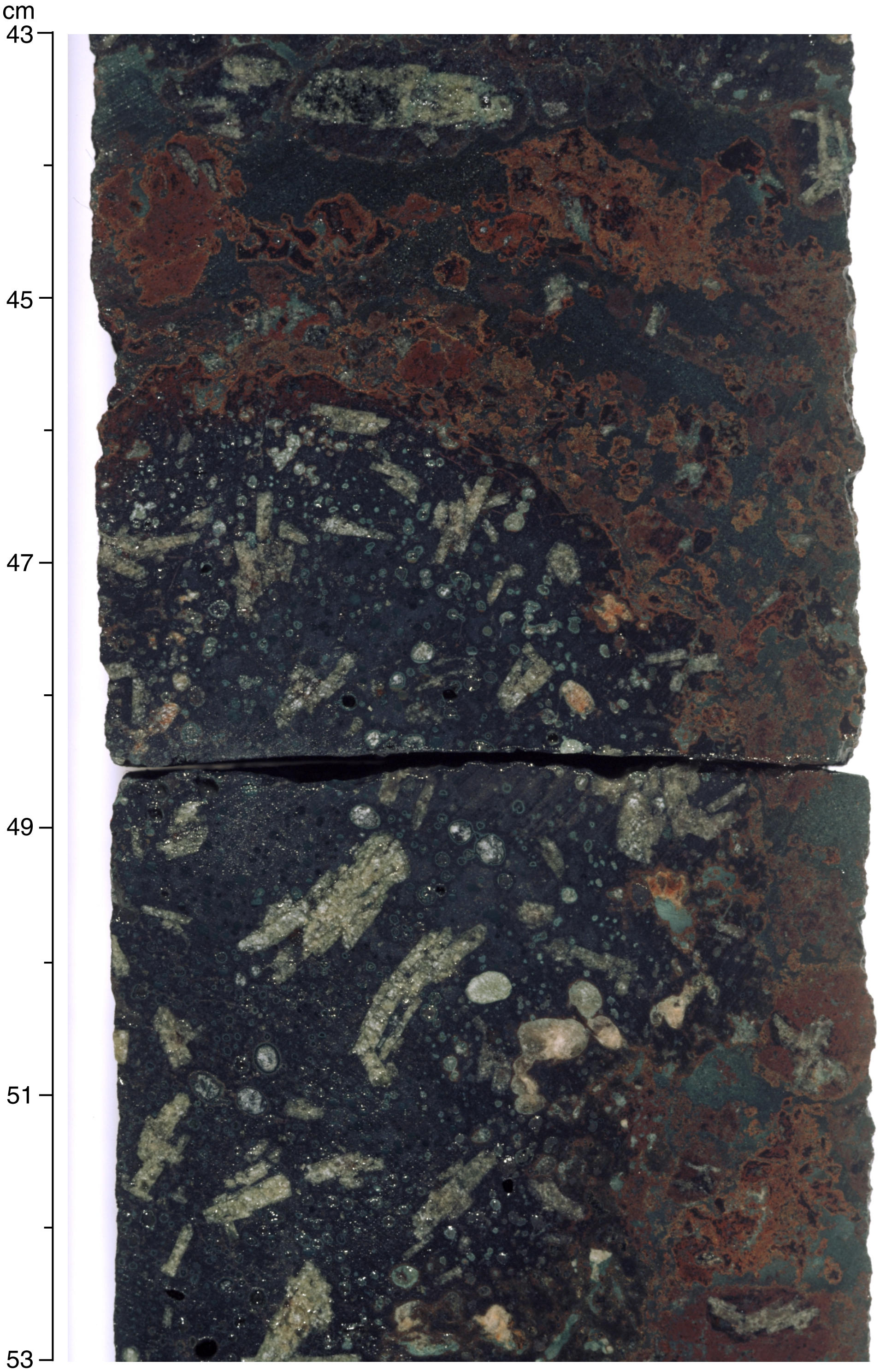

Figure F33. Photomicrograph of Sample 183-1137A-45R-1 (Piece 1, 80–84 cm) showing a constriction through which sediment has flowed into flow-top breccia of basement Unit 10. The sandy silt is either internally massive or it has fine silt distributed around and between clasts, with coarser sand concentrated in stringers or domains of aligned particles farther from clasts. Field of view = 2.75 mm (plane-polarized light).

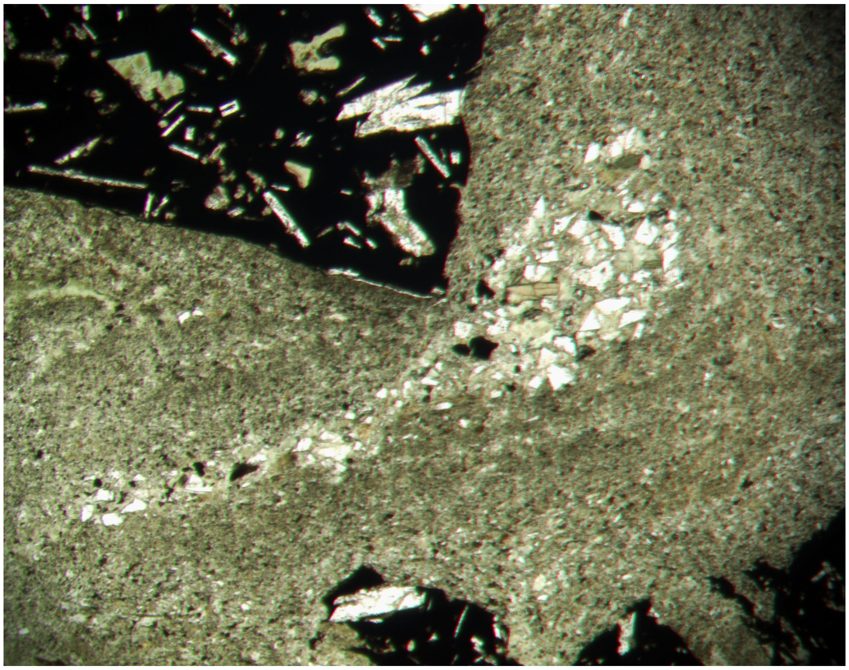

Figure F34. Photomicrograph of Sample 183-1137A-45R-1 (Piece 1, 80–84 cm) from the breccia at the top of basement Unit 10 showing the glassy to aphanitic textures of basaltic clasts. The clasts have angular polygonal shapes with some curviplanar surfaces, and there is evidence of breakage across some crystals and through vesicles. However, breakage seems to preferentially take place through the glassy parts of the basalt. Penetrative brecciation can be caused by the dynamic injection of fluidized sediment disrupting quenched clasts. Field of view = 2.75 mm (plane-polarized light).

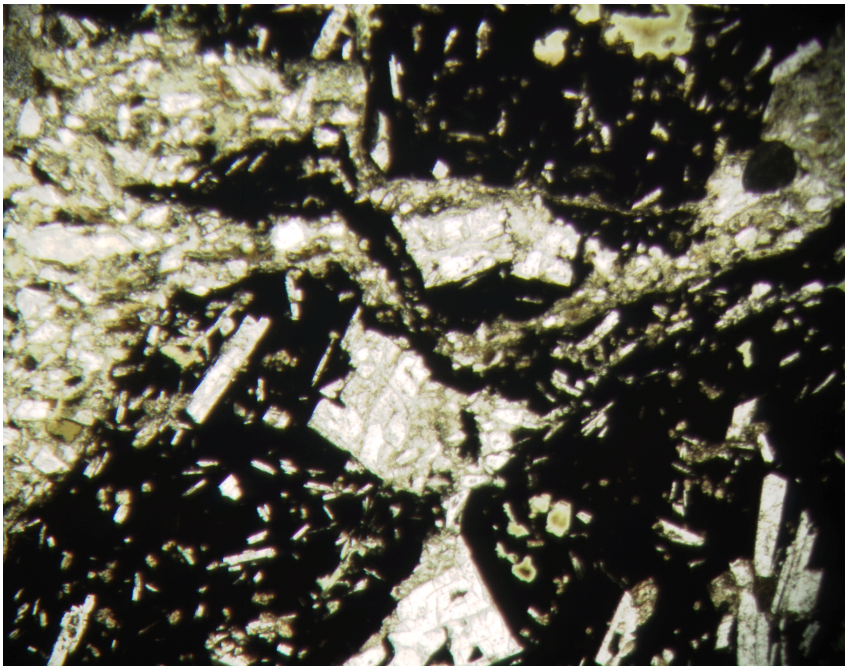

Figure F35. Interpretative summary lithology and some key chemical and physical properties of the volcanic and sedimentary rocks sampled at Site 1137. The depth scale on the left shows the curated positions of the 10 basement units. The depth scale on the right shows the positions inferred from core-log integration (see **"Physical Volcanology,"** p. 13, **"Downhole Measurements,"** p. 54). Vesicularity, degree of alteration, and loss on ignition indicate macroscopic characteristics and level of preservation of the volcanic rocks. Mg# = (molar MgO/[MgO + 0.80 × total FeO]), and Cr contents demonstrate downhole variations in chemical composition.

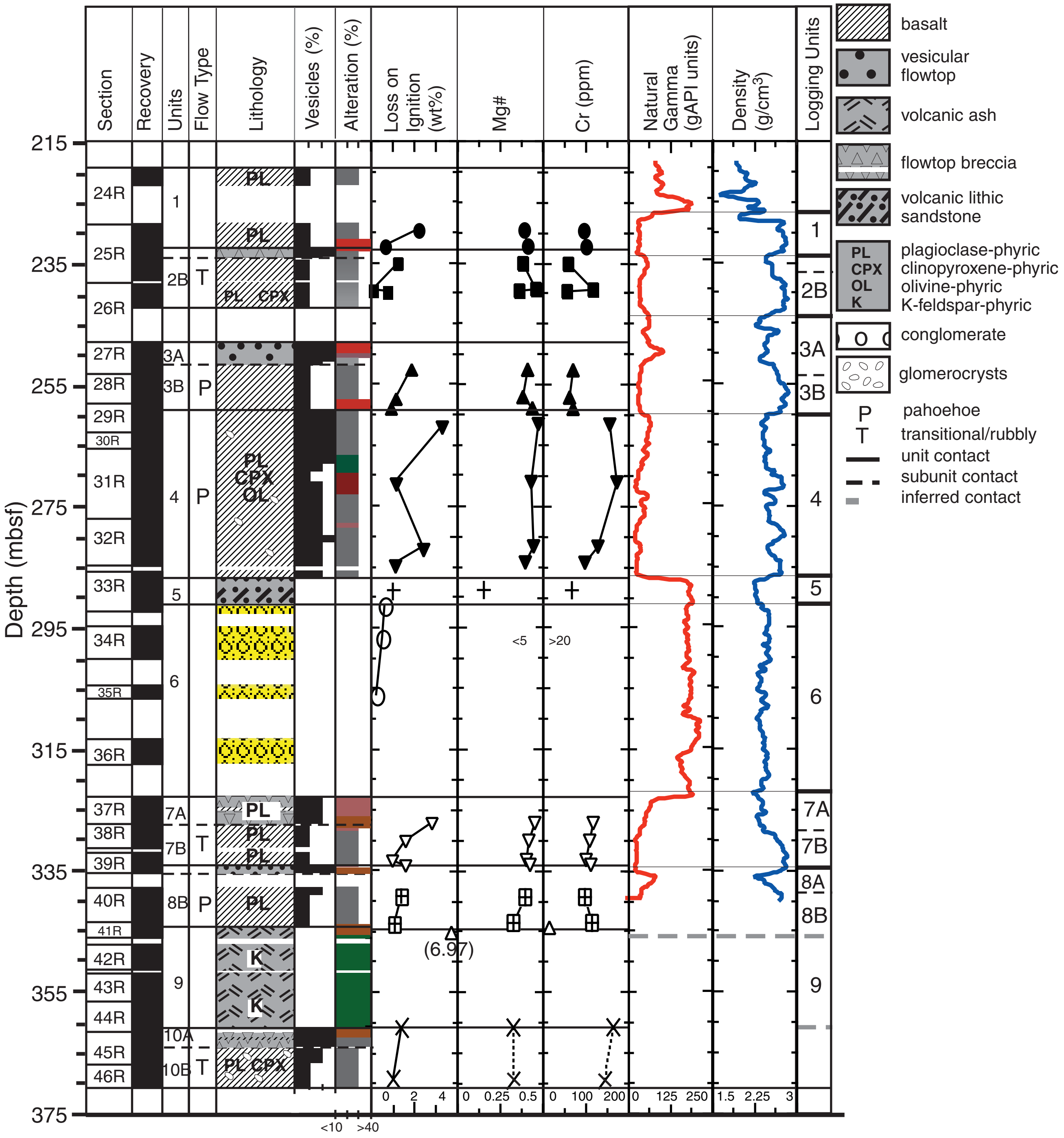

Figure F36. Phenocryst and glomerocryst abundance variations in the basaltic units with depth below the seafloor. As the glomerocrysts are primarily plagioclase, we grouped them with the discrete plagioclase phenocrysts.

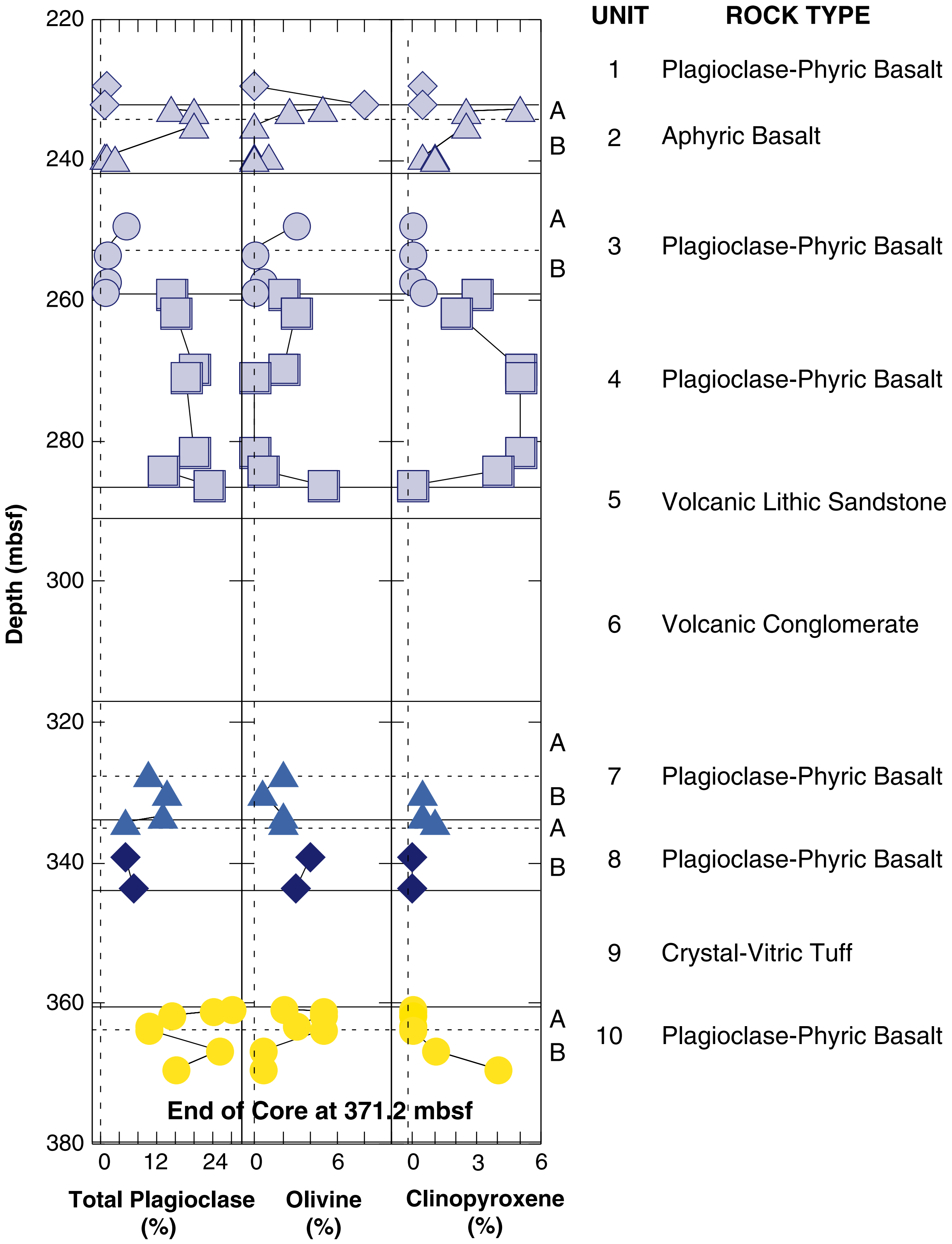

Figure F37. Photomicrograph of plagioclase phenocryst from Unit 4 (Sample 183-1137A-32R-7, 48–50 cm) with sieve texture and plagioclase reaction rim in cross-polarized light; field of view width = 2.75 mm.

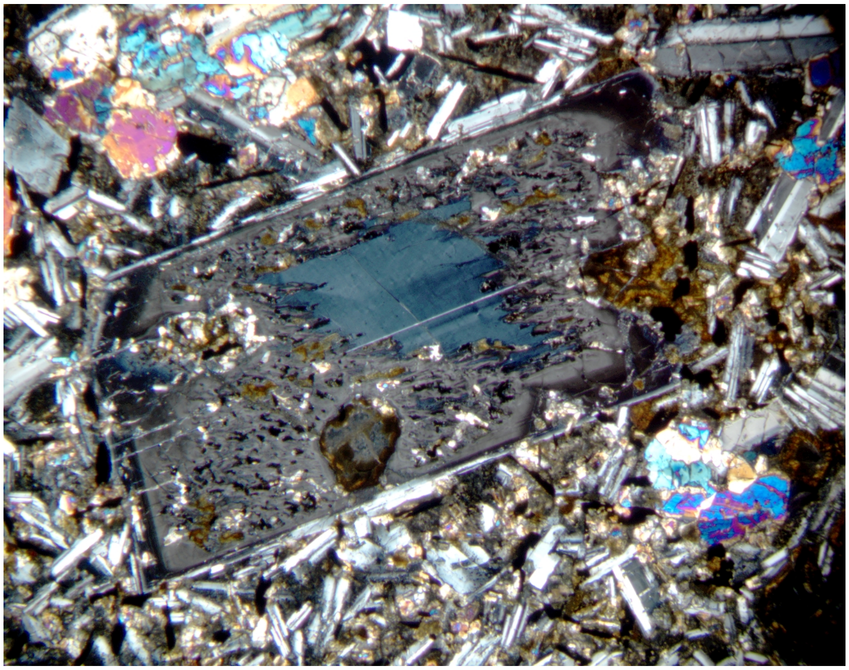

Figure F38. Photomicrograph of a plagioclase glomerocryst from Subunit 10B (Sample 183-1137A-41R-1, 68–73 cm) exhibiting oscillatory zonation in cross-polarized light; field of view width = 1.4 mm.

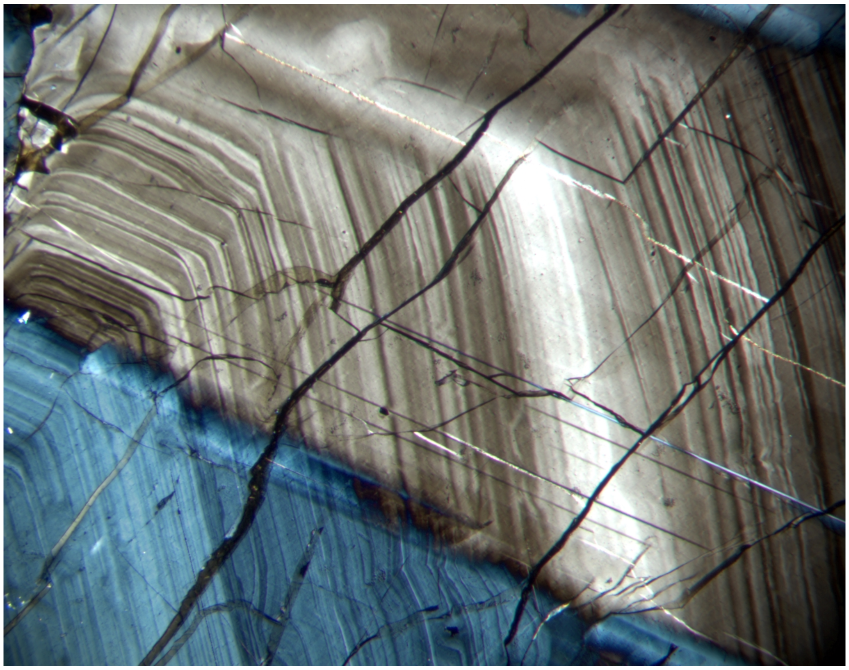

Figure F39. Photomicrograph of the microgabbro xenolith from Unit 2B (Sample 183-1137A-26R-1, 140–142 cm) in cross-polarized light; field of view width = 5.5 mm.

Figure F40. Photomicrograph of a highly altered plagioclase phenocryst from Subunit 10A (Sample 183-1137A-45R-1, 80–82 cm). Albite twinning has been destroyed, but a Carlsbad twin is preserved. The image is in cross-polarized light; field of view width = 5.5 mm.

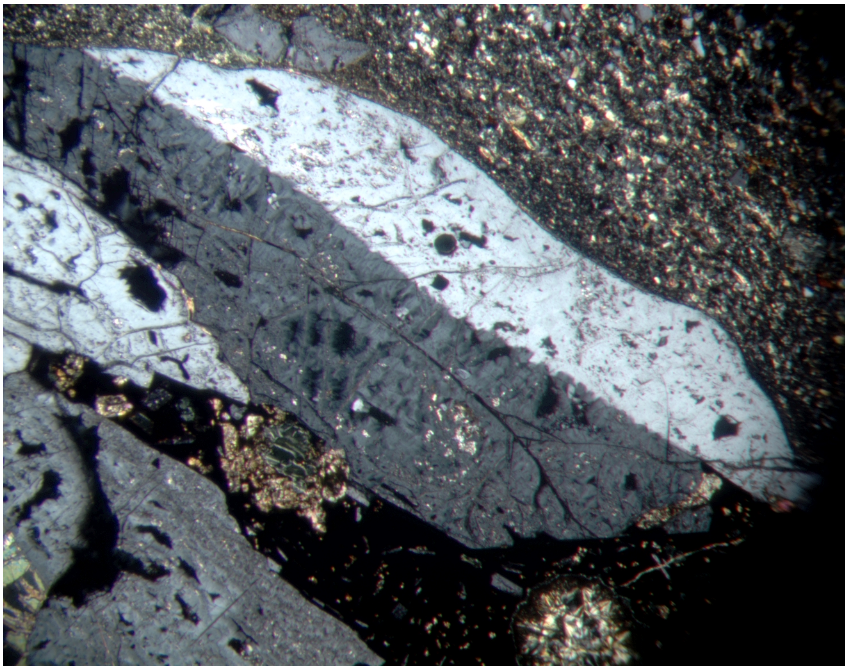

Figure F41. Photomicrographs of altered olivine (Ol). We see similar clay pseudomorphs after olivine throughout the basalt units, especially in the margins of flows. **A.** Typical chilled margin (Sample 183-1137A-25R-3, 90–93 cm, base of Unit 1). **B.** Least-altered chilled margin (Sample 183-1137A-29R-2, 71–74 cm, top of Unit 4). Both images are in plane-polarized light; field of view width = 1.4 mm.

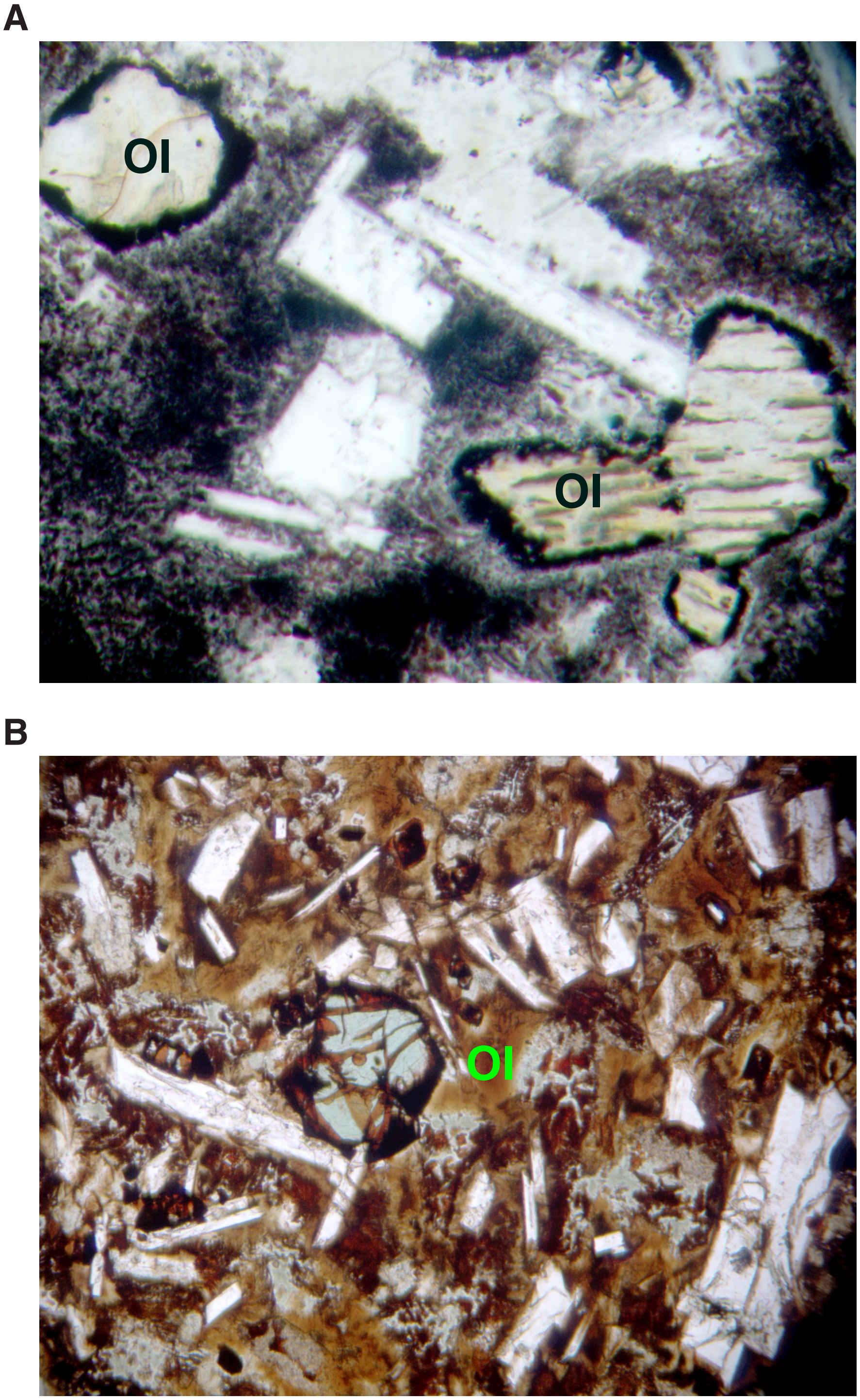

Figure F42. Photomicrograph of ilmenite exsolution in titanomagnetite in Unit 2B (Sample 183-1137A-25R-5, 113–115 cm) in reflected light; field of view width = 0.14 mm.

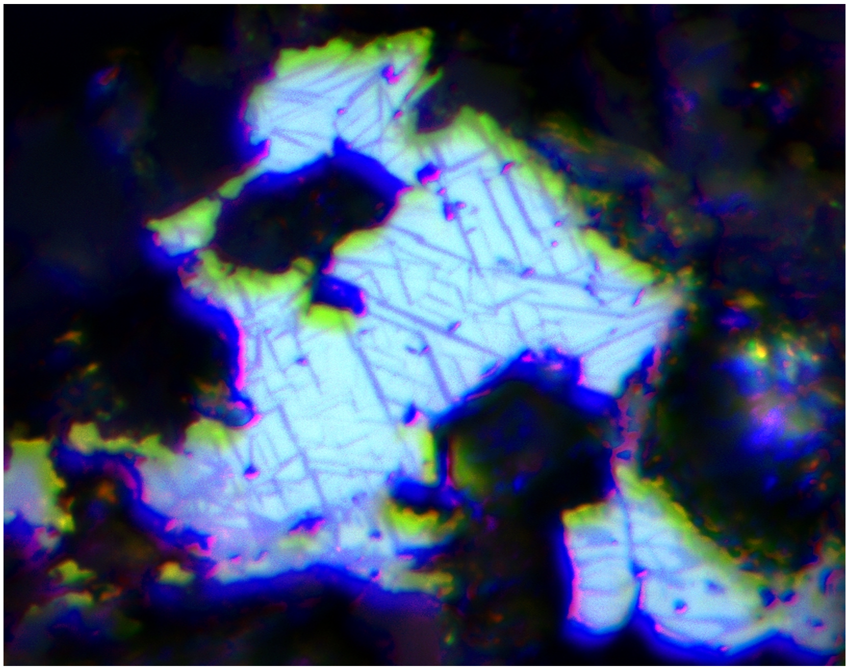

Figure F43. Photomicrograph of pentlandite (Pent) in vein segregation in Unit 2B (Sample 183-1137A-26R-2, 38–40 cm) in reflected light; field of view width = 1.4 mm.

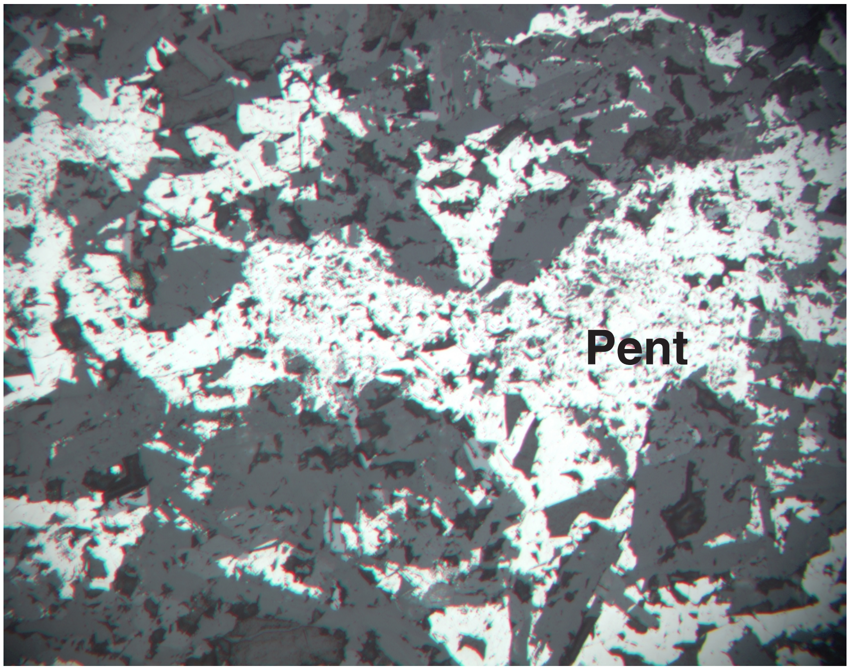

Figure F44. Four photomicrographs of garnet (gt) and brown hornblende (hb) grains in the volcanic sandstone of Unit 5 (Sample 183-1137A-33R-3, 50–53) all in plane-polarized light; each field of view = 1.4 mm.

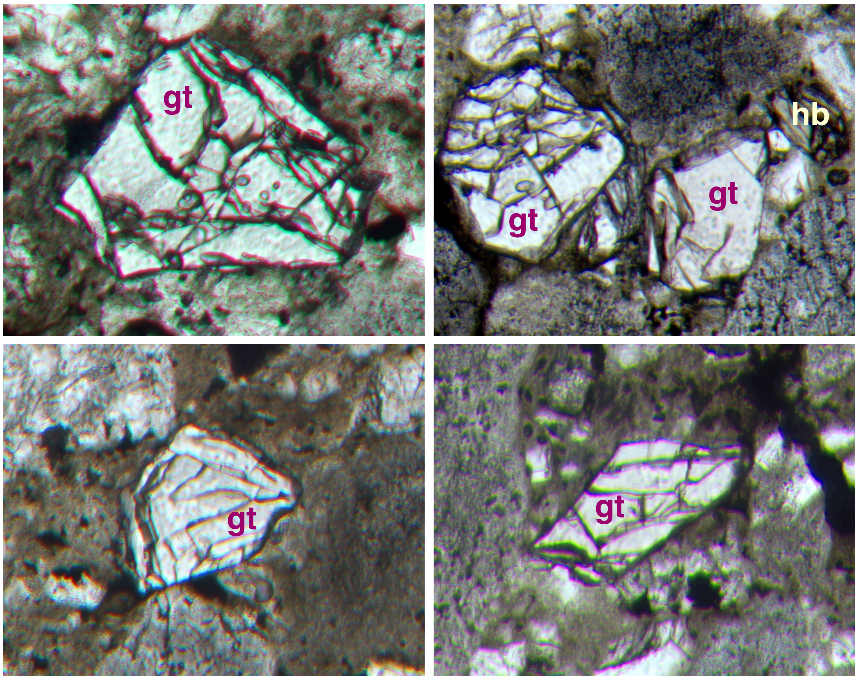

Figure F45. Photomicrographs of plagioclase phenocrysts with continuous feldspar overgrowths in a massive trachyte from Unit 6 (clast in conglomerate, Sample 183-1137A-33R-5, 10–12 cm). **A.** Sodic plagioclase rim, sieve texture. **B.** Alkali felspar rim. The images are in cross-polarized light; field of view width = 2.75 mm.

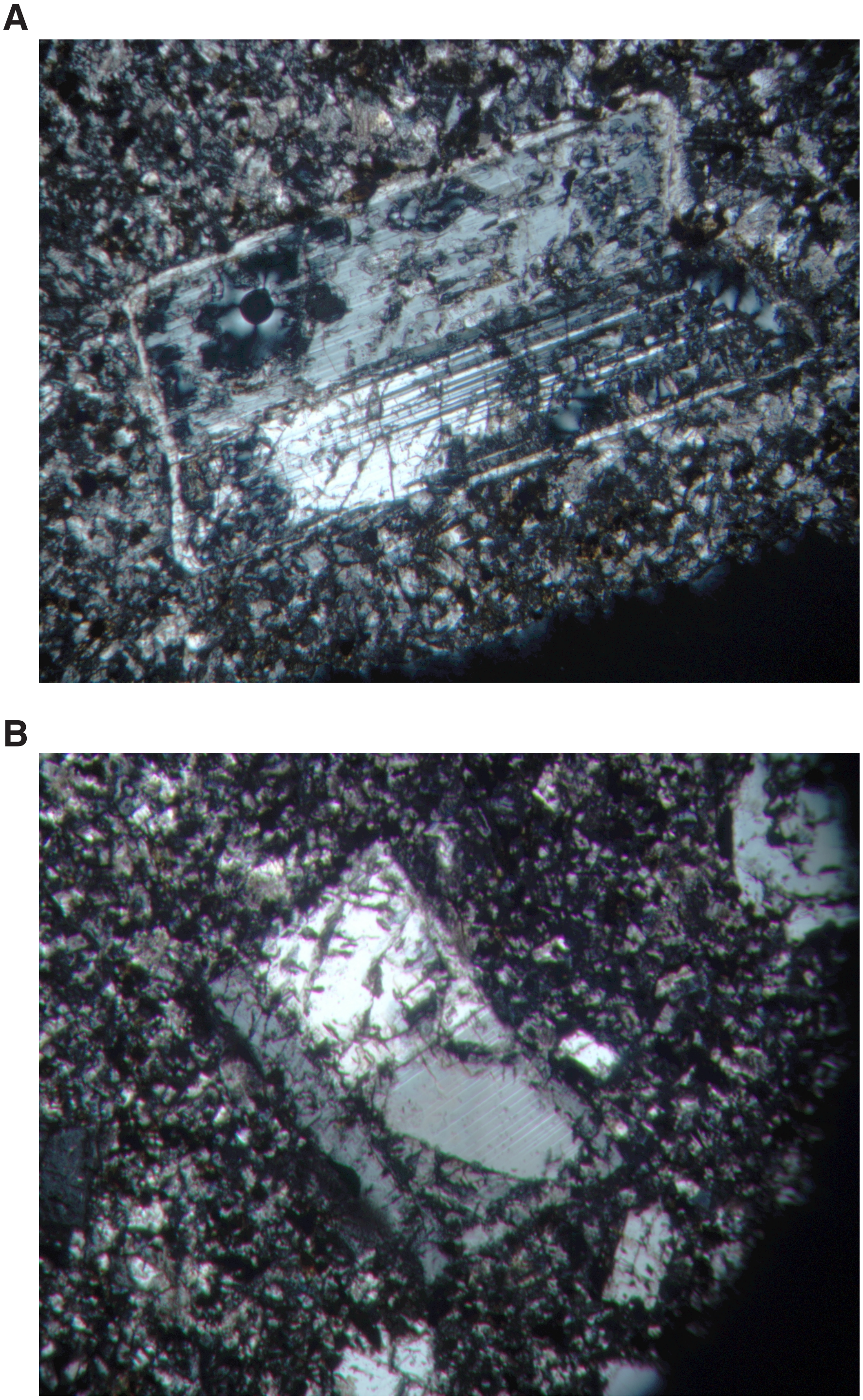

Figure F46. Photomicrograph of flow-banded texture around sanidine phenocryst in the flow-banded rhyolite in Unit 6 (clast in conglomerate, Sample 183-1137A-34R-2, 113–117 cm). Note the microspherulites in the darker bands. The image is in plane-polarized light; field of view width = 1.4 mm.

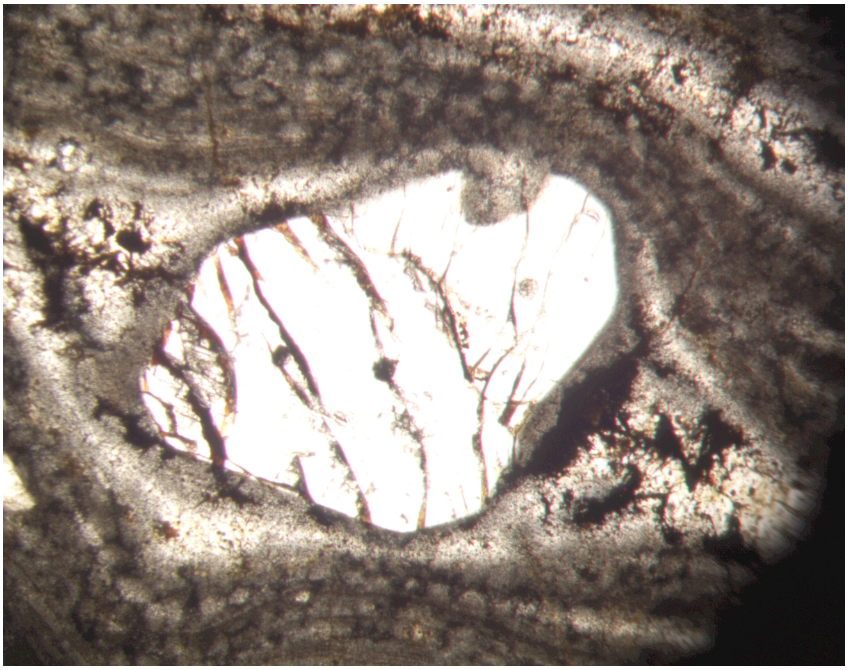

Figure F47. Photomicrograph of symplectite intergrowths between plagioclase and alkali feldspar in a granite clast from the base of Unit 6 conglomerate (Sample 183-1137A-35R-2, 66–89 cm) in cross-polarized light; field of view width = 5.5 mm.

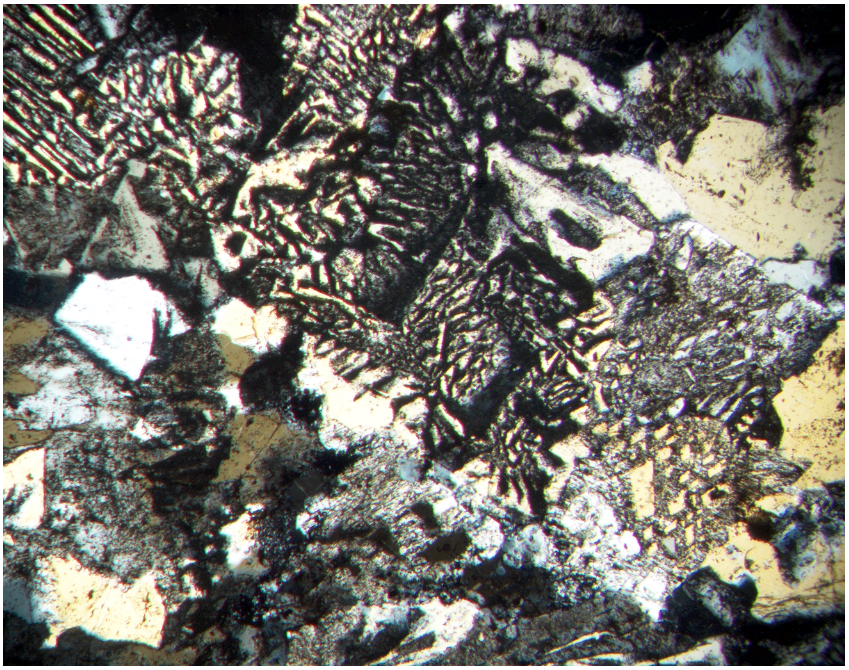

Figure F48. Photomicrographs of garnet-biotite gneiss. **A.** Poikiloblastic garnet (gt) in Unit 6 (clast in conglomerate, Sample 183-1137A-35R-2, 46–47 cm) in plane-polarized light; field of view width = 1.4 mm. **B.** Porphyroblastic garnet (gt) and biotite (bi) from Unit 9 (clast in tuff, Sample 183-1137A-44R-4, 44–46 cm) in plane-polarized light; field of view width = 2.8 mm.

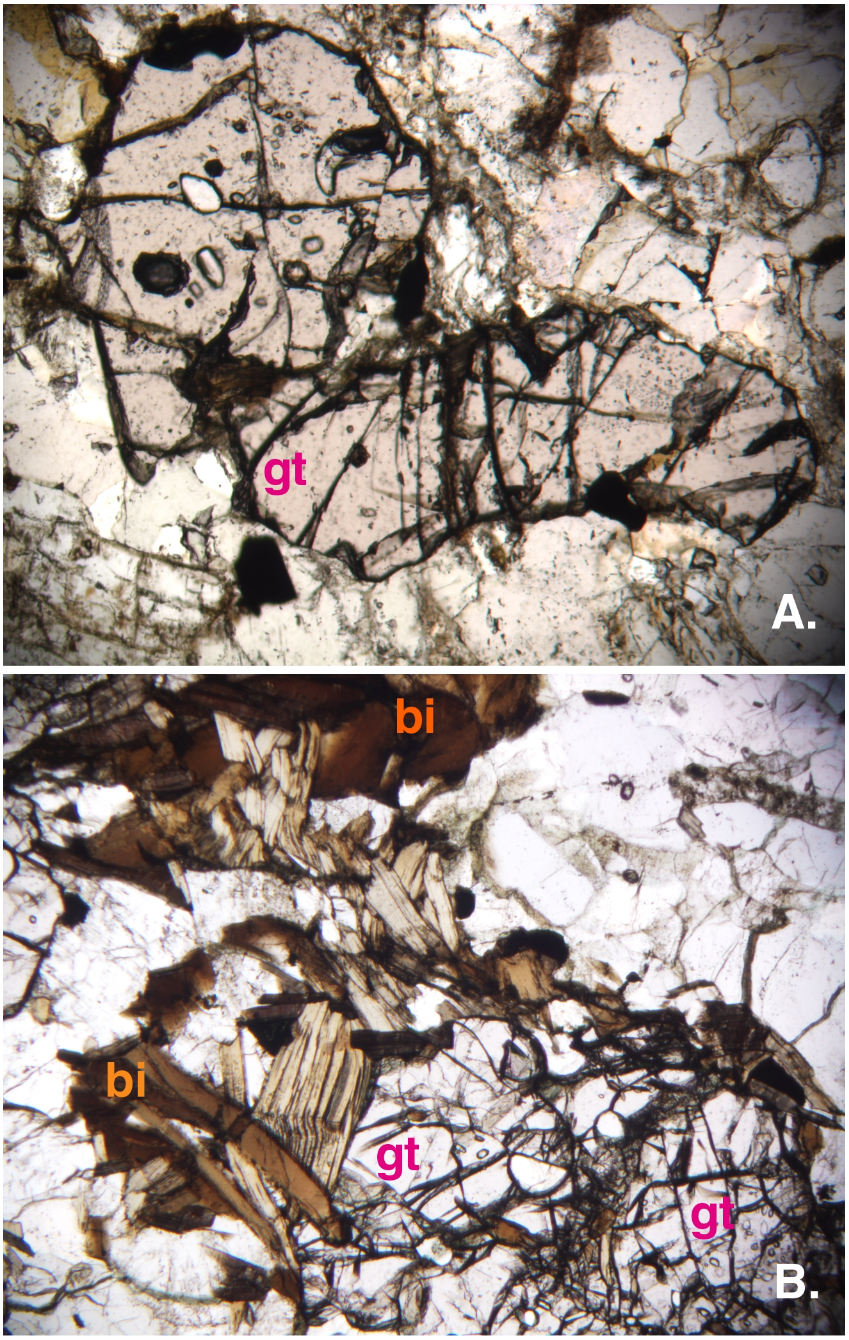

Figure F49. Photomicrograph of actinolite (Act) and microcline (Mic) in the actinolite-bearing gneiss in Unit 6 (clast in conglomerate, Sample 183-1137A-34R-2, 100–103 cm) in cross-polarized light; field of view width = 2.75 mm.

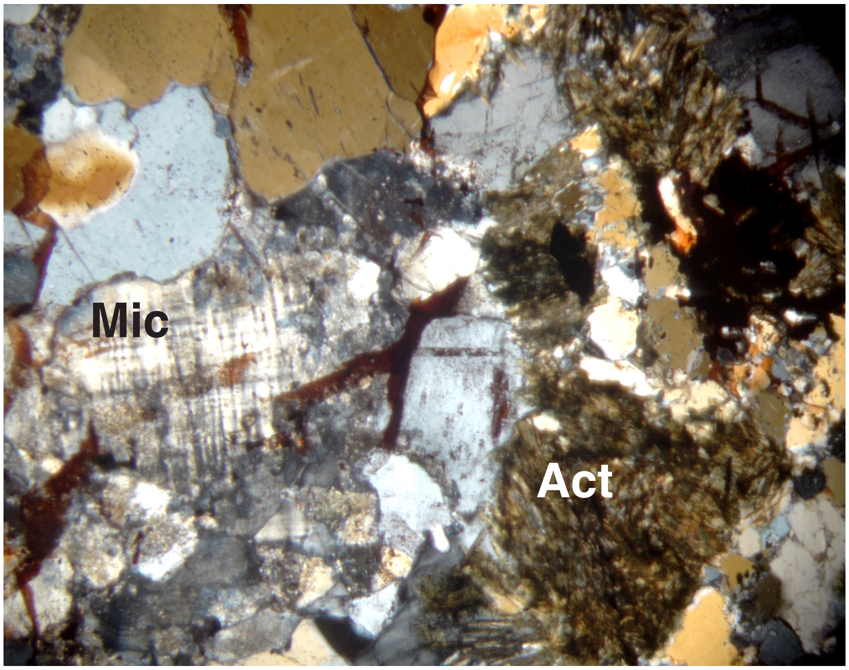

Figure F50. Photomicrograph of a deeply embayed quartz crystal in Unit 9 tuff (Sample 183-1137A-41R-3, 42–46 cm). The outlines of glass shards in the matrix can be seen. The image is in plane-polarized light; field of view width = 2.75 mm.

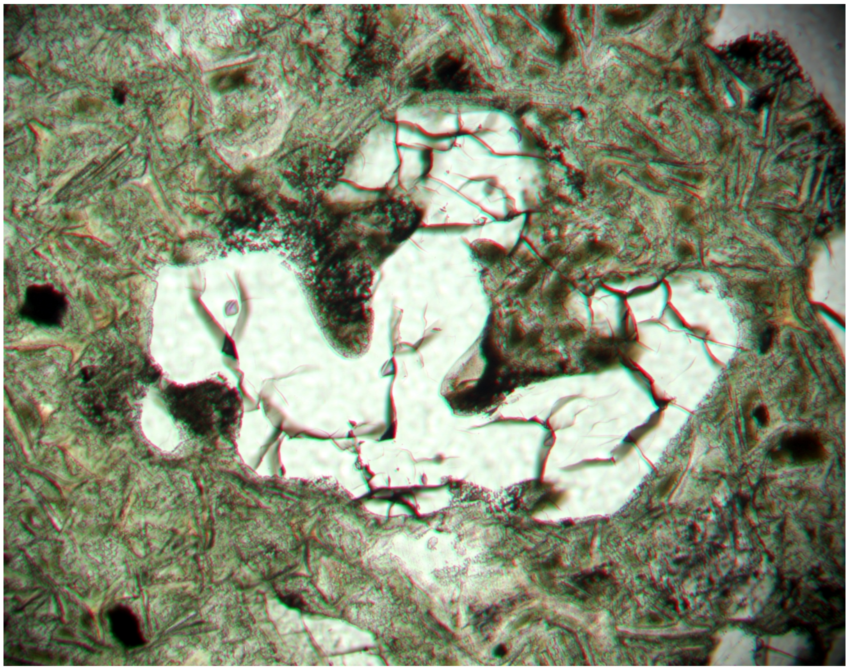

Figure F51. Photomicrograph of a fractured sanidine phenocryst from Unit 9 tuff (Sample 183-1137A-44R-4, 6–9 cm). The outlines of glass shards in the matrix can be seen. The image is in plane-polarized light; field of view width = 2.75 mm.

Figure F52. Photomicrograph of melt inclusions in sanidine crystals from Unit 9 (Sample 183-1137A-44R-4, 44–46 cm) in plane-polarized light; field of view width = 0.275 mm.

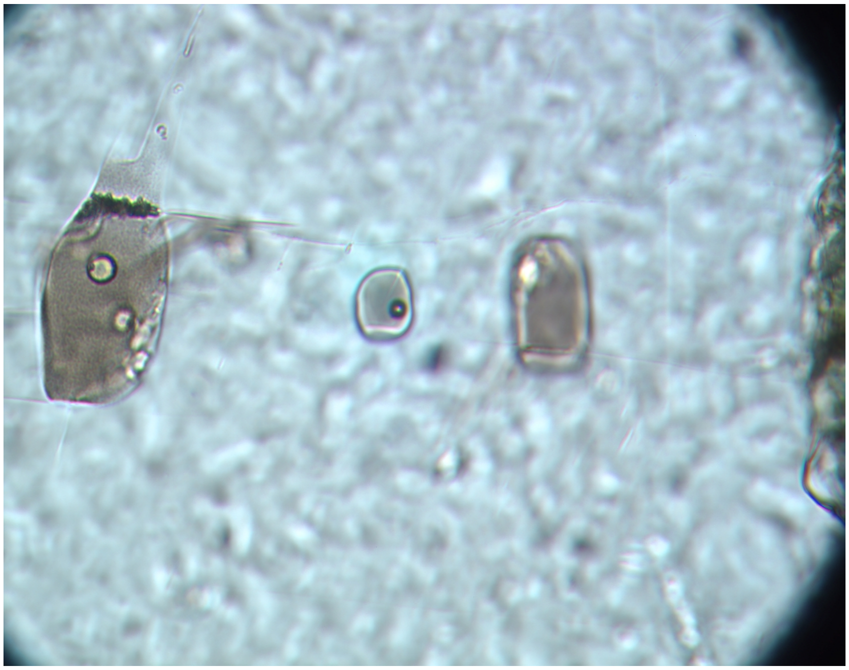

Figure F53. Photomicrographs highlighting the breakdown of mafic crystals in the Unit 9 tuff (Sample 183-1137A-41R-3, 42–44 cm). **A.** Original biotite (Bi) has been replaced by relatively well-crystallized clay; inclusions of titanomagnetite, zircon (Zr), and kaersutite are common. A quartz crystal (Q) is just below the altered biotite; note titanomagnetite and zircon in the large sanidine crystal (S) in the upper right hand corner. The image is in plane-polarized light; field of view width = 2.75 mm. **B.** Isolated kaersutite (Ka), zircon, and titanomagnetite, and perhaps a relic biotite (Bi). The image is in plane-polarized light; field of view width = 1.4 mm.

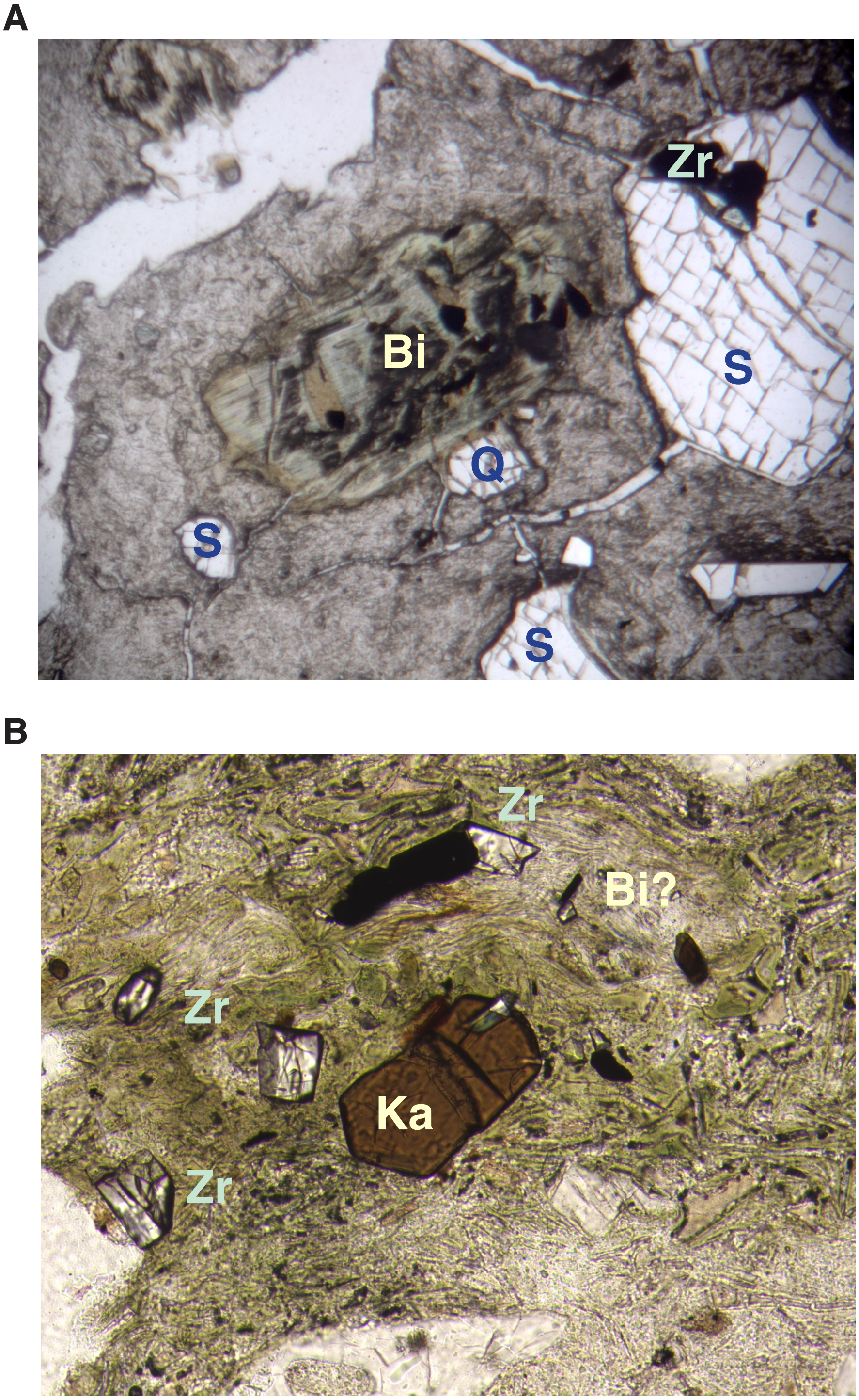

Figure F54. Total alkalis ($Na_2O + K_2O$) vs. SiO_2 abundance. **A.** Site 1137 basalts compared to those from other parts of the Kerguelen Plateau. The boundary between tholeiitic and alkalic basalts from Macdonald and Katsura (1964). The more altered Site 1137 basalts plot distinctly above the general field for Site 1137 because of higher alkali content. Data sources are Davies et al. (1989), Weis et al. (1989), Alibert (1991), Mehl et al. (1991), Salters et al. (1992), Storey et al. (1992), Mahoney et al. (1995), and this study. **B.** Site 1137 basalts and more evolved rocks; chemical classification and nomenclature of Le Bas et al. (1986).

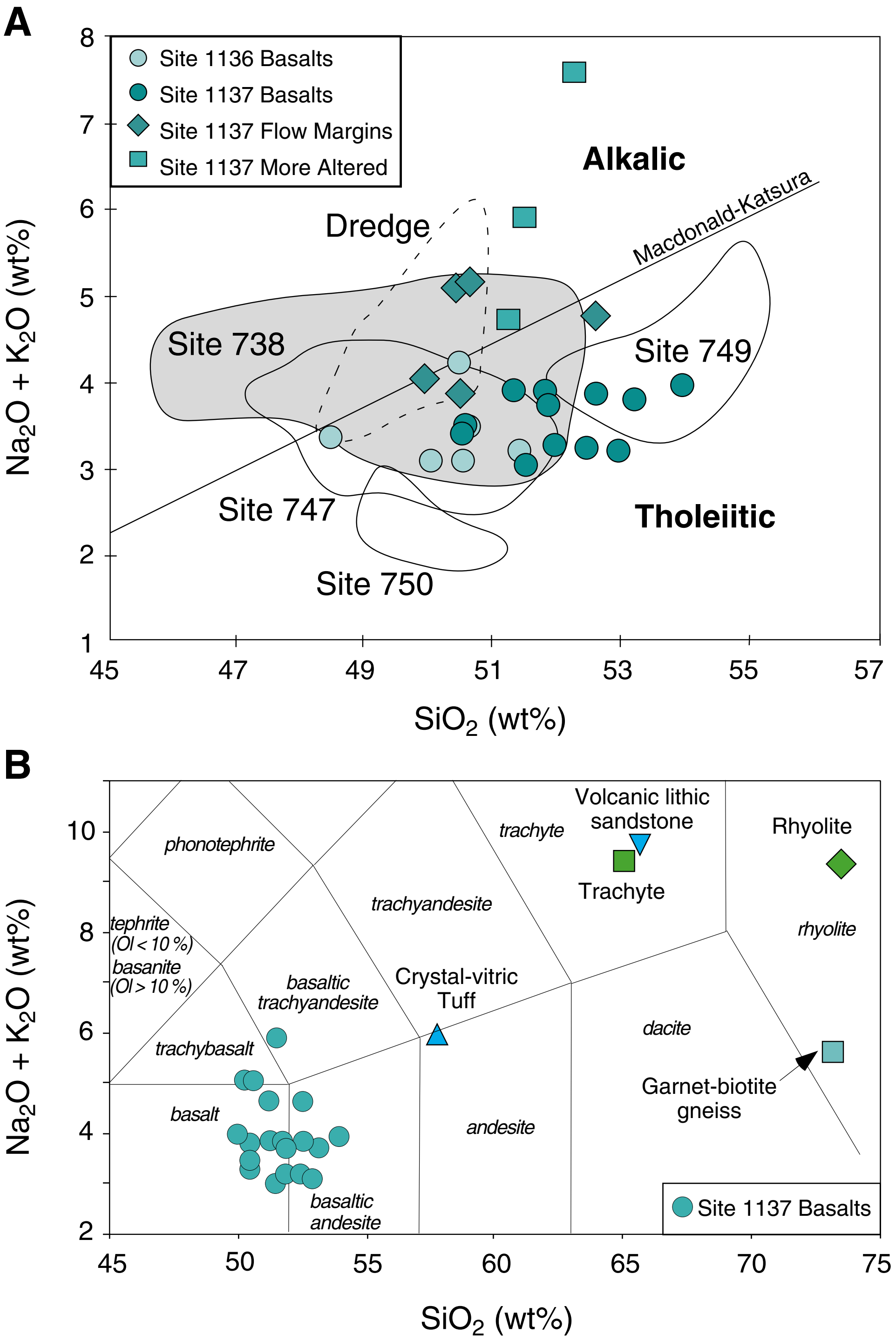

Figure F55. Major and trace element variation diagrams vs. MgO comparing basalts from Site 1137 with those from other parts of the Kerguelen Plateau (data sources listed in Fig. F54, p. 117).

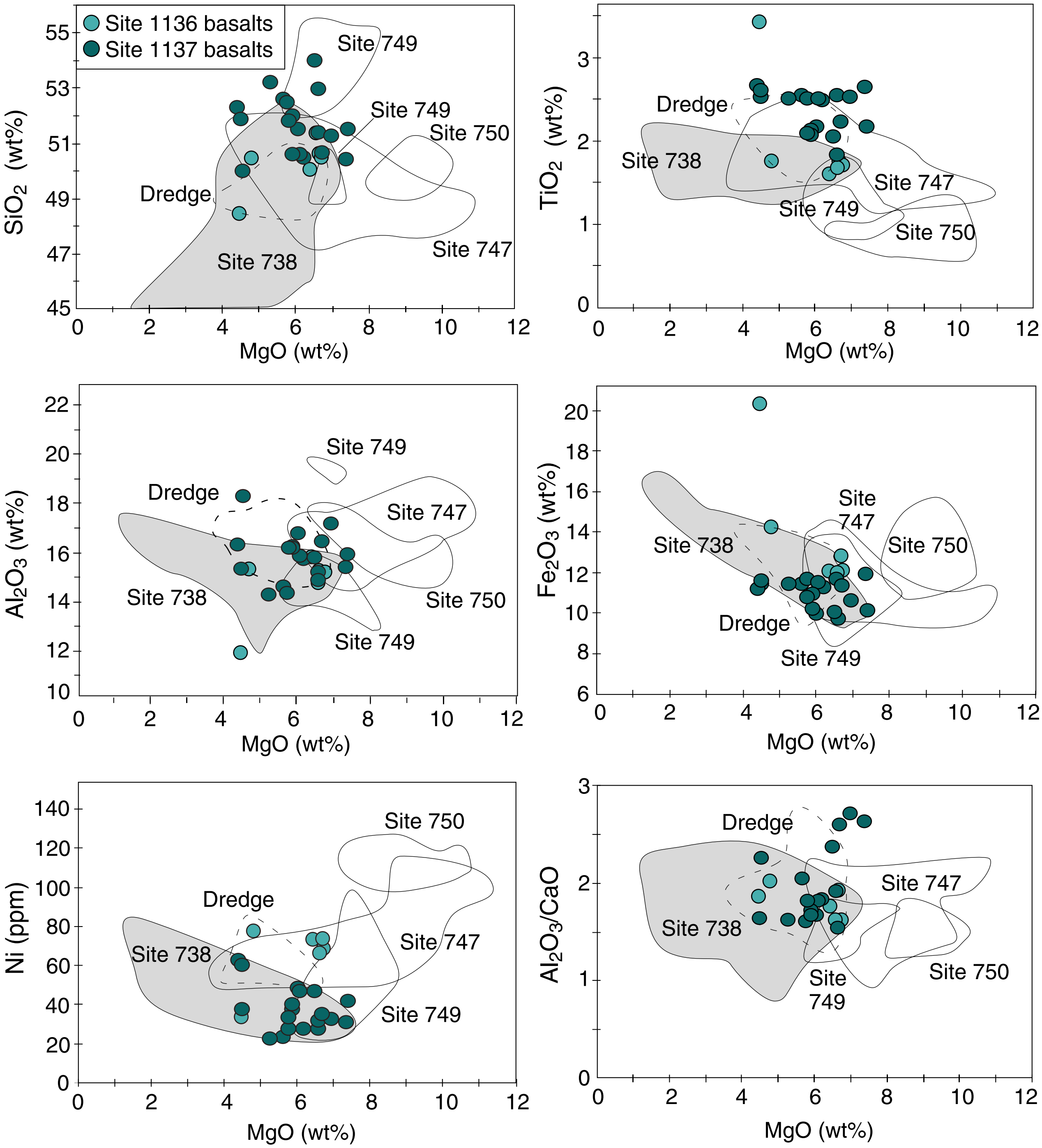

Figure F56. Trace element contents of basalts from Site 1137 normalized to primitive mantle values of Sun and McDonough (1989). All Site 1137 basalts are enriched in incompatible elements. The wide range of Rb and K shows the mobility of these elements during postmagmatic alteration. **A.** All basalt samples from Units 1–4 from Site 1137. **B.** All basalt samples from Units 7, 8, and 10 from Site 1137. **C.** Least-altered samples from Units 1–4 from Site 1137. **D.** Least-altered samples from Units 7, 8, and 10 from Site 1137. (Continued on next page.)

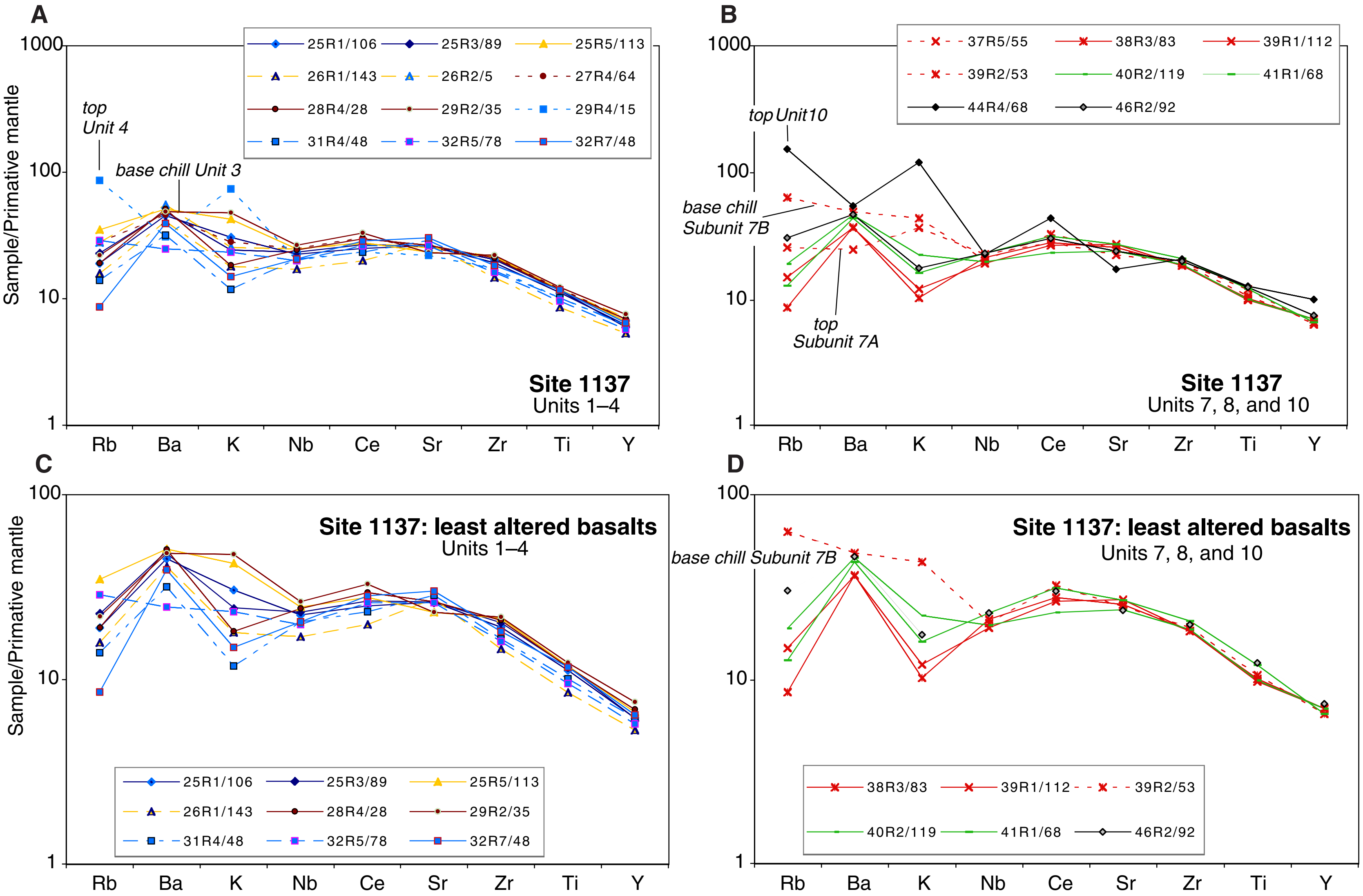

Figure F56 (continued). E. Evolved volcanic and volcaniclastic rocks and garnet gneiss compared with the field for the seven flow interiors of Site 1137 basalts. Note the change of scale. **F.** Altered basalts and other samples from Site 1137.

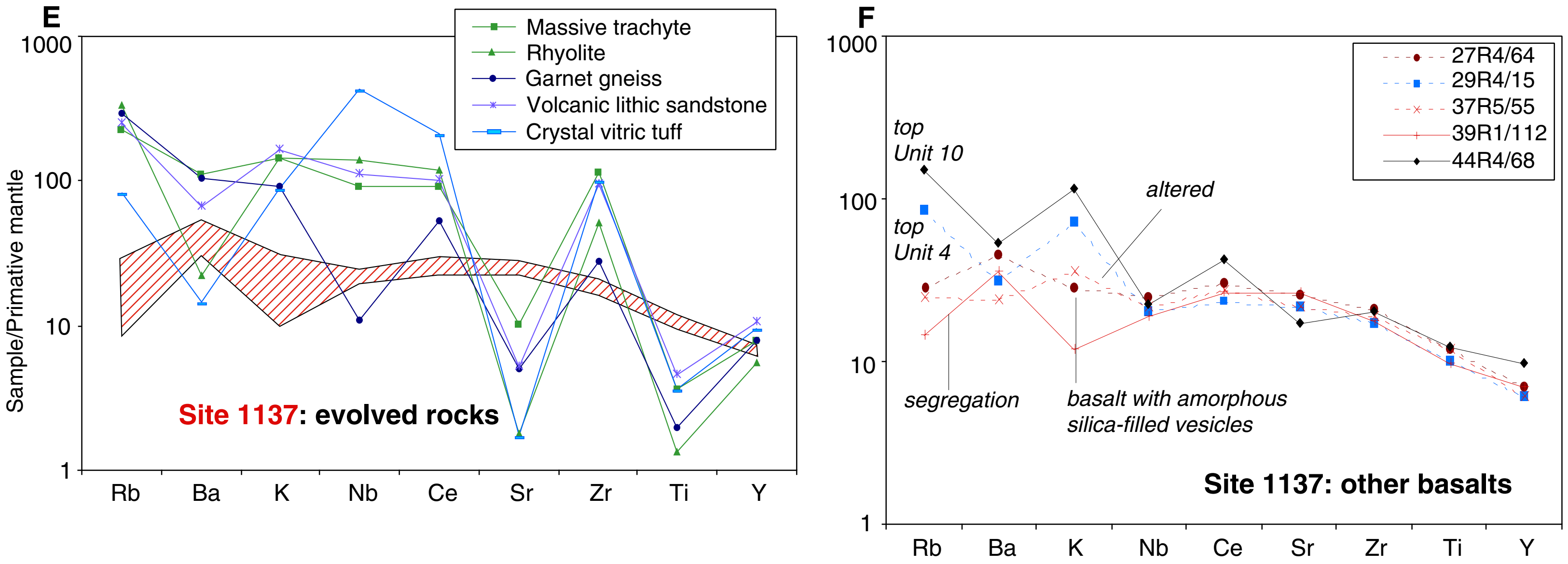

Figure F57. A. Variations of major and trace element abundances and Mg# (Mg# = molar MgO/[MgO + FeO]) with depth in Hole 1137A. Each flow unit is represented by a different symbol. Open symbols represent altered samples and down-pointing triangles represent a xenolith and a melt segregation. Depths correspond to the curated depth in mbsf. (Continued on next page.)

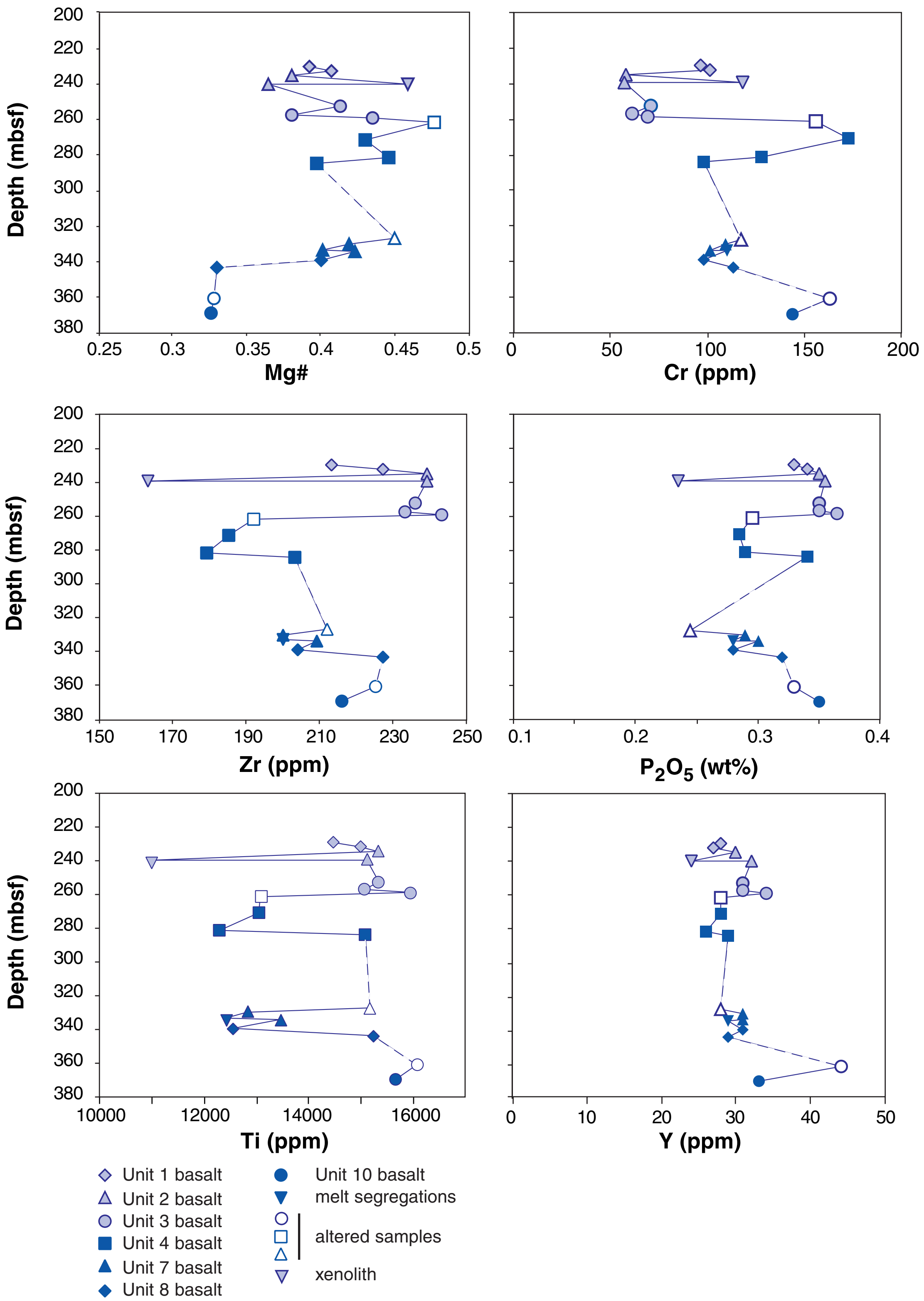

Figure F57 (continued). B. Variations of trace element ratios normalized to primitive mantle values of Sun and McDonough (1989), for basalts from Site 1137, three clasts in the conglomerate, the lithic volcanic sandstone, and the crystal vitric tuff, plotted against depth in the basement section of Hole 1137A.

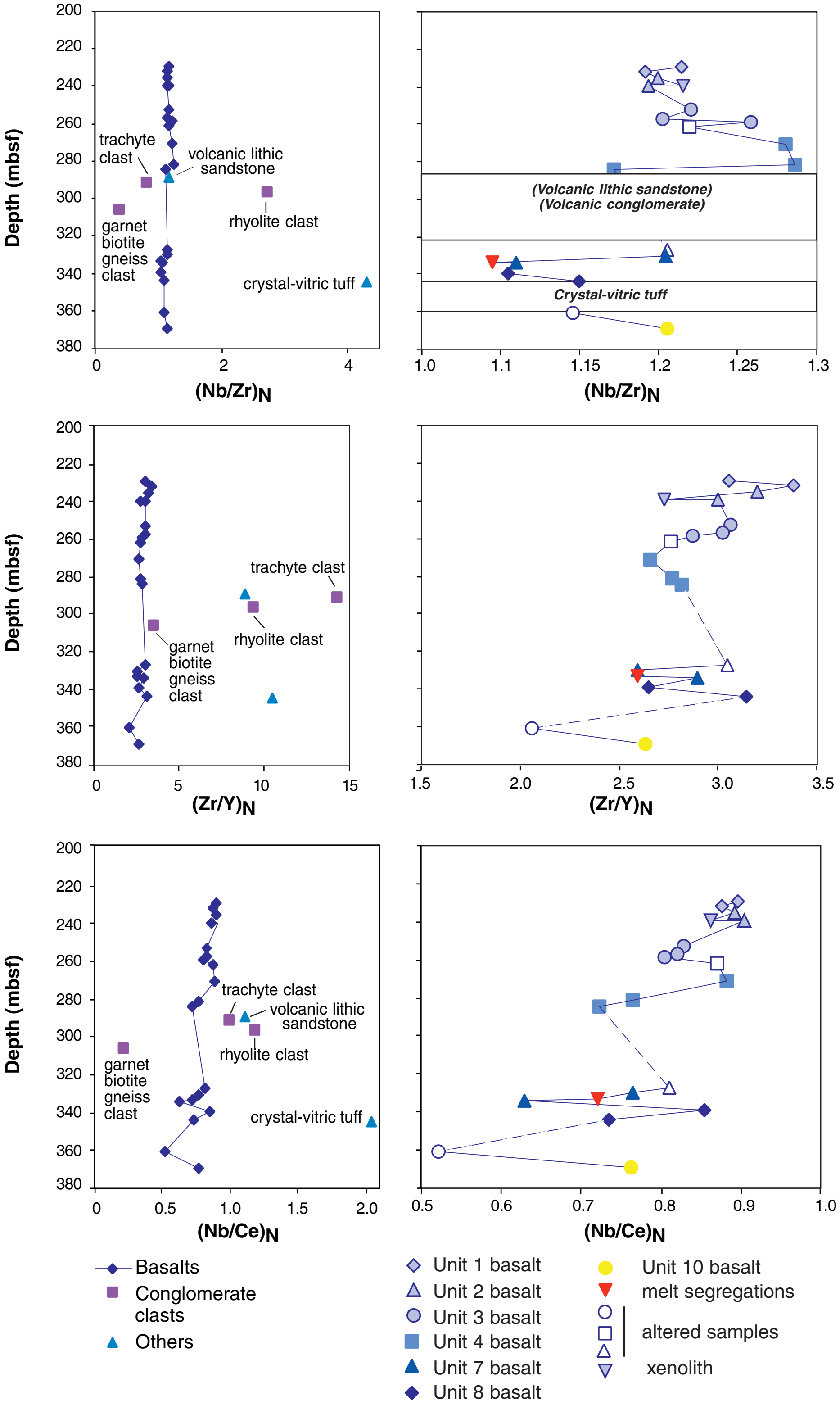

Figure F58. Incompatible trace element compositions of basalts from Site 1137, compared with those from other parts of the Kerguelen Plateau. Symbols and data sources are as in Figure F54, p. 117.

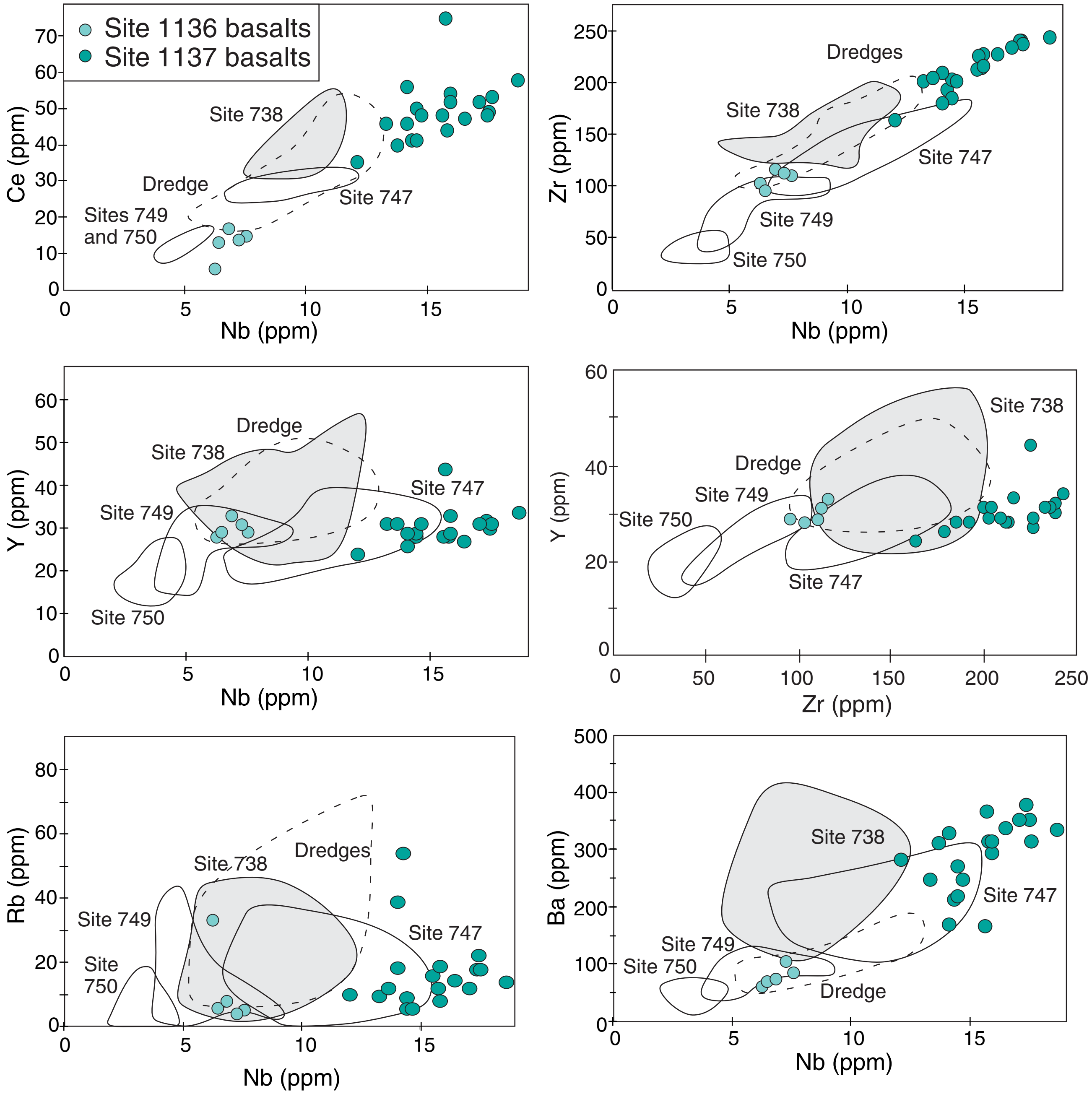

Figure F59. Primitive mantle–normalized incompatible element contents of basalts from Site 1137 compared to basalts from other basement sites on the Kerguelen Plateau. Symbols and data sources are as in Figure F54, p. 117.

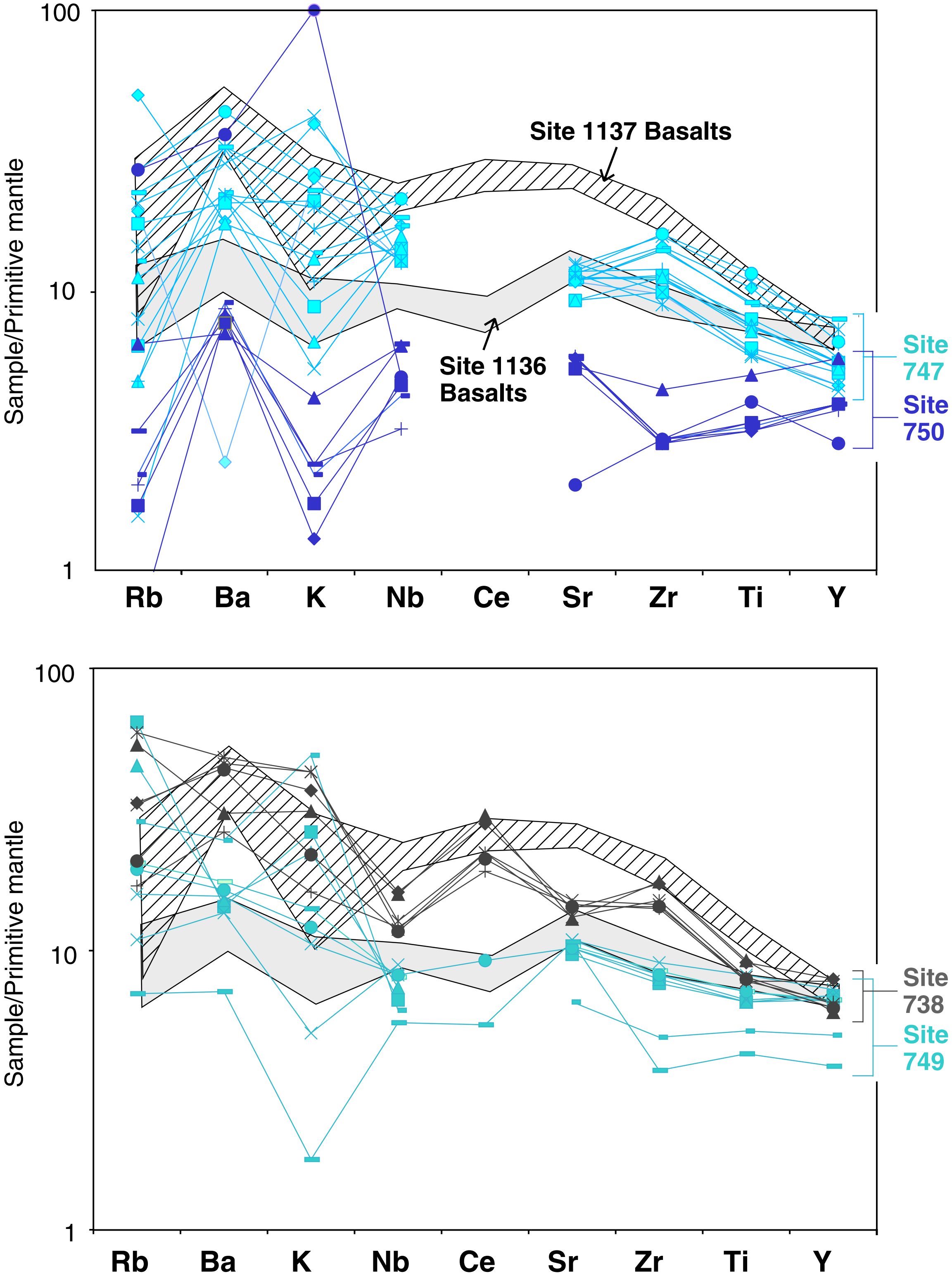

Figure F60. Primitive mantle–normalized Nb/Ce, Zr/Ti, and Nb/Zr vs. Zr/Y ratio or Zr content. These ratios are sensitive to the presence of a component from continental crust. Note that basalts from Site 738, which have been shown to contain such a continental component, have the lowest Nb/Ce and Nb/Zr and highest Zr/Ti values. Site 1137 basalts have a comparable Zr/Ti range but higher Nb and Zr contents and, consequently, higher Zr/Y, Nb/Ce, and Nb/Zr. Ratios are normalized using estimated primitive-mantle abundances of Sun and McDonough (1989). Data sources are the same as in Figure F54, p. 117.

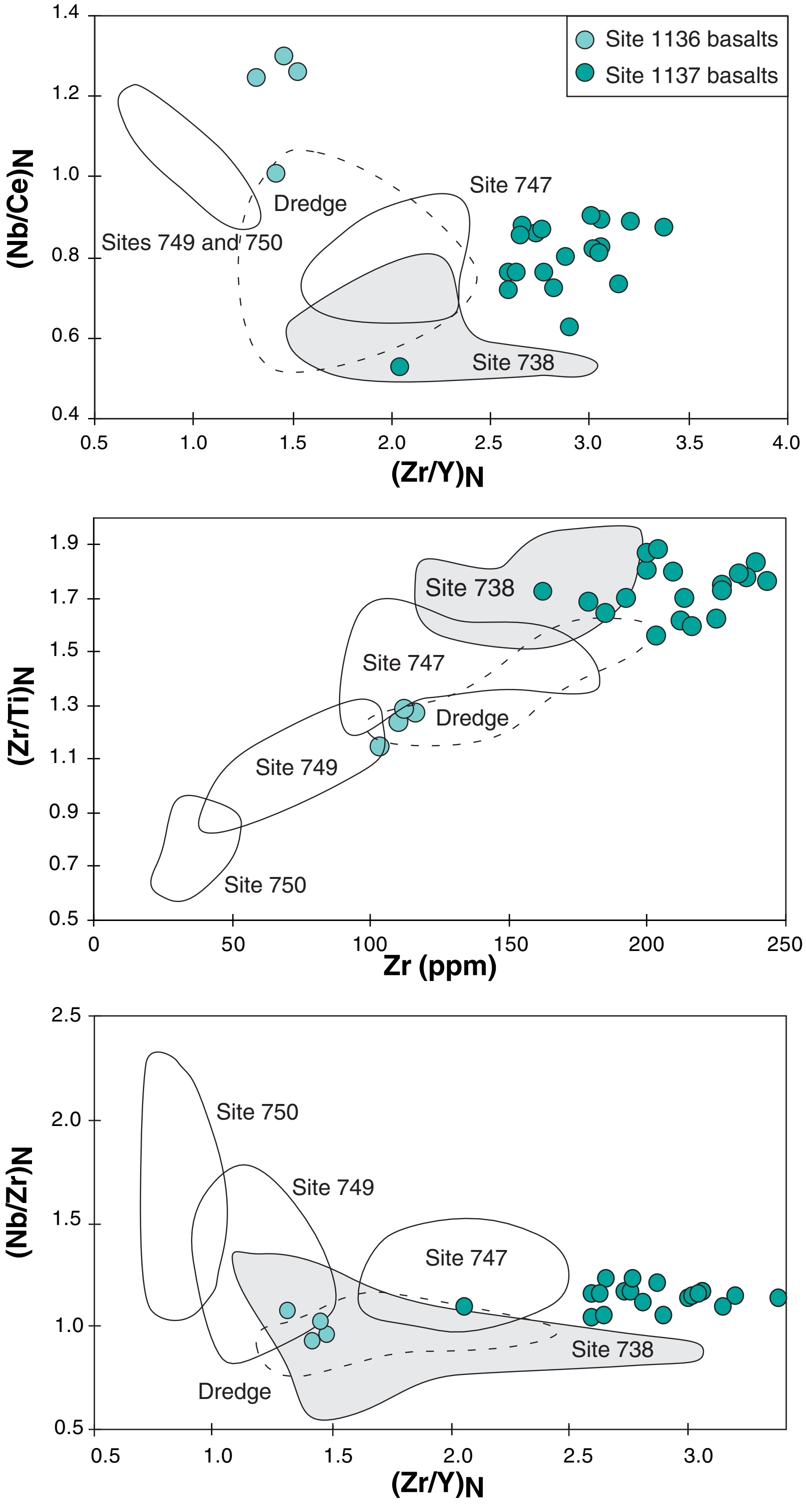

Figure F61. Nb/Y vs. Zr/Y diagram for Kerguelen Plateau basement basalt from Sites 738, 747, 749, 750, 1136, and 1137. The diagonal lines delimit the field of plume-derived Icelandic lavas and mid-ocean ridge basalt (MORB) plots to the right of this field. Fitton et al. (1997, 1998) argued that melts derived by varying extents of melting from a common peridotite source define trajectories nearly parallel to these boundary lines. Average MORB and ocean island basalt (OIB) (Sun and McDonough, 1989), average lower and upper crust (LCC and UCC, respectively) (Rudnick and Fountain, 1995), alkalic basalts from Site 748 (recovered above basement), and the evolved rocks from Site 1137 are shown for reference.

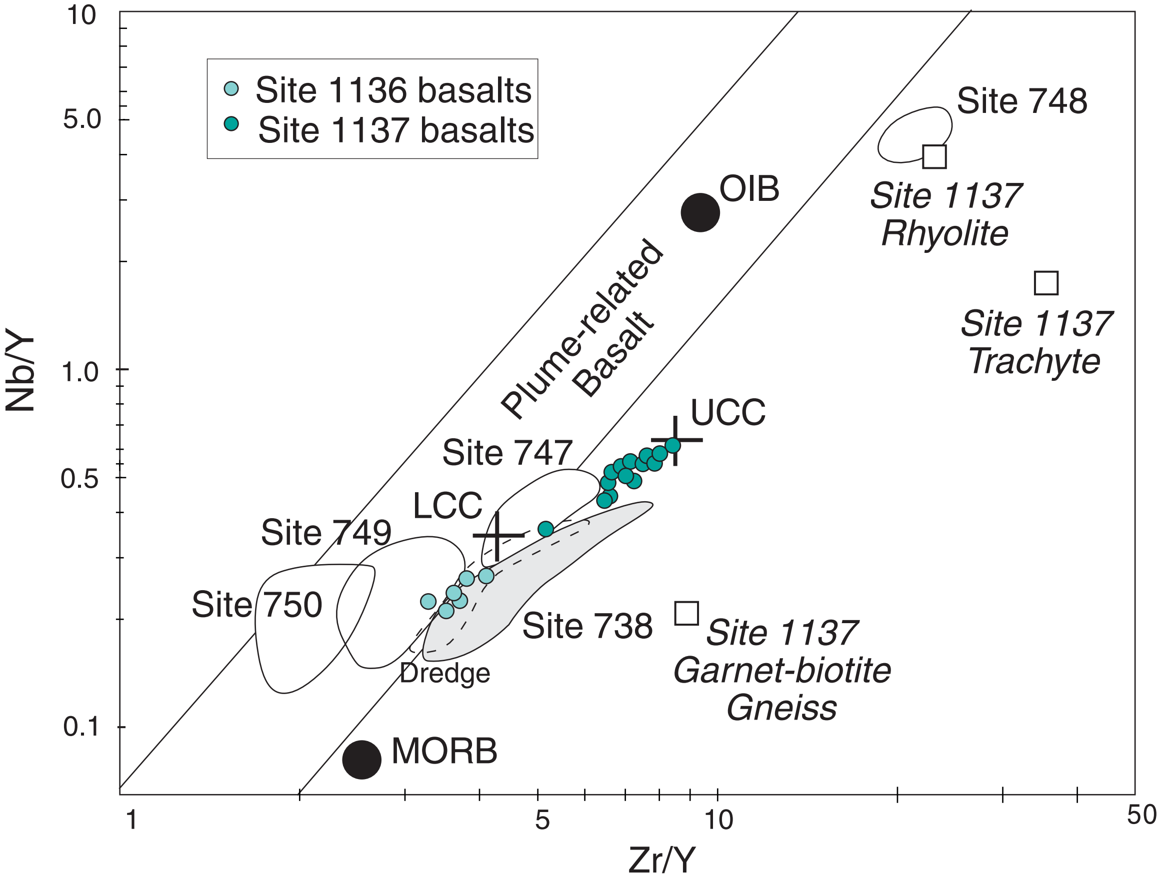

Figure F62. Primitive mantle–normalized incompatible element composition of felsic volcanic rocks from Site 1137 compared to those of trachytes from Heard Island and the Kerguelen Archipelago (Weis et al., 1993, 1998; Barling et al., 1994).

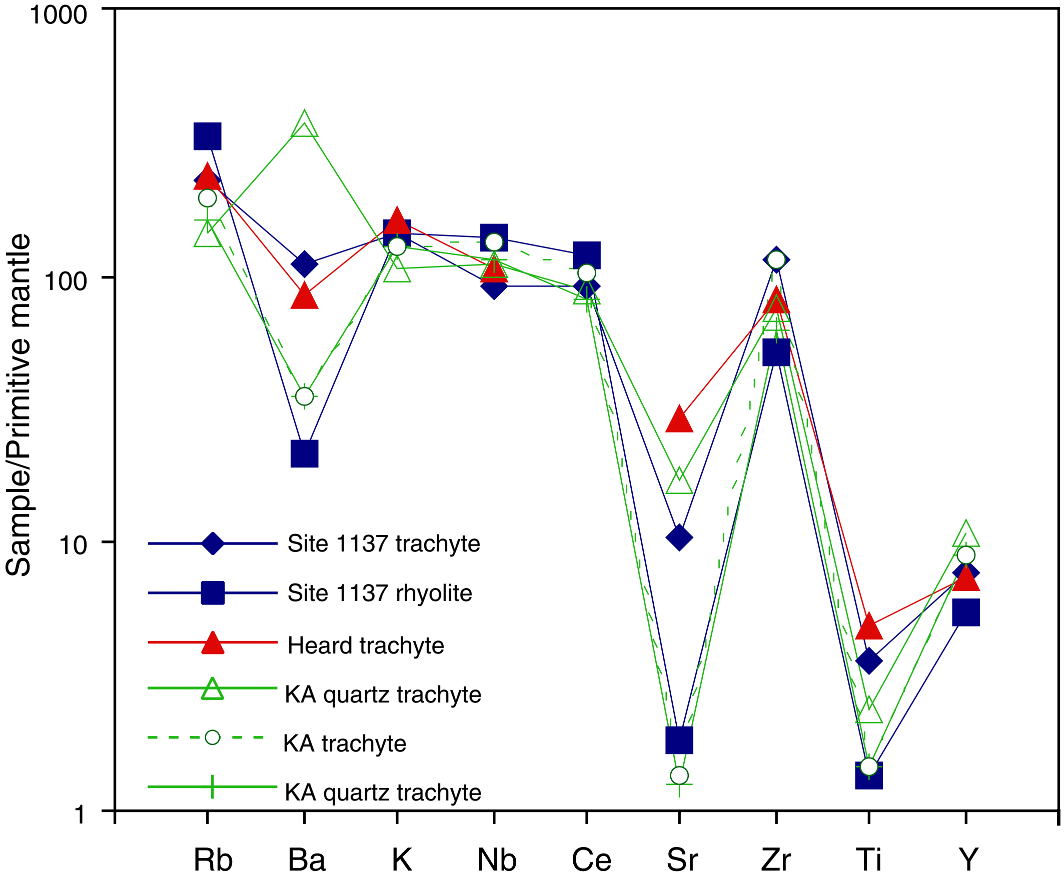

Figure F63. Distribution and abundance of secondary minerals as well as other alteration features in Hole 1137A vs. depth (mbsf), based on macroscopic features and mineral occurrences we observed in hand specimen from the core. The color is the hue of the bulk rock; dark gray = the least-altered basalts. The breccia column shows the distribution of clastic flow tops and flow bottoms. Horizontal dashed lines = unit boundaries. Colors: Bl = blue green, Gn = green, G = dark gray, Pk = pink brown, Bl = black, R = red. Alteration: f = fresh, s = slight, m = moderate, h = high, c = complete. Sediments: Bl = blue-green well-indurated sediments, S = sandstone, C = conglomerate, B = baked sediments, V = crystal vitric tuff, Bx = volcanic breccia. Abundance: 0 = absent, t = trace, c = common, a = abundant. AmSi = amorphous silica, $CaCO_3$ = calcium carbonate. (**Figure shown on next page.**)

Figure F63. (Caption on previous page.)

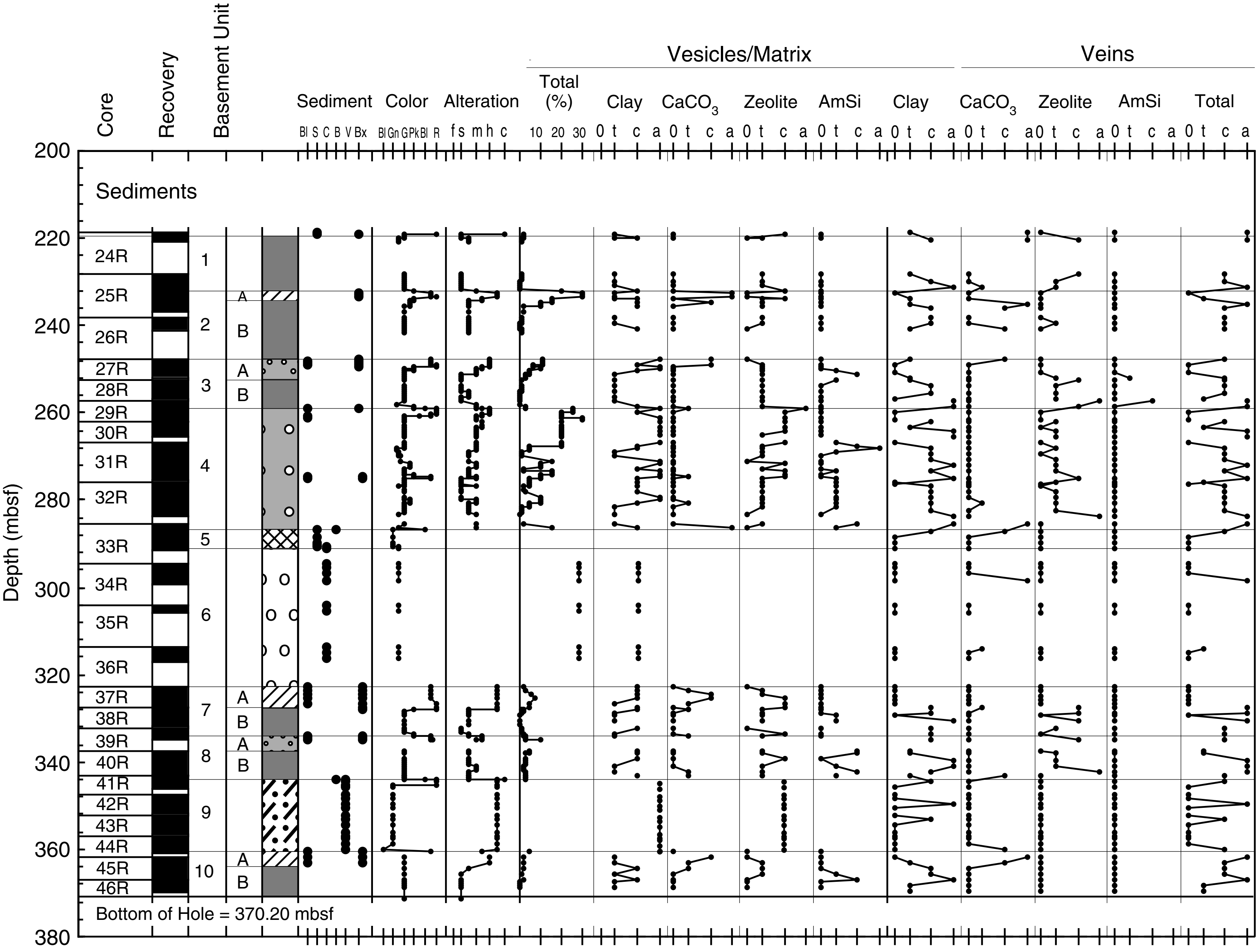

Figure F64. Color close-up photograph of Sample 183-1137A-25R-4 (Piece 1, 10–30 cm). Brecciated flow top of basement Subunit 2A showing oxidized clasts with calcite cement and chilled margin along lobe of dark gray basalt.

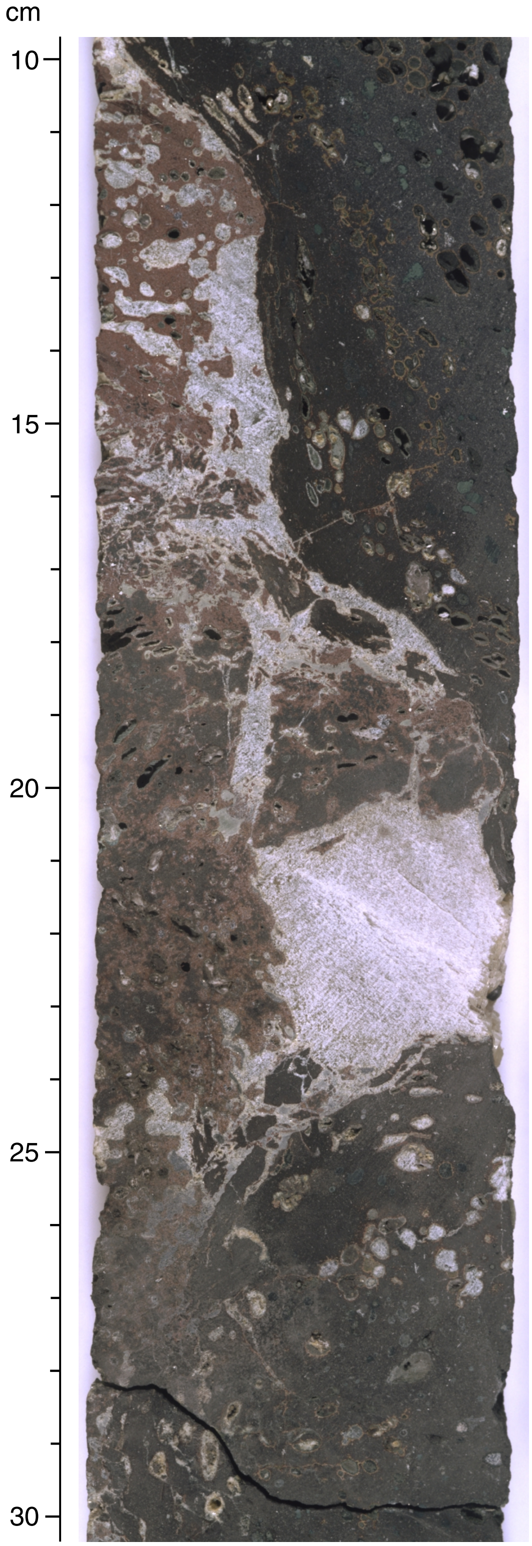

Figure F65. Color close-up photograph of Sample 183-1137A-27R-1 (Piece 12, 77–84 cm). Highly laminated and well-indurated blue-green siltstone from the weakly oxidized interior of Subunit 3A. An intricate contact between basalt and siltstone can be seen as well as clay-filled vesicles and calcite-bearing veins.

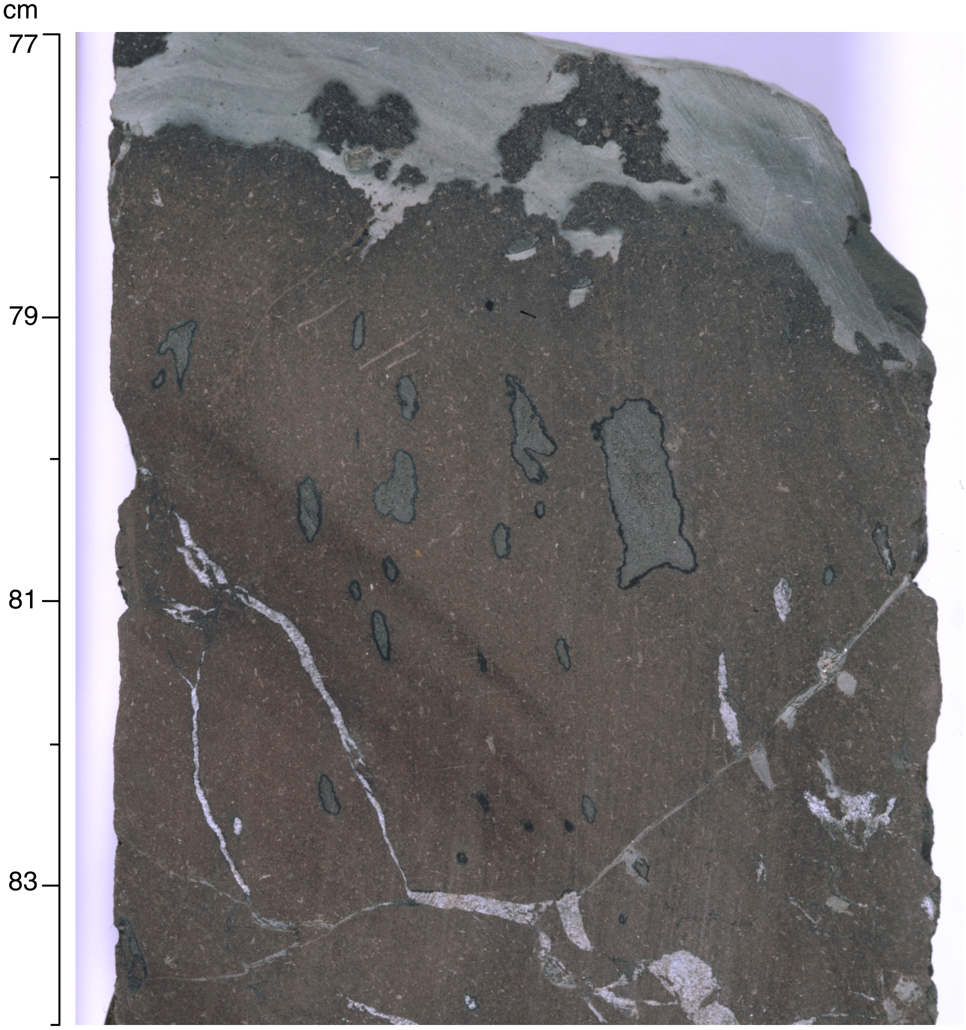

Figure F66. Color close-up photograph of Sample 183-1137A-27R-4 (Piece 4, 14–23 cm). Large vesicle in Subunit 3A showing geopetal structure with subhorizontal boundary between banded agate and zeolite.

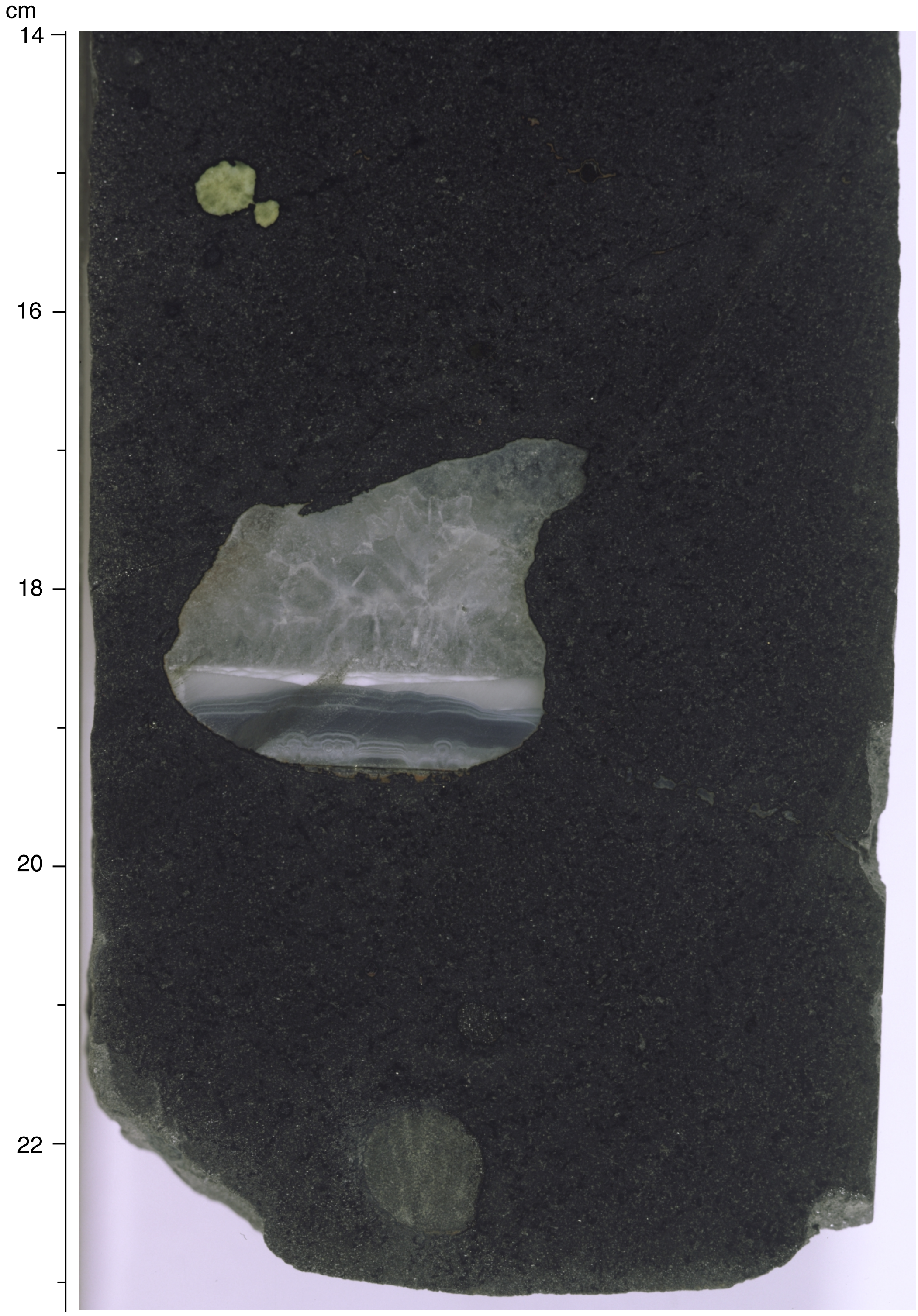

Figure F67. Color close-up photograph of Sample 183-1137A-28R-2 (Piece 4, 83–102 cm). Slightly altered basalt with well-defined moderately dipping mesostasis segregations altered to dark green clay (saponite).

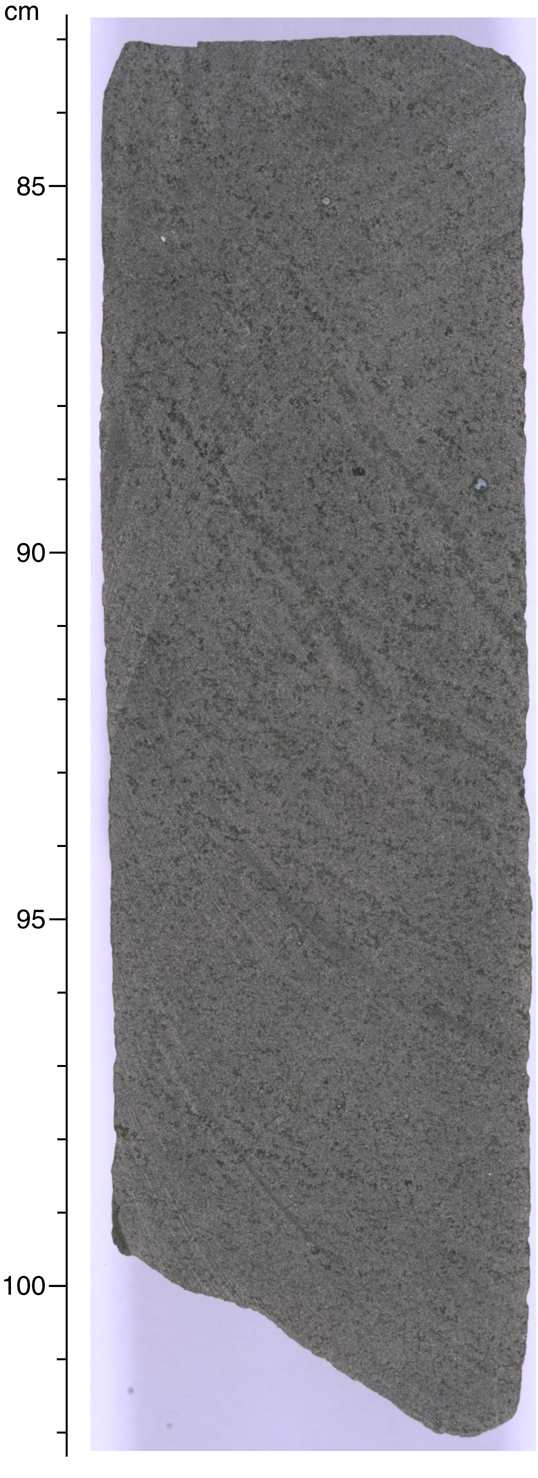

Figure F68. Color close-up photograph of Sample 183-1137A-29R-2 (Pieces 2–4, 50–80 cm). Volcaniclastic debris and well-indurated sediments along contact between basement Units 3 and 4. A distinct clast (?) of oxidized lava and indurated sediment is discordant to bedding, and multiple-graded beds are also present. The well-oxidized flow top of Unit 4 is also shown (75–80 cm).

Figure F69. Color close-up photograph of Sample 183-1137A-31R-5 (Piece 9, 101–113 cm). Large vesicle within plagioclase phyric basalt of Unit 4. The vesicle is lined with zeolite (clinoptilolite) and filled with barite. Blue-green smectite fills smaller vesicles.

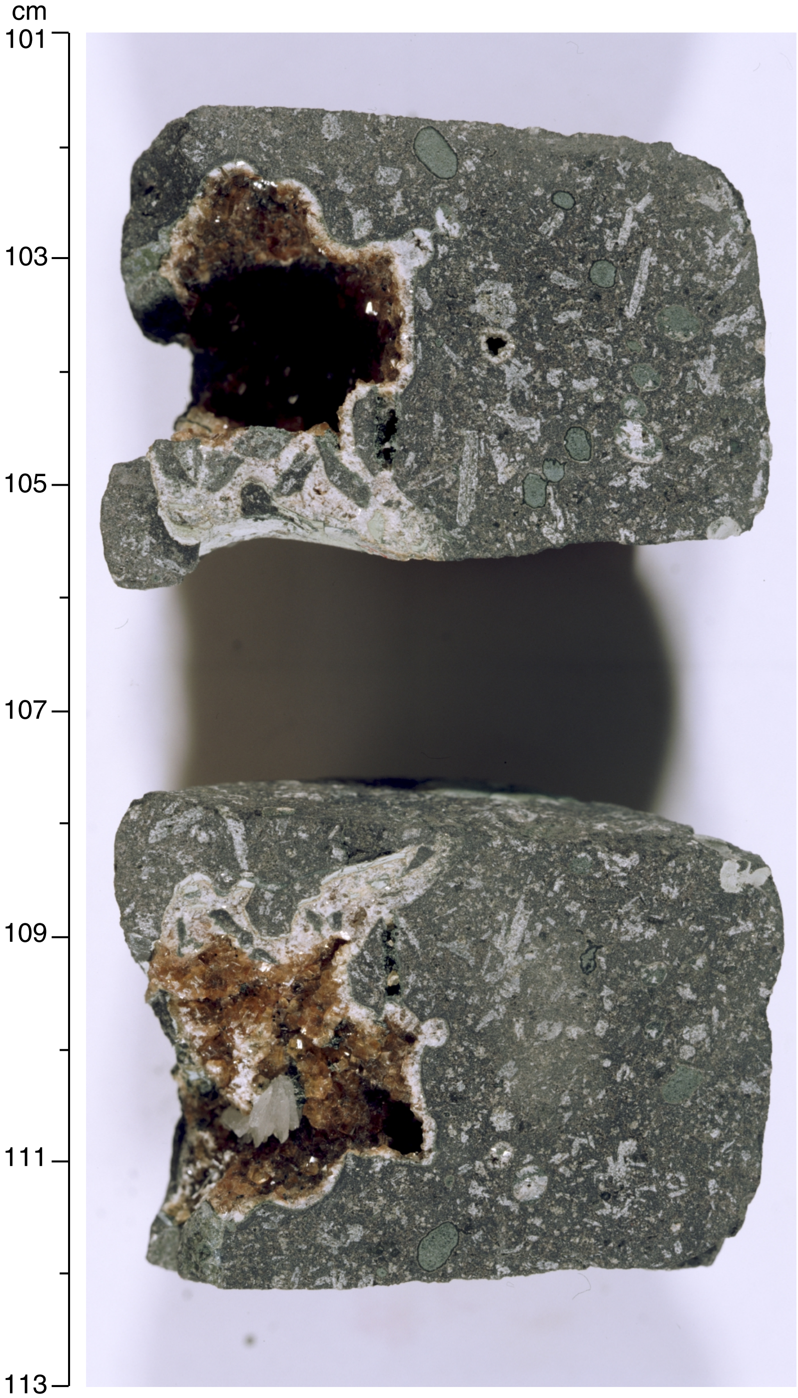

Figure F70. Color close-up photograph of Sample 183-1137A-37R-3 (Piece 1, 35–55 cm). Brecciated flow top of Subunit 7A showing oxidized and well-indurated sediments along with calcite (white) and zeolite (pink/amber) filling matrix.

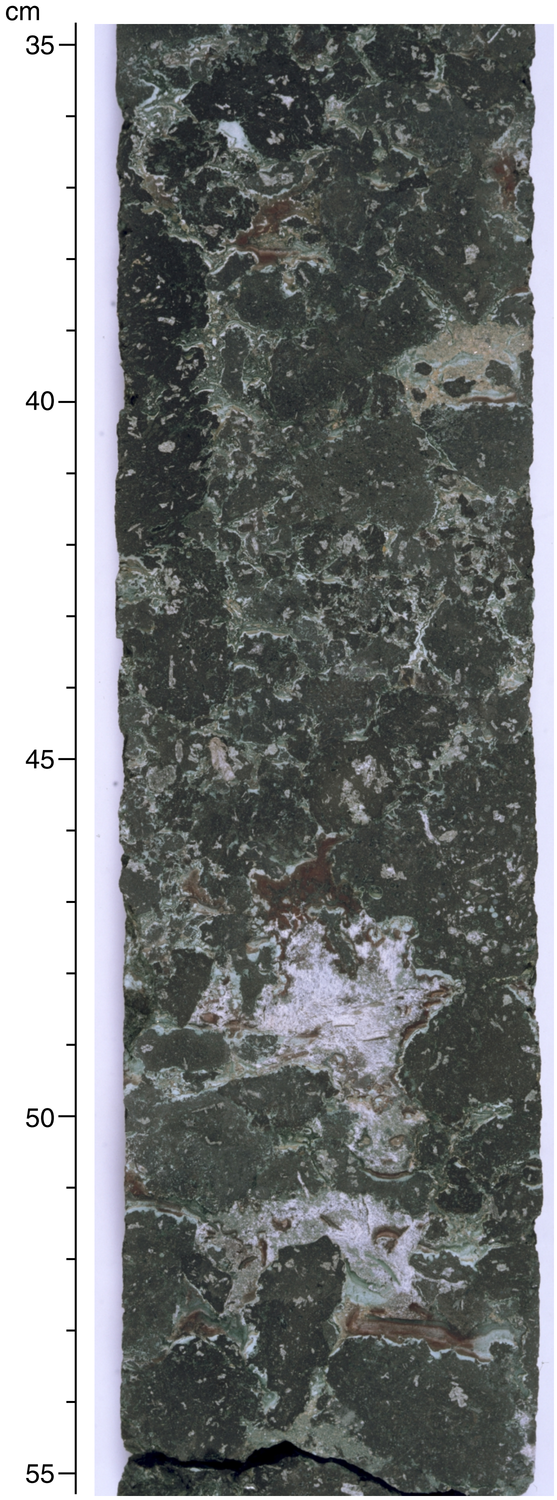

Figure F71. Color close-up photograph of Sample 183-1137A-42R-4 (Piece 1, 20–30 cm). Crystal vitric tuff composing basement Unit 9. Abundant potassium feldspar clasts and lithic fragments are set in a glassy matrix that has been altered to green clay (saponite/nontronite). Lithic fragments are surrounded by dark green clay-rich halos containing a trace of native copper.

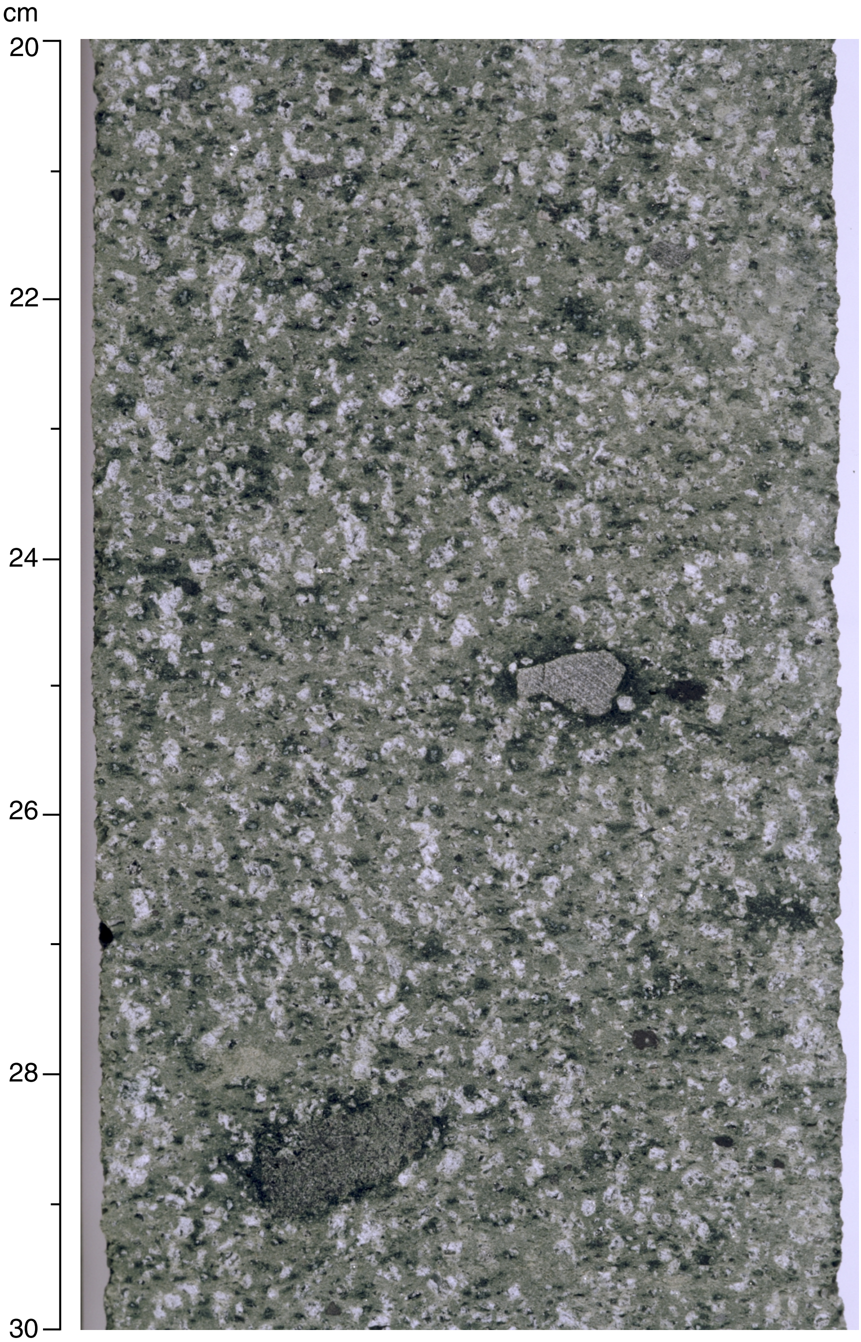

Figure F72. A. Diagram showing the unoriented true dip of veins in basement rocks from Hole 1137A. Veins are subdivided by the dominant mineral filling, and the true dip is plotted vs. depth. Rare veins in the intercalated volcaniclastic sediments are also shown. Zones of igneous brecciation are delineated by horizontal gray bands. **B.** Histogram showing the distribution of vein orientations subdivided by mineral filling in basement Units 1 to 4. **C.** Histogram showing the distribution of vein orientations subdivided by mineral filling in basement Units 7 and 8. **D.** Histogram showing the distribution of vein orientations subdivided by mineral filling in basement Unit 10. Note that crosses = clay; open circles = calcium carbonate; solid triangles = zeolites; solid squares = amorphous silica.

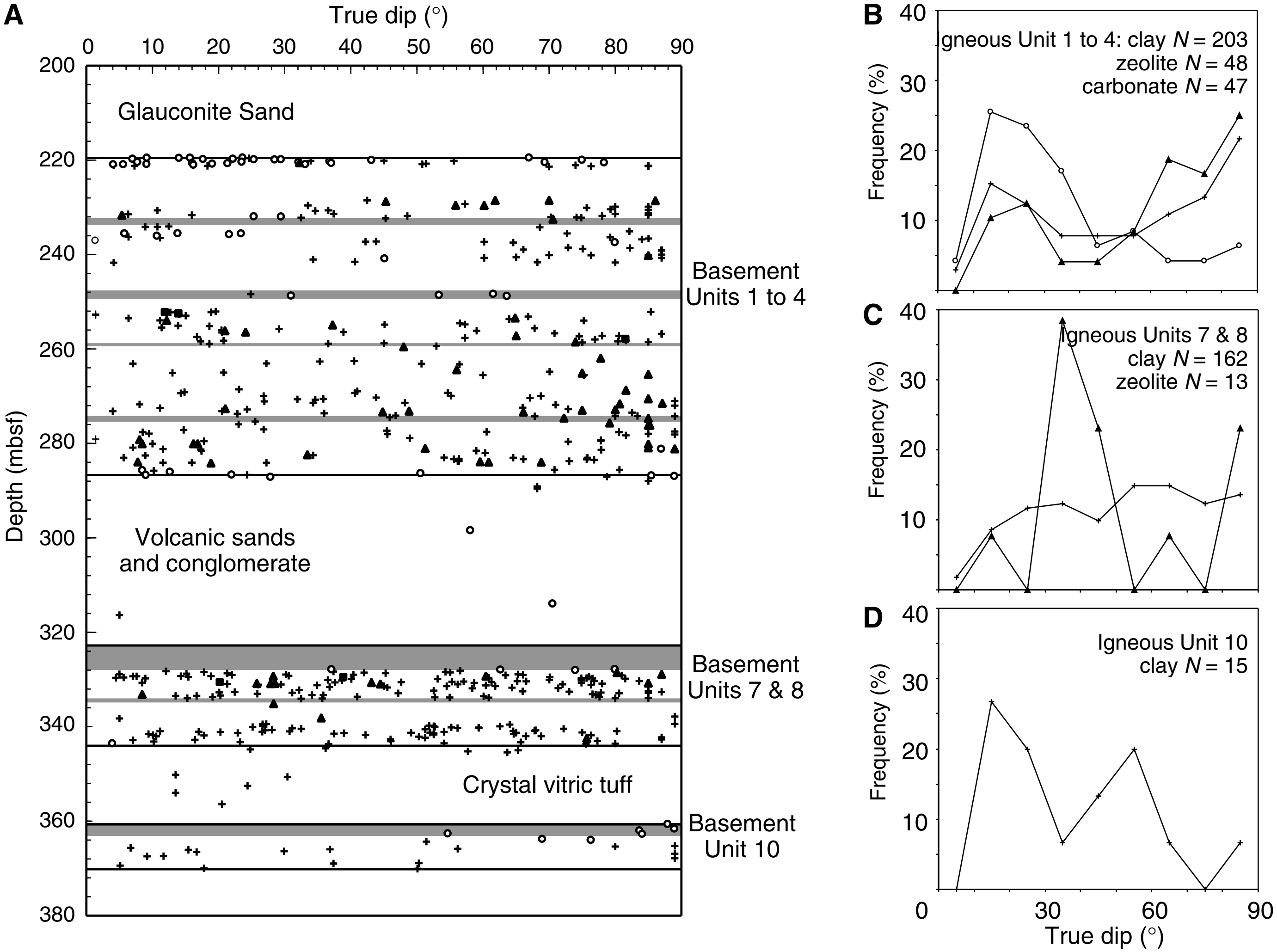

Figure F73. A. Diagram showing the abundance of mineral filled veins with depth in Hole 1137A. Veins are subdivided by the dominant mineral filling, and the vein abundance is calculated as an equivalent vein thickness in millimeters of vein material per meter of recovered drill core. **B.** Diagram showing the total fracture distribution, which is calculated from the total number of veins of any thickness per meter of recovered core. Data are presented on a core by core basis. Note that solid diamonds = total vein abundance; crosses = clay; open circles = calcium carbonate; solid triangles = zeolites; solid squares = amorphous silica; open diamonds = total fracture density.

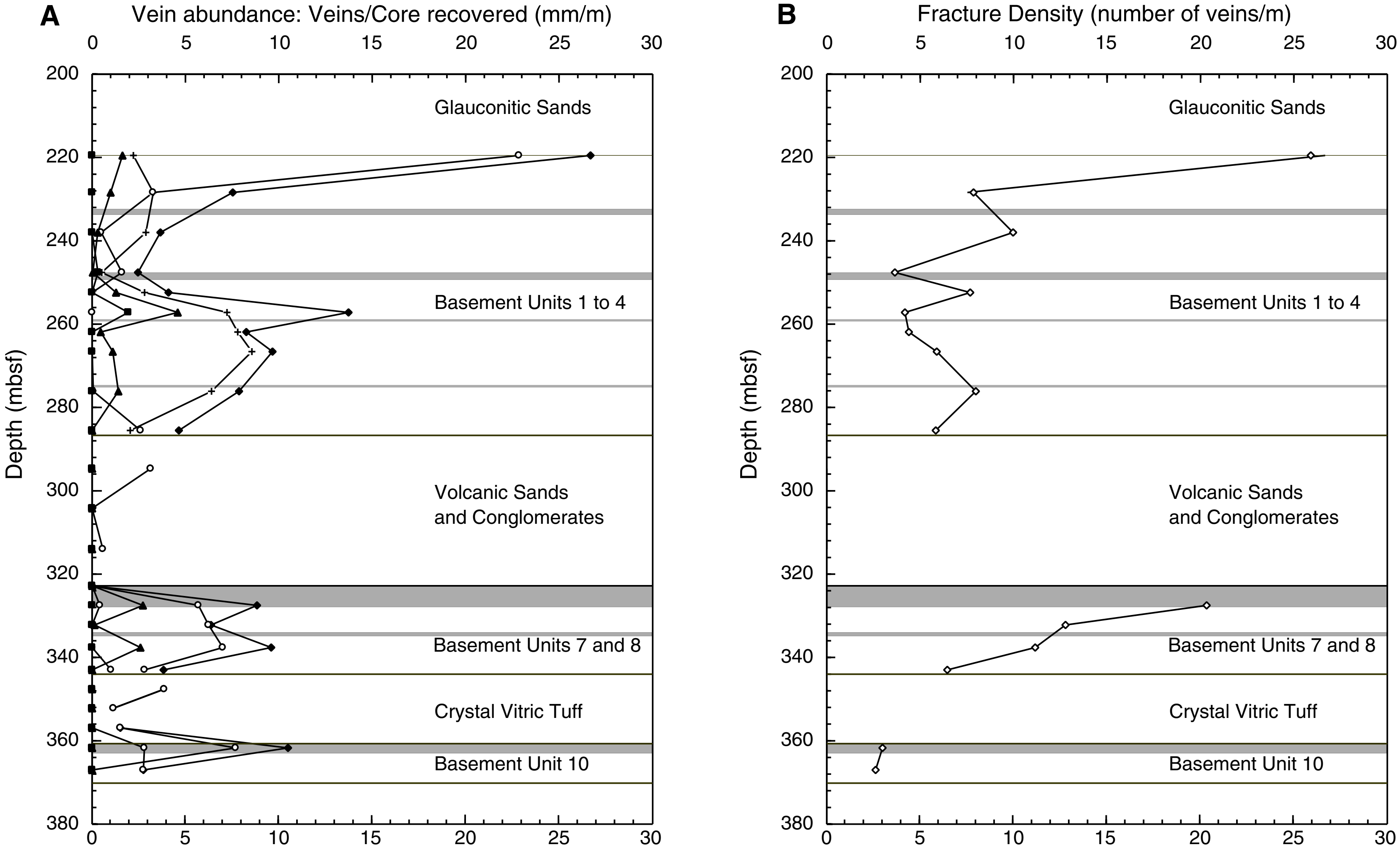

Figure F74. Unoriented true dips of mesostasis segregations (diamonds) and vesicle trails (open circles) with depth in Hole 1137A.

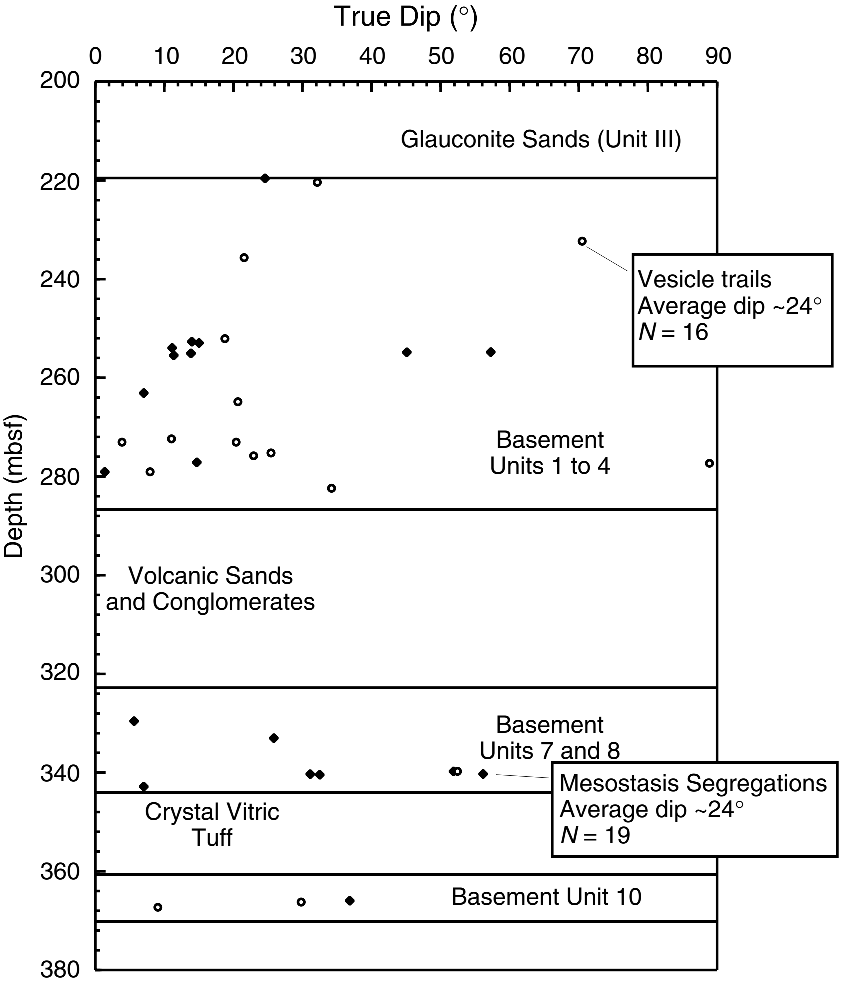

Figure F75. Example of progressive AF demagnetization of a discrete sediment sample from Hole 1137A. The intensity decay curve is plotted on the left, and the directional change is plotted on an orthogonal vector projection on the right. Magnetic directions that tend toward the origin with high median destructive fields are considered reliable. J_0 is the magnetization intensity before AF treatment.

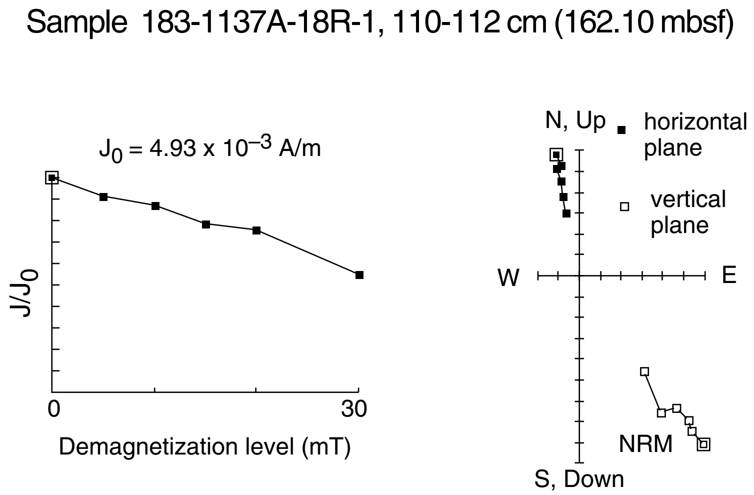

Figure F76. Hole 1137A inclination (left), intensity of remanent magnetization (middle), and MST susceptibility (right) of sediments from (**A**) 0–110 mbsf and (**B**) 110–220 mbsf. Crosses and lines represent remanent magnetization before and after AF demagnetization at 20 mT, respectively. Inclination data used for polarity interpretations are shown by open circles. Interpreted normal and reversed geomagnetic chrons are shown by black and white rectangles, respectively. Inclinations from discrete samples are shown by solid circles. Lithologic units are shown on the right. (Continued on next page.)

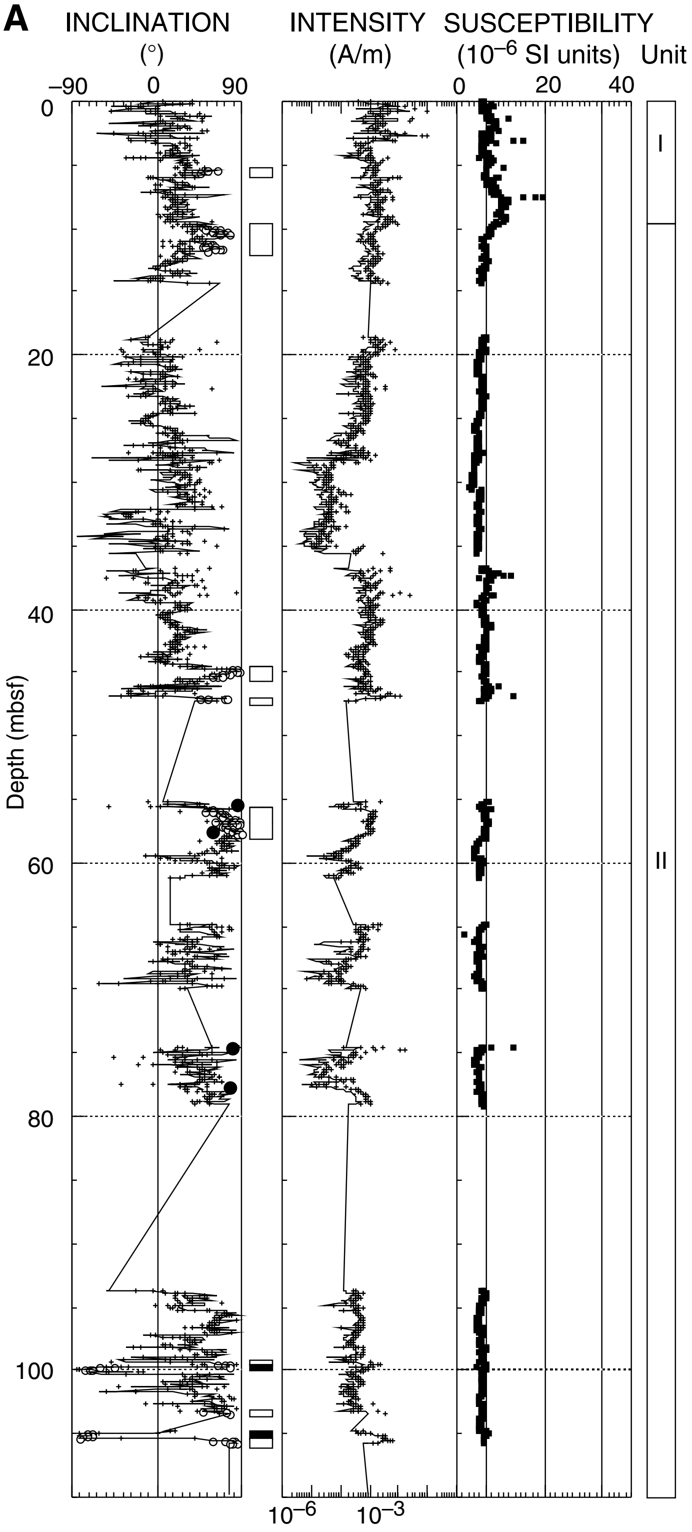

Figure F76 (continued).

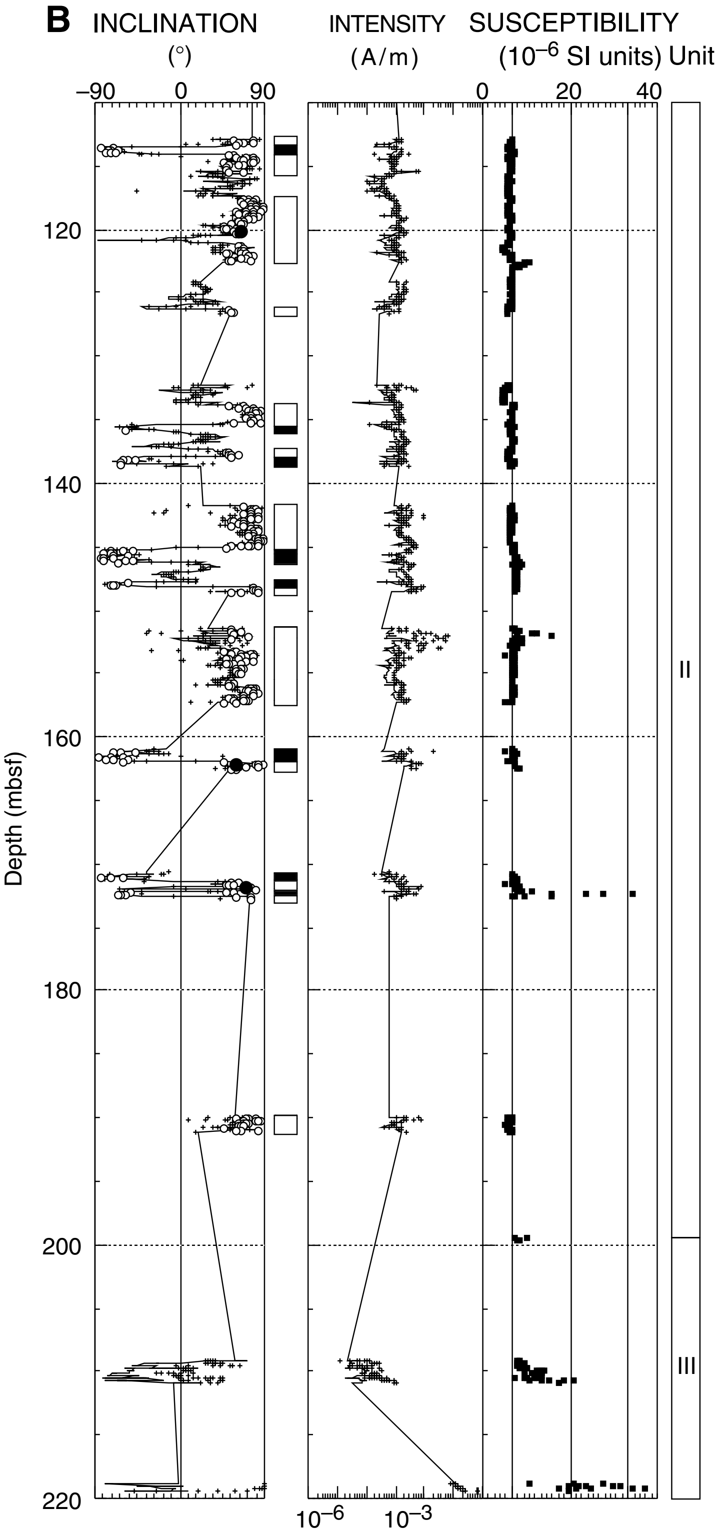

Figure F77. Hole 1137A inclination (left), intensity of remanent magnetization (middle), and susceptibility (right) of basement rocks for (**A**) 215–295 mbsf and (**B**) 295–375 mbsf. Crosses and lines represent remanent magnetization before and after AF demagnetization at 40 mT, respectively. Inclinations of NRM and characteristic inclinations of discrete samples are represented by solid and open circles, respectively. MST, AMST, and discrete-sample susceptibilities are represented by lines, crosses, and open circles, respectively. Basement units are shown on the right. (Continued on next page.)

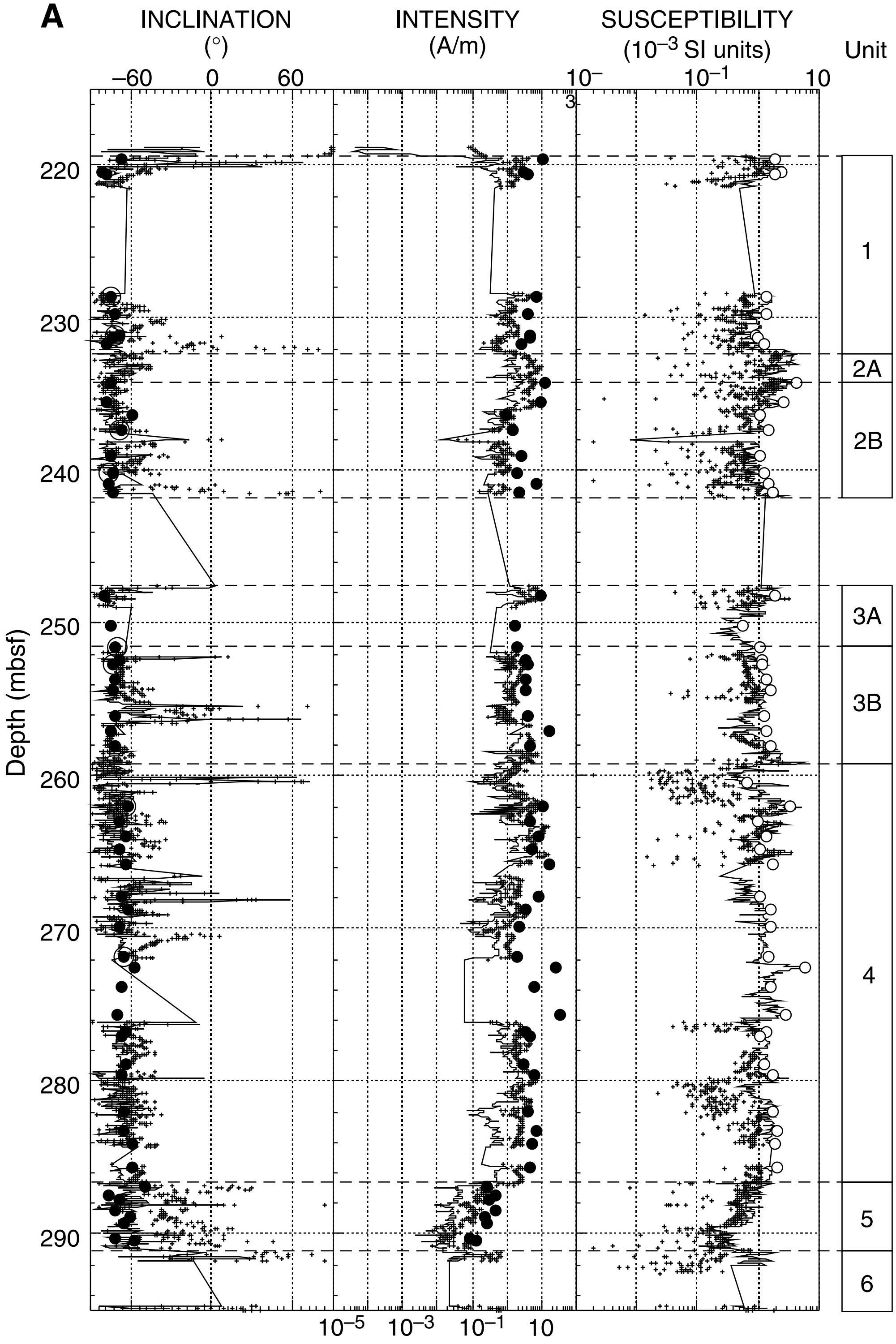

Figure F77 (continued).

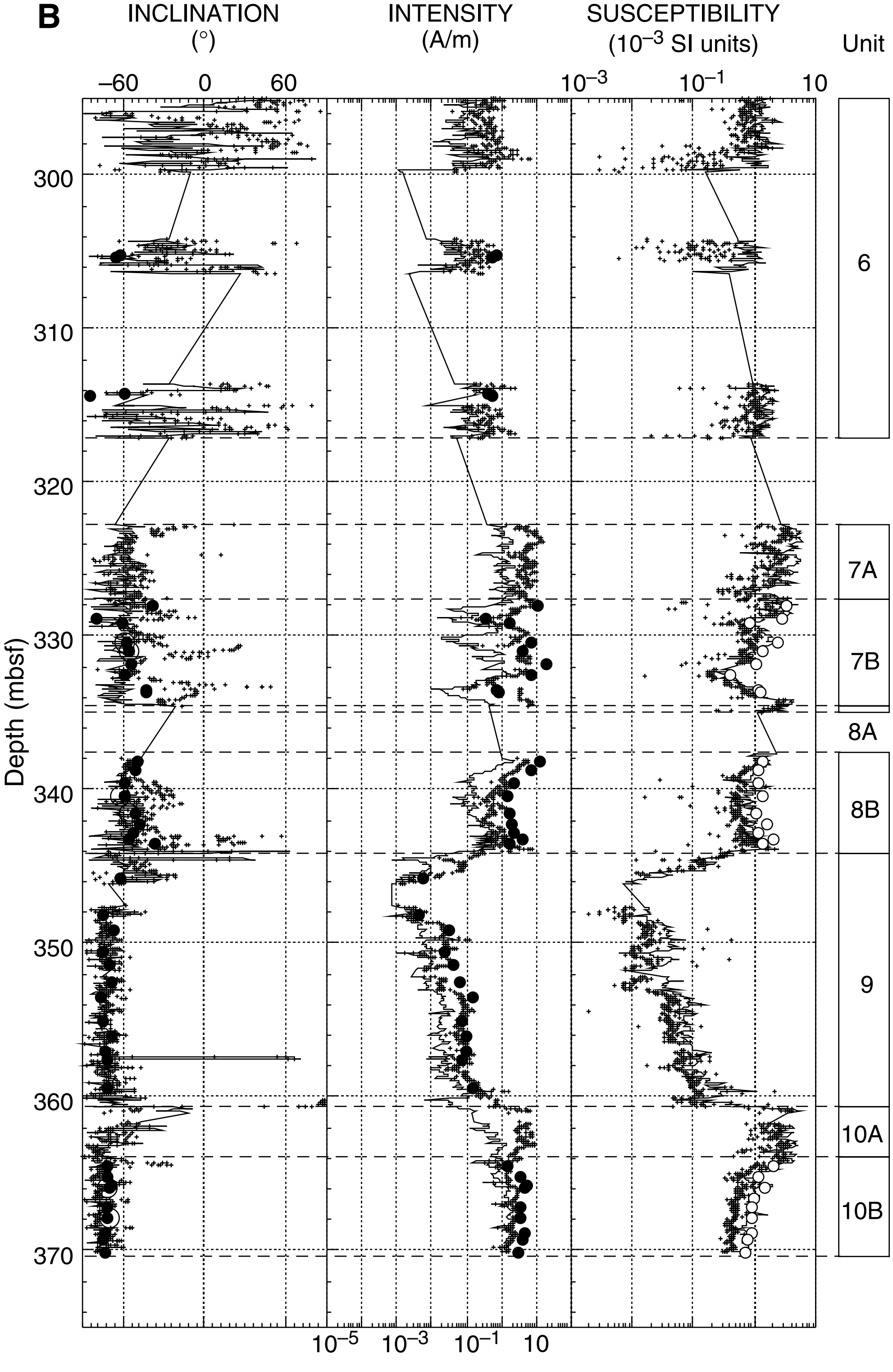

Figure F78. Directional anisotropy data from eight discrete samples of basement Unit 1 plotted on an equal-area stereographic projection. The directions of maximum principal axes are plotted as empty squares, of intermediate principal axes as gray squares, and of minimum principal axes as black squares.

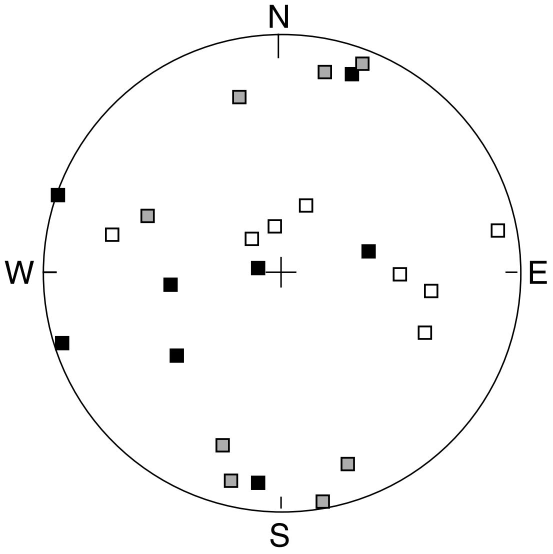

Figure F79. **A.** Stepwise AF demagnetization up to 60 mT of Sample 183-1137A-26R-2, 55–57 cm. The sample has a high MDF and a single-component magnetization as is evident from the straight lines in the orthogonal vector projections. **B.** The MDF of Sample 183-1137A-38R-3, 105–107 cm, is very low as is evident from the decay curve (left). However, the orthogonal vector projection (right) shows a single-component magnetization with an inclination that is different from the present geomagnetic inclination. Hence, the remanent magnetization is not a recent overprint (see **"Paleomagnetism,"** p. 45). J_0 is the magnetization intensity before AF treatment.

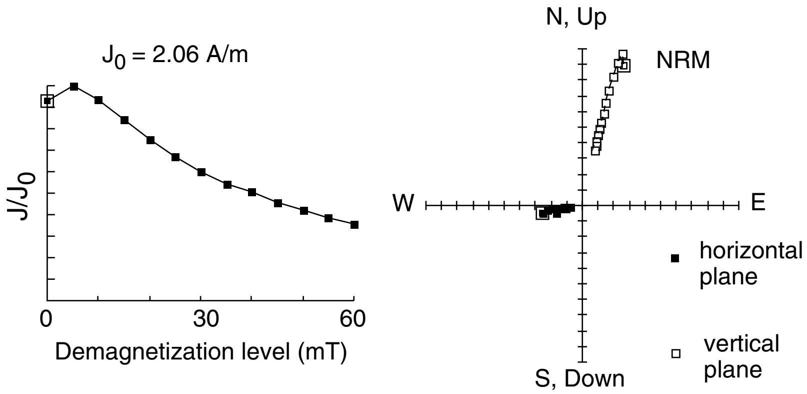

A Sample 183-1137A-26R-2, 55-57 cm (240.03 mbsf)

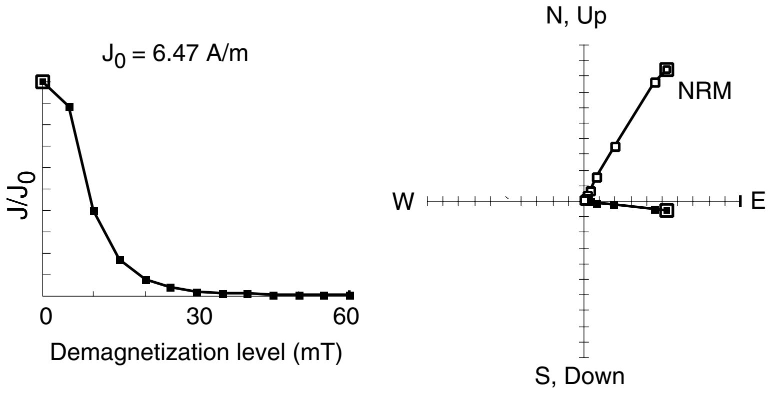

B Sample 183-1137A-38R-3, 105-107 cm (330.37 mbsf)

Figure F80. A. Thermal demagnetization of Sample 183-1137A-40R-4, 50–52 cm, from basement Unit 8. The NRM is a stable, single-component magnetization. Most unblocking temperatures are above 500°C. The decay curve gives no indication of a second magnetic phase. The magnetic mineral is most likely magnetite, which has a Curie temperature of 580°C. **B.** Thermal demagnetization of Sample 183-1137A-29R-4, 56–58 cm, from basement Unit 4. The unblocking temperatures are ~580° and ~300°C and indicate that both magnetite and titanomaghemite are the magnetic minerals. The NRM is a stable, single-component magnetization. J_0 is the magnetization intensity before thermal treatment.

A Sample 183-1137A-40R-4, 50-52 cm (341.42 mbsf)

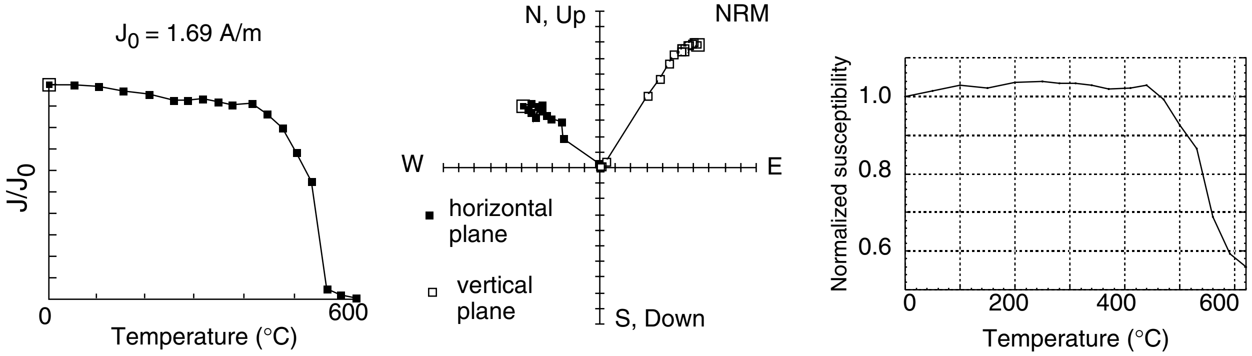

B Sample 183-1137A-29R-4, 56-58 cm (261.96 mbsf)

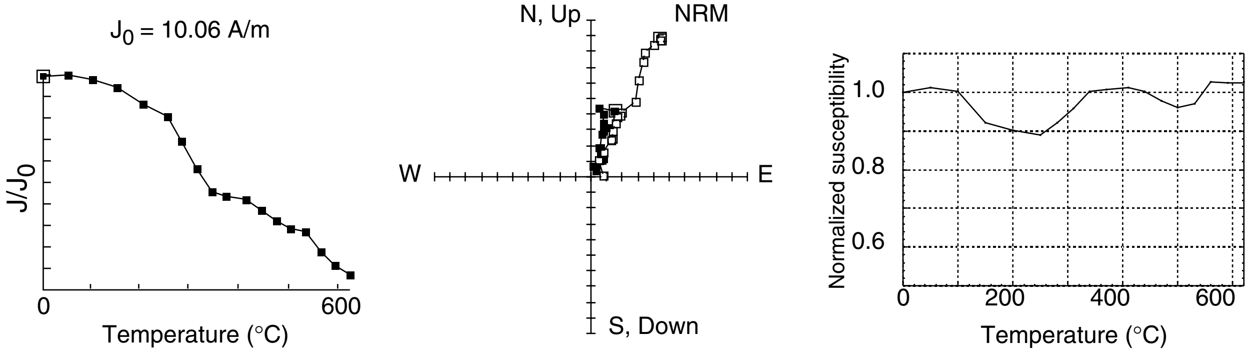

Figure F81. Downhole index properties and compressional wave velocities (V_p) at Site 1137. Lithologic units, discrete measurements (symbols), and logging results (solid lines) are also shown for **(A)** bulk density, **(B)** grain density, **(C)** porosity, and **(D)** velocities.

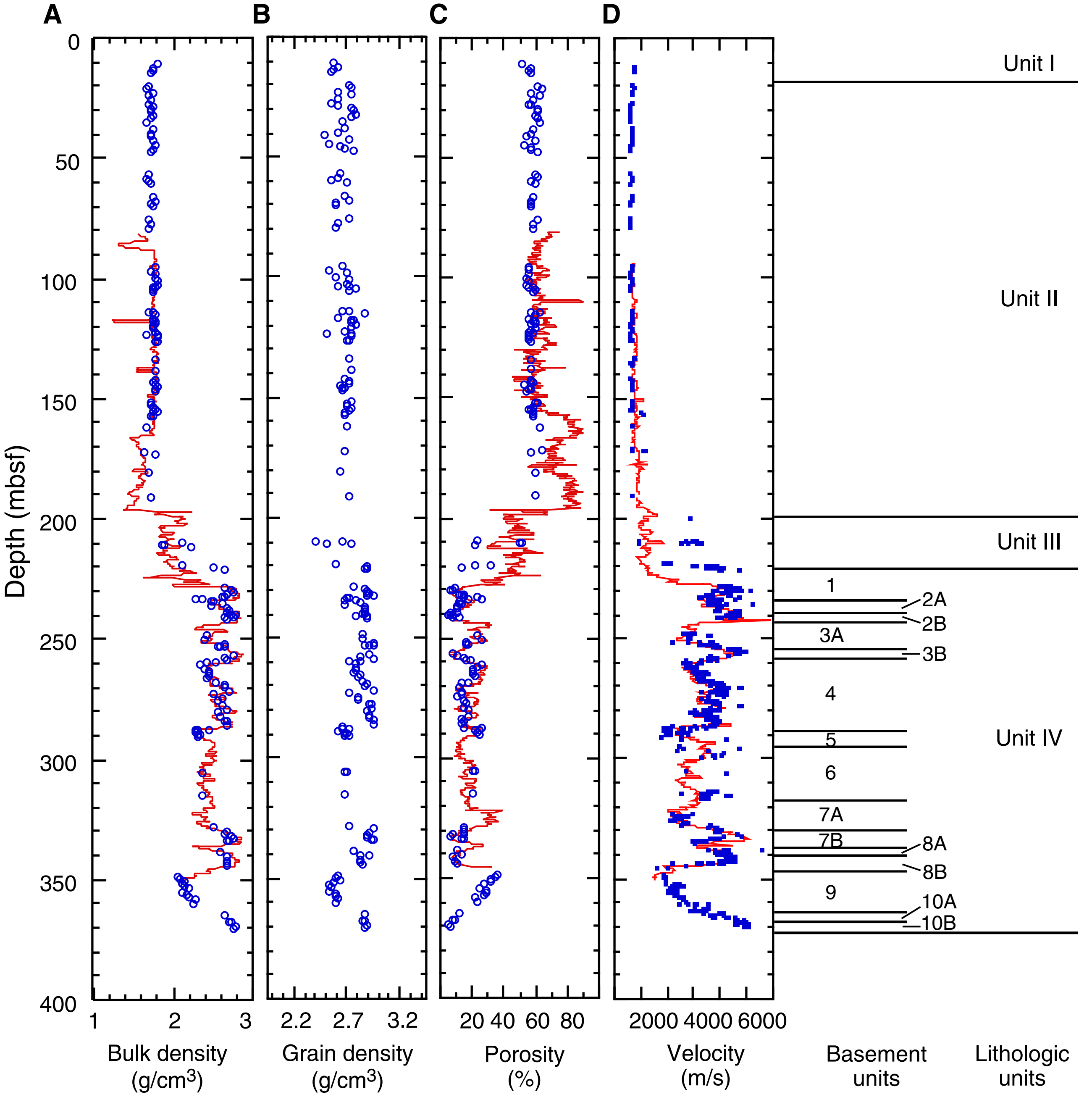

Figure F82. Downhole physical properties profiles of basement units in Hole 1137A (Unit IV). **A.** Magnetic susceptibility. **B.** Discrete index properties bulk density. **C.** Grain density. **D.** Porosity. **E.** Discrete velocities. The corresponding logging results are represented by solid lines. This figure is an enlarged subset of results shown in Figure F81, p. 149.

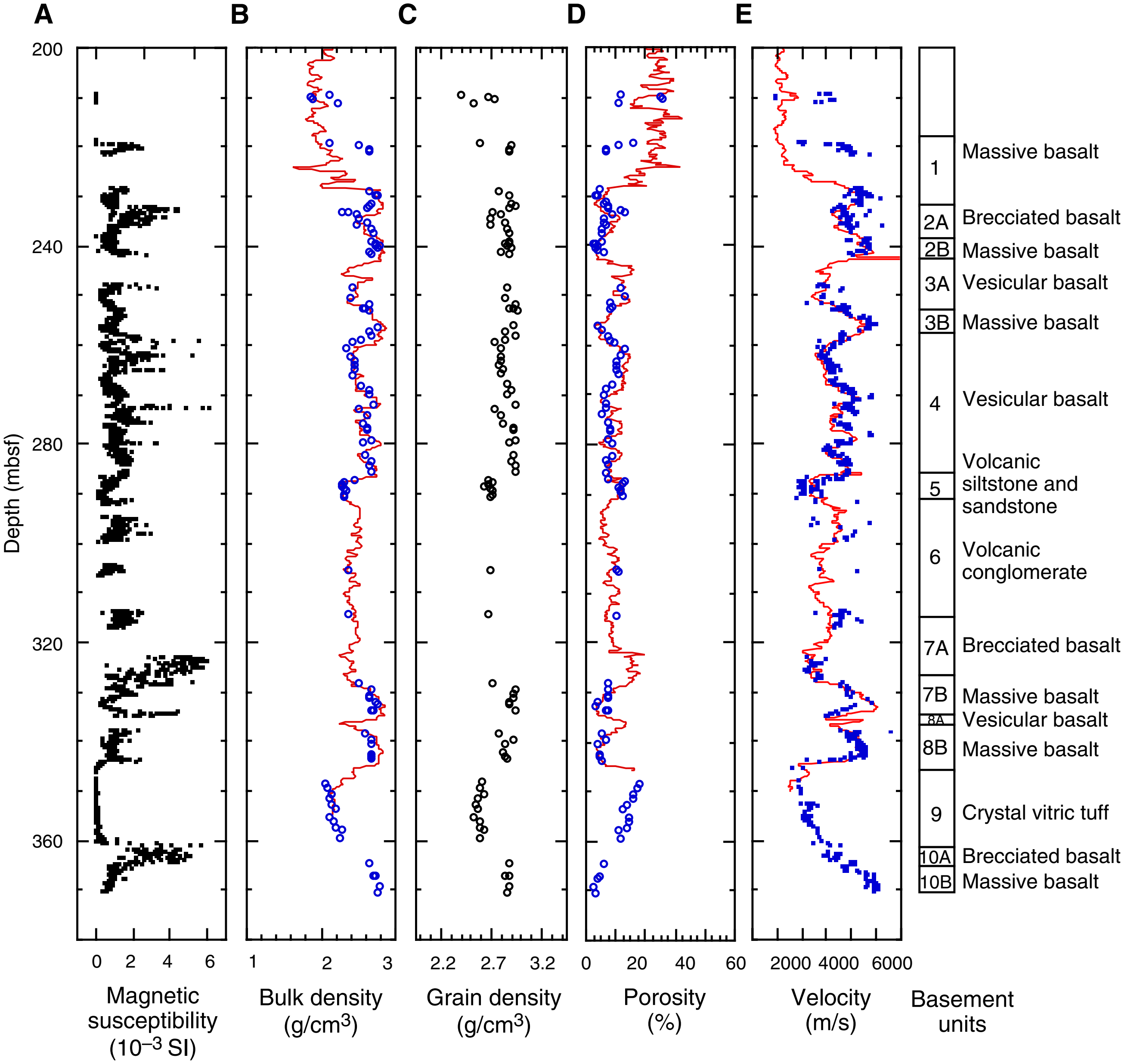

Figure F83. Downhole profiles of MST measurements along with discrete sample densities. **(A)** GRAPE bulk density (small squares) and bulk density (solid circles) are derived from discrete samples at Site 1137, **(B)** whole-core measurements of magnetic susceptibility, and **(C)** natural gamma-ray data.

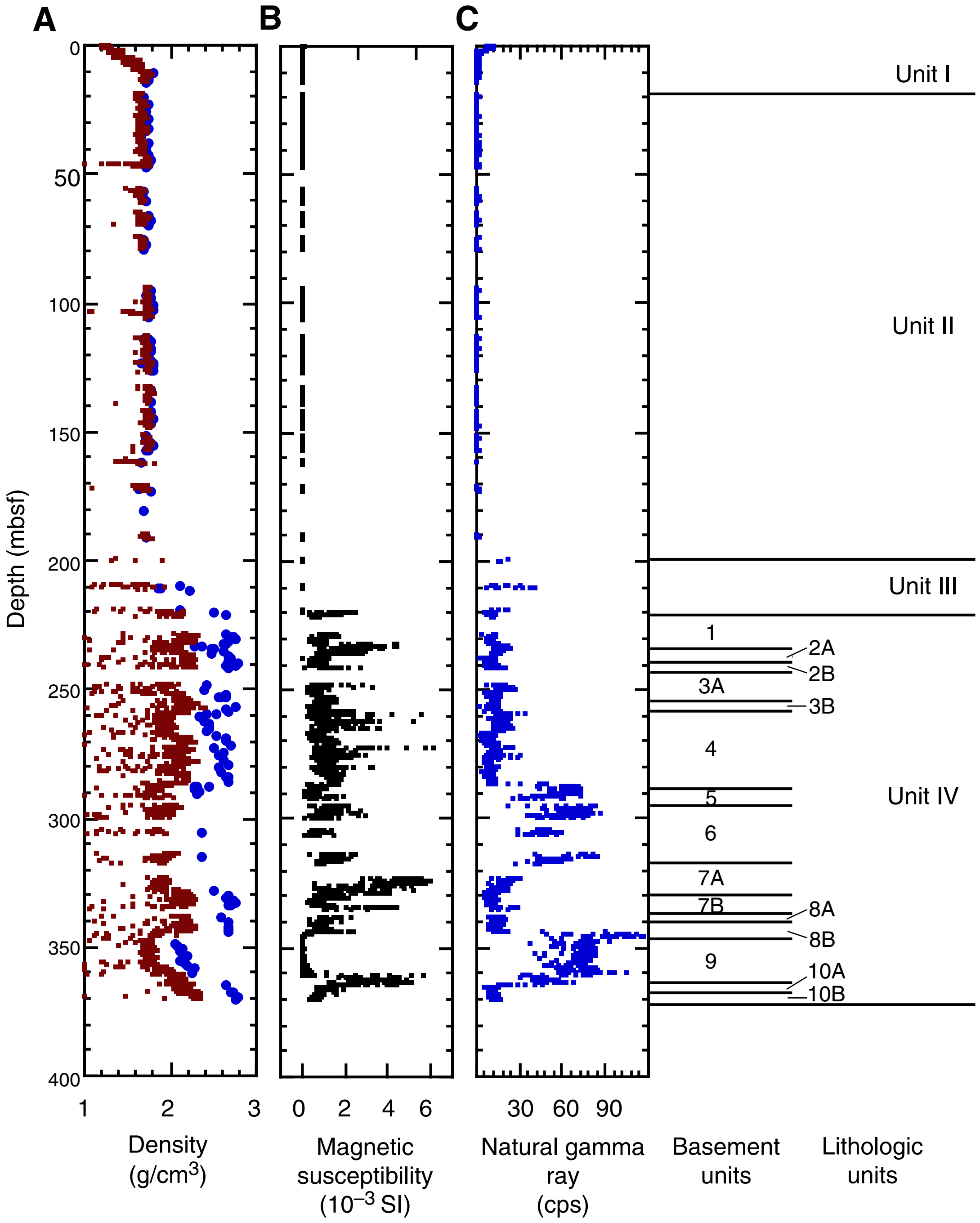

Figure F84. Downhole profile of whole-core measurements of thermal conductivity on soft sediments and on split-core pieces of consolidated sediments and hard rocks from Hole 1137A. Note the local increase in thermal conductivity in basement Unit IV.

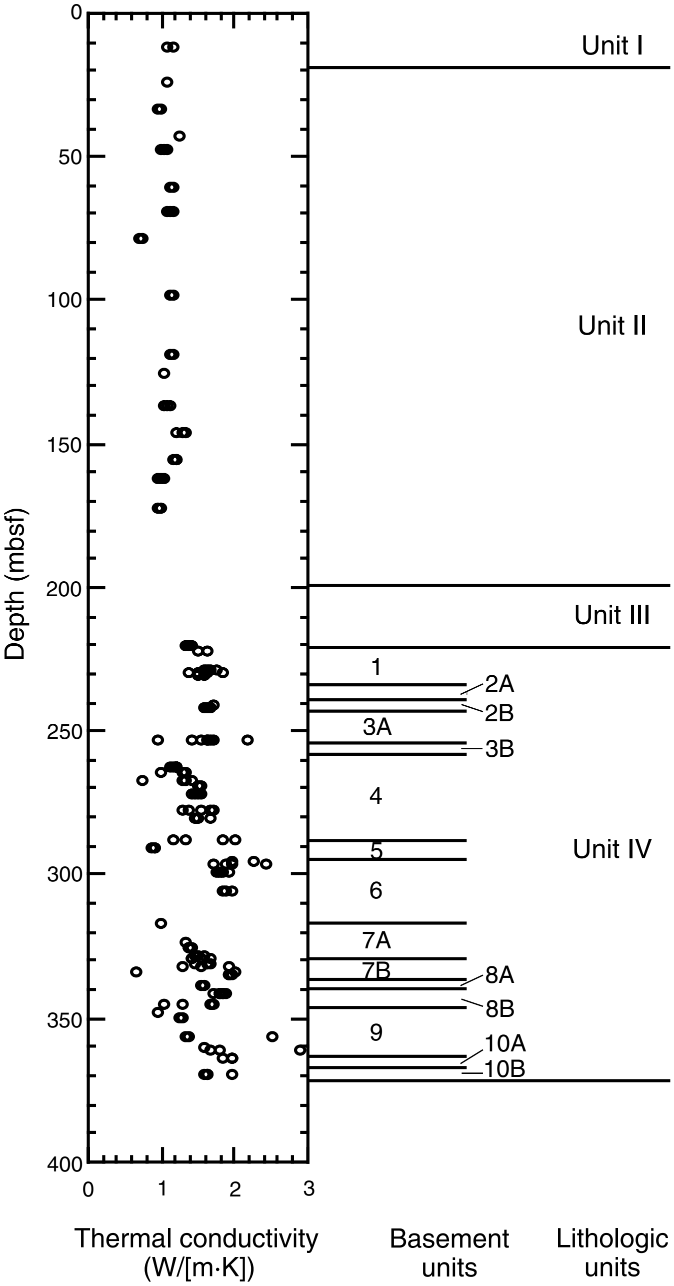

Figure F85. Comparison of densities determined from core samples, gamma-ray attenuation porosity evaluator and the multisensor track, and compressional-wave velocities from downhole logs and core samples. Raw and robust mode filtered data are shown. (Continued on next page.)

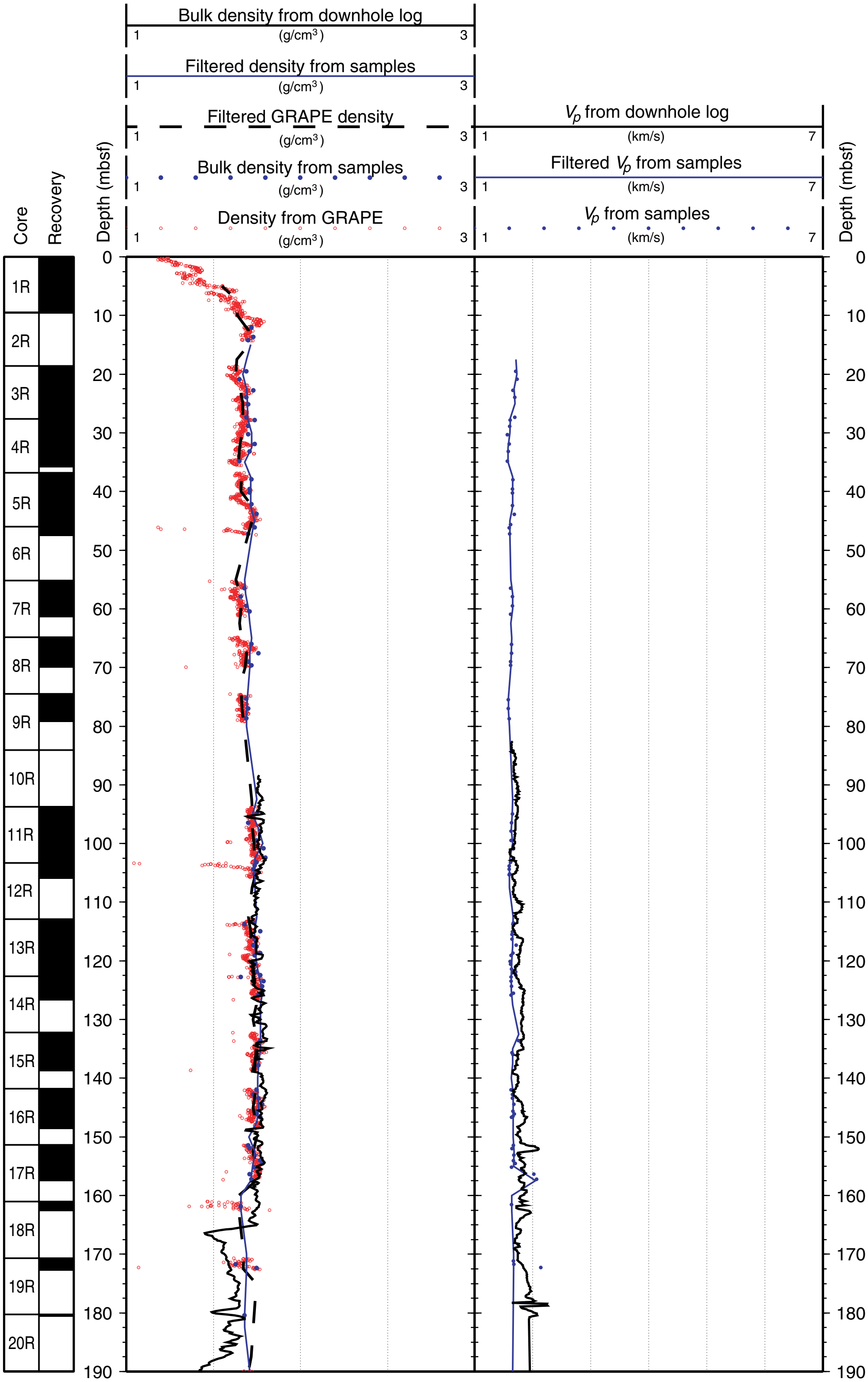

Figure F85 (continued).

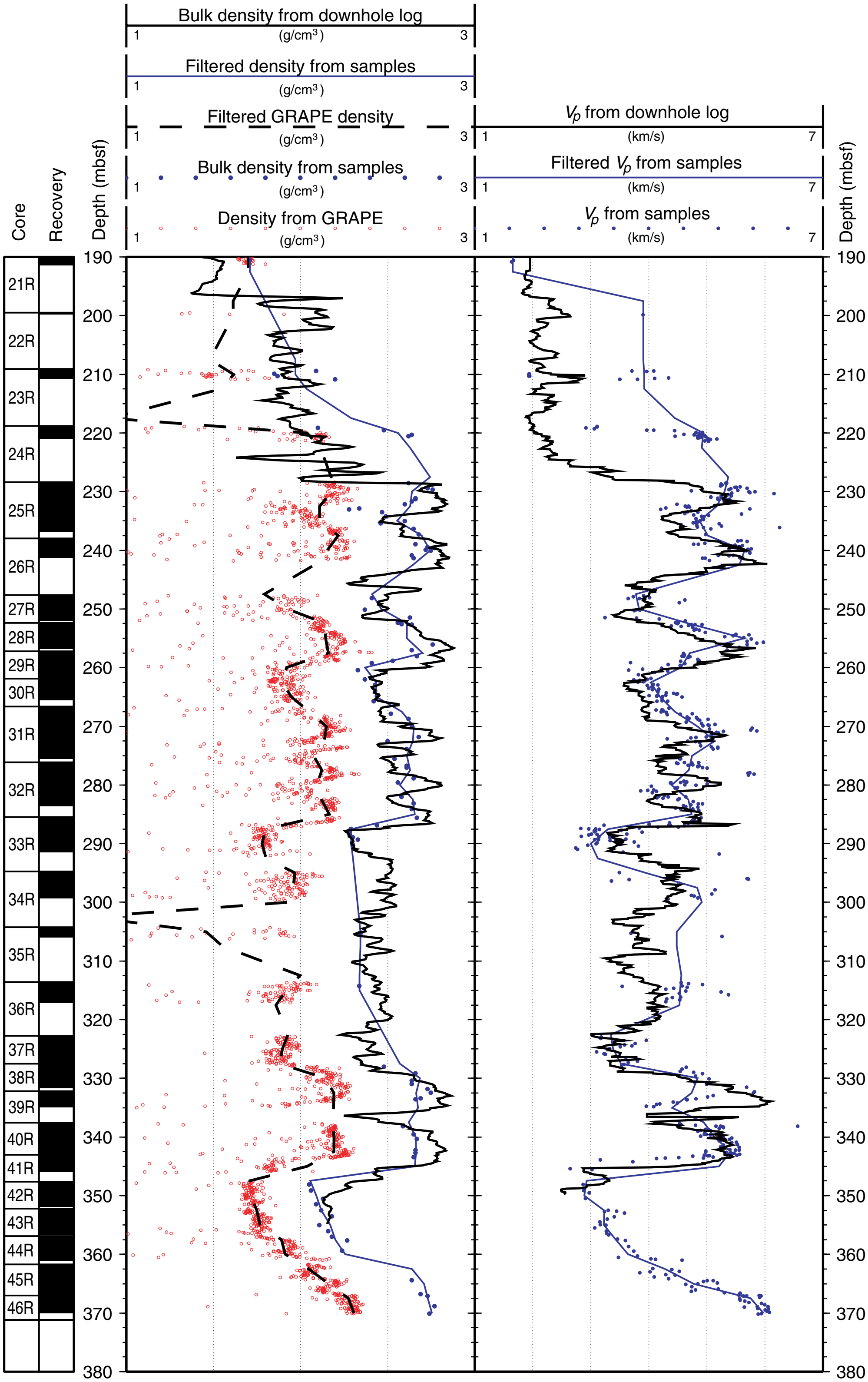

Figure F86. Coherence function estimate of velocities from downhole logs and discrete samples, based on applying Welch's periodiogram averaging method to sample segments 128 points long, corresponding to ~50 m. It illustrates that a unit has to be at least ~5 m thick to be detected at the same location downhole both by logs and index properties measurements on average.

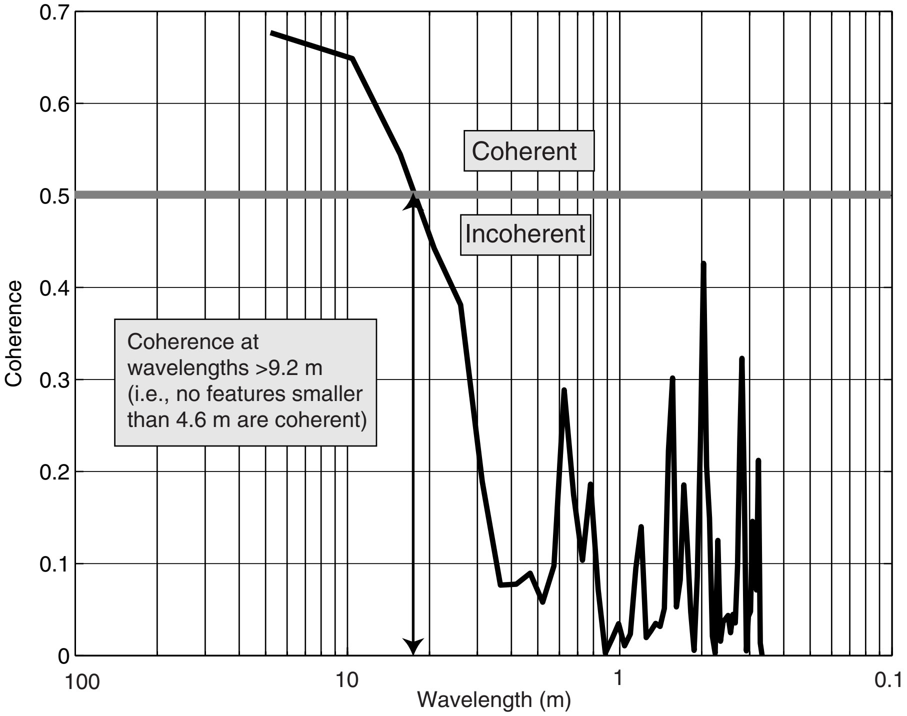

Figure F87. Composite of core recovery, lithostratigraphy, and age (on left), and (**A**) density and velocity as a function of depth, (**B**) density and velocity as a function of two-way traveltime (TWT), (**C**) impedance, (**D**) reflection coefficients without interbed multiples and transmission losses, (**E**) reflection coefficients with interbed multiples and transmission losses, and (**F**) synthetic seismograms based on (D) (black) and (E) (red) as a function of TWT. (**Figure shown on next page.**)

Figure F87. (Caption on previous page.)

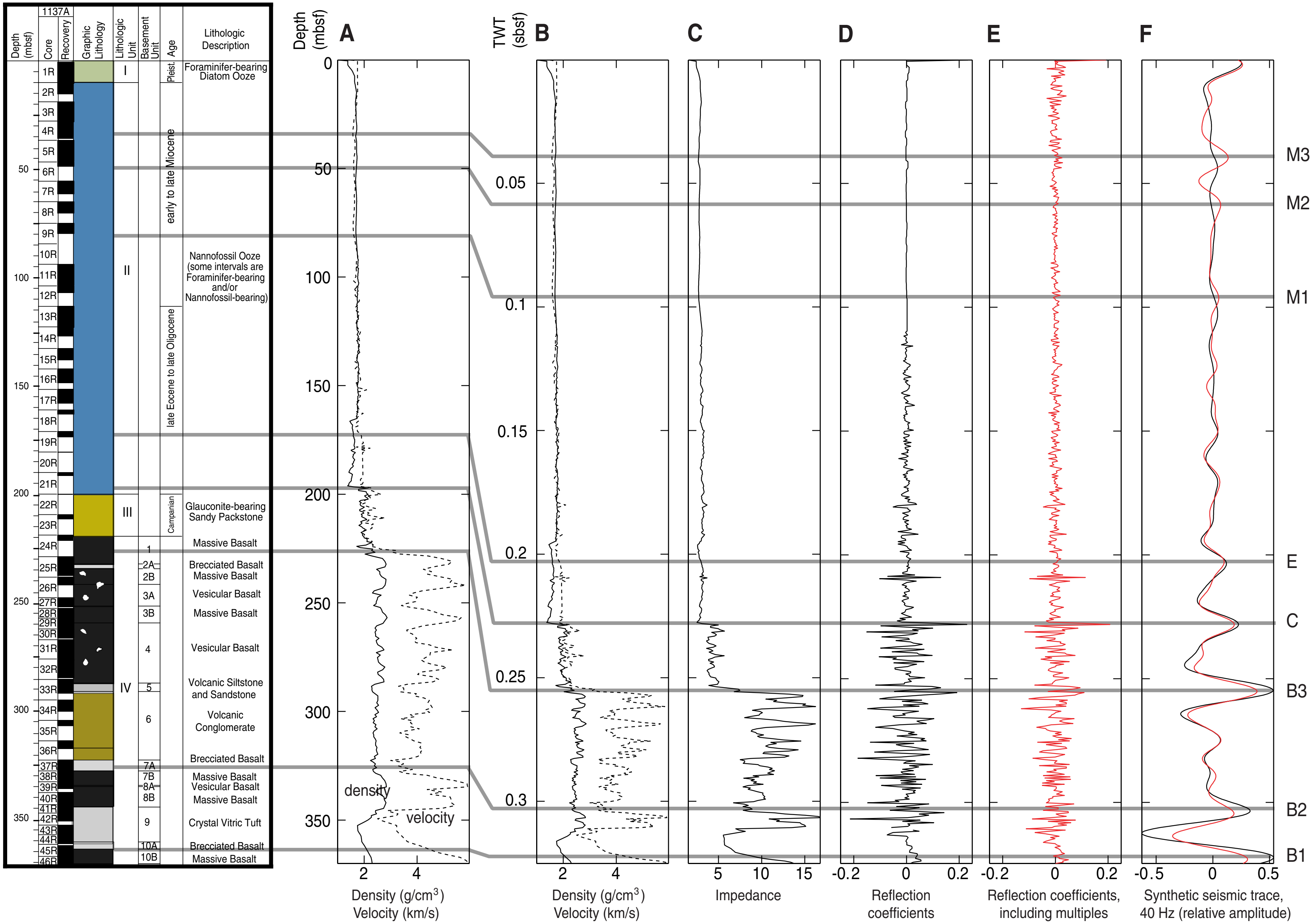

Figure F88. Seismic reflection data from *Rig Seismic* cruise 179, line 601, across Site 1137, and a synthetic seismic trace from Figure F87, p. 156, including multiples and transmission losses. Reflections tied to the synthetic seismogram are labeled. M = early–late Miocene, E = late Eocene–late Oligocene, C = Campanian, B = basement. Vertical exaggeration at seafloor = ~16:1.

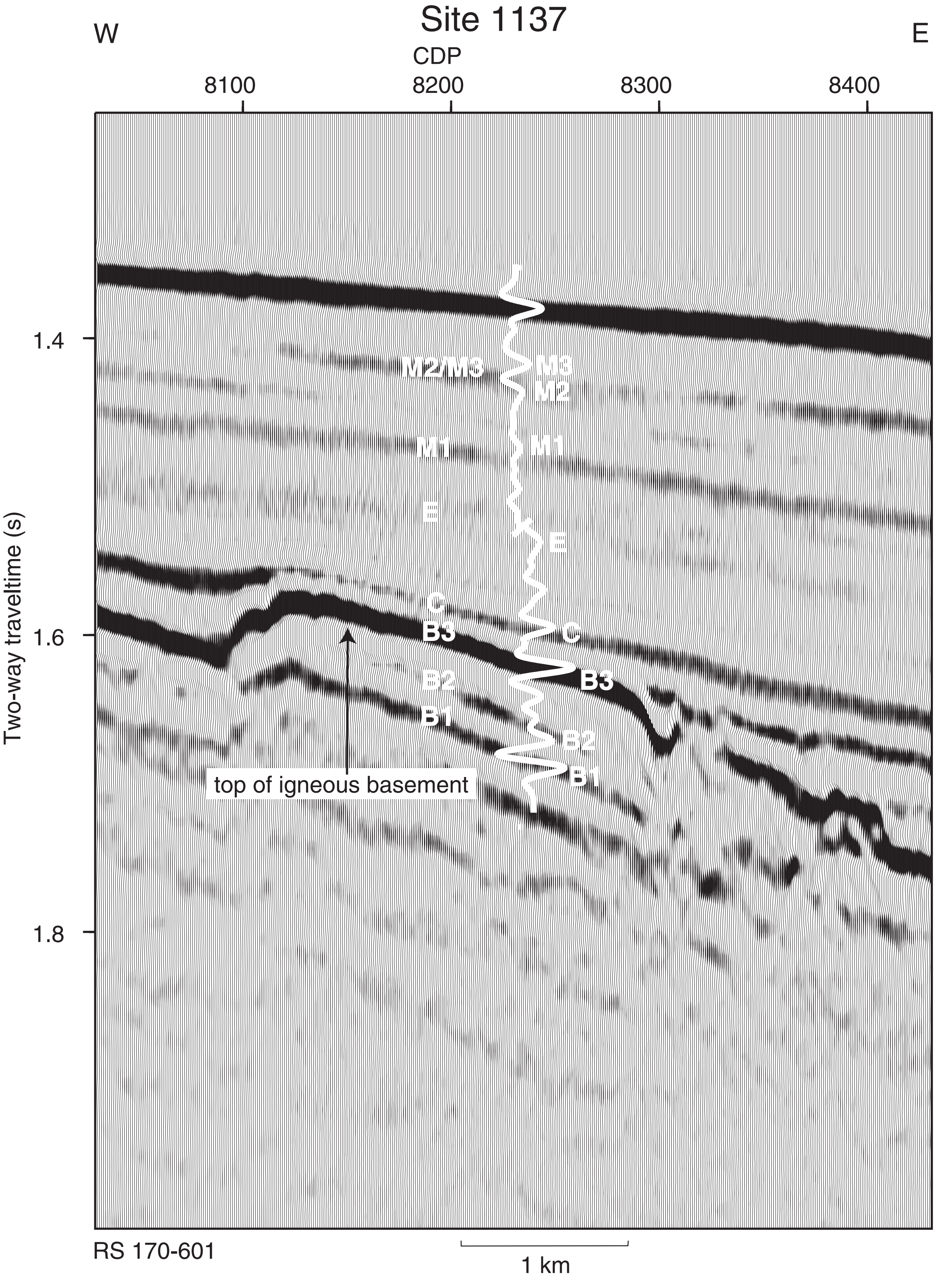

Figure F89. Logging data from Hole 1137A. Natural gamma-ray data are from the first logging run only. **A.** Logging data from the first run. (Continued on next page.)

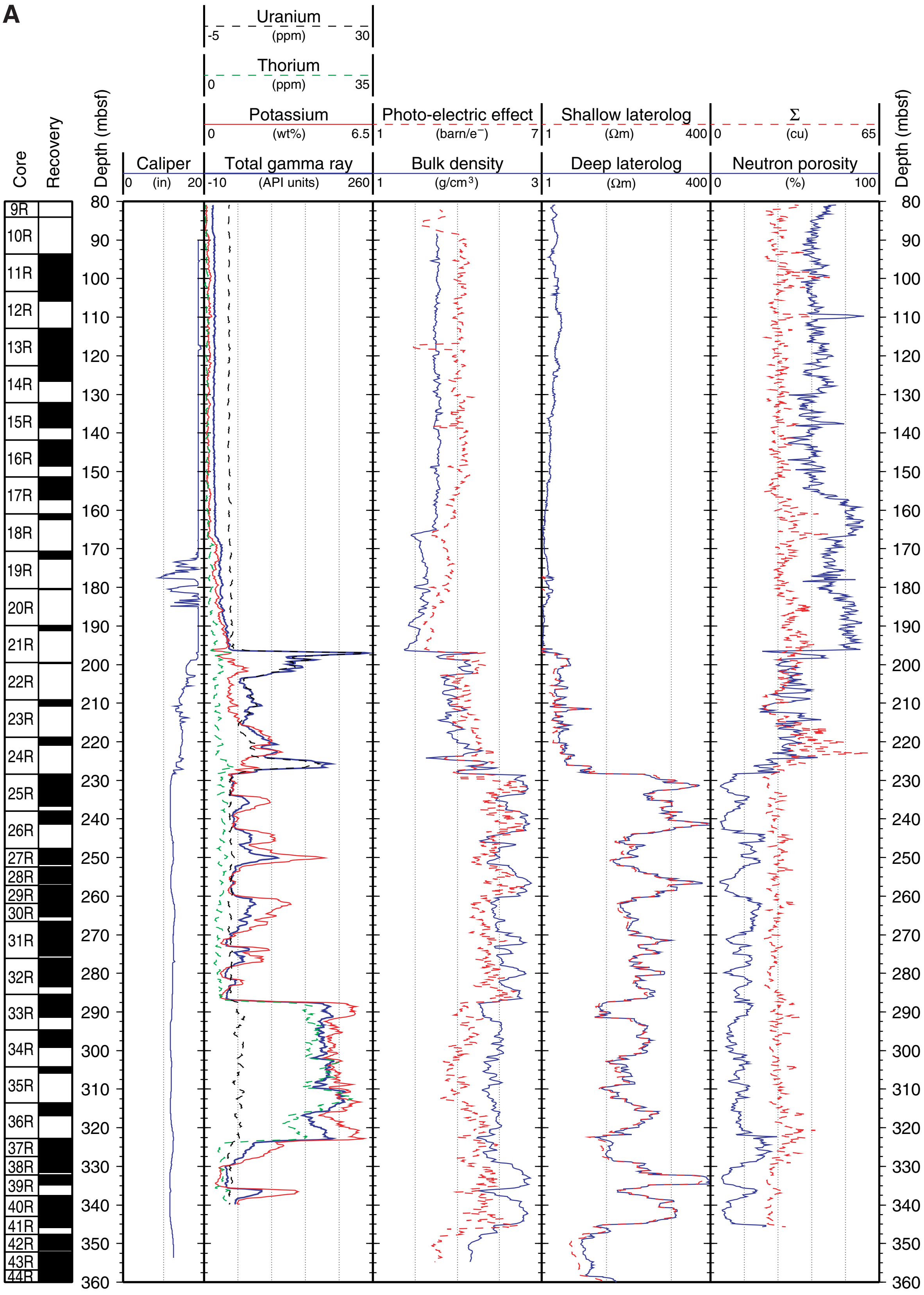

Figure F89 (continued). B. Logging data from the second run and calculated V_p/V_s ratio. Σ = thermal neutron cross section, cu = capture units.

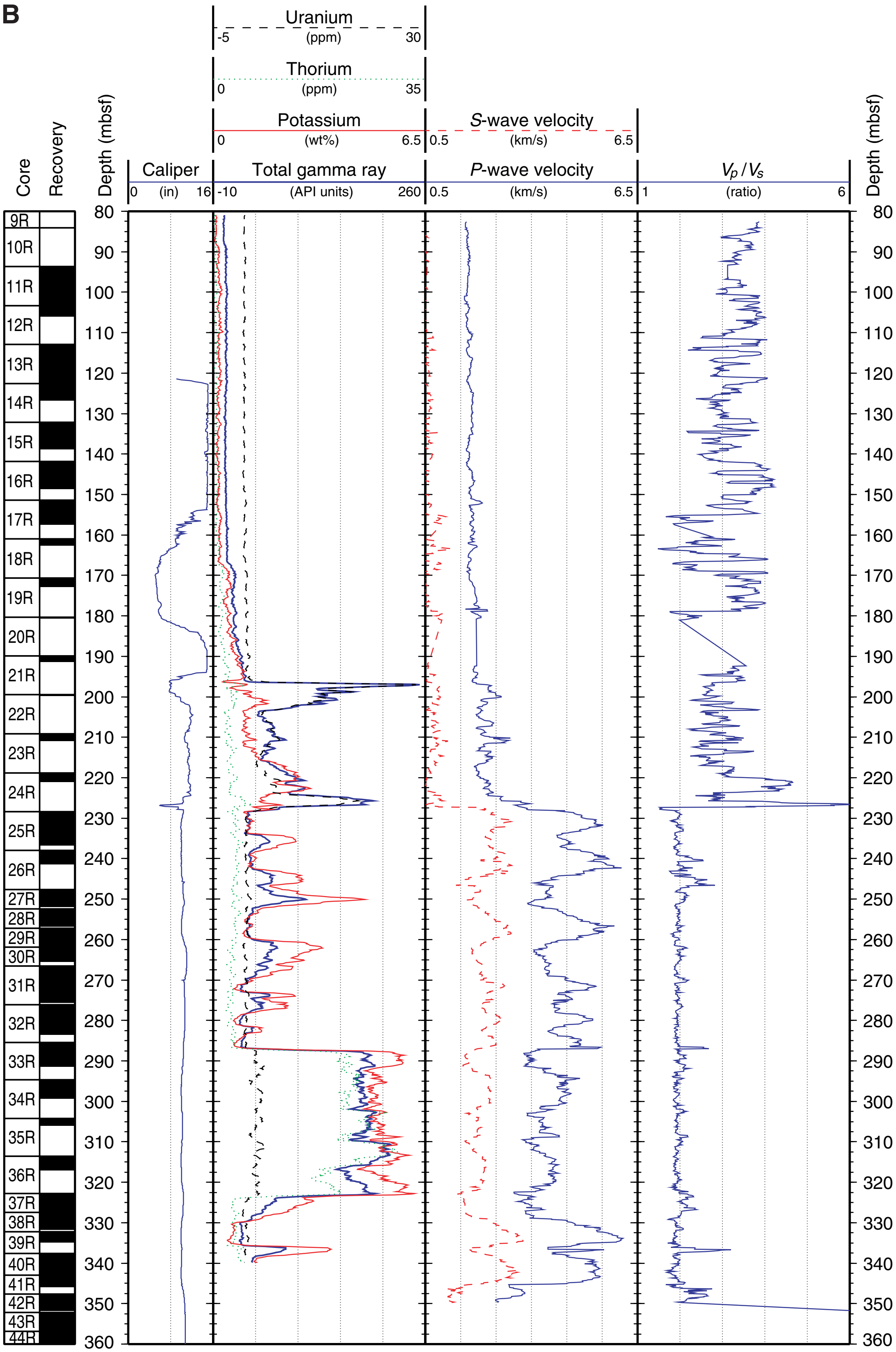

Figure F90. Comparison of densities determined from downhole logs, discrete samples of cores, multisensor track GRAPE measurements, and of compressional wave velocities from downhole logs and discrete core samples (see **"Physical Properties,"** p. 48). Also shown are trends for the data from discrete samples and from the MST after applying a robust mode filter, as described in the text (see **"Seismic Stratigraphy,"** p. 52). This facilitates more rapid comparison among data sets, as outliers are removed by the filter.

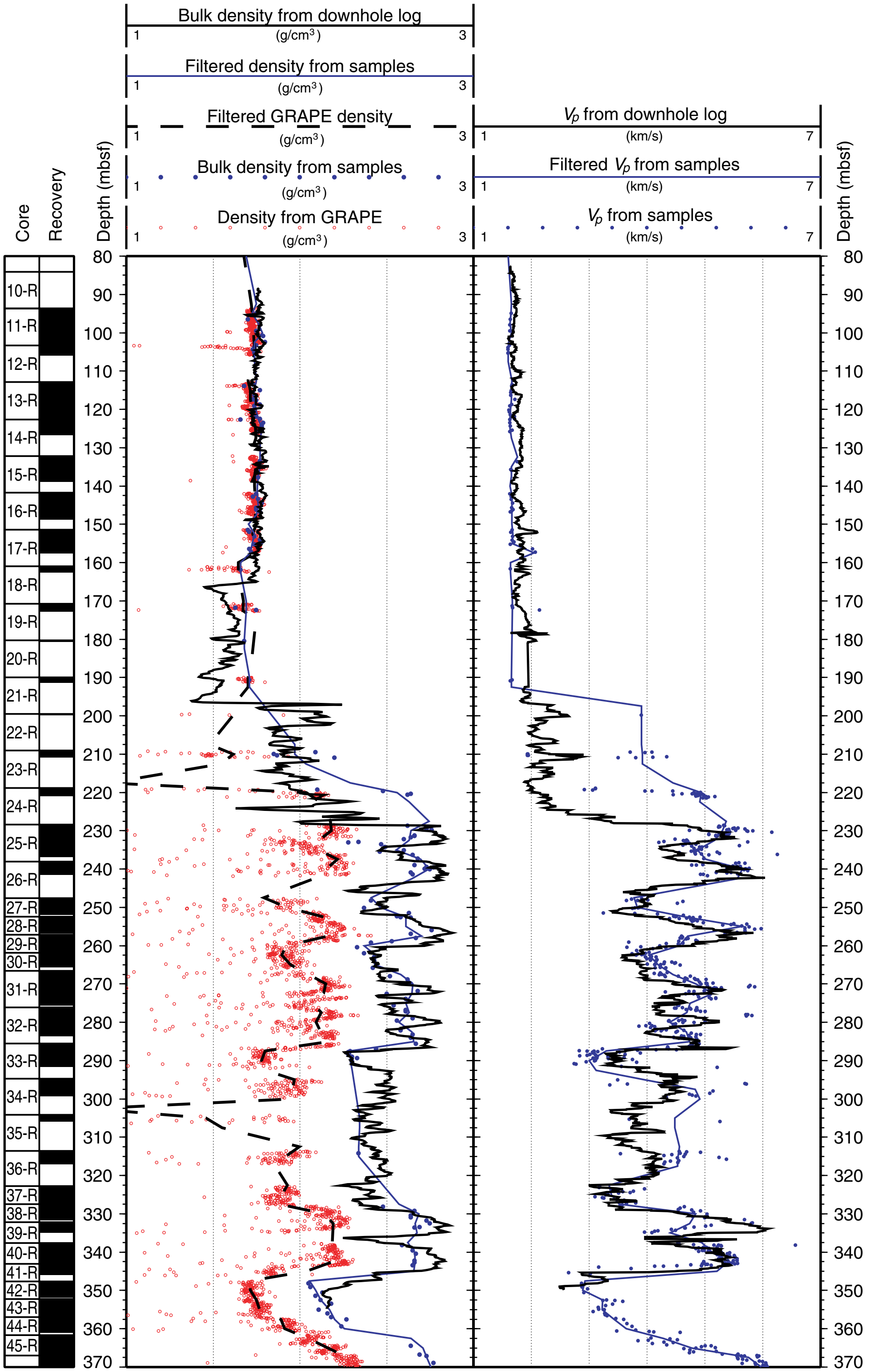

Figure F91. Comparison of logging data and core-derived lithology (see "Lithostratigraphy," p. 3) in Hole 1137A. The integrated interpretation of FMS images and standard logs enables clear identification of the displayed unit boundaries. The log-derived basement unit boundaries are given in Table T13, p. 187 (see "Physical Volcanology," p. 13).

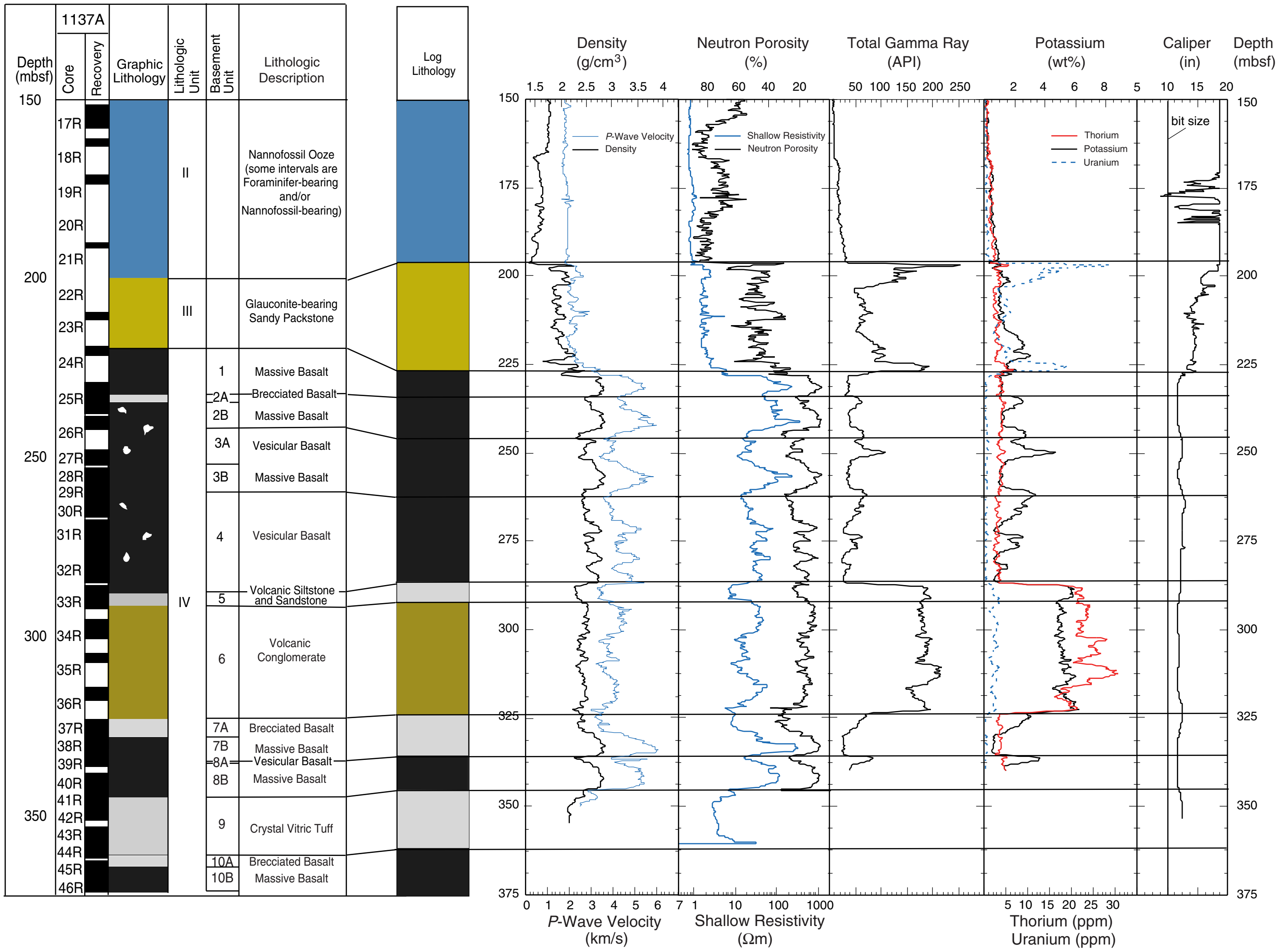

Figure F92. FMS image displaying the sediment–igneous basement transition at 227 mbsf. The horizontal exaggeration = ~4.

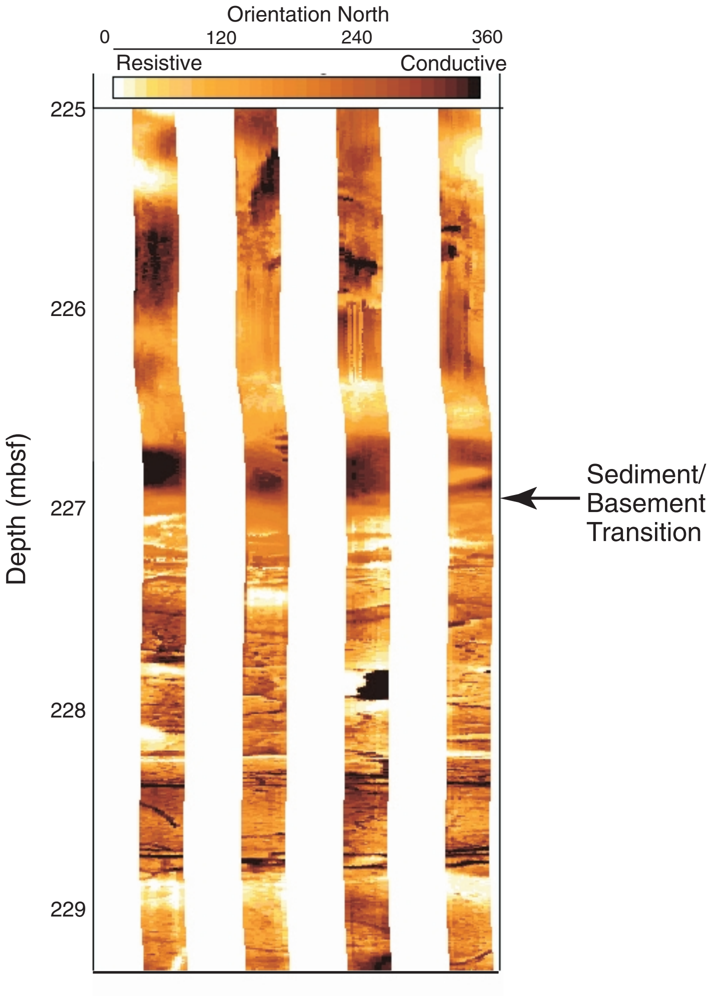

Figure F93. FMS image displaying basement Unit 2. Vesicles can be seen in the upper part of the flow (above 238 mbsf), but they are missing in the massive part. In contrast, the massive part is more fractured. The horizontal exaggeration = ~4.

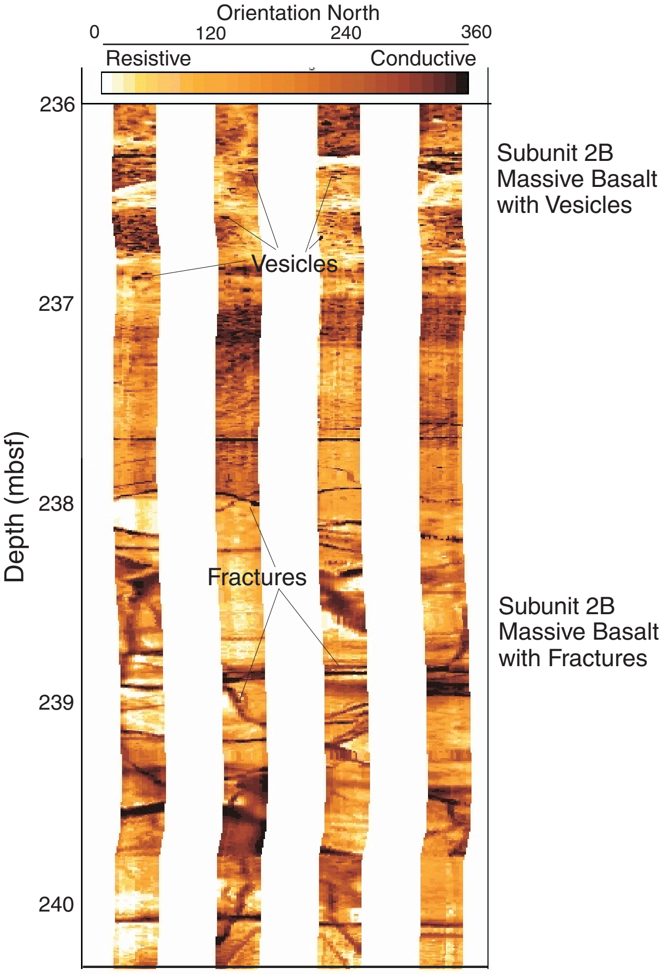

Figure F94. FMS image displaying basement Unit 6. In the volcanic conglomerate, we can identify individual cobbles. The sandy volcanic interbed from 308.4 to 309.3 mbsf reveals bedding structures with a dip of 20° and strike of 151° at the base. The horizontal exaggeration = ~4.

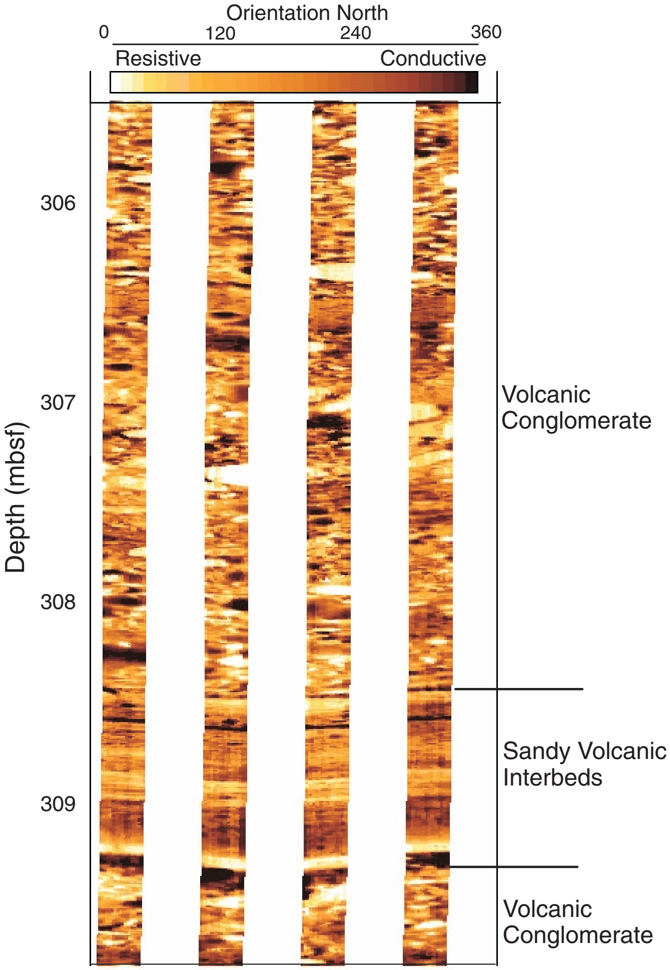

Figure F95. Scatter plots of bulk density vs. compressional wave velocity, shear wave velocity, and porosity, and resistivity vs. porosity.

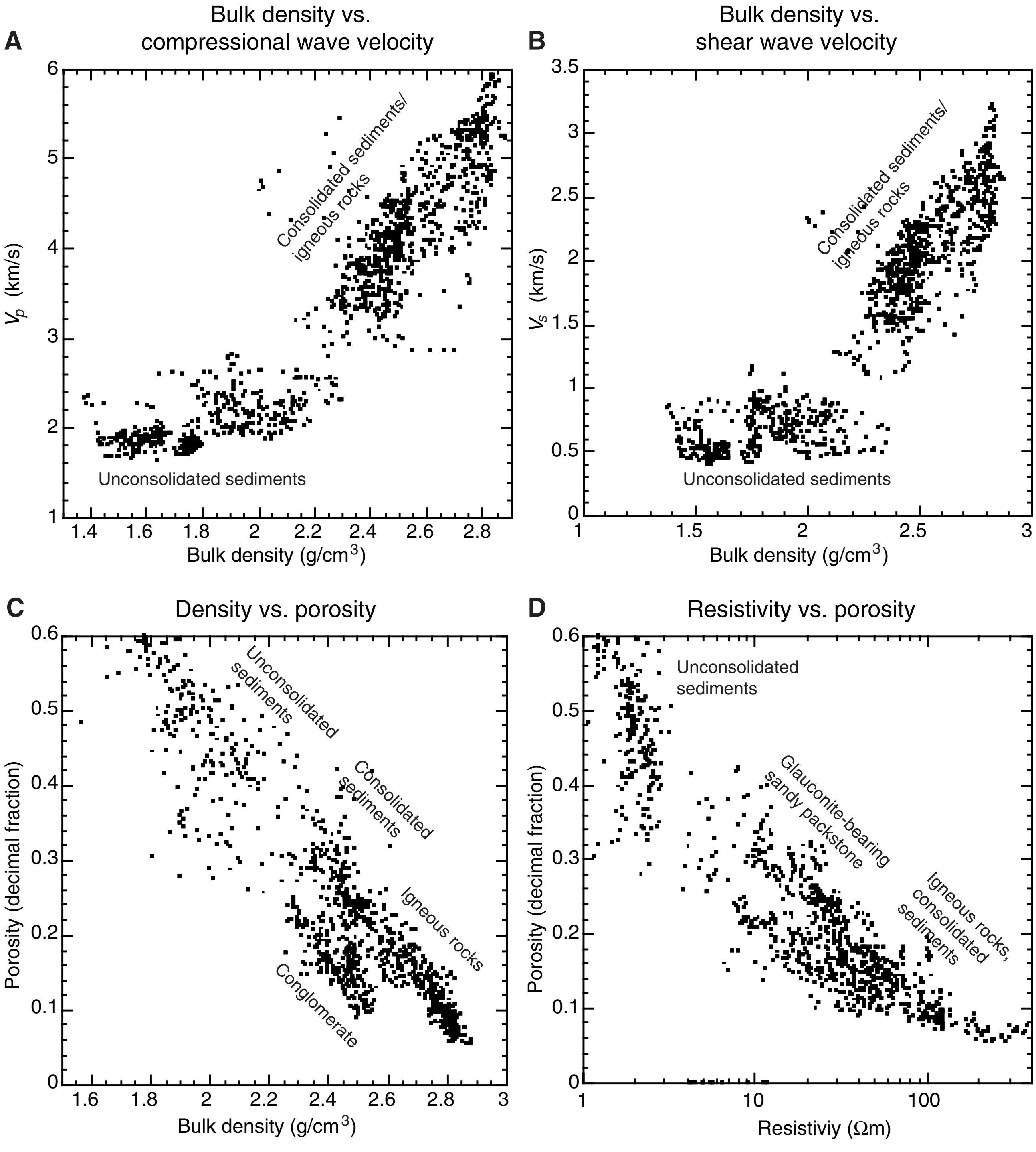

Figure F96. Caliper log showing changes in hole diameter measured along two perpendicular axes (caliper 1 and 2) and the azimuth of caliper 1.

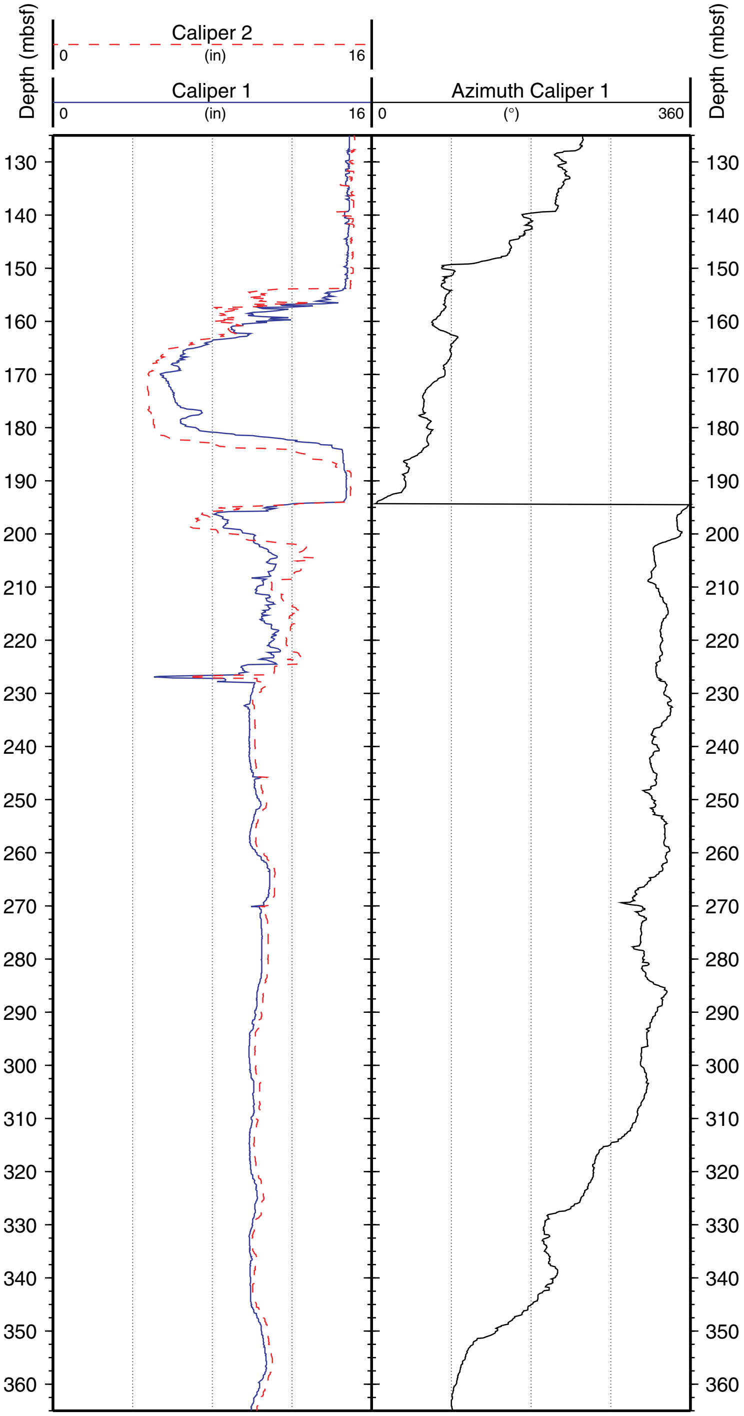

Table T1. Coring summary for Hole 1137A.

Core	Date (1998/ 1999)	Time (UTC)	Depth (mbsf)	Length cored (m)	Length recovered (m)	Recovery (%)
183-1137A-						
1R	31 Dec	1850	0.0-9.5	9.5	9.62	101.3
2R	31 Dec	1940	9.5-18.6	9.1	4.96	54.5
3R	31 Dec	2020	18.6-27.6	9.0	9.73	108.1
4R	31 Dec	2100	27.6-36.8	9.2	8.24	89.6
5R	31 Dec	2135	36.8-46.0	9.2	9.71	105.5
6R	31 Dec	2205	46.0-55.2	9.2	1.59	17.3
7R	31 Dec	2315	55.2-64.8	9.6	6.24	65.0
8R	31 Dec	2355	64.8-74.5	9.7	5.25	54.1
9R	1 Jan	0035	74.5-84.1	9.6	4.73	49.3
10R	1 Jan	0105	84.1-93.7	9.6	0.00	0.0
11R	1 Jan	0140	93.7-103.3	9.6	9.81	102.2
12R	1 Jan	0215	103.3-112.9	9.6	2.70	28.1
13R	1 Jan	0250	112.9-122.6	9.7	9.80	101.0
14R	1 Jan	0325	122.6-132.2	9.6	4.13	43.0
15R	1 Jan	0405	132.2-141.8	9.6	6.62	69.0
16R	1 Jan	0440	141.8-151.4	9.6	6.90	71.9
17R	1 Jan	0515	151.4-161.0	9.6	6.12	63.8
18R	1 Jan	0545	161.0-170.7	9.7	1.65	17.0
19R	1 Jan	0615	170.7-180.3	9.6	2.13	22.2
20R	1 Jan	0645	180.3-189.9	9.6	0.38	4.0
21R	1 Jan	0725	189.9-199.5	9.6	1.51	15.7
22R	1 Jan	0805	199.5-209.1	9.6	0.32	3.3
23R	1 Jan	0915	209.1-218.8	9.7	1.75	18.0
24R	1 Jan	1120	218.8-228.4	9.6	2.20	22.9
25R	1 Jan	1550	228.4-238.0	9.6	8.40	87.5
26R	1 Jan	2015	238.0-247.6	9.6	3.41	35.5
27R	1 Jan	2320	247.6-252.4	4.8	4.39	91.5
28R	2 Jan	0225	252.4-257.2	4.8	4.43	92.3
29R	2 Jan	0515	257.2-261.9	4.7	4.78	101.7
30R	2 Jan	0745	261.9-266.6	4.7	3.64	77.4
31R	2 Jan	1215	266.6-276.1	9.5	9.00	94.7
32R	2 Jan	1700	276.1-285.5	9.4	7.52	80.0
33R	2 Jan	1925	285.5-294.7	9.2	6.02	65.4
34R	2 Jan	2245	294.7-304.2	9.5	4.62	48.6
35R	3 Jan	0115	304.2-313.6	9.4	1.75	18.6
36R	3 Jan	0430	313.6-322.8	9.2	3.45	37.5
37R	3 Jan	0635	322.8-327.5	4.7	4.72	100.4
38R	3 Jan	0920	327.5-332.2	4.7	4.23	90.0
39R	3 Jan	2335	332.2-337.6	5.4	2.74	50.7
40R	4 Jan	0245	337.6-343.0	5.4	5.83	108.0
41R	4 Jan	0525	343.0-347.6	4.6	2.99	65.0
42R	4 Jan	0705	347.6-352.2	4.6	4.27	92.8
43R	4 Jan	0900	352.2-356.9	4.7	4.53	96.4
44R	4 Jan	1045	356.9-361.7	4.8	4.14	86.3
45R	4 Jan	1420	361.7-367.0	5.3	5.37	101.3
46R	4 Jan	1745	367.0-371.2	4.2	3.06	72.9
Totals:				371.2	219.38	59.1

Note: UTC = Universal Time Coordinated. This table is also available in **ASCII format.**

Table T2. Expanded coring summary for Hole 1137A. (See table note. Continued on next four pages.)

Core	Date (1998/ 1999)	Time (UTC)	Depth (mbsf)	Length (m)		Recovery (%)	Section	Length (m)		Section depth (mbsf)	Catwalk samples	Comment
				Cored	Recovered			Liner	Curator			
183-1137A-												
1R	31 Dec	1850	0.0-9.5	9.5	9.62	101.3						
							1	1.50	1.50	0.0-1.5		
							2	1.50	1.50	1.5-3.0		
							3	1.50	1.50	3.0-4.5		
							4	1.50	1.50	4.5-6.0		
							5	1.50	1.50	6.0-7.5	HS	
							6	1.50	1.50	7.5-9.0		
							7	0.52	0.52	9.0-9.5		
							CC(NS)	0.10	0.10	9.52-9.62	PAL	All to PAL
								9.62	9.62			
2R	31 Dec	1940	9.5-18.6	9.1	4.96	54.5						
							1	1.50	1.50	9.5-11.0		
							2	1.50	1.50	11.0-12.5		
							3	1.50	1.50	12.5-14.0	HS	
							4	0.31	0.31	14.0-14.3		
							CC(w/4)	0.15	0.15	14.31-14.46	PAL	
								4.96	4.96			
3R	31 Dec	2020	18.6-27.6	9.0	9.73	108.1						
							1	1.50	1.50	18.6-20.1		
							2	1.50	1.50	20.1-21.6		
							3	1.50	1.50	21.6-23.1		
							4	1.50	1.50	23.1-24.6		
							5	1.50	1.50	24.6-26.1	HS	
							6	1.50	1.50	26.1-27.6		
							7	0.63	0.63	27.6-28.23		
							CC(NS)	0.10	0.10	28.23-28.33	PAL	All to PAL
								9.73	9.73			
4R	31 Dec	2100	27.6-36.8	9.2	8.24	89.6						
							1	1.50	1.50	27.6-29.1		
							2	1.50	1.50	29.1-30.6		
							3	1.50	1.50	30.6-32.1		
							4	1.50	1.50	32.1-33.6		
							5	1.50	1.50	33.6-35.1	HS	
							6	0.53	0.53	35.1-35.63		
							CC(w/6)	0.21	0.21	35.63-35.84		
								8.24	8.24			
5R	31 Dec	2135	36.8-46.0	9.2	9.71	105.5						
							1	1.50	1.50	36.8-38.3		
							2	1.50	1.50	38.3-39.8		
							3	1.50	1.50	39.8-41.3		
							4	1.50	1.50	41.3-42.8		
							5	1.50	1.50	42.8-44.3	HS	
							6	1.50	1.50	44.3-45.8		
							7	0.66	0.66	45.8-46.46		
							CC(NS)	0.05	0.05	46.46-46.51	PAL	All to PAL
								9.71	9.71			
6R	31 Dec	2205	46.0-55.2	9.2	1.59	17.3						
							1	1.36	1.36	46.0-47.36	HS	
							CC(w/CC)	0.23	0.23	47.36-47.59	PAL	
								1.59	1.59			
7R	31 Dec	2315	55.2-64.8	9.6	6.24	65						
							1	1.50	1.50	55.2-56.7		
							2	1.50	1.50	56.7-58.2		
							3	1.50	1.50	58.2-59.7	HS	
							4	1.50	1.50	59.7-61.2		
							CC(w/CC)	0.24	0.24	61.2-61.44	PAL	
								6.24	6.24			
8R	31 Dec	2355	64.8-74.5	9.7	5.25	54.1						
							1	1.50	1.50	64.8-66.3		
							2	1.50	1.50	66.3-67.8		
							3	1.50	1.50	67.8-69.3	HS	
							4	0.70	0.70	69.3-70.0		
							CC(NS)	0.05	0.05	70.0-70.05	PAL	All to PAL
								5.25	5.25			
9R	1 Jan	0035	74.5-84.1	9.6	4.73	49.3						
							1	1.50	1.50	74.5-76.000		
							2	1.50	1.50	76.0-77.500		

Table T2 (continued).

Core	Date (1998/ 1999)	Time (UTC)	Depth (mbsf)	Length (m)		Recovery (%)	Section	Length (m)		Section depth (mbsf)	Catwalk samples	Comment
				Cored	Recovered			Liner	Curator			
							3	1.50	1.50	77.5-79.000	HS	
							4	0.18	0.18	79.0-79.18		
							CC(NS)	0.05	0.05	79.18-79.23	PAL	All to PAL
								4.73	4.73			
10R	1 Jan	0105	84.1-93.7	9.6	0.0	0.0						
11R	1 Jan	0140	93.7-103.3	9.6	9.81	102.2						
							1	1.50	1.50	93.7-95.2		
							2	1.50	1.50	95.2-96.7		
							3	1.50	1.50	96.7-98.2		
							4	1.50	1.50	98.2-99.7		
							5	1.50	1.50	99.7-101.2	HS	
							6	1.50	1.50	101.2-102.7		
							7	0.66	0.66	102.7-103.36		
							CC(w/7)	0.15	0.15	103.36-103.51	PAL	
								9.81	9.81			
12R	1 Jan	0215	103.3-112.9	9.6	2.7	28.1						
							1	1.50	1.50	103.3-104.8		
							2	0.96	0.96	104.8-105.76	HS	
							CC(w/2)	0.24	0.24	105.76-106	PAL	
								2.70	2.70			
13R	1 Jan	0250	112.9-122.6	9.7	9.8	101.0						
							1	1.50	1.50	112.9-114.4		
							2	1.50	1.50	114.4-115.9		
							3	1.50	1.50	115.9-117.4		
							4	1.50	1.50	117.4-118.9		
							5	1.50	1.50	118.9-120.4	HS	
							6	1.50	1.50	120.4-121.9		
							7	0.70	0.60	121.9-122.5		
							CC(NS)	0.10	0.10	122.5-122.6	PAL	All to PAL
								9.80	9.70			
14R	1 Jan	0325	122.6-132.2	9.6	4.13	43.0						
							1	1.50	1.50	122.6-124.1		
							2	1.50	1.50	124.1-125.6	HS	
							3	1.03	1.03	125.6-126.63		
							CC(NS)	0.10	0.10	126.63-126.73	PAL	All to PAL
								4.13	4.13			
15R	1 Jan	0405	132.2-141.8	9.6	6.62	69.0						
							1	1.50	1.50	132.2-133.7		
							2	1.50	1.50	133.7-135.2		
							3	1.50	1.50	135.2-136.7		
							4	1.50	1.50	136.7-138.2	HS	
							5	0.52	0.52	138.2-138.72		
							CC(NS)	0.10	0.10	138.72-138.82	PAL	All to PAL
								6.62	6.62			
16R	1 Jan	0440	141.8-151.4	9.6	6.9	71.9						
							1	1.50	1.50	141.8-143.3		
							2	1.50	1.50	143.3-144.8		
							3	1.50	1.50	144.8-146.3		
							4	1.50	1.50	146.3-147.8	HS	
							5	0.80	0.80	147.8-148.6		
							CC(NS)	0.10	0.10	148.6-148.7	PAL	All to PAL
								6.90	6.90			
17R	1 Jan	0515	151.4-161	9.6	6.12	63.8						
							1	1.50	1.50	151.4-152.9		
							2	1.50	1.50	152.9-154.4		
							3	1.50	1.50	154.4-155.9	HS	
							4	1.47	1.47	155.9-157.37		
							CC(NS)	0.15	0.15	157.37-157.52	PAL	All to PAL
								6.12	6.12			
18R	1 Jan	0545	161.0-170.7	9.7	1.65	17.0						
							1	1.50	1.50	161.0-162.5	HS	
							CC(NS)	0.15	0.15	162.5-162.65	PAL	All to PAL
								1.65	1.65			
19R	1 Jan	0615	170.7-180.3	9.6	2.13	22.2						
							1	1.50	1.50	170.7-172.2		
							2	0.48	0.48	172.2-172.68	HS	
							CC(NS)	0.15	0.15	172.68-172.83	PAL	All to PAL

Table T2 (continued).

Core	Date (1998/ 1999)	Time (UTC)	Depth (mbsf)	Length (m)		Recovery (%)	Section	Length (m)		Section depth (mbsf)	Catwalk samples	Comment
				Cored	Recovered			Liner	Curator			
								2.13	2.13			
20R	1 Jan	0645	180.3-189.9	9.6	0.38	4.0						
							1	0.28	0.28	180.3-180.58	HS	
							CC(NS)	0.10	0.10	180.58-180.68	PAL	All to PAL
								0.38	0.38			
21R	1 Jan	0725	189.9-199.5	9.6	1.51	15.7						
							1	1.34	1.34	189.9-191.24	HS	
							CC(w/1)	0.17	0.17	191.24-191.41	PAL	
								1.51	1.51			
22R	1 Jan	0805	199.5-209.1	9.6	0.32	3.3						
							1	0.32	0.32	199.5-199.82		
								0.32	0.32			
23R	1 Jan	0915	209.1-218.8	9.7	1.75	18.0						
							1	0.25	1.48	209.1-210.58		
							2	1.50	0.30	210.58-210.88		
								1.75	1.78			
24R	1 Jan	1120	218.8-228.4	9.6	2.2	22.9						
							1	0.70	1.49	218.8-220.29		
							2	1.50	1.16	220.29-221.45		
								2.20	2.65			
25R	1 Jan	1550	228.4-238	9.6	8.4	87.5						
							1	1.02	1.44	228.4-229.84		
							2	1.38	1.38	229.84-231.22		
							3	1.46	1.47	231.22-232.69		
							4	1.35	1.17	232.69-233.86		
							5	1.50	1.47	233.86-235.33		
							6	1.39	0.85	235.33-236.18		
							7	0.30	1.41	236.18-237.59		
								8.40	9.19			
26R	1 Jan	2015	238.0-247.6	9.6	3.41	35.5						
							1	0.50	1.48	238-239.48		
							2	1.27	1.46	239.48-240.94		
							3	1.40	0.93	240.94-241.87		
							4	0.24	0.00			
								3.41	3.87			
27R	1 Jan	2320	247.6-252.4	4.8	4.39	91.5						
							1	1.44	1.49	247.6-249.09		
							2	1.46	1.49	249.09-250.58		
							3	1.49	1.34	250.58-251.92		
							4	0.00	1.08	251.92-253		
								4.39	5.4			
28R	2 Jan	0225	252.4-257.2	4.8	4.43	92.3						
							1	1.50	1.50	252.4-253.9		
							2	1.47	1.49	253.9-255.39		
							3	1.46	1.50	255.39-256.89		
							4	0.00	0.44	256.89-257.33		
								4.43	4.93			
29R	2 Jan	0515	257.2-261.9	4.7	4.78	101.7						
							1	0.95	1.26	257.2-258.46		
							2	0.83	1.44	258.46-259.9		
							3	1.50	1.50	259.9-261.4		
							4	1.50	1.05	261.4-262.45		
								4.78	5.25			
30R	2 Jan	0745	261.9-266.6	4.7	3.64	77.4						
							1	1.20	1.34	261.9-263.24		
							2	0.94	0.99	263.24-264.23		
							3	1.50	1.28	264.23-265.51		
							4	0.00	0.33	265.51-265.84		
								3.64	3.94			
31R	2 Jan	1215	266.6-276.1	9.5	9.0	94.7						
							1	1.39	1.50	266.6-268.1		
							2	1.21	1.50	268.1-269.6		
							3	1.30	0.90	269.6-270.5		
							4	1.28	1.50	270.5-272		
							5	0.85	1.39	272.0-273.39		
							6	1.47	1.50	273.39-274.89		
							7	1.50	1.49	274.89-276.38		
							8	0.00	0.23	276.38-276.61		
								9.00	10.01			
32R	2 Jan	1700	276.1-285.5	9.4	7.52	80.0						

Table T2 (continued).

Core	Date (1998/ 1999)	Time (UTC)	Depth (mbsf)	Length (m)		Recovery (%)	Section	Length (m)		Section depth (mbsf)	Catwalk samples	Comment
				Cored	Recovered			Liner	Curator			
							1	0.48	0.87	276.1-276.97		
							2	1.35	1.09	276.97-278.06		
							3	1.33	1.34	278.06-279.4		
							4	1.50	1.41	279.4-280.81		
							5	1.46	1.41	280.81-282.22		
							6	1.40	1.50	282.22-283.72		
							7	0.00	0.59	283.72-284.31		
								7.52	8.21			
33R	2 Jan	1925	285.5-294.7	9.2	6.02	65.4						
							1	1.43	1.47	285.5-286.97		
							2	1.41	1.50	286.97-288.47		
							3	1.50	1.33	288.47-289.8		
							4	1.44	1.39	289.8-291.19		
							5	0.24	0.95	291.19-292.14		
								6.02	6.64			
34R	2 Jan	2245	294.7-304.2	9.5	4.62	48.6						
							1	0.40	0.74	294.7-295.44		
							2	1.46	1.45	295.44-296.89		
							3	1.28	1.45	296.89-298.34		
							4	1.48	1.43	298.34-299.77		
								4.62	5.07			
35R	3 Jan	0115	304.2-313.6	9.4	1.75	18.6						
							1	0.30	1.46	304.2-305.66		
							2	1.45	0.76	305.66-306.42		
								1.75	2.22			
36R	3 Jan	0430	313.6-322.8	9.2	3.45	37.5						
							1	0.60	1.35	313.6-314.95		
							2	1.50	1.40	314.95-316.35		
							3	1.35	0.81	316.35-317.16		
								3.45	3.56			
37R	3 Jan	0635	322.8-327.5	4.7	4.72	100.4						
							1	0.73	0.73	322.8-323.53		
							2	1.19	1.19	323.53-324.72		
							3	0.95	0.95	324.72-325.67		
							4	0.92	0.92	325.67-326.59		
							5	0.93	0.93	326.59-327.52		
								4.72	4.72			
38R	3 Jan	0920	327.5-332.2	4.7	4.23	90.0						
							1	1.28	1.35	327.5-328.85		
							2	1.50	0.47	328.85-329.32		
							3	1.45	1.36	329.32-330.68		
							4	0.00	1.20	330.68-331.88		
								4.23	4.38			
39R	3 Jan	2335	332.2-337.6	5.4	2.74	50.7						
							1	1.24	1.30	332.2-333.5		
							2	1.50	1.50	333.5-335.0		
							3	0.00	0.14	335.0-335.14		
								2.74	2.94			
40R	4 Jan	0245	337.6-343.0	5.4	5.83	108.0						
							1	1.50	0.43	337.6-338.03		
							2	1.12	1.42	338.03-339.45		
							3	1.50	1.47	339.45-340.92		
							4	1.47	1.45	340.92-342.37		
							5	0.24	1.38	342.37-343.75		
								5.83	6.15			
41R	4 Jan	0525	343.0-347.6	4.6	2.99	65.0						
							1	1.44	1.50	343.0-344.5		
							2	1.30	1.12	344.5-345.62		
							3	0.25	0.69	345.62-346.31		
								2.99	3.31			
42R	4 Jan	0705	347.6-352.2	4.6	4.27	92.8						
							1	0.61	0.61	347.6-348.21		
							2	1.50	1.50	348.21-349.71		
							3	0.98	0.98	349.71-350.69		
							4	1.18	1.18	350.69-351.87		
								4.27	4.27			
43R	4 Jan	0900	352.2-356.9	4.7	4.53	96.4						
							1	0.85	0.85	352.2-353.05		

Table T2 (continued).

Core	Date (1998/ 1999)	Time (UTC)	Depth (mbsf)	Length (m)		Recovery (%)	Section	Length (m)		Section depth (mbsf)	Catwalk samples	Comment
				Cored	Recovered			Liner	Curator			
							2	1.47	1.47	353.05-354.52		
							3	1.41	1.41	354.52-355.93		
							4	0.80	0.80	355.93-356.73		
								4.53	4.53			
44R	4 Jan	1045	356.9-361.7	4.8	4.14	86.3						
							1	0.62	0.62	356.9-357.52		
							2	1.28	1.28	357.52-358.8		
							3	1.38	1.38	358.8-360.18		
							4	0.86	0.86	360.18-361.04		
								4.14	4.14			
45R	4 Jan	1420	361.7-367	5.3	5.37	101.3						
							1	1.27	1.27	361.7-362.97		
							2	1.30	1.30	362.97-364.27		
							3	1.30	1.30	364.27-365.57		
							4	1.50	1.50	365.57-367.07		
								5.37	5.37			
46R	4 Jan	1745	367.0-371.2	4.2	3.06	72.9						
							1	0.42	1.47	367.0-368.47		
							2	1.17	1.33	368.47-369.8		
							3	1.47	0.37	369.8-370.17		
								3.06	3.17			
			Totals:	371.2	219.38	59.1						

Notes: UTC = Universal Time Coordinated. CC = core catcher (number in parenthesis indicates which section the core catcher is stored with), NS = all of the core catcher was used for paleontology sample. HS = headspace gas sample, PAL = paleontology sample. This table is also available in **ASCII format.**

Table T3. Summary of lithologic units at Site 1137.

Lithologic unit	Basement unit	Core interval	Depth (mbsf)	Thickness (m)	Age	Lithology	Interpretation
I		1R-1, 0 cm, to 1R-CC, 10 cm	0–9.50	9.50	Pleistocene	Foraminifer-bearing diatom ooze	Pelagically deposited sediment—deep marine
II		2R-1, 0 cm, to 21R-CC, 10 cm	9.50–199.50	190.00	Miocene to Eocene	Nannofossil ooze	Pelagically deposited sediment—deep marine
III		22R-1, 0 cm, to 24R-1, 71 cm	199.50–219.51	19.91	Campanian	Gray to green glauconite-bearing sandy packstone	Mixed biogenic and altered volcanic sand deposited in a neritic environment
IV	1–10	24R-1, 71 cm, to 46R-3, 36 cm	219.51–370.17	150.76	Cretaceous(?) Campanian or older	Basement—basalt and sedimentary rocks	Volcanic extrusions and fluvial and marine deposition
IV	5	33R-1, 122 cm, to 33R-4, 121 cm	286.72–291.01	4.29	Cretaceous(?) Campanian or older	Volcanic lithic siltstone and sandstone	Fluvial(?)—braided river
IV	6	33R-4, 121 cm, to 37R-3, 0 cm	291.01–322.80	31.79	Cretaceous(?) Campanian or older	Volcanic conglomerate	Fluvial(?)—braided river
IV	9	41R-1, 103 cm, to 44R-4, 49 cm	344.03–360.67	16.64	Cretaceous(?) Campanian or older	Crystal-vitric tuff	Debris flow(?) in marine environment

Table T4. X-ray diffraction results and carbonate contents expressed as $CaCO_3$ for Hole 1137A.

Core, section, interval (cm)	Depth (mbsf)	Minerals	$CaCO_3$ (wt%)
Unit I			
183-1137A-			
1R-1, 89	0.89	Opal-A, opal-CT, calcite, ?orthoclase, (quartz)	51
Unit II			
183-1137A-			
2R-1, 59	10.09	Calcite	88
3R-1, 89	19.49	Calcite	92
4R-1, 89	28.49	Calcite	95
5R-1, 89	37.69	Calcite	91
6R-1, 89	46.89	Calcite	89
7R-1, 89	56.09	Calcite	92
8R-1, 89	65.69	Calcite	95
9R-1, 89	75.39	Calcite	94
11R-1, 89	94.59	Calcite	95
12R-1, 91	104.21	Calcite	95
13R-1, 89	113.79	Calcite	92
14R-1, 89	123.49	Calcite	95
15R-1, 89	133.09	Calcite	95
16R-1, 89	142.69	Calcite	95
17R-1, 89	152.29	Calcite	95
18R-1, 88	161.88	Calcite	94
19R-1, 89	171.59	Calcite	96
21R-1, 87	190.77	Calcite	93
Unit III			
183-1137A-			
22R-1, 6	199.56	—	77
23R-2, 10	210.68	—	76
24R-1, 40	219.20	Quartz, glass/opal-A, opal-CT, glauconite, calcite, hematite, marcasite, pyrite	3

Note: See **"Organic and Inorganic Geochemistry,"** p. 51.

Table T5. Summary of thin sections at Site 1137.

Core, section, interval (cm)	Lithologic unit	Lithology	Mineral components (%)	Lithic components (%)	Bioclastic components (%)	Matrix and cement (%)	Texture
22R-1, 26-31	III	Glauconite-bearing sandy packstone	Glauconite, quartz	None	Shells, benthic foraminifers, ostracodes, bivalves (molds), planktonic foraminifers, sponge spicules	Micrite, chalcedony	High matrix content, packstone
24R-1, 35-38	III	Glauconite-bearing sandy packstone	Glauconite, hornblende, superficial ooids	None	Shells, benthic foraminifers, planktonic foraminifers	Silicified micrite, opal cements	High matrix content, packstone
33R-3, 50-53	IV, Basement Unit 5	Siltstone and sandstone	Feldspar, quartz, garnet, hornblende, biotite	Volcanic rocks	None	None	Well sorted, angular grains, fine- to medium-sand size, matrix poor

Table T6. Summary of Site 1137 volcaniclastic components.

Lithologic (basement) unit	Core interval	Depth (mbsf)	Thickness (m)	Age	Lithologies with volcanic components	Volcanic components	Authigenic and secondary minerals
I	1R-1, 0 cm, to 1R-CC, 10 cm	0-9.50	9.50	middle Pleistocene	Foraminifer-bearing diatom ooze	<2% silt- to sand-sized basaltic lithic fragments and glass shards, <2% felsic glass shards and pumice lapilli	Mafic glass has green smectite clay minerals (nontronite, saponite) forming rims
IV (5)	33R-1, 122 cm, to 33R-4,121 cm	286.72-291.00	4.28	late Campanian or older	Volcaniclastic dark greenish gray siltstones and light gray sandstones	65%-70% volcanic lithics (basalt, trachyte), 10%-15% feldspar (K-feldspar)	Green to gray iron-rich smectite clay minerals (nontronite, saponite)
IV (6)	33R-4, 120 cm, to 37R-1, 0 cm	291.01-322.80	31.80	late Campanian or older	Gray volcanic conglomerate	Principal clast types: plagioclase-phyric basalt, feldspar-phyric flow-banded and massive trachyte	Green iron-rich smectite clay (nontronite, saponite), minor hematite/goethite in oxidized rims
IV (9)	41R-1, 103 cm, to 44R-4, 49 cm	344.03-360.67	16.60	late Campanian or older	Green crystal-vitric tuff	50% felsic glass shards, 40% sanidine, 1%-2% amphibole, quartz and plagioclase feldspar, <5% lithic rip-up clasts	Green nontronite, saponite and possibly celadonite, some kaolinite, minor hematite and goethite in oxidized zone

Table T7. Curated positions and depths of Site 1137 basement units.

Unit/ Subunit	Curated position of top (cm)	Curated depth (mbsf)	Dominant lithology
1	24R-1, 71	219.51	Massive basalt
2A	25R-3, 100	232.22	Brecciated basalt
2B	25R-5, 27	234.13	Massive basalt
3A	27R-1, 0	247.60	Vesicular basalt
3B	28R-1, 0	252.40	Massive basalt
4	29R-2, 64	259.10	Vesicular basalt
5	33R-1, 122	286.72	Volcanic lithic sandstone/siltstone
6	33R-4, 121	291.01	Volcanic conglomerate
7A	37R-1, 0	322.80	Brecciated basalt
7B	38R-1, 23	327.73	Massive basalt
8A	39R-2, 64	334.14	Vesicular basalt
8B	40R-1, 0	337.60	Massive basalt
9	41R-1, 103	344.03	Crystal vitric tuff
10A	44R-4, 49	360.67	Brecciated basalt
10B	45R-2, 100	363.97	Massive basalt

Table T8. Curated downhole depths of key horizons in the Site 1137 lava flows.

Feature	Depth from logging (mbsf)	Curated depth (mbsf)
First intact lava (top of Unit 1)	227	219.51
Contact between Units 1 and 2	233.1	232.22
Unit 2 breccia becomes coherent	235-237	234.20
Contact between Units 2 and 3	243.2	247.60
Zone with extensive fracturing	244.6-246.0	NM
Unit 3 transition from vesicular top to massive interior	252.8	251.42
Base of Unit 3 (flow on Unit 4 silt)	259.8	259.10
Top of lava of Unit 4 (under ~8 cm of silt)	259.9	259.18
Contact between Units 4 and 5 (lava over volcanic sandstone)	286.5	286.72
Contact between Units 5 and 6 (sandstone over conglomerate)	290.9	291.01
Contact between Units 6 and 7 (conglomerate over lava)	321.9	322.80
Unit 7 breccia becomes coherent	327.7	327.73
Contact between Units 7 and 8 (massive lava over basal breccia)	334.6	334.14
Basal breccia over Unit 8 flow top	335	NM
Unit 8 transition from vesicular flow top to massive interior	338	335.14
Contact between Units 8 and 9 (lava over crystal vitric tuff)	345.6	344.03
Contact between Units 9 and 10 (crystal vitric tuff over lava)	360.5	360.67
Unit 10 breccia becomes coherent	364	363.97
Base of Hole 1137A	371.2	371.20

Note: NM = not measured.

Table T9. Site 1137 lava-flow thickness and recovery.

Basement unit/subunit	Thickness (m) Based on logging depths	Thickness (m) Based on curated depths	Recovery (m)	Recovery (%)
1	6.1	12.71	5.42	89
2A	2.9	1.98	1.79	62
2B	7.2	13.40	6.82	95
2 totals:	10.1	15.38	8.61	85
3A	9.6	3.82	4.68	49
3B	7.0	7.68	6.46	92
3 totals:	16.6	11.50	11.14	67
4	26.7	27.62	24.22	91
5	4.4	4.29	4.29	98
6	31.0	31.79	11.98	39
7A	5.8	4.93	4.62	83
7B	7.2	6.41	5.66	99
7 totals:	13.0	11.34	10.28	77
8A	3.4	1.00	0.92	27
8B	7.6	8.89	7.03	92
8 totals:	11.0	9.89	7.95	72
9	14.9	16.64	12.67	85
10A	3.5	3.30	3.05	87
10B	6.2	6.24	6.20	100
10 totals:	9.7	9.54	9.25	95

Note: Percent recovery is calculated using downhole logging-derived unit thicknesses.

Table T10. Petrographic and unit summary of igneous basement sampled at Site 1137. (**See table note.** Continued on next page.)

Basement unit	Unit type	Thickness (m) Total	Thickness (m) Subunit	Rock/flow type	Phenocryst/ major minerals	Groundmass/ minor minerals	Thin sections detailed in "**Petrography and Primary Mineralogy,**" p. 30
1	Plagioclase-phyric basalt	6.1		Massive	Plagioclase (1%) Olivine (0%-8%) Clinopyroxene (<1%)	Basaltic groundmass*	25R-1, 105-106 cm 25R-3, 90-93 cm
2	Aphyric basalt	10.1	A 2.9	Brecciated	Plagioclase (20%-25%) Olivine (2%-5%) Clinopyroxene (2%-5%)	Basaltic groundmass	25R-4, 11-13 cm 25R-4, 33-35 cm 25R-4, 77-81 cm
			B 7.2	Massive	Plagioclase (<1%) Clinopyroxene (0%-1%) Olivine (0%-1%)	Basaltic groundmass Pentlandite (tr)	25R-5, 113-115 cm 26R-1, 140-142 cm 26R-2, 7-8; 38-40 cm
3	Plagioclase-phyric basalt	16.6	A 9.6	Vesicular	Plagioclase (5%) Olivine (3%)	Basaltic groundmass	27R-2, 24-27 cm
			B 7	Massive	Plagioclase (1%) Clinopyroxene (0%-1%) Olivine (0%-0.5%)	Basaltic groundmass	27R-4, 66-68 cm 28R-4, 30-32 cm 29R-2; 35-38 cm
4	Plagioclase-phyric basalt	26.6		Vesicular	Plagioclase (11%-20%); Clinopyroxene (1.5%-5%); Olivine (0.5%-3%)	Basaltic groundmass Pentlandite (tr)	29R-2, 71-74 cm 29R-4, 17-18 cm 31R-3, 3-5 cm 31R-4, 48-51 cm 32R-5, 73-75; 7, 48-50 cm
5	Volcanic lithic sandstone	4.4		Medium Sandstone	Lithic fragments (75%) Feldspar (10%) Quartz (5%)	Garnet (1%) Brown hornblende (tr)	33R-1, 121-124 cm 33R-3, 50-53 cm
6	Volcanic conglomerate	31.0	Clast	Trachyte	Sanidine (20% Plagioclase (4%) Clinopyroxene (2%)	Feldspar Titanomagnetite Zircon	33R-5, 10-12 cm
			Clast	Flow-banded rhyolite	Sanidine (8%-15%) Plagioclase (1%-3%)	Glass; titanomagnetite Apatite; zircon; sulfide	33R-5 19-25 cm 34R-2, 113-117 cm 34R-3, 119-122 cm
			Clast	Garnet-biotite gneiss	Feldspar (55%); quartz (20%) Garnet (15%); biotite (10%)	Zircon; magnetite Amphibole	35R-2, 46-47 cm
			Clast	Actinolite gneiss	Potassic feldspar (70%) Quartz (22%)	Microcline; plagioclase Actinolite; magnetite Zircon	34R-2, 100-103 cm
			Clast	Granite	Potassic feldspar (50%) Plagioclase (40%) Quartz (12%)	Titanomagnetite Zircon	35R-2, 66-69 cm
7	Plagioclase-phyric basalt	13.0	A 5.8	Brecciated	Plagioclase (10%) Olivine (2%)	Basaltic groundmass	37R-5, 80-83 cm
			B 7.2	Massive	Plagioclase (5%-14%); Olivine (0.5%-2%); Clinopyroxene (<1%)	Basaltic groundmass	38R-3, 80-83 cm 39R-1, 112-115 cm 39R-2, 53-56 cm
8	Plagioclase-phyric basalt	10.6	A 3.4	Vesicular	Plagioclase	Basaltic groundmass	
			B 7.6	Massive	Plagioclase (7%-9%) Olivine (3%-4%)	Basaltic groundmass	40R-2, 121-122 cm 41R-1 68-73 cm

Table T10 (continued).

Basement unit	Unit type	Thickness (m)		Rock/flow type	Phenocryst/ major minerals	Groundmass/ minor minerals	Thin sections detailed in "Petrography and Primary Mineralogy," p. 30
		Total	Subunit				
9	Crystal-vitric tuff	14.9	Tuff	Massive	Sanidine (35%-40%) Plagioclase (2%-3%) Quartz (<2%)	Oxidized mafics (3-5%) Lithic clasts (<5%) Titanomagnetite (tr) Kaersutite (tr) Zircon (tr)	41R-1, 127-128 cm 41R-2, 98-99; 3, 42-46 cm 43R-3, 42-44; 4, 57-60 cm 44R-4, 6-9; 44-46 cm
			Clast	Garnet-biotite gneiss	Feldspar (65%) Garnet (10%-15%) Biotite (5%-20%)	Titanomagnetite Zircon, pyrite	43R-4, 57-60 cm 44R-4, 44-46 cm
10	Plagioclase-phyric basalt	10.7	A 3.5	Brecciated	Plagioclase (10%-28%) Olivine (2%-5%)	Basaltic groundmass	44R-4, 71-72 cm 45R-1, 80-84 cm 45R-2, 7-10; 19-21; 77-80 cm
			B 7.2	Massive	Plagioclase (15%-25%) Clinopyroxene (1%-4%) Olivine (<1%)	Basaltic groundmass Pyrrhotite (tr) Chalcopyrite (tr)	45R-4, 118-120 cm 46R-2, 95-96 cm

Note: * = plagioclase ± clinopyroxene ± titanomagnetite ± mesostasis (altered glass), tr = trace.

Table T11. Major and trace element data for basalt samples from Site 1137. (Continued on next two pages.)

Hole:	1137A	1137A	1137A	1137A	1137A	1137A	1137A	1137A	1137A	1137A
Core, section:	25R-1	25R-3	25R-5	26R-1	26R-2	27R-4	28R-4	29R-2	29R-4	31R-4
Interval (cm):	106-108	89-93	113-115	143-146	5-7	64-66	28-30	35-38	15-17	48-51
Piece:	4	8C	11	12	1	6	5	1	4	1C
Unit:	1	1	2	2	2	3	3	3	4	4
Rock type:	Plagioclase-phyric basalt	Olivine-phyric basalt	Aphyric basalt	Microgabbro	Aphyric basalt	Plagioclase-phyric basalt	Plagioclase-phyric basalt	Aphyric basalt	Plagioclase-phyric basalt	Plagioclase-phyric basalt
	Flow interior	Chill base	Chill top	Xenolith	Flow interior	Silica filled vesicles	Flow interior	Chill base	Altered	Flow interior
Depth (mbsf):	229.46	232.11	234.99	239.43	239.53	252.56	257.17	258.81	261.55	270.98
Major element oxides (wt%):										
SiO_2	52.66	50.50	52.80	52.99	53.21	51.36	52.48	50.43	51.52	51.53
TiO_2	2.42	2.50	2.54	1.84	2.52	2.56	2.51	2.66	2.18	2.18
Al_2O_3	14.58	15.72	14.79	15.18	14.25	14.83	14.32	15.36	15.89	16.77
Fe_2O_3	11.17	11.30	11.51	9.74	11.44	11.70	11.73	11.92	10.20	9.98
MnO	0.13	0.14	0.11	0.14	0.16	0.11	0.15	0.13	0.10	0.15
MgO	5.76	6.19	5.71	6.60	5.25	6.57	5.75	7.33	7.41	6.02
CaO	8.19	8.64	7.19	9.95	8.79	7.75	8.95	5.86	4.51	10.07
Na_2O	2.47	2.74	2.84	2.36	2.61	2.60	2.39	2.92	2.59	2.48
K_2O	1.38	1.10	1.96	0.81	1.15	1.27	0.83	2.16	3.31	0.54
P_2O_5	0.33	0.34	0.35	0.24	0.36	0.35	0.35	0.37	0.30	0.29
Total:	99.06	99.15	99.80	99.81	99.71	99.08	99.44	99.13	97.99	99.98
Total alkali:	3.85	3.84	4.80	3.17	3.76	3.87	3.22	5.08	5.90	3.02
LOI	2.19	0.64	1.21	0.07	0.71	1.84	1.13	0.92	3.32	1.13
Mg #	0.39	0.41	0.38	0.46	0.36	0.41	0.38	0.43	0.48	0.43
Trace elements (ppm):										
Rb	12.0	14.4	22.0	10.0	17.5	17.7	12.0	13.8	54.2	8.8
Ba	314	338	353	283	380	316	352	335	214	221
Sr	549	547	486	575	531	529	553	485	461	601
Ce	44	47	49	35	48	53	52	58	41	41
Nb	15.8	16.5	17.5	12.1	17.4	17.6	17.1	18.7	14.3	14.5
Zr	213	227	239	163	239	236	233	243	192	185
Y	28	27	30	24	32	31	31	34	28	28
V	233	265	245	198	254	254	223	275	231	239
Cr	96	101	58	118	57	71	61	69	156	173
Ni	27	27	23	27	22	31	27	30	41	47
Cu	32	33	25	24	29	28	27	29	34	39
Zn	103	123	112	89	110	116	110	125	85	98
Normative mineralogy:										
Q	6.2	1.9	4.2	5.6	7.0	3.6	7.2	0.0	0.0	4.4
Or	8.0	6.3	11.1	4.7	6.6	7.3	4.8	12.5	19.4	3.1
Ab	20.5	22.7	23.3	19.5	21.5	21.6	19.7	24.1	21.7	20.4
An	24.2	26.8	21.1	27.8	23.2	24.6	25.3	22.0	20.3	32.3
Cor	0.0	0.0	0.0	0.0	0.0	0.0	0.0	0.0	0.6	0.0
Wo (Di)	5.7	5.4	4.7	7.9	7.1	4.5	6.6	1.7	0.0	6.1
En (Di)	2.4	2.3	2.0	3.4	3.1	2.0	2.8	0.7	0.0	2.6
Fs (Di	1.7	1.5	1.5	1.9	2.4	1.2	2.1	0.3	0.0	1.6
En (Hy)	11.6	12.7	11.6	12.6	9.6	14.0	11.1	15.3	18.0	11.9
Fs (Hy)	8.0	8.2	8.3	7.0	7.5	8.9	8.2	7.6	8.6	7.1
Ol (Fo)	0.0	0.0	0.0	0.0	0.0	0.0	0.0	1.2	0.2	0.0
Ol (Fa)	0.0	0.0	0.0	0.0	0.0	0.0	0.0	1.8	0.3	0.0
Ilmenite	4.5	4.7	4.8	3.4	4.7	4.8	4.7	5.0	4.1	4.0
Magnetite	6.4	6.4	6.5	5.5	6.5	6.7	6.7	6.8	5.9	5.7
Apatite	0.7	0.7	0.7	0.5	0.8	0.7	0.7	0.8	0.6	0.6
Total:	99.9	99.9	99.9	99.9	99.9	99.9	99.9	99.9	99.9	99.9

Notes: LOI = loss on ignition at 1025°C for 4 hr. Mg# = MgO/(MgO + FeO), mol%, with FeO calculated (as 80% of total Fe). This table is also available in **ASCII format.**

Table T11 (continued).

Hole:	1137A	1137A	1137A	1137A	1137A	1137A	1137A	1137A
Core, section:	32R-5	32R-7	37R-5	38R-3	39R-1	39R-2	40R-2	41R-1
Interval (cm):	78-82	48-50	55-58	83-86	112-115	53-56	119-121	68-73
Piece:	12B	1C	1C	1	5B	1	1D	1C
Unit:	4	4	7	7	7	7	8	8
Rock type:	Plagioclase-clinopyroxene-phyric basalt	Plagioclase-clinopyroxene-olivine-phyric basalt	Plagioclase-clinopyroxene-phyric basalt	Plagioclase-phyric basalt	Plagioclase-phyric basalt	Plagioclase-clinopyroxene-phyric basalt	Plagioclase-phyric basalt	Plagioclase-olivine-phyric basalt
	Coarser grained	Lower part of Unit 4	Altered	Flow interior	Segregation contact	Chill base	Flow interior	Chill base
Depth (mbsf):	281.59	284.20	327.14	330.15	333.32	334.03	339.22	343.68
Major element oxides (wt%):								
SiO_2	54.00	50.58	51.26	52.00	50.57	50.64	51.82	49.98
TiO_2	2.05	2.52	2.53	2.14	2.07	2.24	2.10	2.54
Al_2O_3	15.74	15.85	17.15	16.26	16.17	16.41	16.14	18.26
Fe_2O_3	10.07	11.52	10.65	10.22	10.98	11.40	10.83	11.50
MnO	0.18	0.12	0.08	0.14	0.17	0.17	0.12	0.23
MgO	6.48	6.06	6.94	5.90	5.88	6.69	5.76	4.52
CaO	6.66	8.75	6.33	9.46	9.68	6.34	8.96	8.14
Na_2O	2.90	2.79	3.08	2.80	2.83	3.22	2.88	3.29
K_2O	1.05	0.68	1.62	0.46	0.54	1.91	0.99	0.71
P_2O_5	0.29	0.34	0.25	0.29	0.28	0.30	0.28	0.32
Total:	99.42	99.20	99.87	99.65	99.15	99.30	99.85	99.48
Total alkali:	3.95	3.47	4.70	3.26	3.37	5.13	3.87	4.00
LOI:	2.37	1.11	2.79	1.55	0.97	1.56	1.37	1.06
Mg #:	0.45	0.40	0.45	0.42	0.40	0.42	0.40	0.33
Trace elements (ppm):								
Rb	18.1	5.4	15.8	5.3	9.2	39.0	11.7	7.9
Ba	171	272	168	250	248	330	311	294
Sr	546	632	460	526	558	511	491	554
Ce	46	50	48	48	46	56	40	54
Nb	14.1	14.5	15.6	14.7	13.3	14.1	13.7	15.9
Zr	179	203	212	200	200	209	204	227
Y	26	29	28	31	31	29	31	29
V	202	252	229	233	238	263	229	274
Cr	128	98	117	109	101	110	98	113
Ni	46	46	32	37	39	34	33	37
Cu	34	37	35	35	34	35	31	37
Zn	123	107	110	109	107	101	105	124
Normative mineralogy:								
Q	7.0	2.9	0.2	4.6	2.2	0.0	7.0	1.3
Or	6.6	3.9	9.3	2.6	3.1	11.0	6.6	4.1
Ab	21.5	23.1	25.4	23.1	23.4	26.6	21.5	27.2
An	23.2	28.1	27.5	29.8	29.3	24.2	23.2	32.2
Cor	0.0	0.0	0.0	0.0	0.0	0.0	0.0	0.0
Wo (Di)	7.1	5.1	0.6	5.9	6.7	1.9	7.1	2.2
En (Di)	3.1	2.2	0.3	2.6	2.9	0.8	3.1	0.9
Fs (Di	2.4	1.5	0.1	1.6	2.0	0.3	2.4	0.9
En (Hy)	9.6	12.5	16.5	11.8	11.4	12.4	9.6	10.0
Fs (Hy)	7.5	8.5	8.6	7.4	8.1	6.0	7.5	9.2
Ol (Fo)	0.0	0.0	0.0	0.0	0.0	2.1	0.0	0.0
Ol (Fa)	0.0	0.0	0.0	0.0	0.0	3.1	0.0	0.0
Ilmenite:	4.7	4.7	4.7	4.0	3.9	4.2	4.7	4.7
Magnetite:	6.5	6.6	6.0	5.8	6.3	6.5	6.5	6.5
Apatite:	0.8	0.7	0.5	0.6	0.6	0.6	0.8	0.7
Total:	99.9	99.9	99.9	99.9	99.9	99.9	99.9	99.9

Table T11 (continued).

Hole:	1137A	1137A
Core, section:	44R-4	46R-2
Interval (cm):	68-71	92-95
Piece:	1B	3B
Unit:	10	10
Rock type:	Plagioclase-olivine-phyric basalt	Plagioclase-clinopyroxene-phyric basalt
	Altered chill top	Flow interior
Depth (mbsf):	360.86	369.39
Major element oxides (wt%):		
SiO_2	52.30	51.89
TiO_2	2.68	2.61
Al_2O_3	16.27	15.32
Fe_2O_3	11.23	11.63
MnO	0.36	0.15
MgO	4.38	4.48
CaO	4.02	9.40
Na_2O	2.29	2.94
K_2O	5.25	0.78
P_2O_5	0.33	0.35
Total:	99.10	99.54
Total alkali:	7.54	3.72
LOI:	1.39	1.02
Mg #:	0.33	0.33
Trace elements (ppm):		
Rb	93.9	18.7
Ba	368	315
Sr	354	489
Ce	75	52
Nb	15.7	15.9
Zr	225	216
Y	44	33
V	228	220
Cr	163	144
Ni	61	59
Cu	66	64
Zn	128	112
Normative mineralogy:		
Q	0.1	5.1
Or	30.4	4.5
Ab	19.0	24.3
An	17.5	25.7
Cor	0.3	0.0
Wo (Di)	0.0	7.3
En (Di)	0.0	3.2
Fs (Di	0.0	2.9
En (Hy)	10.7	7.7
Fs (Hy)	9.8	7.1
Ol (Fo)	0.0	0.0
Ol (Fa)	0.0	0.0
Ilmenite:	5.0	4.8
Magnetite:	6.4	6.6
Apatite:	0.7	0.7
Total:	99.9	99.9

Table T12. Major and trace element data for felsic samples from Site 1137.

Hole:	1137A	1137A	1137A	1137A	1137A
Core, section:	33R-3	33R-5	34R-2	35R-2	41R-1
Interval (cm):	46-49	7-9	111-113	44-46	128-130
Piece:	1B	1	1D	5	6B
Unit:	5	6	6	6	9
Rock type:	Volcanic lithic sandstone	Trachyte	Rhyolite	Garnet-biotite gneiss	Crystal-vitric tuff
Depth (mbsf):	288.93	291.26	296.55	306.10	344.28
Major element oxides (wt%):					
SiO_2	65.59	64.92	73.47	73.25	57.80
TiO_2	1.00	0.80	0.29	0.43	0.78
Al_2O_3	14.79	15.43	13.23	13.45	24.57
Fe_2O_3	5.85	5.88	2.36	3.70	7.82
MnO	0.05	0.06	0.03	0.05	0.07
MgO	0.86	BD	BD	BD	0.20
CaO	0.72	1.53	0.72	2.21	0.68
Na_2O	2.34	3.08	2.89	1.41	1.90
K_2O	7.47	6.47	6.50	4.23	4.05
P_2O_5	0.16	0.18	0.03	0.17	0.07
Total:	98.81	98.34	99.50	98.87	97.92
Total Alkali	9.81	9.55	9.38	5.63	5.95
LOI	0.99	0.62	0.52	0.2	6.92
Trace elements (ppm):					
Rb	157.4	145.9	211.6	188.3	52.9
Ba	465	777	153	740	102
Sr	109	219	38	106	36
Ce	178	164	214	93	373
Nb	78.9	65.2	100.7	7.7	304.7
Zr	1063	1274	582	316	1117
Y	48	36	25	36	43
V	76	12	9	21	40
Cr	66	BD	BD	BD	13
Ni	19	7	6	7	15
Cu	10	9	6	6	9
Zn	111	132	86	54	224
Normative mineralogy:					
Q	18.4	16.8	29.2	42.9	
Or	44.0	38.3	38.3	25.0	
Ab	19.7	26.1	24.4	11.9	
An	2.5	6.4	3.3	9.8	
Cor	1.9	1.0	0.2	3.0	
Wo (Di)	0.0	0.0	0.0	0.0	
En (Di)	0.0	0.0	0.0	0.0	
Fs (Di	0.0	0.0	0.0	0.0	
En (Hy)	2.1	0.0	0.0	0.0	
Fs (Hy)	5.6	6.0	2.5	3.9	
Ol (Fo)	0.0	0.0	0.0	0.0	
Ol (Fa)	0.0	0.0	0.0	0.0	
Ilmenite	1.9	1.5	0.6	0.8	
Magnetite	3.4	3.4	1.4	2.2	
Apatite	0.3	0.4	0.1	0.4	
Total:	99.9	99.9	99.9	99.9	

Notes: BD = below detection limit. LOI = loss on ignition at 1025°C for 4 hr.

Table T13. Alteration minerals within basement units in Hole 1137A identified by X-ray diffraction.

Core, section, piece, interval (cm)	Depth (mbsf)	Description	XRD identification
183-1137A-			
25R-4, (Piece 3, 89)	233.58	Breccia matrix	Calcite
27R-2, (Piece 7, 24)	249.33	Well-indurated sediment	Celadonite, quartz, orthoclase
29R-3, (Piece 2, 12	260.02	Clastic volcanic debris	Nontronite/saponite
29R-3, (Piece 12, 88-89)	260.78	Clastic volcanic debris	Clinoptilolite, saponite/nontronite
29R-3, (Piece 14, 107-108)	260.97	Clastic volcanic debris	Saponite, nontronite, illite
30R-1, (Piece 1, 62-65)	262.52	Vein	Celadonite, saponite/nontronite
31R-1, (Piece 4, 26-27)	266.86	Vesicle filling	Clinoptilolite, saponite/nontronite
31R-1, (Piece 9, 49-50)	267.09	Vesicle filling	Heulandite, saponite/nontronite
31R-2, (Piece 11B, 142-145)	269.52	Large 4-cm vesicle	Quartz
31R-5, (Piece 7, 97-98)	272.97	Vesicle filling	Clinoptilolite
31R-5, (Piece 9, 107-108)	273.07	Zeolite on rim of vesicle	Clinoptilolite
31R-5, (Piece 9, 107-108)	273.08	Mineral filling vesicle	Barite
33R-1, (Piece 1B, 19-20)	285.69	Silica-rich vesicle	Amorphous silica
39R-2, (Piece 4, 79-80)	334.29	Breccia matrix	Clinoptilolite, quartz, saponite/nontronite
39R-2, (Piece 10, 124)	334.74	Vesicle filling	Chabazite
41R-2, (Piece 1, 49-50)	344.99	Alteration in shear zone within tuff	Celadonite, saponite/nontronite, quartz, goethite
42R-2, (Piece 1, 85-86)	349.06	Green clay in tuff	Saponite/nontronite
44R-4, (Piece 1, 36-37)	360.54	Blue-green clay in tuff	Nontronite, quartz

Note: XRD = X-ray diffraction.

Table T14. Summary of natural remanent magnetization intensity and susceptibility of Hole 1137A.

Unit		Average	Maximum	Minimum	Median
Sediment:					
Unit I	NRM intensity	4.82×10^{-3}	9.88×10^{-2}	2.75×10^{-4}	1.99×10^{-3}
	Susceptibility	2.16×10^{-6}	1.98×10^{-5}	-2.5×10^{-6}	1.5×10^{-6}
Unit II	NRM intensity	1.40×10^{-3}	6.90×10^{-2}	7.27×10^{-6}	8.45×10^{-4}
	Susceptibility	-9.21×10^{-7}	4.15×10^{-5}	-7.20×10^{-6}	-1.00×10^{-6}
Unit III	NRM intensity	4.69×10^{-2}	6.52×10^{-1}	1.27×10^{-5}	3.03×10^{-4}
	Susceptibility	1.12×10^{-5}	5.08×10^{-5}	1.20×10^{-6}	7.50×10^{-6}
Hole 1137A sediment average:					
	NRM intensity	3.72×10^{-3}	6.52×10^{-1}	7.27×10^{-6}	9.12×10^{-4}
	Susceptibility	-3.49×10^{-7}	5.08×10^{-5}	-7.20×10^{-6}	-8.00×10^{-7}
Basement:					
Unit 1	NRM intensity	1.63	5.53	2.16×10^{-1}	1.46
	Susceptibility	1.13×10^{-3}	3.23×10^{-3}	3.54×10^{-4}	1.05×10^{-3}
Unit 2	NRM intensity	2.77	1.00×10^{1}	1.07×10^{-1}	1.40
	Susceptibility	1.52×10^{-3}	4.46×10^{-3}	7.80×10^{-6}	1.14×10^{-3}
Unit 3	NRM intensity	2.85	8.52	4.69×10^{-1}	2.29
	Susceptibility	9.89×10^{-4}	3.26×10^{-3}	2.01×10^{-4}	9.44×10^{-4}
Unit 4	NRM intensity	3.14	1.67×10^{1}	1.53×10^{-1}	2.34
	Susceptibility	1.37×10^{-3}	6.08×10^{-3}	1.98×10^{-4}	1.24×10^{-3}
Unit 5	NRM intensity	1.47×10^{-1}	2.01	6.85×10^{-3}	9.43×10^{-2}
	Susceptibility	6.33×10^{-4}	1.64×10^{-3}	1.02×10^{-4}	6.51×10^{-4}
Unit 6	NRM intensity	4.94×10^{-1}	6.29	1.88×10^{-2}	3.57×10^{-1}
	Susceptibility	1.16×10^{-3}	2.96×10^{-3}	8.32×10^{-5}	1.22×10^{-3}
Unit 7	NRM intensity	4.38	1.53×10^{1}	6.69×10^{-2}	3.80
	Susceptibility	2.38×10^{-3}	5.96×10^{-3}	2.29×10^{-4}	1.74×10^{-3}
Unit 8	NRM intensity	1.65	7.66	1.60×10^{-1}	1.03
	Susceptibility	1.29×10^{-3}	4.42×10^{-3}	3.15×10^{-4}	1.02×10^{-3}
Unit 9	NRM intensity	9.98×10^{-2}	1.60	9.51×10^{-4}	5.23×10^{-2}
	Susceptibility	1.01×10^{-4}	1.10×10^{-3}	6.20×10^{-6}	6.88×10^{-5}
Unit 10	NRM intensity	2.65	8.68	3.40×10^{-1}	2.21
	Susceptibility	1.85×10^{-3}	5.67×10^{-3}	4.14×10^{-4}	1.06×10^{-3}
Hole 1137A lava flow average:					
	NRM intensity	2.93	1.67×10^{1}	6.69×10^{-2}	2.17
	Susceptibility	1.50×10^{-3}	6.08×10^{-3}	7.80×10^{-6}	1.15×10^{-3}
Hole 1137A basement rock average:					
	NRM intensity	2.15	1.67×10^{1}	9.51×10^{-4}	1.42
	Susceptibility	1.25×10^{-3}	6.08×10^{-3}	6.20×10^{-6}	1.02×10^{-3}

Notes: NRM = natural remanent magnetization. Units for NRM = A/m; units for susceptibility = SI units.

Table T15. Characteristic inclinations and natural remanent magnetization intensities of discrete basalt samples from Hole 1137A.

Core, section, interval (cm)	Basement unit/subunit	Inclination (°)	NRM intensity (A/m)	Demagnetization range (°C or mT)
183-1137A-				
25R-1,18-20	1	–76	6.45	AF 10-60
25R-1,127-129	1	–73	3.8	TH 310-620
25R-7,107-109	2B	–70	1.35	TH 340-620
26R-2,55-57	2B	–77	1.92	AF 15-60
27R-3,87-89	3A	–73	1.85	TH 280-620
28R-1,25-27	3B	–75	3.62	AF 15-60
29R-4,56-58	4	–65	10.5	TH 340-620
31R-4,125-127	4	–66	1.77	AF 15-60
38R-3,105-107	7B	–62	6.47	AF 10-60
38R-4,107-109	7B	–56	17.2	TH 310-530
40R-3,91-93	8B	–63	1.41	AF 15-60
40R-4,50-52	8B	–56	1.69	TH 340-620
45R-4,27-29	10B	–72	4.49	AF 15-60
46R-1,77-79	10B	–71	3.34	TH 200-620

Notes: Inclination = characteristic inclination determined from progressive demagnetization. NRM = natural remanent magnetization. Demagnetization range = demagnetization method and characteristic inclination is determined from the component in this range. AF = alternating field demagnetization, TH = thermal demagnetization.

Table T16. Index properties data from Site 1137. (See table note. Continued on next two pages.)

Core, section, interval (cm)	Depth (mbsf)	Water content (wet%)	Water content (dry%)	Density			Porosity (%)
				Bulk (g/cm³)	Dry (g/cm³)	Grain (g/cm³)	
183-1137A-							
2R-1, 114	10.64	28.8	40.5	1.79	1.27	2.57	50.4
2R-2, 106	12.06	33.7	50.8	1.72	1.14	2.61	56.4
2R-3, 108	13.58	32.3	47.7	1.73	1.17	2.58	54.5
2R-4, 17	14.17	33.8	51.1	1.70	1.13	2.56	56.1
3R-1, 85	19.45	37.0	58.8	1.69	1.06	2.72	61.0
3R-2, 71	20.81	39.4	65.0	1.65	1.00	2.74	63.5
3R-3, 110	22.70	33.2	49.6	1.73	1.15	2.61	55.9
3R-4, 78	23.88	37.3	59.6	1.69	1.06	2.74	61.5
3R-5, 49	25.09	34.7	53.2	1.70	1.11	2.62	57.6
3R-6, 118	27.28	34.0	51.6	1.69	1.12	2.56	56.3
3R-7, 16	27.76	32.2	47.5	1.74	1.18	2.61	54.7
4R-1, 124	28.84	36.3	57.1	1.70	1.08	2.74	60.4
4R-2, 118	30.28	36.9	58.4	1.70	1.07	2.76	61.1
4R-3, 129	31.89	34.9	53.6	1.74	1.13	2.77	59.2
4R-4, 106	33.16	36.1	56.4	1.71	1.09	2.74	60.2
4R-5, 125	34.85	38.3	62.1	1.65	1.02	2.65	61.6
5R-1, 115	37.95	34.2	52.0	1.72	1.13	2.67	57.5
5R-2, 125	39.55	34.1	51.8	1.71	1.13	2.61	56.9
5R-3, 37	40.17	32.3	47.7	1.71	1.16	2.50	53.8
5R-4, 81	42.11	35.2	54.3	1.72	1.11	2.72	59.0
5R-5, 101	43.81	30.4	43.7	1.75	1.22	2.54	52.0
5R-6, 128	45.58	33.7	50.8	1.72	1.14	2.63	56.6
5R-7, 30	46.10	33.1	49.5	1.74	1.17	2.68	56.4
6R-1, 115	47.15	36.4	57.2	1.70	1.08	2.75	60.5
7R-1, 121	56.41	36.4	57.2	1.68	1.07	2.64	59.5
7R-2, 115	57.85	37.2	59.1	1.66	1.04	2.61	60.1
7R-3, 123	59.43	34.3	52.3	1.69	1.11	2.55	56.6
7R-4, 71	60.41	35.3	54.6	1.71	1.11	2.70	59.0
8R-1, 118	65.98	34.8	53.4	1.72	1.12	2.68	58.3
8R-2, 123	67.53	33.1	49.4	1.76	1.18	2.72	56.8
8R-3, 112	68.92	34.2	52.0	1.70	1.12	2.59	56.8
8R-4, 31	69.61	33.3	49.8	1.72	1.15	2.60	55.9
9R-1, 82	75.32	36.7	57.9	1.69	1.07	2.71	60.5
9R-2, 94	76.94	34.8	53.5	1.70	1.11	2.62	57.8
9R-3, 115	78.65	34.6	52.9	1.69	1.11	2.59	57.2
11R-1, 118	94.88	32.3	47.7	1.75	1.19	2.66	55.3
11R-2, 120	96.40	33.0	49.3	1.70	1.14	2.53	54.9
11R-3, 115	97.85	32.1	47.4	1.77	1.20	2.70	55.6
11R-4, 121	99.41	31.6	46.1	1.75	1.20	2.60	53.9
11R-5, 111	100.81	31.1	45.2	1.79	1.23	2.72	54.5
11R-6, 120	102.40	30.5	43.9	1.80	1.25	2.69	53.6
11R-7, 44	103.14	33.6	50.7	1.75	1.16	2.72	57.3
12R-1, 44	103.74	32.1	47.3	1.74	1.18	2.61	54.7
12R-1, 101	104.31	35.3	54.6	1.73	1.12	2.77	59.6
12R-2, 33	105.13	34.3	52.1	1.74	1.14	2.72	58.0
13R-1, 58	113.48	33.4	50.2	1.73	1.15	2.65	56.4
13R-1, 88	113.78	37.5	60.1	1.68	1.05	2.71	61.4
13R-2, 58	114.98	34.0	51.5	1.77	1.17	2.85	58.9
13R-3, 36	116.26	32.0	47.0	1.74	1.19	2.61	54.4
13R-3, 141	117.31	35.0	54.0	1.73	1.12	2.76	59.2
13R-4, 18	117.58	33.7	50.9	1.75	1.16	2.74	57.6
13R-4, 126	118.66	32.5	48.1	1.77	1.20	2.74	56.2
13R-5, 13	119.03	34.8	53.5	1.74	1.13	2.77	59.1
13R-5, 122	120.12	34.7	53.0	1.73	1.13	2.73	58.6
13R-6, 20	120.60	34.7	53.2	1.73	1.13	2.73	58.6
13R-6, 144	121.84	33.2	49.6	1.75	1.17	2.68	56.5
13R-7, 52	122.42	31.8	46.7	1.77	1.20	2.67	54.8
14R-1, 9	122.69	35.3	54.5	1.66	1.08	2.51	57.2
14R-1, 84	123.44	31.6	46.2	1.79	1.22	2.73	55.2
14R-2, 22	124.32	32.0	47.1	1.78	1.21	2.73	55.6
14R-2, 135	125.45	31.6	46.2	1.78	1.22	2.71	55.0
14R-3, 18	125.78	32.6	48.4	1.76	1.19	2.70	56.0
15R-1, 138	133.58	32.2	47.5	1.77	1.20	2.71	55.7
15R-4, 102	137.72	33.1	49.5	1.76	1.18	2.73	56.9
16R-1, 17	141.97	32.8	48.8	1.75	1.17	2.67	55.9
16R-1, 94	142.74	34.2	51.9	1.73	1.14	2.71	57.9

Table T16 (continued).

Core, section, interval (cm)	Depth (mbsf)	Water content (wet%)	Water content (dry%)	Density			Porosity (%)
				Bulk (g/cm^3)	Dry (g/cm^3)	Grain (g/cm^3)	
16R-2, 7	143.37	33.0	49.2	1.76	1.18	2.72	56.6
16R-2, 111	144.41	30.3	43.5	1.78	1.24	2.63	52.8
16R-3, 76	145.56	32.8	48.8	1.75	1.18	2.68	56.1
16R-3, 125	146.05	32.4	48.0	1.75	1.18	2.66	55.5
16R-4, 35	146.65	31.2	45.3	1.77	1.22	2.65	53.9
17R-1, 6	151.46	36.4	57.2	1.70	1.08	2.74	60.5
17R-1, 54	151.94	35.3	54.5	1.71	1.11	2.70	59.0
17R-2, 17	153.07	33.8	51.0	1.74	1.15	2.69	57.2
17R-2, 111	154.01	32.7	48.6	1.77	1.19	2.73	56.5
17R-3, 15	154.55	31.7	46.5	1.78	1.22	2.71	55.1
17R-3, 75	155.15	34.2	51.9	1.74	1.14	2.72	58.0
17R-4, 46	156.36	34.9	53.5	1.71	1.12	2.68	58.3
17R-4, 129	157.19	34.5	52.7	1.72	1.13	2.67	57.9
18R-1, 82	161.82	37.9	60.9	1.66	1.03	2.69	61.5
19R-1, 101	171.71	39.9	66.3	1.63	0.98	2.68	63.4
19R-2, 11	172.31	32.9	49.1	1.75	1.17	2.68	56.2
20R-1, 12	180.42	36.2	56.7	1.68	1.07	2.63	59.3
21R-1, 61	190.51	35.8	55.7	1.71	1.10	2.72	59.7
23R-1, 26	209.36	11.2	12.6	2.09	1.86	2.41	22.9
23R-1, 77	209.87	27.6	38.1	1.85	1.34	2.66	49.8
23R-1, 117	210.27	27.6	38.2	1.87	1.35	2.73	50.4
23R-2, 24	210.82	9.8	10.8	2.20	1.99	2.52	21.0
24R-1, 34	219.14	15.3	18.1	2.10	1.78	2.59	31.5
24R-1, 73	219.53	8.8	9.6	2.48	2.26	2.87	21.3
24R-2, 1	220.30	4.7	4.9	2.64	2.52	2.86	12.1
24R-2, 27	220.56	5.0	5.3	2.62	2.49	2.85	12.8
25R-1, 18	228.58	3.2	3.3	2.62	2.53	2.76	8.3
25R-1, 106	229.46	2.4	2.5	2.73	2.67	2.85	6.4
25R-1, 127	229.67	2.0	2.1	2.76	2.70	2.86	5.5
25R-2, 127	231.11	4.7	4.9	2.66	2.53	2.88	12.1
25R-3, 2	231.24	4.5	4.7	2.66	2.54	2.87	11.6
25R-3, 44	231.66	5.7	6.0	2.64	2.49	2.92	14.6
25R-3, 89	232.11	5.6	5.9	2.60	2.46	2.86	14.1
25R-4, 11	232.80	9.6	10.6	2.34	2.12	2.71	22.0
25R-4, 33	233.02	11.2	12.6	2.28	2.02	2.70	24.9
25R-4, 77	233.46	7.0	7.5	2.47	2.30	2.77	16.9
25R-5, 29	234.15	4.8	5.0	2.49	2.37	2.68	11.6
25R-5, 113	234.99	4.7	4.9	2.60	2.48	2.81	11.8
25R-6, 4	235.37	5.4	5.8	2.46	2.33	2.68	13.1
25R-7, 10	236.28	4.0	4.2	2.65	2.54	2.84	10.3
25R-7, 107	237.25	3.6	3.7	2.68	2.58	2.85	9.3
26R-1, 93	238.93	4.0	4.1	2.66	2.56	2.85	10.3
26R-1, 140	239.40	1.9	2.0	2.73	2.68	2.82	5.2
26R-2, 5	239.53	1.7	1.8	2.77	2.72	2.85	4.7
26R-2, 38	239.86	2.5	2.6	2.72	2.65	2.84	6.6
26R-2, 55	240.03	2.3	2.4	2.75	2.69	2.87	6.3
26R-2, 133	240.81	3.0	3.1	2.64	2.56	2.77	7.7
26R-3, 35	241.29	4.4	4.6	2.65	2.53	2.86	11.4
27R-1, 54	248.14	9.9	10.9	2.41	2.18	2.83	23.2
27R-2, 102	250.11	10.7	11.9	2.37	2.12	2.82	24.7
27R-3, 87	251.45	6.0	6.3	2.63	2.47	2.92	15.3
27R-4, 35	252.27	7.0	7.6	2.56	2.38	2.89	17.6
27R-4, 66	252.58	5.9	6.3	2.58	2.43	2.85	14.8
28R-1, 25	252.65	6.0	6.4	2.64	2.48	2.93	15.4
28R-3, 60	255.99	2.7	2.8	2.76	2.68	2.89	7.2
28R-4, 5	256.94	3.8	4.0	2.64	2.54	2.81	9.9
29R-1, 83	258.03	5.2	5.5	2.67	2.53	2.92	13.5
29R-2, 35	258.81	6.4	6.8	2.53	2.37	2.81	15.8
29R-2, 71	259.17	7.8	8.5	2.41	2.22	2.72	18.4
29R-3, 48	260.38	11.2	12.6	2.33	2.07	2.77	25.4
29R-4, 56	261.96	10.0	11.1	2.37	2.13	2.77	23.1
30R-1, 102	262.92	8.2	8.9	2.43	2.23	2.77	19.5
30R-2, 71	263.95	8.2	8.9	2.43	2.23	2.76	19.4
30R-3, 56	264.79	8.5	9.3	2.44	2.23	2.80	20.4
30R-4, 20	265.71	8.7	9.5	2.42	2.21	2.78	20.5
31R-1, 124	267.84	6.9	7.4	2.52	2.35	2.83	16.9
31R-2, 60	268.70	5.1	5.4	2.62	2.49	2.87	13.2
31R-3, 20	269.80	4.1	4.3	2.64	2.53	2.84	10.7

Table T16 (continued).

Core, section, interval (cm)	Depth (mbsf)	Water content (wet%)	Water content (dry%)	Density			Porosity (%)
				Bulk (g/cm^3)	Dry (g/cm^3)	Grain (g/cm^3)	
31R-4, 125	271.75	4.9	5.1	2.68	2.55	2.92	12.8
31R-5, 53	272.53	5.3	5.6	2.50	2.37	2.72	13.0
31R-6, 42	273.81	3.8	4.0	2.61	2.51	2.78	9.7
31R-7, 64	275.53	5.8	6.2	2.54	2.39	2.79	14.4
32R-1, 58	276.68	5.8	6.2	2.61	2.46	2.89	14.8
32R-2, 5	277.02	6.1	6.5	2.61	2.45	2.90	15.5
32R-3, 80	278.86	5.3	5.6	2.65	2.51	2.91	13.7
32R-4, 12	279.52	6.6	7.1	2.56	2.39	2.86	16.5
32R-5, 117	281.98	6.5	7.0	2.58	2.42	2.89	16.5
32R-6, 91	283.13	4.8	5.0	2.65	2.53	2.88	12.3
32R-7, 30	284.02	5.7	6.0	2.64	2.49	2.92	14.7
33R-1, 2	285.52	5.1	5.4	2.67	2.53	2.92	13.3
33R-1, 136	286.86	5.7	6.0	2.44	2.30	2.66	13.5
33R-2, 45	287.42	11.1	12.4	2.29	2.04	2.71	24.8
33R-2, 77	287.74	10.4	11.7	2.28	2.04	2.66	23.3
33R-2, 138	288.35	9.4	10.3	2.28	2.07	2.62	20.9
33R-3, 41	288.88	10.2	11.4	2.30	2.06	2.68	22.9
33R-3, 79	289.26	9.7	10.7	2.33	2.11	2.70	22.0
33R-4, 37	290.17	11.0	12.3	2.30	2.04	2.71	24.6
33R-4, 51	290.31	10.4	11.6	2.30	2.06	2.68	23.3
35R-1, 102	305.22	8.9	9.7	2.35	2.14	2.68	20.3
35R-1, 110	305.30	9.0	9.9	2.34	2.13	2.69	20.7
36R-1, 62	314.22	8.8	9.6	2.34	2.13	2.67	20.0
38R-1, 52	328.02	5.6	5.9	2.48	2.35	2.71	13.5
38R-2, 28	329.13	5.2	5.4	2.66	2.53	2.92	13.4
38R-3, 105	330.37	5.3	5.5	2.64	2.50	2.89	13.5
38R-4, 20	330.88	5.3	5.6	2.64	2.50	2.89	13.7
38R-4, 107	331.75	2.6	2.6	2.73	2.66	2.86	6.9
39R-1, 21	332.41	2.2	2.2	2.75	2.69	2.86	5.8
39R-1, 121	333.41	4.6	4.8	2.69	2.56	2.92	12.1
39R-2, 6	333.56	5.2	5.5	2.66	2.52	2.91	13.4
40R-2, 6	338.09	3.7	3.8	2.59	2.49	2.75	9.3
40R-3, 9	339.54	5.1	5.4	2.65	2.51	2.89	13.2
40R-3, 91	340.36	2.8	2.9	2.67	2.60	2.81	7.4
40R-4, 128	342.20	3.1	3.2	2.66	2.58	2.80	8.1
40R-5, 35	342.72	3.2	3.3	2.66	2.57	2.81	8.3
40R-5, 108	343.45	4.0	4.1	2.65	2.54	2.83	10.2
42R-1, 51	348.11	17.6	21.3	2.05	1.69	2.61	35.2
42R-2, 88	349.09	16.7	20.0	2.06	1.72	2.59	33.6
42R-3, 82	350.53	14.9	17.5	2.13	1.81	2.63	31.0
42R-4, 71	351.40	15.3	18.0	2.09	1.77	2.57	31.2
43R-1, 27	352.47	13.2	15.2	2.12	1.84	2.54	27.4
43R-2, 43	353.48	11.5	13.0	2.18	1.93	2.56	24.5
43R-3, 46	354.98	13.3	15.4	2.11	1.83	2.53	27.5
43R-4, 10	356.03	13.2	15.2	2.16	1.87	2.59	27.8
44R-1, 10	357.00	12.3	14.0	2.18	1.91	2.59	26.2
44R-2, 4	357.56	9.8	10.9	2.27	2.05	2.62	21.7
44R-3, 54	359.34	10.1	11.3	2.24	2.01	2.59	22.2
45R-3, 17	364.44	4.5	4.7	2.64	2.52	2.85	11.6
45R-4, 118	366.75	3.0	3.0	2.69	2.61	2.82	7.8
46R-1, 10	367.10	2.5	2.6	2.73	2.66	2.85	6.6
46R-2, 40	368.87	1.8	1.8	2.77	2.72	2.86	4.8
46R-3, 30	370.10	2.2	2.2	2.74	2.68	2.84	5.8

Note: This table is also available in **ASCII format.**

Table T17. Compressional wave velocity measured using the contact-probe system, Site 1137. (See table note. Continued on next five pages.)

Core, section, interval (cm)	Depth (mbsf)	Direction	Type of sample	Velocity (m/s)
183-1137A-				
2R-2, 110	12.10	X	1	1785
2R-4, 17	14.17	X	1	1752
3R-1, 87	19.47	X	1	1713
3R-2, 75	20.85	X	1	1737
3R-3, 114	22.74	X	1	1663
3R-4, 81	23.91	X	1	1693
3R-6, 121	27.31	X	1	1694
3R-7, 16	27.76	X	1	1618
4R-1, 126	28.86	X	1	1608
4R-2, 119	30.29	X	1	1564
4R-3, 132	31.92	X	1	1597
4R-4, 106	33.16	X	1	1582
4R-5, 125	34.85	X	1	1569
5R-1, 117	37.97	X	1	1668
5R-2, 126	39.56	X	1	1652
5R-3, 39	40.19	X	1	1657
5R-4, 102	42.32	X	1	1660
5R-5, 102	43.82	X	1	1688
5R-6, 129	45.59	X	1	1621
5R-7, 32	46.12	X	1	1601
6R-1, 115	47.15	X	1	1609
7R-1, 123	56.43	X	1	1626
7R-2, 116	57.86	X	1	1660
7R-3, 123	59.43	X	1	1660
7R-4, 119	60.89	X	1	1624
8R-1, 119	65.99	X	1	1640
8R-2, 125	67.55	X	1	1639
8R-3, 113	68.93	X	1	1625
8R-4, 32	69.62	X	1	1623
9R-1, 95	75.45	X	1	1585
9R-2, 95	76.95	X	1	1585
9R-3, 116	78.66	X	1	1598
11R-1, 119	94.89	X	1	1653
11R-2, 122	96.42	X	1	1641
11R-3, 116	97.86	X	1	1628
11R-4, 121	99.41	X	1	1632
11R-5, 112	100.82	X	1	1673
11R-6, 122	102.42	X	1	1674
11R-7, 45	103.15	X	1	1624
12R-1, 46	103.76	X	1	1597
12R-1, 102	104.32	X	1	1603
12R-2, 34	105.14	X	1	1604
12R-2, 46	105.26	X	1	1597
13R-1, 60	113.50	X	1	1671
13R-1, 90	113.80	X	1	1663
13R-2, 61	115.01	X	1	1652
13R-2, 112	115.52	X	1	1650
13R-3, 37	116.27	X	1	1650
13R-3, 142	117.32	X	1	1721
13R-4, 127	118.67	X	1	1662
13R-5, 14	119.04	X	1	1636
13R-5, 122	120.12	X	1	1614
13R-6, 21	120.61	X	1	1626
13R-6, 97	121.37	X	1	1641
13R-6, 146	121.86	X	1	1712
13R-7, 7	121.97	X	1	1658
13R-7, 53	122.43	X	1	1711
14R-1, 10	122.70	X	1	1633
14R-1, 85	123.45	X	1	1635
14R-2, 22	124.32	X	1	1638
14R-2, 136	125.46	X	1	1673
14R-3, 18	125.78	X	1	1631
15R-1, 139	133.59	X	1	1761
15R-3, 45	135.65	X	1	1646
15R-3, 45	135.65	X	1	1612
15R-3, 71	135.91	X	1	1661
16R-1, 18	141.98	X	1	1632
16R-1, 95	142.75	X	1	1654
16R-2, 8	143.38	X	1	1660
16R-2, 112	144.42	X	1	1678
16R-3, 77	145.57	X	1	1667
16R-3, 77	145.57	X	1	1678
16R-3, 127	146.07	X	1	1691
16R-4, 14	146.44	X	1	1666
16R-4, 35	146.65	X	1	1642
17R-1, 7	151.47	X	1	1673
17R-1, 57	151.97	X	1	1651
17R-2, 19	153.09	X	1	1684
17R-2, 113	154.03	X	1	1670
17R-3, 17	154.57	X	1	1703
17R-3, 79	155.19	X	1	1638
17R-4, 47	156.37	X	1	2024
17R-4, 129	157.19	X	1	2069
18R-1, 52	161.52	X	1	1643
19R-1, 48	171.18	X	1	1669
19R-1, 103	171.73	X	1	1681
19R-2, 10	172.30	X	1	2147
19R-2, 10	172.30	Y	4	2129
21R-1, 63	190.53	X	1	1670
21R-1, 92	190.82	X	1	1641
22R-1, 29	199.79	X	2	3901
23R-1, 26	209.36	X	3	3714
23R-1, 28	209.38	X	2	4091
23R-1, 38	209.48	X	2	3965
23R-1, 77	209.87	X	3	1947
23R-1, 82	209.92	X	2	1939
23R-1, 108	210.18	X	2	1940
23R-1, 117	210.27	X	3	1939
23R-1, 120	210.30	X	2	1953
23R-2, 4	210.62	X	2	4342
23R-2, 12	210.70	X	2	4103
23R-2, 25	210.83	X	3	3505
23R-2, 26	210.84	X	2	3810
24R-1, 9	218.89	X	2	3113
24R-1, 20	219.00	X	2	3108
24R-1, 35	219.15	X	2	2923
24R-1, 36	219.16	Z	2	2835
24R-1, 50	219.30	X	2	3064
24R-1, 74	219.54	X	2	3970
24R-1, 75	219.55	X	2	4090
24R-1, 80	219.60	X	2	4445
24R-1, 80	219.60	X	2	4673
24R-1, 112	219.92	X	2	4815
24R-1, 114	219.94	X	2	4924
24R-1, 133	220.13	X	2	4871
24R-1, 144	220.24	X	2	4604
24R-2, 2	220.31	X	4	4786
24R-2, 2	220.31	X	4	4662
24R-2, 4	220.33	X	2	4909
24R-2, 11	220.40	X	2	4960
24R-2, 17	220.46	X	2	4916
24R-2, 26	220.55	X	2	4840
24R-2, 28	220.57	X	2	4455
24R-2, 35	220.64	X	2	4983
24R-2, 41	220.70	X	2	4896
24R-2, 47	220.76	X	2	4879
24R-2, 56	220.85	X	2	4847
24R-2, 69	220.98	X	2	5025
24R-2, 72	221.01	X	2	5178
24R-2, 86	221.15	X	2	5065
24R-2, 93	221.22	X	2	5013
24R-2, 108	221.37	X	2	4966
24R-2, 112	221.41	X	2	5030
24R-2, 112	221.41	X	2	5727
25R-1, 12	228.52	X	2	5392

Table T17 (continued).

Core, section, interval (cm)	Depth (mbsf)	Direction	Type of sample	Velocity (m/s)
25R-1, 12	228.52	X	2	5331
25R-1, 12	228.52	X	2	5178
25R-1, 12	228.52	X	2	5352
25R-1, 12	228.52	X	2	5208
25R-1, 12	228.52	X	2	5174
25R-1, 12	228.52	X	2	5228
25R-1, 12	228.52	X	2	5280
25R-1, 12	228.52	X	2	5365
25R-1, 19	228.59	X	3	5341
25R-1, 19	228.59	X	2	4962
25R-1, 30	228.70	X	2	5251
25R-1, 45	228.85	X	2	5266
25R-1, 60	229.00	X	2	5242
25R-1, 80	229.20	X	2	5577
25R-1, 87	229.27	X	2	5511
25R-1, 90	229.30	X	2	5487
25R-1, 106	229.46	X	4	5698
25R-1, 106	229.46	Y	4	5746
25R-1, 106	229.46	Z	4	5212
25R-1, 114	229.54	X	2	5416
25R-1, 125	229.65	Y	3	5652
25R-1, 128	229.68	X	2	5387
25R-1, 128	229.68	X	2	4913
25R-1, 138	229.78	X	3	5532
25R-1, 144	229.84	X	2	4732
25R-2, 13	229.97	X	2	5673
25R-2, 13	229.97	X	2	5730
25R-2, 13	229.97	X	2	5679
25R-2, 13	229.97	X	2	5723
25R-2, 13	229.97	X	2	5705
25R-2, 13	229.97	X	2	5697
25R-2, 13	229.97	X	2	5696
25R-2, 13	229.97	X	2	5654
25R-2, 13	229.97	X	2	5660
25R-2, 13	229.97	X	2	5689
25R-2, 15	229.99	X	2	5832
25R-2, 26	230.10	X	2	5743
25R-2, 35	230.19	X	2	5432
25R-2, 47	230.31	X	2	6157
25R-2, 65	230.49	X	2	5367
25R-2, 76	230.60	X	2	5344
25R-2, 85	230.69	X	2	5423
25R-2, 95	230.79	X	2	5248
25R-2, 102	230.86	X	2	5076
25R-2, 112	230.96	X	2	5073
25R-2, 125	231.09	X	3	5321
25R-2, 128	231.12	X	2	5195
25R-3, 3	231.25	X	2	5188
25R-3, 4	231.26	X	3	5390
25R-3, 20	231.42	X	2	5362
25R-3, 29	231.51	X	2	5408
25R-3, 45	231.67	X	3	5306
25R-3, 45	231.67	X	2	4587
25R-3, 91	232.13	X	4	4488
25R-3, 91	232.13	Y	4	4695
25R-3, 91	232.13	Z	4	4571
25R-3, 119	232.41	X	2	4687
25R-3, 124	232.46	X	2	4631
25R-3, 134	232.56	X	2	4653
25R-3, 141	232.63	X	2	4707
25R-4, 5	232.74	X	2	4294
25R-4, 22	232.91	X	2	5744
25R-4, 22	232.91	X	2	5705
25R-4, 29	232.98	X	2	4209
25R-4, 53	233.22	X	2	4737
25R-4, 66	233.35	X	2	4672
25R-4, 75	233.44	X	2	4847
25R-4, 75	233.44	Z	2	4770
25R-4, 99	233.68	X	2	4625
25R-4, 108	233.77	X	2	5597
25R-5, 9	233.95	X	2	4774
25R-5, 15	234.01	X	2	5035
25R-5, 30	234.16	X	3	4909
25R-5, 30	234.16	X	3	4595
25R-5, 36	234.22	X	2	4950
25R-5, 48	234.34	X	2	4926
25R-5, 69	234.55	X	2	4819
25R-5, 87	234.73	X	2	4944
25R-5, 103	234.89	X	2	4891
25R-5, 124	235.10	X	2	4812
25R-5, 130	235.16	X	2	4844
25R-5, 139	235.25	X	2	4770
25R-6, 5	235.38	X	3	4826
25R-6, 5	235.38	X	3	4639
25R-6, 15	235.48	X	2	5214
25R-6, 27	235.60	X	2	4557
25R-6, 42	235.75	X	2	4832
25R-6, 51	235.84	X	2	5256
25R-6, 66	235.99	X	2	4840
25R-6, 72	236.05	X	2	4942
25R-6, 78	236.11	X	2	6255
25R-7, 11	236.29	X	3	5071
25R-7, 11	236.29	X	3	4902
25R-7, 108	237.26	X	3	4980
26R-1, 30	238.30	X	2	5588
26R-1, 40	238.40	X	2	5536
26R-1, 46	238.46	X	2	5696
26R-1, 80	238.80	X	2	4969
26R-1, 93	238.93	X	2	4856
26R-1, 94	238.94	X	3	4775
26R-1, 108	239.08	X	2	5489
26R-1, 120	239.20	X	2	5612
26R-1, 130	239.30	X	2	5559
26R-2, 2	239.50	Z	2	5692
26R-2, 4	239.52	X	2	5538
26R-2, 20	239.68	X	2	5387
26R-2, 22	239.70	X	2	5767
26R-2, 33	239.81	X	2	5708
26R-2, 42	239.90	X	2	5701
26R-2, 57	240.05	X	3	5683
26R-2, 92	240.40	X	2	5743
26R-2, 133	240.81	X	2	5457
26R-2, 134	240.82	X	3	5203
26R-2, 143	240.91	X	2	5384
26R-3, 31	241.25	X	2	5565
26R-3, 35	241.29	X	2	4975
26R-3, 36	241.30	X	3	4929
26R-3, 75	241.69	X	2	5049
27R-1, 15	247.75	X	2	3908
27R-1, 24	247.84	X	2	3732
27R-1, 42	248.02	X	2	4018
27R-1, 56	248.16	X	3	3842
27R-1, 60	248.20	X	2	3648
27R-1, 84	248.44	X	2	4623
27R-1, 128	248.88	X	2	4530
27R-2, 91	250.00	X	2	3869
27R-2, 103	250.12	X	2	3789
27R-2, 108	250.17	X	2	3850
27R-2, 117	250.26	X	2	3755
27R-3, 88	251.46	X	2	3244
27R-3, 96	251.54	X	2	3788
27R-3, 108	251.66	X	2	4188
27R-4, 6	251.98	Y	4	4706
27R-4, 9	252.01	X	2	4629
27R-4, 36	252.28	X	2	4514
27R-4, 41	252.33	X	2	4465
27R-4, 52	252.44	X	2	4497
27R-4, 67	252.59	X	4	4734

Table T17 (continued).

Core, section, interval (cm)	Depth (mbsf)	Direction	Type of sample	Velocity (m/s)
28R-1, 19	252.59	X	2	4520
27R-4, 68	252.60	X	3	4920
27R-4, 68	252.60	Y	3	4695
27R-4, 68	252.60	Z	3	4431
28R-1, 26	252.66	X	2	4798
27R-4, 85	252.77	X	2	4232
28R-1, 38	252.78	X	2	4686
27R-4, 97	252.89	X	2	4388
28R-1, 50	252.90	X	2	4556
28R-1, 71	253.11	X	2	4762
28R-1, 100	253.40	X	2	4817
28R-1, 117	253.57	X	2	4874
28R-1, 121	253.61	X	2	4784
28R-2, 10	254.00	X	2	4975
28R-2, 37	254.27	X	2	5505
28R-2, 46	254.36	X	2	5726
28R-2, 59	254.49	X	2	5456
28R-2, 74	254.64	X	2	5312
28R-2, 95	254.85	X	2	5638
28R-2, 119	255.09	X	2	5764
28R-3, 10	255.49	X	2	5694
28R-3, 23	255.62	X	2	5972
28R-3, 36	255.75	X	2	5862
28R-3, 61	256.00	X	2	5694
28R-3, 114	256.53	X	2	5561
28R-3, 125	256.64	X	2	5709
28R-4, 6	256.95	X	2	5351
29R-1, 35	257.55	X	2	4602
29R-1, 57	257.77	X	2	4614
29R-1, 77	257.97	X	2	4573
29R-1, 84	258.04	X	2	4606
29R-1, 90	258.10	X	2	4713
29R-1, 101	258.21	X	2	4679
29R-2, 13	258.59	X	2	4850
29R-2, 35	258.81	X	2	4875
29R-2, 43	258.89	X	2	4555
29R-2, 65	259.11	X	2	3688
29R-2, 85	259.31	X	2	4623
29R-2, 96	259.42	X	2	4338
29R-2, 112	259.58	X	2	4540
29R-3, 15	260.05	X	2	4227
29R-3, 34	260.24	X	2	3897
29R-3, 48	260.38	X	2	3656
29R-3, 67	260.57	X	2	4332
29R-3, 90	260.80	X	2	4102
29R-3, 130	261.20	X	2	3826
29R-4, 39	261.79	X	2	4037
30R-1, 10	262.00	X	2	3975
29R-4, 66	262.06	X	2	3742
30R-1, 20	262.10	X	2	3847
29R-4, 81	262.21	X	2	3940
30R-1, 45	262.35	X	2	3914
29R-4, 100	262.40	X	2	3812
30R-1, 90	262.80	X	2	4081
30R-1, 103	262.93	X	3	4156
30R-1, 110	263.00	X	2	3973
30R-2, 2	263.26	X	2	4055
30R-2, 20	263.44	X	2	3998
30R-2, 40	263.64	X	2	4179
30R-2, 50	263.74	X	2	4060
30R-2, 72	263.96	X	3	4160
30R-2, 84	264.08	X	2	4158
30R-3, 5	264.28	X	2	4302
30R-3, 10	264.33	X	2	4434
30R-3, 15	264.38	X	2	4496
30R-3, 23	264.46	X	2	4480
30R-3, 41	264.64	X	2	4296
30R-3, 53	264.76	X	2	4006
30R-3, 57	264.80	X	2	4144
30R-3, 61	264.84	X	2	4136
30R-3, 70	264.93	X	2	4243
30R-3, 76	264.99	X	2	4574
30R-3, 111	265.34	X	2	4234
30R-4, 6	265.57	X	2	4231
30R-4, 18	265.69	X	2	4147
30R-4, 20	265.71	X	3	4328
31R-1, 29	266.89	X	2	4351
31R-1, 50	267.10	X	2	4236
31R-1, 57	267.17	X	2	4126
31R-1, 72	267.32	X	2	4226
31R-1, 78	267.38	X	2	4257
31R-1, 90	267.50	X	2	4218
31R-1, 101	267.61	X	2	4305
31R-1, 125	267.85	X	2	4749
31R-1, 125	267.85	X	3	4393
31R-1, 131	267.91	X	2	4547
31R-1, 138	267.98	X	2	4317
31R-2, 25	268.35	X	2	4660
31R-2, 38	268.48	X	2	4821
31R-2, 43	268.53	X	2	4670
31R-2, 48	268.58	X	2	4699
31R-2, 54	268.64	X	2	4674
31R-2, 61	268.71	X	3	4842
31R-2, 65	268.75	X	2	5024
31R-2, 80	268.90	X	2	4882
31R-2, 112	269.22	X	2	4651
31R-2, 139	269.49	X	2	4911
31R-3, 3	269.63	Z	3	5092
31R-3, 7	269.67	X	2	5146
31R-3, 13	269.73	X	2	5022
31R-3, 21	269.81	X	3	5040
31R-3, 30	269.90	X	2	4934
31R-3, 69	270.29	X	2	5784
31R-3, 87	270.47	X	2	5048
31R-4, 12	270.62	X	2	5763
31R-4, 22	270.72	X	2	5862
31R-4, 36	270.86	X	2	5286
31R-4, 46	270.96	X	2	5164
31R-4, 56	271.06	X	2	5199
31R-4, 69	271.19	X	2	5132
31R-4, 86	271.36	X	2	5083
31R-4, 125	271.75	X	2	4991
31R-4, 125	271.75	X	3	4817
31R-4, 133	271.83	X	2	4818
31R-4, 144	271.94	X	2	4727
31R-5, 6	272.06	X	2	4322
31R-5, 50	272.50	X	2	4672
31R-5, 54	272.54	X	3	4805
31R-5, 60	272.60	X	2	5099
31R-5, 73	272.73	X	2	4879
31R-5, 131	273.31	X	2	4896
31R-6, 2	273.41	X	2	5082
31R-6, 15	273.54	X	2	5190
31R-6, 26	273.65	X	2	5194
31R-6, 42	273.81	X	2	5109
31R-6, 115	274.54	X	2	4595
31R-7, 24	275.13	X	2	4334
31R-7, 62	275.51	X	2	4555
31R-7, 64	275.53	X	3	4534
31R-7, 123	276.12	X	2	4618
32R-1, 4	276.14	X	2	4860
31R-7, 129	276.18	X	2	4740
32R-1, 14	276.24	X	2	4478
31R-7, 140	276.29	X	2	4500
32R-1, 40	276.50	X	2	4757
32R-1, 51	276.61	X	2	4683
32R-1, 59	276.69	X	3	4868
32R-1, 65	276.75	X	2	4844

Table T17 (continued).

Core, section, interval (cm)	Depth (mbsf)	Direction	Type of sample	Velocity (m/s)
32R-1, 74	276.84	X	2	4850
32R-2, 6	277.03	X	3	4928
32R-2, 10	277.07	X	2	5008
32R-2, 94	277.91	X	2	5744
32R-2, 96	277.93	X	2	5715
32R-3, 6	278.12	X	2	5813
32R-3, 19	278.25	X	2	5722
32R-3, 81	278.87	X	3	4999
32R-3, 82	278.88	X	2	5001
32R-3, 123	279.29	X	2	4610
32R-4, 5	279.45	X	2	4653
32R-4, 13	279.53	X	3	4550
32R-4, 14	279.54	X	2	4381
32R-4, 23	279.63	X	2	4376
32R-4, 36	279.76	X	2	5011
32R-4, 54	279.94	X	2	4621
32R-4, 61	280.01	X	2	4815
32R-4, 81	280.21	X	2	4049
32R-4, 100	280.40	X	2	4496
32R-4, 110	280.50	X	2	4452
32R-4, 140	280.80	X	2	4092
32R-5, 4	280.85	X	2	3982
32R-5, 14	280.95	X	2	3866
32R-5, 24	281.05	X	2	4140
32R-5, 50	281.31	X	2	4068
32R-5, 94	281.75	X	2	4273
32R-5, 103	281.84	X	2	4179
32R-5, 116	281.97	X	2	4337
32R-5, 118	281.99	X	3	4638
32R-5, 132	282.13	X	2	4145
32R-5, 140	282.21	X	2	4245
32R-6, 10	282.32	X	2	4530
32R-6, 25	282.47	X	2	4506
32R-6, 55	282.77	X	2	4771
32R-6, 92	283.14	X	3	4930
32R-6, 93	283.15	X	2	4858
32R-6, 110	283.32	X	2	4727
32R-6, 130	283.52	X	2	4596
32R-6, 140	283.62	X	2	4639
32R-7, 4	283.76	X	2	4850
32R-7, 14	283.86	X	2	4465
32R-7, 30	284.02	X	3	4757
32R-7, 34	284.06	X	2	4549
32R-7, 40	284.12	X	2	4761
32R-7, 51	284.23	Z	4	4996
32R-7, 55	284.27	X	2	4864
33R-1, 3	285.53	X	3	4776
33R-1, 7	285.57	X	2	4904
33R-1, 28	285.78	X	2	4874
33R-1, 39	285.89	X	2	4780
33R-1, 53	286.03	X	2	4755
33R-1, 74	286.24	X	2	4770
33R-1, 80	286.30	X	2	4727
33R-1, 92	286.42	X	2	4362
33R-1, 103	286.53	X	2	4676
33R-1, 115	286.65	X	2	4012
33R-1, 124	286.74	X	2	4351
33R-1, 131	286.81	X	2	3230
33R-1, 136	286.86	X	3	4376
33R-1, 140	286.90	X	2	4619
33R-2, 14	287.11	X	2	4509
33R-2, 19	287.16	X	2	4158
33R-2, 30	287.27	X	2	3836
33R-2, 41	287.38	X	2	2831
33R-2, 45	287.42	X	3	3085
33R-2, 49	287.46	X	2	2964
33R-2, 59	287.56	X	2	3153
33R-2, 70	287.67	X	2	3530
33R-2, 70	287.67	X	2	3596
33R-2, 77	287.74	X	3	3066
33R-2, 83	287.80	X	2	3084
33R-2, 95	287.92	X	2	3068
33R-2, 102	287.99	X	2	3892
33R-2, 133	288.30	X	2	3014
33R-2, 133	288.30	X	2	3035
33R-2, 138	288.35	X	2	3626
33R-2, 145	288.42	X	2	3110
33R-3, 3	288.50	X	2	2967
33R-3, 23	288.70	X	2	2840
33R-3, 34	288.81	X	2	3140
33R-3, 44	288.91	X	2	3331
33R-3, 70	289.17	X	2	3605
33R-3, 79	289.26	X	3	3430
33R-3, 80	289.27	X	2	3135
33R-3, 83	289.30	X	2	3074
33R-3, 94	289.41	X	2	3334
33R-3, 121	289.68	X	2	3753
33R-4, 3	289.83	X	2	3113
33R-4, 19	289.99	X	2	3098
33R-4, 43	290.23	X	2	2954
33R-4, 56	290.36	X	2	3824
33R-4, 93	290.73	X	2	2741
33R-4, 110	290.90	X	2	2772
33R-5, 23	291.42	X	2	3559
33R-5, 57	291.76	X	2	5214
33R-5, 57	291.76	X	2	3499
34R-1, 23	294.93	X	2	3493
34R-2, 50	295.94	X	2	5696
34R-2, 55	295.99	X	2	5722
34R-2, 67	296.11	X	2	3662
34R-2, 91	296.35	X	2	3361
34R-2, 130	296.74	X	2	4524
34R-3, 93	297.82	X	2	5142
34R-4, 17	298.51	X	2	5090
34R-4, 40	298.74	X	2	4736
34R-4, 58	298.92	X	2	4786
34R-4, 91	299.25	X	2	4849
34R-4, 110	299.44	X	2	4339
35R-1, 103	305.23	X	2	3694
35R-2, 17	305.83	X	2	5265
36R-1, 6	313.66	X	2	4557
36R-1, 20	313.80	X	2	4685
36R-1, 36	313.96	X	2	4930
36R-1, 63	314.23	X	3	4575
36R-1, 71	314.31	X	3	3543
36R-1, 87	314.47	X	2	4662
36R-1, 97	314.57	X	2	4431
36R-1, 113	314.73	X	2	4293
36R-2, 10	315.05	X	2	4642
36R-2, 30	315.25	X	2	5251
36R-2, 49	315.44	X	2	4528
36R-2, 74	315.69	X	2	5378
36R-2, 114	316.09	X	2	4553
36R-2, 123	316.18	X	2	4409
36R-3, 9	316.44	X	2	4315
36R-3, 27	316.62	X	2	4533
36R-3, 56	316.91	X	2	4295
37R-1, 9	322.89	X	2	3180
37R-1, 36	323.16	X	2	3179
37R-1, 65	323.45	X	2	3963
37R-2, 27	323.80	X	2	3399
37R-2, 51	324.04	X	2	3767
37R-2, 71	324.24	X	2	3581
37R-2, 88	324.41	X	2	3708
37R-2, 106	324.59	X	2	3508
37R-3, 15	324.87	X	2	3329
37R-3, 36	325.08	X	2	3284
37R-3, 77	325.49	X	2	3105

Table T17 (continued).

Core, section, interval (cm)	Depth (mbsf)	Direction	Type of sample	Velocity (m/s)
37R-4, 13	325.80	X	2	3232
37R-4, 20	325.87	X	2	3255
37R-4, 76	326.43	X	2	3606
37R-5, 14	326.73	X	2	3806
37R-5, 46	327.05	X	2	3806
37R-5, 65	327.24	X	2	3649
38R-1, 10	327.60	X	2	3572
38R-1, 27	327.77	X	2	3537
38R-1, 53	328.03	X	3	4647
38R-1, 92	328.42	X	2	4579
38R-1, 131	328.81	X	3	4545
38R-2, 6	328.91	X	2	4772
38R-2, 29	329.14	X	3	4930
38R-3, 26	329.58	X	2	4806
38R-3, 69	330.01	X	2	5040
38R-3, 126	330.58	X	2	4788
38R-4, 21	330.89	X	3	4998
38R-4, 31	330.99	X	2	4996
38R-4, 79	331.47	X	2	5686
39R-1, 6	332.26	X	2	5822
39R-1, 22	332.42	X	3	5804
39R-1, 67	332.87	X	2	5112
39R-1, 91	333.11	X	2	5016
39R-1, 122	333.42	X	3	4817
39R-2, 7	333.57	X	3	4657
39R-2, 8	333.58	X	2	4662
39R-2, 50	334.00	X	2	4427
39R-2, 68	334.18	X	2	4496
39R-2, 84	334.34	X	2	4189
39R-2, 92	334.42	X	2	4135
39R-2, 124	334.74	X	2	3961
39R-2, 132	334.82	X	2	4087
40R-1, 4	337.64	X	2	4533
40R-1, 27	337.87	X	2	4563
40R-1, 40	338.00	X	2	4808
40R-2, 6	338.09	X	2	6565
40R-2, 7	338.10	X	3	5238
40R-2, 10	338.13	X	2	5159
40R-2, 20	338.23	X	2	5282
40R-2, 35	338.38	X	2	5286
40R-2, 50	338.53	X	2	5212
40R-2, 66	338.69	X	3	4978
40R-2, 68	338.71	X	2	5030
40R-2, 80	338.83	X	2	4895
40R-2, 90	338.93	X	2	5075
40R-2, 100	339.03	X	2	4849
40R-2, 130	339.33	X	2	4971
40R-3, 8	339.53	X	2	4958
40R-3, 10	339.55	X	3	4994
40R-3, 18	339.63	X	2	5061
40R-3, 18	339.63	X	2	5143
40R-3, 40	339.85	X	2	4895
40R-3, 50	339.95	X	2	5254
40R-3, 60	340.05	X	2	5291
40R-3, 70	340.15	X	2	5430
40R-3, 94	340.39	X	2	5390
40R-3, 103	340.48	X	2	5253
40R-3, 123	340.68	X	2	5219
40R-3, 144	340.89	X	2	5513
40R-4, 4	340.96	X	2	5435
40R-4, 40	341.32	X	2	5529
40R-4, 46	341.38	X	2	5291
40R-4, 76	341.68	X	2	5242
40R-4, 85	341.77	X	2	5561
40R-4, 126	342.18	X	2	5401
40R-4, 129	342.21	X	3	5557
40R-4, 132	342.24	X	2	5498
40R-5, 5	342.42	X	2	4986
40R-5, 18	342.55	X	2	4980
40R-5, 28	342.65	X	2	5342
40R-5, 36	342.73	X	3	5417
40R-5, 40	342.77	X	2	5434
40R-5, 46	342.83	X	2	5468
40R-5, 56	342.93	X	2	5566
40R-5, 70	343.07	X	2	5518
41R-1, 8	343.08	X	2	4959
40R-5, 80	343.17	X	2	5045
41R-1, 20	343.20	X	2	5021
41R-1, 21	343.21	X	3	5016
41R-1, 30	343.30	X	2	4757
40R-5, 109	343.46	X	3	5108
40R-5, 109	343.46	X	2	5076
41R-1, 50	343.50	X	2	4517
40R-5, 120	343.57	X	2	4942
41R-1, 60	343.60	X	2	4291
41R-1, 66	343.66	X	2	4134
41R-1, 88	343.88	X	2	3171
41R-1, 123	344.23	X	2	3728
41R-2, 90	345.40	X	2	2648
41R-2, 108	345.58	X	2	3024
42R-1, 52	348.12	X	4	2871
42R-2, 94	349.15	X	2	2881
42R-2, 134	349.55	X	2	2979
42R-3, 80	350.51	X	2	2909
43R-1, 28	352.48	X	4	3301
43R-1, 28	352.48	Z	4	2950
43R-1, 28	352.48	Y	4	3419
43R-1, 44	352.64	X	2	3445
43R-1, 45	352.65	X	2	3243
43R-1, 70	352.90	X	2	3584
43R-2, 44	353.49	Y	4	3383
43R-2, 44	353.49	Z	4	3263
43R-2, 50	353.55	X	2	3405
43R-2, 90	353.95	X	2	3287
43R-2, 140	354.45	X	2	3158
43R-3, 40	354.92	X	2	3167
43R-3, 47	354.99	X	4	3267
43R-3, 47	354.99	Y	4	3297
43R-3, 47	354.99	Z	4	3031
43R-3, 47	354.99	Z	4	3366
43R-3, 95	355.47	X	2	3072
43R-4, 11	356.04	X	4	3271
43R-4, 11	356.04	Z	4	3152
43R-4, 11	356.04	Y	4	3240
43R-4, 47	356.40	X	2	3281
43R-4, 47	356.40	Y	2	3369
43R-4, 68	356.61	X	2	3310
44R-1, 45	357.35	X	2	3464
44R-2, 4	357.56	X	2	3597
44R-2, 108	358.60	X	2	3657
44R-3, 60	359.40	X	2	3742
44R-4, 12	360.30	X	2	3808
44R-4, 34	360.52	X	2	3476
44R-4, 55	360.73	X	2	4043
44R-4, 68	360.86	X	2	4119
44R-4, 80	360.98	X	2	4572
45R-1, 73	362.43	X	2	4075
45R-1, 90	362.60	X	2	4400
45R-1, 120	362.90	X	2	4524
45R-2, 4	363.01	X	2	4028
45R-2, 15	363.12	X	2	3848
45R-2, 45	363.42	X	2	4297
45R-2, 60	363.57	X	2	4453
45R-2, 90	363.87	X	2	4093
45R-2, 120	364.17	X	2	4345
45R-3, 18	364.45	X	3	5009
45R-3, 20	364.47	X	2	5112
45R-3, 40	364.67	X	2	4942

Table T17 (continued).

Core, section, interval (cm)	Depth (mbsf)	Direction	Type of sample	Velocity (m/s)
45R-3, 60	364.87	X	2	5181
45R-3, 80	365.07	X	2	4847
45R-3, 84	365.11	X	3	4642
45R-3, 84	365.11	X	2	4796
45R-3, 125	365.52	X	2	4745
45R-4, 30	365.87	X	2	5202
45R-4, 50	366.07	X	2	4808
45R-4, 70	366.27	X	2	4735
45R-4, 100	366.57	X	2	5307
45R-4, 102	366.59	X	3	5577
45R-4, 116	366.73	X	2	5578
45R-4, 140	366.97	X	2	5553
46R-1, 2	367.02	X	2	5904
45R-4, 150	367.07	X	2	5631
46R-1, 10	367.10	X	2	5938
46R-1, 11	367.11	X	3	5685
46R-1, 30	367.30	X	2	5909
46R-1, 55	367.55	X	2	5564
46R-1, 80	367.80	X	2	5577
46R-1, 100	368.00	X	2	5658
46R-1, 120	368.20	X	2	5724
46R-1, 140	368.40	X	2	5942
46R-2, 12	368.59	X	2	6000
46R-2, 41	368.88	X	3	5868
46R-2, 45	368.92	X	2	6057
46R-2, 54	369.01	X	2	5648
46R-2, 78	369.25	X	3	5880
46R-2, 78	369.25	X	2	5604
46R-2, 88	369.35	X	2	6067
46R-2, 101	369.48	X	2	6004
46R-2, 121	369.68	X	2	6041
46R-3, 8	369.88	X	2	6080
46R-3, 31	370.11	X	3	5943
46R-3, 35	370.15	X	2	5890

Notes: The directions of the velocity measurements are represented by X (into the core), Y (across the core) and Z (along the core). Type of samples denoted by numbers: 1 = split section with liner, 2 = split section without liner, 3 = minicore, and 4 = cube. This table is also available in **ASCII format.**

Table T18. Thermal conductivity values for Site 1137.

Core, section, interval (cm)	Depth (mbsf)	Thermal conductivity (W/[m·K])
183-1137A-		
2R-2, 75	11.75	1.115
3R-4, 75	23.85	1.052
4R-4, 75	32.85	0.974
5R-4, 75	42.05	1.216
6R-1, 75	46.75	1.019
7R-4, 75	60.45	1.111
8R-3, 75	68.55	1.109
9R-3, 75	78.25	0.708
11R-3, 75	97.45	1.129
13R-4, 75	118.15	1.131
14R-2, 75	124.85	1.013
15R-3, 75	135.95	1.063
16R-3, 75	145.55	1.252
17R-3, 75	155.15	1.165
18R-1, 75	161.75	0.98
19R-1, 75	171.45	0.941
21R-1, 75	190.65	0.983
24R-1, 72-85	219.59	1.354
24R-2, 98-113	221.35	1.563
25R-1, 6-15	228.51	1.643
25R-1, 106-117	229.52	1.522
25R-2, 11-19	229.99	1.54
26R-2, 70-80	240.23	1.672
26R-3, 70-80	241.69	1.632
27R-4, 46-56	252.43	1.593
28R-1, 42-52	252.87	1.541
29R-4, 26-33	261.70	1.155
30R-2, 44-53	263.73	1.201
31R-1, 36-45	267.01	1.454
31R-2, 59-74	268.77	1.496
31R-4, 51-60	271.06	1.471
32R-1, 46-55	276.61	1.656
32R-2, 2-14	277.05	1.418
32R-4, 25-36	279.71	1.5
33R-1, 125-142	286.84	1.94
33R-2, 74-87	287.78	1.225
33R-4, 47-65	290.36	0.867
34R-1, 54-65	295.30	2.647
34R-2, 44-60	295.96	1.978
34R-3, 127-137	298.21	1.804
35R-1, 98-110	305.24	1.873
36R-3, 1-12	316.42	0.962
37R-1, 59-70	323.45	1.314
37R-3, 1-12	324.79	1.367
37R-5, 75-92	327.43	1.474
38R-1, 70-78	328.24	1.498
38R-3, 74-83	330.11	1.573
38R-4, 70-82	331.44	1.572
39R-1, 89-100	333.15	1.985
39R-2, 73-84	334.29	1.915
40R-1, 1-8	337.64	1.387
40R-2, 13-24	338.22	1.538
40R-3, 116-125	340.66	1.807
41R-2, 20-33	344.77	1.414
42R-1, 10-18	347.74	0.912
42R-2, 134-147	349.62	1.241
43R-3, 140-150	355.88	1.724
44R-3, 57-66	359.42	1.572
44R-4, 49-86	360.98	1.927
45R-2, 48-68	363.55	1.901
46R-2, 82-96	369.36	1.687

Note: This table is also available in ASCII format.

Table T19. Carbon, nitrogen, sulfur, and hydrogen analyses of sediments from Site 1137.

Core, Type, Section	Depth (mbsf)	$CaCO_3$ (wt%)	IC (wt%)	OC (wt%)	N (wt%)	S (wt%)	H (wt%)
183-1137A-							
1R-1	0.89–0.90	50.94	6.12	0.11	BD	0.12	0.66
2R-1	10.09–10.10	88.05	10.57				
3R-1	19.49–19.50	91.77	11.02				
4R-1	28.49–28.50	95.28	11.44	0.17	0.02	BD	0.02
5R-1	37.69–37.70	91.21	10.95				
6R-1	46.89–46.90	89.35	10.73				
7R-1	56.09–56.10	91.94	11.04	0.36	BD	BD	0.04
8R-1	65.69–65.70	94.97	11.40				
9R-1	75.39–75.40	93.86	11.27				
11R-1	94.59–94.60	94.94	11.40	0.22	BD	BD	0.05
12R-1	104.21–104.22	94.61	11.36				
13R-1	113.79–113.80	92.21	11.07				
14R-1	123.49–123.50	95.17	11.42	0.13	BD	BD	0.04
15R-1	133.09–133.10	95.49	11.46				
16R-1	142.69–142.70	94.73	11.37				
17R-1	152.29–152.30	94.71	11.37	0.07	BD	BD	0.06
18R-1	161.88–161.89	94.34	11.33				
19R-1	171.59–171.60	95.58	11.47				
21R-1	190.77–190.78	92.87	11.15	BD	BD	0.04	0.10
22R-1	199.56–199.57	77.16	9.26				
23R-2	210.68–210.69	75.78	9.10	0.39	BD	0.36	0.14
24R-1	219.20–219.21	3.45	0.41	0.42	BD	0.27	0.46

Note:BD = below detection limit.

Table T20. Carbon, nitrogen, sulfur, and hydrogen analyses of volcanic rocks from Site 1137.

Core, Type, Section	Depth (mbsf)	TC (wt%)	N (wt%)	S (wt%)	H (wt%)
183-1137A-					
25R-1 (Piece 4)	229.46-229.48	0.05	0.04	BD	0.10
25R-3 (Piece 8C)	232.11-232.15	0.04	0.01	BD	0.15
25R-5 (Piece 11)	234.99-235.01	0.04	0.01	BD	0.17
26R-1 (Piece 12)	239.43-239.46	0.03	0.04	BD	0.06
26R-2 (Piece 1)	239.53-239.55	0.03	0.01	BD	0.11
27R-4 (Piece 6)	252.56-252.58	0.07	0.04	BD	0.23
28R-4 (Piece 5)	257.17-257.19	0.04	0.01	BD	0.14
29R-2 (Piece 1)	258.81-258.84	0.06	0.05	BD	0.24
29R-4 (Piece 4)	261.55-261.57	0.10	0.01	BD	0.39
31R-4 (Piece 1C)	270.98-271.01	0.08	0.01	BD	0.22
32R-5 (Piece 12)	281.59-281.63	0.06	0.02	BD	0.29
32R-7 (Piece 1C)	284.20-284.22	0.06	0.01	BD	0.19
33R-3 (Piece 1B)	288.93-288.96	0.02	0.01	BD	0.13
33R-5 (Piece 1)	291.26-291.28	0.01	0.04	BD	0.09
34R-2 (Piece 1D)	296.55-296.57	0.04	0.05	BD	0.03
35R-2 (Piece 5)	306.10-306.12	0.02	0.02	BD	0.02
37R-5 (Piece 1C)	327.14-327.17	0.14	0.05	BD	0.33
38R-3 (Piece 1)	330.15-330.18	0.07	0.04	BD	0.20
39R-1 (Piece 5B)	333.32-333.35	0.04	0.04	BD	0.18
39R-2 (Piece 1)	334.03-334.06	0.04	0.03	BD	0.24
40R-2 (Piece 1D)	339.22-339.24	0.04	0.02	BD	0.19
41R-1 (Piece 1C)	343.68-343.73	0.08	0.02	BD	0.23
41R-1 (Piece 6B)	344.28-344.30	0.03	0.04	BD	0.76
44R-4 (Piece 1B)	360.86-360.89	0.04	0.01	BD	0.22
46R-2 (Piece 3B)	369.39-369.42	0.02	0.05	BD	0.15

Note: BD = below detection limit.

Table T21. Summary of logging operations.

Date (Jan 1999)	Time (UTC)	
5	1530	Hole preparation complete, rig up wireline.
	1740	RIH with HNGS-APS-HLDS-LLD(+TAP).
	1830	Uplog at 900 ft/hr from 364.7 mbsf to seafloor. Rig into hole to TD.
	2030	Uplog at 900 ft/hr from 364.7 to 310 mbsf. Pull out of hole.
	2250	Rig up NGT-FMS-DSI.
6	0010	Rig into hole with NGT-FMS-DSI.
	0055	Uplog at 900 ft/hr from 367.9 mbsf to EOP. Rig into hole for repeat.
	0230	Tight spot prevents the tool going down. Pull out of hole and rig down.
	0330	End of logging operations.

Notes: Drillers total depth = 1387 mbsf; water depth = 1016 mbrf; end of pipe = 81 mbsf. UTC = universal time coordinated. RIH = run in hole. HGNS = hostile-environment natural gamma-ray sonde. APS = accelerator porosity sonde. HLDS = high temperature lithodensity sonde. LLD = deep laterolog. TAP = high-temperature/acceleration/pressure tool. TD = total depth. NGT = natural gamma-ray tool. FMS = Formation MicroScanner. DSI = dipole shear sonic imager. EOP = end of pipe.